Spring 5-7-2011

Defining a Molecular Mechanism for Lead Toxicity via Calcium-Binding Proteins

Michael Kirberger

DEFINING A MOLECULAR MECHANISM FOR LEAD TOXICITY VIA CALCIUM-BINDING PROTEINS

by

MICHAEL KIRBERGER

Under the Direction of Professor Jenny J. Yang

ABSTRACT

Essential metals like Ca^{2+} and Zn^{2+} play critical roles in biological processes through protein interactions. Conversely, non-essential metals (e.g., Gd^{3+} and Pb^{2+}) also interact with proteins, often with toxic effects. Molecular metal toxicity is assumed to be due to ionic displacement, and studies have demonstrated that Pb^{2+} replaces Zn^{2+}, Ca^{2+} and other essential metals in proteins. The focus of this work was to compare protein Ca^{2+} and Pb^{2+} -binding sites and to investigate a mechanism of Pb^{2+} toxicity in Ca^{2+}-binding proteins, particularly the intracellular trigger protein calmodulin (CaM) which binds four Ca^{2+} ions and interacts with numerous molecular targets via Ca^{2+}-induced conformational change.

A statistical analysis of PDB structural data for Pb^{2+} and Ca^{2+}-binding (EF-hand and non-EF-hand) proteins revealed fewer binding ligands in Pb^{2+} sites (4 ± 2), than non-EF-Hand (6 ± 2) and EF-Hand (7 ± 1) Ca^{2+}-binding sites. Pb^{2+} binds predominantly with sidechain Glu (38.4%), which is less prevalent in both non-EF-Hand (10.4%) and EF-Hand (26.6%) sites. Interestingly, analyses of proteins where Pb^{2+} replaces Ca^{2+} (calmodulin) or Zn^{2+} (5-aminolaevulinic acid dehydratase) revealed structural changes presumably unrelated to ionic displacement. These results suggested that Pb^{2+} adopts

diverse binding geometries and that opportunistic binding outside of known Ca^{2+}-binding sites may play a role in molecular metal toxicity.

Ca^{2+}-binding affinities (K_d) using phenylalanine and tyrosine fluorescence were found to be 1.15 ± 0.68 X 10^{-5} M and 2.04 ± 0.02 X 10^{-6} M for the N- and C-terminal domains, respectively. The K_d for Pb^{2+}-binding in the N-terminal domain, 1.40 ± 0.30 X 10^{-6} M, was 8-fold higher than Ca^{2+}. Binding of Pb^{2+} in the C-terminal domain produced a biphasic response with K_d values 7.34 ± 0.95 X 10^{-7} M and 1.93 ± 0.32 X 10^{-6} M, suggesting a single higher affinity Pb^{2+}-binding site in the C-terminal domain with nearly equivalent affinity for the remaining sites. Competitive effects of Pb^{2+} added to Ca^{2+}-loaded CaM were examined using multiple NMR techniques. Pb^{2+} was found to displace Ca^{2+} only in the N-terminal domain, however structural/dynamic changes were observed in the central helix apparently due to Pb^{2+}-binding in secondary sites. These data supported our hypothesis that CaM structure and function is altered by opportunistic Pb^{2+}-binding.

INDEX WORDS: Calcium, Lead, EF-Hand, Calmodulin, Toxicity

DEFINING A MOLECULAR MECHANISM FOR LEAD TOXICITY VIA CALCIUM-BINDING PROTEINS

by

MICHAEL KIRBERGER

A Dissertation Submitted in Partial Fulfillment of the Requirements for the Degree of

Doctor of Philosophy

in the College of Arts and Sciences

Georgia State University

2011

DEFINING A MOLECULAR MECHANISM FOR LEAD TOXICITY VIA CALCIUM-BINDING PROTEINS

by

MICHAEL KIRBERGER

Committee Chair: Jenny Yang

Committee: Markus Germann

Aimin Liu

Robert Wolhueter

Electronic Version Approved:

Office of Graduate Studies

College of Arts and Sciences

Georgia State University

May 2011

Acknowledgements

I would like to express my appreciation for the many people who have either contributed to the work presented in this dissertation, or have supported my efforts during the course of my time at Georgia State University. First and foremost I would like to thank my research advisor, Dr. Jenny J. Yang, for her support and guidance. I would also like to thank my dissertation committee members Dr. Markus Germann, Dr. Aimin Liu and Dr. Robert Wolheuter, as well as other instructors at Georgia State who have shared their knowledge with me and encouraged me to stay and complete my doctoral degree: Dr. Keith Pascoe; Dr. Laura Kibler-Herzog; and Dr. Giovanni Gadda.

Additionally, I would like to express my appreciation for the members in Dr. Yang's lab with whom I have worked, including: Dr. Hing-Cheung Wong, Dr. Xue Wang, Dr. Ning Chen, Dr. Jin Zou, Dr. Hsiau-wei Lee, Dr. Yubin Zhou, Jingjuan Qiao, Jie Jieng, Shen Tang, Yanyi Chen, Shenghui Xue, Ling Wei and Adriana Castiblanco.

Finally, I wish to thank my wife Barbara, and my children, Connor, Caoilinn, and Logan, for their love, support, and for patience while enduring this long process.

Funding for this work was provided by NIH Grants GM070555, GM 62999-1 and a Molecular Basis of Disease Fellowship from Georgia State University.

Table of Contents

List of Tables

List of Figures

List of Abbreviations

BCA	Bifunctional Chelating Agent
CaBP	Calcium-Binding Protein
CaM	Calmodulin
CD	Circular Dichroism
CD2	Cell Differentiation 2
Cx	Connexin
DTT	Dithiothreitol
EDTA	ethylenediaminetetraacetic acid
EGTA	ethylene glycol tetraacetic acid
FID	Free induction decay
FPLC	Fast Protein Liquid Chromatography
HSQC	Heteronuclear Single Quantum Coherence
ICP	Inductively-Coupled Plasma
IPTG	Isopropyl-beta-D-thiogalactopyranoside
K_d	Dissociation constant
LB	Luria-Bertani
mAb	Monoclonal Antibody
ME	Molar Equivalents
MS	Mass Spectrometry
NMR	Nuclear Magnetic Resonance Spectroscopy
NOESY	Nuclear Overhauser Enhancement Spectroscopy
NTA	nitrilotriacetic acid
RNT	Radionuclide Therapy
SDS	Sodium dodecyl sulfate
TOCSY	TOtal Correlation Spectroscopy
UV	Ultraviolet

1. Introduction

1.1 Metals and metal-binding in protein biochemistry

In the complex chemistry of life, the versatile adaptations of evolution are no more clearly evident than at the interface between the organic and the inorganic. It is not coincidental that metals essential to biological functions are also those abundant in the earth's crust, including sodium, potassium, iron, zinc, magnesium, calcium and manganese. These metals confer or alter the functions of biological processes by binding with proteins and nucleic acids.

Metalloproteins play significant roles in numerous biological processes, and approximately 40% of all natural proteins are known to bind metals [1-7]. Proteins exhibit selectivity for different physiologically-relevant metals depending on their environment and the nature of their functions, which is how Ca^{2+}-sensor proteins selectively bind intracellular Ca^{2+} in an environment with 4-fold higher levels of Mg^{2+}. Properties of both the protein and the metal ion contribute to both affinity and selectivity. These properties include formal charge (FC) on the ion and in the microenvironment of the binding site; ligand atom type and sidechain preference; ionic radius, and; electronegativity and electron-donating capability.

Metal-binding sites in proteins can be characterized by a central shell of hydrophilic ligands to chelate the ion, with a surrounding shell of hydrophobic residues (Figure 1.1) [8-9]. The most common biologically-important metals (e.g. – Mg^{2+}, Zn^{2+}, Ca^{2+}, Mn^{2+}) frequently bind proteins selectively in different geometric configurations, utilizing different electron-donating Lewis bases as ligand atoms, mainly oxygen, nitrogen and sulfur from sidechain groups, and oxygen from mainchain carbonyls [10-19].

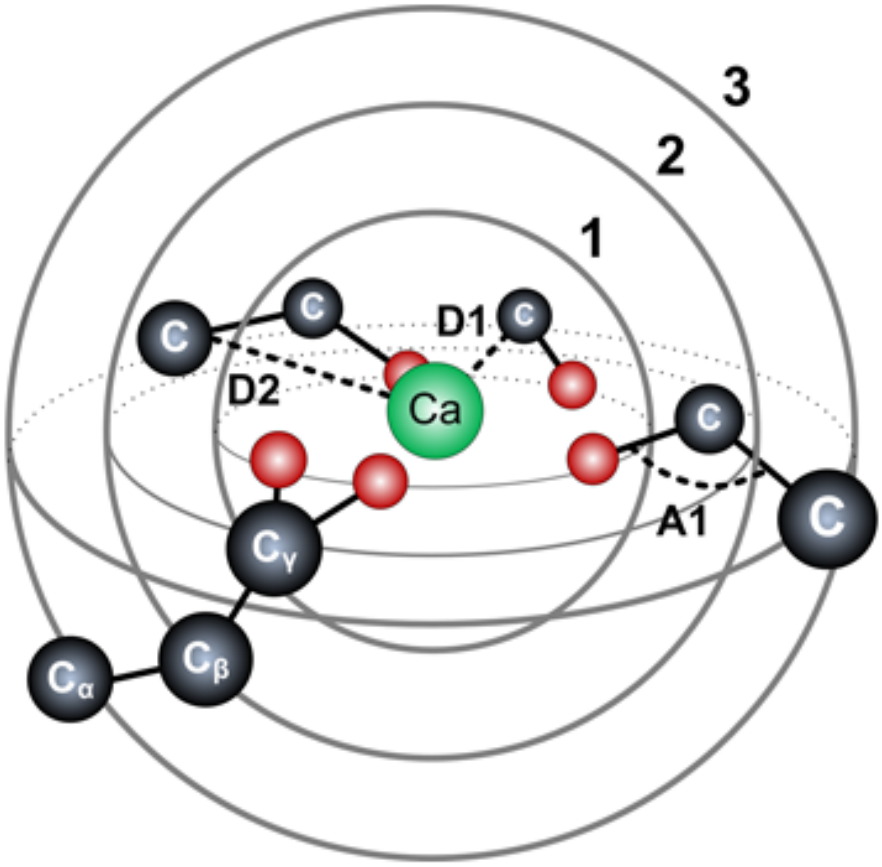

Figure 1.1 General model of metal binding site
Ca^{2+} is surrounded by a 1st shell of hydrophilic ligands (oxygen), which is in turn surrounded by concentric 2nd and 3rd shells of hydrophobic atoms; in this example covalently-bound carbon from sidechains.

Proteins that require metal cofactors become functionally active upon binding their target ions. This does not however, preclude occupancy of the binding site by other ions, which may initiate weak activity in the protein, or may be benign. Calcium-binding proteins may, for example, bind Mg^{2+} ions at low affinity in a resting state, which is then replaced by Ca^{2+} resulting in a fully-potentiated conformer. Additionally, competing metals may induce toxicity by effectively occupying the native site, which alters the microenvironment, and thus the overall conformation, sufficiently enough to inhibit protein function.

1.2 Non-essential metals: toxicity and potential applications

The interactions between proteins and non-essential metals are not understood as well as those between proteins and essential metals. It can generally be assumed that the majority of these metals (e.g., Be^{2+}, Cd^{2+}, Pb^{2+}, Hg^{3+}, Cr^{6+}, As^{3+}, Tl^{3+}, Gd^{3+}, Lu^{3+}, Ga^{3+}, In^{3+}, Y^{3+}) fulfill no beneficial biochemical roles, and nature provides us with few examples of proteins designed to bind these metals. Two recent studies have reported bacterium capable of encoding sensor proteins for toxic metals [20-22], including *Ralstonia metallidurans*, which possesses the first identified bacterial resistance determinant found to be specific for Pb^{2+} [23].

Understanding the behavior of these metals in biological systems is important for several reasons. First, many of these metals are toxic and represent serious global health threats. Examples of this include: As^{3+} in groundwater which affects ~40 million people in Bangladesh, India and China; Hg^{3+} (as methylmercury) which bioaccumulates in the aquatic food chain; and Pb^{2+}, an anthropogenic toxicant whose bioavailability has increased as a result of human industry.

Lead (Pb^{2+}) toxicity remain a persistent threat in the United States primarily in the form of paint used in houses prior to the 1970's and residual lead absorbed in the soil from lead-based gasoline. According to the most recent CDC survey, data collected from 1997-2006 indicated 250 000 children in the US exhibiting Blood Lead Levels (BLL's) exceeding the current, standard 'acceptable' level of 10µg/dL [24]. Additionally, studies from other countries in the last decade have reported high percentages of children with BLL's >=10µg/dL, including China (33.8%) [25], India (51.4%) [26] and South Africa (78%) [27].

Second, many of these non-essential metals have known or potential diagnostic or therapeutic applications, including: Gd^{3+} in MRI contrast agents, Pt^{2+} in cisplatin used

in chemotherapy, and Lu^{3+} or Pb^{2+} which may eventually play important roles in radionuclide therapy (RNT).

1.3 Physiological effects of lead (Pb^{2+}) toxicity

From a clinical perspective, the effects of exposure to toxic metals are well-documented. General physiological and biochemical problems associated with exposure to Pb^{2+} include neurological disorders related to the central and peripheral nervous systems [28-32], interference with heme biosynthesis [33], anemia [34], nephrotoxicity [35], hypertension [36] and both male [37-38] and female [39] reproductive disorders. Potential carcinogenic and genetic effects associated with lead toxicity have been reviewed by Johnson [40]. These effects also vary by age: Children having BLL's less than 5 µg/dL may exhibit impaired neurological development including learning disabilities and behavioral problems [41-42]. The extensive systemic nature of these effects (Figure 1.2), also observed with other toxic metals, suggests that toxic metals like Pb^{2+} likely affect multiple molecular targets.

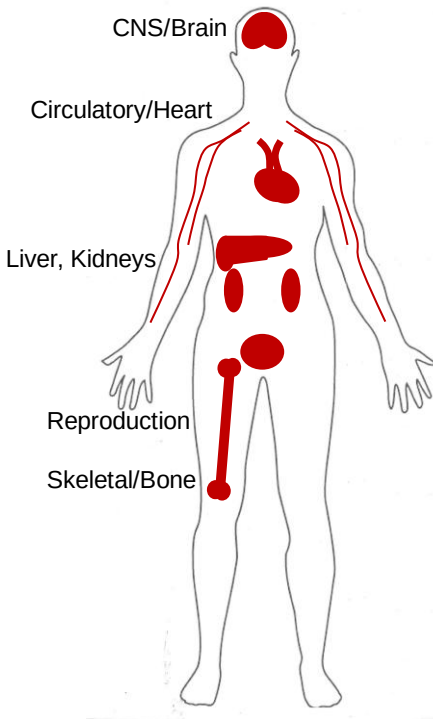

Figure 1.2 Physiological targets for Pb^{2+} toxicity

1.4 Mechanisms of metal toxicity and Pb^{2+}-binding in proteins

At a molecular level, two general mechanisms are believed to be responsible for metal toxicity: primary displacement of essential metals (e.g., ionic mimicry [43], Figure

1.3), and a secondary effect of oxidative stress due to interference with enzymes that maintain reducing state in cells [44].

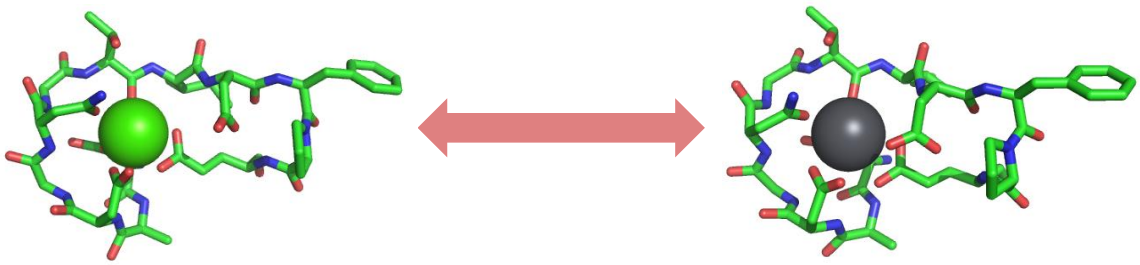

Figure 1.3 Ionic displacement as mechanism of metal toxicity
The Ca^{2+} ion (left) in site EF-II of calmodulin is displaced by Pb^{2+} (right).

Ionic displacement is believed to be the mechanism associated with several types of Pb^{2+}-induced anemia, first identified almost a century ago [34]. Pb^{2+} has been found to displace Mg^{2+} in pyrimidine 5'-nucleotidase type 1 (P5N-1) [45], inhibiting the activity of the enzyme. This decreased activity results in increased concentrations of pyrimidines with an increased rate of destruction of red blood cells leading to anemia [46]. Pb^{2+} has also been shown to replace Zn^{2+} in 5-aminolevulinic acid dehydratase (ALAD), an important enzyme in heme synthesis, resulting in iron-deficiency anemia. Interestingly, an important study related to this latter mechanism demonstrated that Mg^{2+}-dependent ALAD activity in plants is not inhibited by Pb^{2+}-binding with oxygen ligands in the Mg^{2+} site, while activity associated with Zn^{2+}-dependent ALAD in animals was significantly diminished as a result of Pb^{2+} interacting with cysteine residues in the Zn^{2+} site [47]. Iron is another important metal which may be a target for Pb^{2+} displacement. Iron plays important roles in heme biosynthesis, including the formation of the heme precursor protoporphyrin, and in the function of Ribonucleotide reductase (RNR) which catalyzes the formation of deoxyribonucleotides through a free radical mechanism. The extent to which Pb^{2+} may be able to directly interfere with the biological roles of iron is not known, but Pb^{2+} has been found to displace Fe^{2+} in divalent cation

transporter-1 (DCT1) [48] which may be involved in transport of Pb^{2+} and cellular uptake, and in the crystal structure of RNR (Appendix, Table A.1).

1.5 Roles of calmodulin and other Ca^{2+}-binding proteins in Pb^{2+}-toxicity

In addition to a strong relationship with proteins that bind Zn^{2+} [49-53], Pb^{2+} toxicity has also been closely-linked to calcium metabolism and calcium-binding proteins [54-57]. Pb^{2+}, Sr^{2+}, Hg^{2+} and Cd^{2+}, and most lanthanides have been found to occupy Ca^{2+}-binding sites in both natural and engineered CaBPs [58-62]. Pb^{2+} has been shown to enter cells through calcium channels [63-65], activate skeletal muscle troponin C (TnC) [66], inhibit CaM-related Ca^{2+}-ATPase activity in rhesus monkey brain [67], and displace Ca^{2+} in synaptotagmin [30].

Two Ca^{2+}-binding proteins that have been strongly implicated as playing potential roles in molecular Pb^{2+} toxicity are protein kinase C (PKC), which is activated by Pb^{2+} at subnanomolar concentrations [68-69] and may be involved in neurological effects of Pb^{2+} toxicity, and the intracellular trigger protein calmodulin (CaM) [52, 70].

Calmodulin (CaM) is one of the most well-known CaBPs. CaM is an α-helical protein comprised of ~148 residues (Figure 1.4a) that undergoes significant conformational changes from the apo-state (Figure 1.4b) after binding up to four calcium ions (Figure 1.4c) in EF-hand sites (Chapter 3).

At a macromolecular level, CaM is divided into two structurally similar domains separated by a transdomain linker region comprising residues 74-82 (Figure 1.4a).

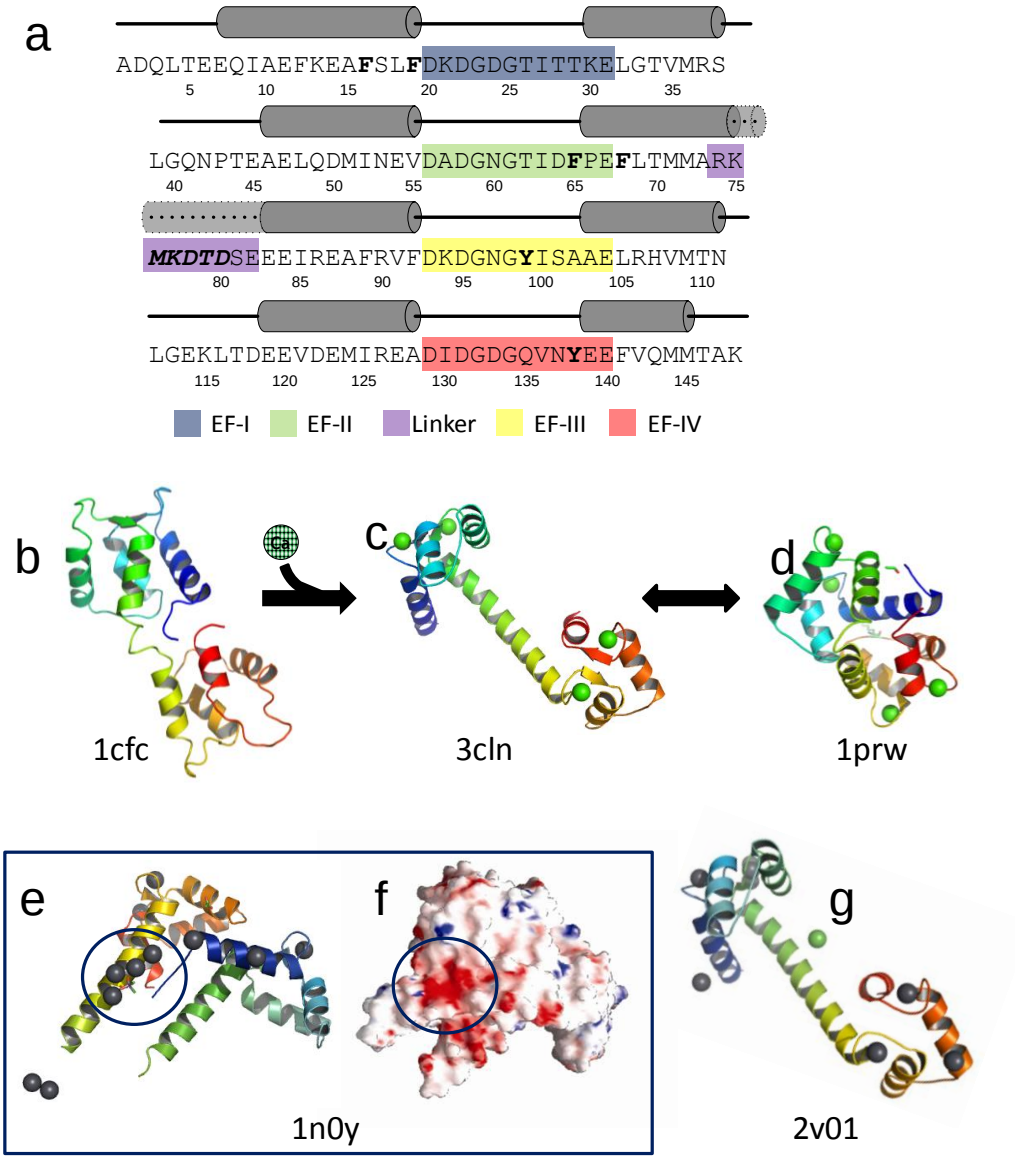

Figure 1.4 CaM sequence and structures

(**a**) Sequence of rat CaM with secondary structure. Fluorescent residues tyrosine and phenylalanine are highlighted in bold. Residues in linker removed for CaM-Delete variant are highlighted in bold italics. This region has been characterized as random coil in (**b**) apo-CaM and as a continuous helix in (**c**) calcium-bound X-ray structures. A dotted line within a transparent grey helix (**a**) depicts the dual nature of this region (residues 75-82). (**d**) NMR studies indicate this region is flexible in solution, and Ca^{2+}-bound CaM may adopt a more compact structure. (**e**) In Pb^{2+}-bound paramecium CaM the two domains converge, presenting a channel between the helices where Pb^{2+} ions cluster in the crystal structure corresponding to (**f**) a region of dense electronegativity. This effect is not observed in a more recent PDB structure (**g**) which suggests an extended helix that may be stabilized by Ca^{2+}. Additional binding sites for Pb^{2+} are observed in both (**e**) 1n0y and (**g**) 2v01 compared to the Ca^{2+}-bound structures.

This functionally-important region appears helical (Figure 1.4c) in X-ray structures [71-72] and as a flexible loop in NMR solution structures [73-74]. The intrinsic flexibility of this region appears to allow the two domains to adopt a closer conformation to one another in solution (Figure 1.4d) [75] and to find their most favorable binding orientation on the surface of bound peptide(s), enabling CaM to perform its myriad functions [74]. Several studies have reported positive intradomain cooperativity observed between EF-Hand binding site pairs in each of the CaM domains in the presence of Ca^{2+} [76-77]. Some level of positive interdomain cooperativity may also exist between the N- and C-terminal domains of CaM [74, 78-79]. This cooperativity may be dependent upon peptide binding [80-82] and would necessarily involve structural or dynamic changes in the transdomain linker region.

A number of studies have investigated the manner in which Pb^{2+} interact with CaM, however, many of these published results and conclusions were frequently contradictory, either with each other or with an assumed mechanism of ionic displacement. A study by Kern [83] reported that Pb^{2+} and Ca^{2+} interact positively to activate CaM. These results suggested that Pb^{2+} occupied the Ca^{2+} sites, but that this occupation did not inhibit the activity of CaM, which argues against displacement as a mechanism of toxicity. Shirran and Barran reported that Pb^{2+} affinity for CaM increases relative to other divalent cations in the presence of Ca^{2+} [84]. These results suggested that Ca^{2+}-induced conformational change either enhanced the binding of Pb^{2+} in some of the Ca^{2+} sites, or produced conformational changes that effectively created new binding sites unique for binding of Pb^{2+}. Chao *et al*. reported that Pb^{2+} and other metals may allosterically bind and activate Ca^{2+}-bound CaM, which suggested that binding of Pb^{2+} outside of the Ca^{2+}-binding sites enhanced Ca^{2+} activation [85].

Interestingly, a later study, also by Chao, reported that Pb^{2+} binding with CaM initially activates then inhibits myosin light-chain kinase (MLCK) [86] in a concentration-

dependent manner. Similar results were reported for CaM-sensitive phosphodiesterase (PDE) [87-88]. These results suggested that Pb^{2+} initially occupied the Ca^{2+} sites to activate the protein, and then inhibited activity by either (a) binding outside of the Ca^{2+} sites, or (b) binding in the Ca^{2+} sites but altering the protein conformation. Assuming that Pb^{2+} can bind CaM outside of the known Ca^{2+} sites, it thus becomes important to determine where and how this occurs.

The potential existence of secondary metal sites in CaM was reported by Milos et al. [89] who indicated that CaM has six auxiliary (secondary) metal binding sites capable of binding both Mg^{2+} and Zn^{2+}, and that all six sites have approximately equivalent affinity for each type of metal ion. This study also indicated that binding of these metals in the secondary sites allosterically antagonized the binding of Ca^{2+} in the known Ca^{2+} sites and vice-versa. The location of these secondary sites was not identified, however, a later study by Bertini *et al*. [90] suggested the presence of a secondary binding site in the trans-domain linker region of CaM based on the reported disappearance of chemical shifts in the HSQC NMR spectrum for residues 78-81(Figure 1.4a) following addition of 0.3 equivalents of Yb^{3+}. The presence of an additional binding site in the linker region of CaM is also observed in the crystal structures of paramecium CaM (1n0y.pdb, Figure 1.4e) corresponding to a region of dense electronegativity, and human CaM (2v01.pdb, Figure 1.4f).

The significant impact of metal binding in the linker region of CaM is illustrated in Figure 1.4. Because intrinsic flexibility in this region (Figure 1.4c) is critical to CaM's ability to bind to target peptides and enzymes in a collapsed conformation (Figure 1.4d), loss of flexibility in this region accompanying binding of a metal ion such as Pb^{2+} would directly interfere with the proteins function.

Ca^{2+}-binding proteins may also play a role in hypertension and heart disease associated with Pb^{2+} toxicity. It is widely-acknowledged that disruption of Ca^{2+}-induced

functions plays a major role in heart disease. Wu *et al*. reported that calpain and calcineurin, two CaBPs that are critical effectors of intracellular Ca^{2+}, may be deregulated due to disruption of calcium homeostasis, resulting in the pathogenesis of several calcium-dependent diseases, including hypertension, heart disease and diabetes [91]. Mattiazzi *et al* [92] demonstrated that activation of the Ca^{2+}-calmodulin dependent protein kinase II is an essential step in contractile recovery of the heart following persistent acidosis.

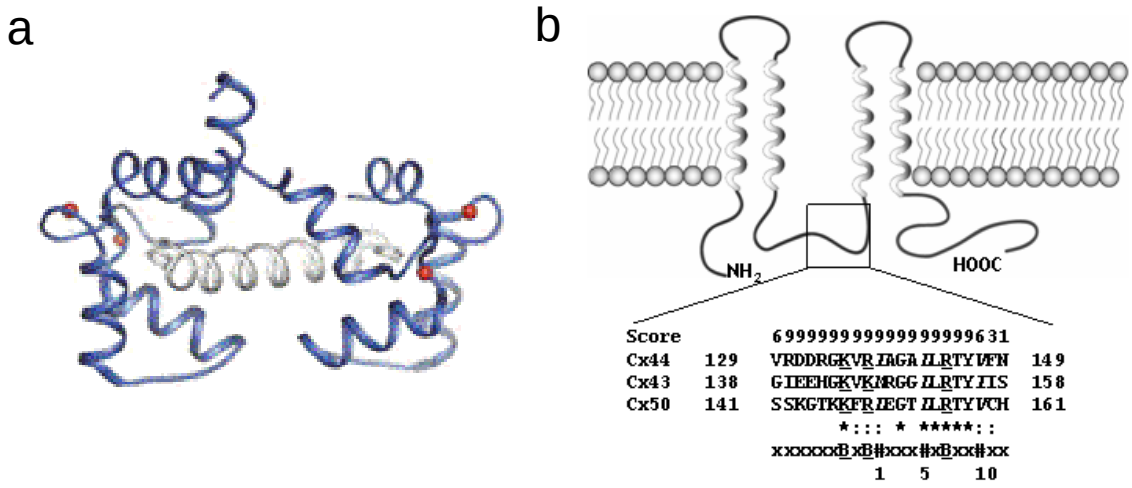

Figure 1.5 Cam:RyR1 complex and putative CaM:connexin interactions
(**a**) Cam:RyR1 peptide complex. CaM is drawn in blue, the RYR1 peptide in white, and the four calcium atoms are shown in red. The sidechains of the RYR1 hydrophobic residues that anchor the two lobes of CaM are shown as sticks. Images were generated in PyMOL [93]. Reproduced from Maximciuc [94]. (**b**) Membrane topology and putative CaM-binding sites predicted in Cx44 and Cx43.

Additionally, Yamaguchi [95] reported that CaM inhibition of cardiac muscle cell Ca^{2+}-release channel ryanodine receptor 2 (RyR2), under certain conditions, can lead to cardiac hypertrophy and early death in mice.

Previous work has demonstrated that CaM regulates the sarcoplasmic reticulum ryanodine receptor Ca^{2+} release channel in both cardiac and skeletal muscle [96-98], and disturbances in both the ryanodine receptor and the voltage gated L-type Ca^{2+} channel that controls Ca^{2+} entry into the myocyte may result in cardiac arrhythmias [99].

Novel work by Maximciuc *et al* [94] revealed the Ca^{2+}-CaM/RyR1 peptide complex (Figure 1.5a).

Similar binding is observed in the case of gap junction connexin complexes with CaM. The gap junctions are comprised of six transmembrane proteins (connexins) embedded in the plasma membrane, forming an extracellular channel that allows for non-selective cell-to-cell transport of low molecular weight molecules. In mammals, gap junctions between cardiac myocytes assist in the coordinated electrical and metabolic coupling between myocytes [100-101]. Three different connexins, Cx43, Cx40 and Cx45, have been identified in cardiac myocyte gap junctions, where Cx43 is dominant in the ventricles and atria [102-103]. Cx40 appears to be limited to the atrial myocytes, Purkinje fibers and sinoatrial and atrioventricular nodes [104-105], while Cx45 is expressed at low levels in the atria and ventricles [102]. Previous studies have demonstrated that normal cardiac function is dependent on all three of these connexins [106-108].

Ryanodine Receptor RyR2, the myocardial muscle channel protein that regulates release of Ca^{2+} from the endo/sarcoplasmic reticulum, is believed to be regulated in turn, by CaM-binding [109-112]. In addition, binding of CaM with gap junction proteins regulates communication and intracellular cytosolic Ca^{2+} concentration which maintains electrical activation and metabolic coupling in the myocardium [113]. Recent work in our laboratory has identified CaM-binding motifs in the primary gap junction proteins in heart muscle connexin43 [114], and connexin44. Calcium binding and calcium dependent conformational change is essential for the regulation of gap junction activities (Figure 1.5b). Various metals including Pb^{2+}, Cd^{2+}, Tb^{3+}, Gd^{3+} and La^{3+} are able to bind with CaM and other CaBPs [58-62, 85, 115-118]. Different toxic metals have been implicated in heart diseases [119-128], therefore an additional future objective of this research is to investigate the mechanism of metal-mediated diseases.

1.6 Statistical and structural analyses of Pb^{2+}-binding and molecular toxicity

To further our understanding of Pb^{2+} toxicity at the molecular level, we conducted statistical analyses of structural parameters associated with the binding of both Ca^{2+} and Pb^{2+} in protein structures deposited in the Protein Data Bank (PDB). Comparative structural analyses were also conducted for two proteins: yeast 5-aminolaevulinic acid dehydratase (ALAD) bound with Zn^{2+} and Pb^{2+}, and CaM from the species *Paramecium tetraurelia* (1exr.pdb and 1n0y.pdb) bound with Ca^{2+} and Pb^{2+}.

CaM was specifically analyzed in both our statistical and empirical studies for several reasons. First, it is an essential signaling protein involved in over 100 biological processes [129-132] and several studies have previously suggested a link between formation of a Pb^{2+}/CaM complex and lead toxicity [52, 70]. Second, two significant studies, using different spectroscopic methods, have reported high affinity binding of Pb^{2+} in the EF-Hand sites of CaM [57, 133]. Similarly, recent work in our lab has confirmed the displacement of Ca^{2+} by Pb^{2+} binding with higher affinity in isolated CaM EF-Hand loops (Chapter 5). This potential for high affinity binding in concert with the essential role of calmodulin involved in various biological processes and calcium signaling may represent an important link to Pb^{2+} toxicity at the molecular level which can be revealed through detailed structural analysis. Third, CaM contains four EF-hand motifs. The availability of two pairs of EF-Hand sites also provided us with an opportunity to study the effects of Pb^{2+}-binding on cooperativity both within the individual domains and globally, and to compare any differences in binding between Ca^{2+} and Pb^{2+}.

Results of our preliminary statistical analysis led us to hypothesize that while ionic displacement of Ca^{2+} by a competing metal ion may represent one mechanism of metal toxicity, an additional opportunistic binding mechanism, resulting from metal-protein interactions in regions lacking an established binding site and related to

electrostatic potential interactions, may contribute to protein misfolding or conformational changes resulting in diminished protein activity and/or metal toxicity. Binding of Pb^{2+} to CaM is illustrated in two crystal structures of the complex from the PDB: 1n0y.pdb and 2v01.pdb (Figure 1.4e and Figure 1.4g). In these figures, Pb^{2+} is observed to bind in the four EF-Hand Ca^{2+}-binding sites of CaM, as well as in regions outside of the known Ca^{2+}-binding sites. Significant conformational changes are apparent in 1n0y (Paramecium CaM) [134] which may be related to binding of Pb^{2+} in the transdomain linker region, which appears folded in Figure 1.4e, forming a pocket of dense electronegative charge (Figure 1.4f). Binding of Pb^{2+} in the EF-Hand sites in solution was reported by Aramini [135] and by Ouyang and Vogel [133]. However, an RMSD analysis of the residues in the binding sites comparing the Ca^{2+}-bound and Pb^{2+}-bound X-ray crystal proteins revealed only minor conformational changes as a result of displacement by Pb^{2+} [136], suggesting that global conformational changes may be associated with some mechanism other than ionic mimicry. Both mechanisms may offer partial explanations for the activation/inhibition of CaM activity reported in related studies [83, 85-86, 88, 137-138].

To test this hypothesis, CaM was used as a model system due to its potential role in toxicity and the extensive data available regarding its calcium-binding properties. Direct titrations of Pb^{2+} and competitive titrations between Pb^{2+} and Ca^{2+} with CaM were analyzed by proton NMR, HSQC-NMR and fluorescence experiments based on metal-induced conformational changes altering the proteins intrinsic Phe and Tyr fluorescences for the N- and C-terminal domains, respectively.

Fluorescence changes in phenylalanine and tyrosine indicate that Pb^{2+} binds CaM with 8-fold higher affinity than Ca^{2+} in the N-terminal domain. An unusual biphasic response was observed in Tyrosine fluorescence associated with C-terminal domain sites EF-III and EF-IV, indicating a single higher affinity Pb^{2+}-binding site with a 3-fold

higher affinity than Ca^{2+}, coupled with a second site exhibiting affinity equivalent to that of the N-terminal domain sites. Similarly, changes in HSQC chemical shifts associated with addition of Pb^{2+} to Ca^{2+}-free CaM suggested binding of Pb^{2+} in site EF-IV first, followed by concurrent binding in the remaining three EF-Hand sites, which differs from the cooperative pairwise binding of Ca^{2+} in the C-terminal domain followed by the N-terminal domain as observed in our results and previously reported by others [139-141].

HSQC spectra, dynamic NOE data and calculation of S2 order parameters for the titration of Pb^{2+} to Ca^{2+}-loaded CaM all indicate that Pb^{2+} displaces Ca^{2+} only in sites EF-I and EF-II. Additionally, the most significant chemical shift changes were observed in the carboxyl-rich linker region (residues 76-84). This provides strong evidence for opportunistic binding of Pb^{2+} outside of the known Ca^{2+}-binding sites and an alternative mechanism for structural changes in the protein. Moreover, this mechanism is consistent with the reported concentration-dependent, biphasic activation and inhibition associated with Pb^{2+}-binding of CaM.

Analyses of structure using NMR indicated dynamic binding of Pb^{2+} in CaM sites EF-I and EF-II, which may be due to changes in coordination ligands suggested in the crystal structures of CaM with Pb^{2+}. These changes further suggest that displacement of Ca^{2+} by Pb^{2+} could effectively disrupt interdomain cooperativity. HSQC-NMR data and the fluorescence experiments both suggested that Pb^{2+} binds in alternate sites on the protein following presaturation with Ca^{2+}. Potential alternate binding sites for Pb^{2+} were investigated, where Pb^{2+} may allosterically induce conformational changes, with particular attention to the transdomain linker region. A second alternate binding site for Pb^{2+} was identified in the C-terminal domain based on a biphasic plot of Tyr fluorescence during the competitive titration of Ca^{2+} to Pb^{2+}-saturated CaM. Pulsed Field Gradient (PFG) NMR was used to evaluate diffusion data for several Pb^{2+}:CaM complexes and calculate hydrodynamic radii for comparison with Ca^{2+}. T_1, T_2 and NOE

data for CaM bound with both Ca^{2+} and Pb^{2+} were acquired using ^{15}N-labelled CaM. These data were further used as input for dynamic studies using ModelFree software [142-143] to evaluate changes in flexibility of the linker region between the two metal-bound states.

1.7 The significant roles of metals in diagnostics and radiotherapy

Understanding the molecular interactions between non-essential metals and proteins is not only important due to their toxicity, but also because of their potential applications in diagnostics and radiotherapy. Current methods of radionuclide therapy utilze either small molecule chelators or murine monoclonal antibodies (mAbs) coupled with chelating moieties to deliver radioisotopes directly to the sites of tumors. The development of hybridoma/monoclonal antibody (mAb) technology by Kohler and Milstein [144] in the mid-1970's quickly led to the development of modified antibodies designed to target tumor-associated antigens. Murine mAbs appeared to offer promising results in cancer therapy during the 1980's, but were limited in efficacy due to a variety of problems including: insufficient activation of effector function; slow blood compartment clearance; low mAb affinity and avidity; transport into normal tissues; heterogeneous antigen distribution on tumor cells and insufficient tumor penetration. Recent improvements have resolved many of these problems, although tumor heterogeneity and penetration remain active areas of research [145].

Antibody proteins may contribute to therapeutic activity by direct tumor-cell killing in two pathways: antibody-dependent cell cytotoxicity (ADCC) or complement-dependent cytotoxicity (CDC) [146]. ADCC occurs when the Fc region of antibody bound to tumor cell is engaged by Fcγ receptor on effector cells. CDC occurs when complement component Clq binds to Fc region of antibody bound to tumor cell surface [145]. Cell killing may then occur through a cell-independent (lysis) or –dependent (phagocytosis)

mechanism [145]. Research has shown favorable therapeutic results using mAbs to treat certain types of cancers, in particular non-Hodgkins lymphoma (NHL) and HER2-receptor-positive breast cancer [145], and several antibody therapies for these cancers are currently available. Rituximab (Rituxan; Genentech/Biogen Idec), an anti-CD20 antibody for non-Hodgkins lymphoma (NHL), was the first FDA approved antibody for cancer therapy (1997). Trastuzumab (Herceptin; Genentech/Roche), is an anti-HER2 antibody for HER2-receptor-positive breast cancer [145].

However, tumor heterogeneity and penetration problems remain a challenge for mAbs. Additionally, these treatments may not be universal. Clinical results have shown that for some patients receiving mAb therapy, the production of human anti-murine immunoglobulin antibodies (HAMA) after 1-3 treatments may counter the effects of mAbs [147]. As research into this area continued, the idea of utilizing the mAb as a targeting system to deliver a radionuclide to the abnormal cells evolved, and was supported by evidence suggesting that coupling the mAbs cell-killing ability with a radioactive metal may produce a synergistic therapeutic effect in the treatment of metastatic breast cancer [148]. However, related studies have suggested that therapeutic doses of radioactivity by mAb delivery require support from either bone-marrow transplantation (BMT) or stem-cell transplantation (SCT) [149-150].

Two pathways for radionuclide linking (Figure 1.6a) are currently the focus of research into this subject: (1) Direct radionuclide linking to mAb, where halogenation reactions (e.g. – ^{131}I) with Tyr residues on mAb covalently bond the radioisotope to the mAb, and (2) The use of bifunctional Chelating Agents (BCAs).

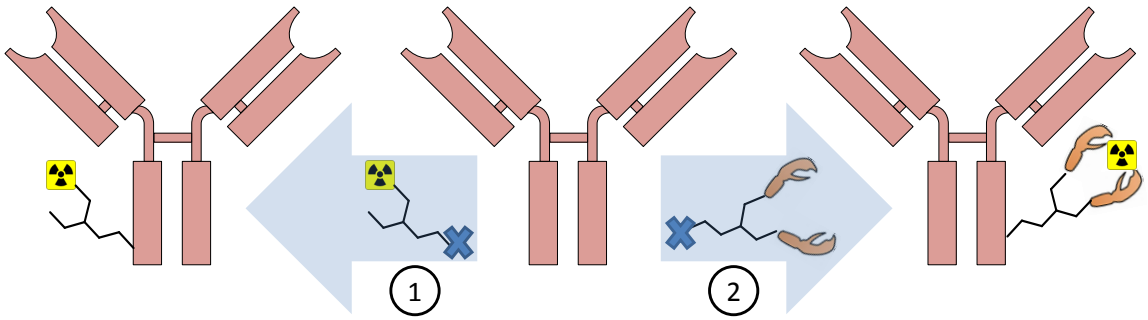

Figure 1.6 Current radionuclide binding methods
Numbers 1-2 in circles indicate pathways for radionuclide association with antibody, either (1) direct iodinization, or (2) conjugation with a bifunctional chelating agent.

These are small molecules that include functional groups to bind both the radionuclide and the protein antibody. Of the two, the latter method appears to offer the most versatility, allowing for the inclusion and application of different radionuclides with different decay pathways. Additionally, problems with the first method include rapid de-iodination that may occur following internalization of the protein [145].

At present, the availability of these treatments is limited, but includes two anti-CD20 mAbs for the treatment of NHL: Zevalin (Biogen Idec), based on radiolabelled mAb ^{90}Y Ibritumomab, and Bexxar (Corixa/GlaxoSmithKline), based on radiolabelled ^{131}I Tositumomab.

The various BCAs currently being evaluated fall into two broad categories: Acyclic or Macrocyclic. Macrocyclic BCAs (Figure 1.7a) include DOTA (1,3,7,10-tetra-azacyclododecane-N,N',N'',N'''-tetraacetic acid). DOTA has been found to form stable complexes with ^{212}Bi and ^{213}Bi, but complex formation requires 15-45 minutes, whereas the half-lives of the two isotopes are 60 and 46 minutes, respectively [151], which arguably limits its effectiveness. Conversely, acyclic BCAs form complexes at faster rates but are reportedly less stable than macrocyclic BCAs (Figure 1.7b). However, the acyclic compound CHX-A'' (a cyclohexyl- DTPA (diethylenetriamine pentaacetic acid)) appears to be an improved alternative to DOTA for labeling mAbs with bismuth [152]. Complex formation with CHX-A'' is nearly instantaneous, and is stable enough for

clinical trials [153]. Additionally, it has exhibited similar stability binding β--emitters ^{90}Y and ^{177}Lu, suggesting the potential for a broader range of clinical applications [154-156].

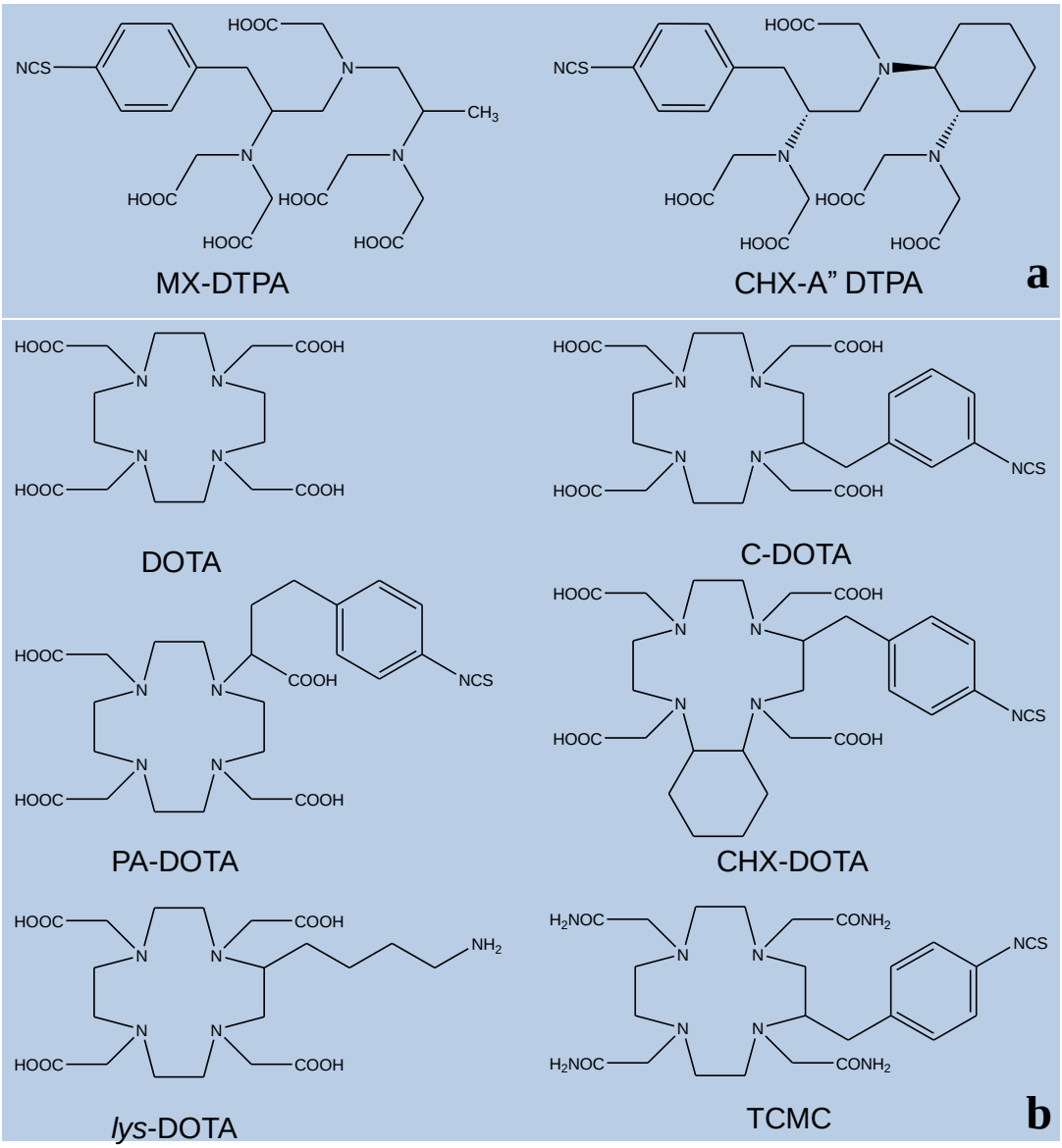

Figure 1.7 Examples of (a) acyclic and (b) macrocyclic BCAs
These small molecules are used in anti-body targeted radiation therapy clinical trials. Conjugation with the antibody occurs via the isothiocyanate functional groups, while radionuclides bind via carboxylate and amine groups.

Thus far, discussion has focused on the therapeutic and targeting capabilities of mAbs, and means of conjugating the radionuclide, ignoring the properties and

importance of the radioisotopes themselves. In another bifurcation, relevant radioisotopes may be generally divided into (a) imaging and (b) therapeutic radionuclides. Imaging radionuclides are used in conjunction with diagnostic technologies, e.g. - γ-Scintigraphy or Single Photon Emission Computed Tomography Imaging (gamma ray imaging). These radionuclide may be introduced intravenously (e.g. - ^{99m}Tc, ^{123}I, ^{131}I, ^{201}Tl, ^{67}Ga, ^{18}F Fluorodeoxyglucose, and ^{111}In Labeled Leukocytes), or as gasses or aerosols (e.g. - ^{133}Xe, ^{81m}Kr, ^{99m}Tc Technegas, ^{99m}Tc DTPA). Imaging radionuclides may be used simultaneously with therapeutic agents, as is the case with ^{90}Y, which lacks an imageable transmission, requiring dosimetry with ^{111}In.

Table 1.1 Properties of metals with known or potential radiotherapy applications

Radionuclide	[a]Ionic Radius (Å)	[a]EN	Decay Type	Half-life	E_{max} (MeV)	Mean Range (mm)	Imageable
$^{90}Y^{3+}$	0.9	1.22	β	2.7 d	2.30	2.76	No
$^{131}I^{1+}$	2.2	2.66	β, γ	8.0 d	0.81	0.40	Yes
$^{177}Lu^{3+}$	0.85	1.27	β, γ	6.7 d	0.50	0.28	Yes
$^{153}Sm^{3+}$	0.96	1.17	β, γ	2.0 d	0.80	0.53	Yes
$^{186}Re^{6+}$	0.56	1.9	β, γ	3.8 d	1.1	0.92	Yes
$^{188}Re^{6+}$	0.56	1.9	β, γ	17.0 h	2.1	2.43	Yes
$^{67}Cu^{2+}$	0.73	1.9	β, γ	2.6 d	0.57	0.6	Yes
$^{225}Ac^{3+}$	1.12	1.1	α, β	10 d	5.83	0.04-0.1	Yes
$^{213}Bi^{3+}$	1.03	2.02	α	45.7 min	5.87	0.04-0.1	Yes
$^{212}Bi^{3+}$	1.03	2.02	α	1.0 h	6.09	0.04-0.1	Yes
$^{211}At^{1\pm}$	[b]1.4	2.2	α	7.2 h	5.87	0.04-0.1	Yes
$^{212}Pb^{2+}$	1.19	2.33	β	10.6 h	0.57	0.6	Yes
$^{125}I^{1+}$	2.2	2.66	Auger	60.1 d	0.35	0.001-0.02	Yes
$^{123}I^{1+}$	2.2	2.66	Auger	13.2 h	0.16	0.001-0.02	No
$^{67}Ga^{3+}$	0.62	1.81	Auger, β, γ	3.3 d	0.18	0.001-0.02	Yes
$^{195m}Pt^{4+}$	0.63	2.28	Auger	4.0 d	0.13	0.001-0.02	No

[a] [157] Pauling electronegativity. [b]atomic radius.

At present, general consensus suggests that most relevant therapeutic radionuclides have been identified, and these are summarized in Table 1.1 [145]. In addition to obvious chemical requirements for stable complex formation, several properties related to the decay type are particularly relevant with respect to

radionuclides. Table 1.2 briefly summarizes the decay modes reported for different nuclides.

Table 1.2 Radioactive decay

Decay	Description
β-	Conversion of neutron to proton due to loss of electron.
E	Also described as inverse β decay. Electron captured by proton to form neutron. Subsequent decay to ground state produces x-ray photon.
A	^{4}He (α-particle) ejected.
Γ	emission of high energy photon.
Auger	An incident electron ejects core electrons from a sample atom, releasing a photoelectron and producing a core hole. Electrons with lower binding energy fill the hole during relaxation, releasing energy either in the form of an Xray or by emitting an electron.

Nuclides that exhibit β^- emissions (^{131}I, ^{90}Y, ^{67}Cu, ^{186}Re, ^{177}Lu) have, to date, received the most attention. Of these, ^{131}I and ^{90}Y are currently being used with FDA approved therapeutics, while ^{67}Cu and ^{177}Lu have been evaluated in clinical trials only [154, 158-159]. The β^- emitters are characterized by low linear energy transfer (LET), or energy transferred to material as ionizing particle travels through it, and longer emission path lengths (275 μm mean, 500-600 μm for ^{90}Y) than α emitters (Figure 1.8) [145]. Moreover, β^- emitters are less constrained by tumor antigen heterogeneity, exhibit differential penetration of the mAb, and may target the lesion uniformly when the emission range exceeds the radius of the targeted lesion. Conversely, disadvantages are also apparent and warrant consideration, particularly as they are correlative with the advantages in many cases. The long linear path length means that energy deposition actually occurs more distant from the decay event, so that the therapeutic effect is experienced not only by the targeted cell, but those cells surrounding it. Although the targeted cell would still receive decay energy from decay of nuclides on adjacent cells,

this reduces the effectiveness of β^- emitters for treatment of single-cell metastatic diseases, leukaemias and disseminated diseases [160]. Additionally, while ^{90}Y delivers ~4.5 more radiation per mCi to tumor than ^{131}I, most of decay energy is deposited in tumors greater than 1 cm in diameter, and damage is likely to occur in surrounding tissues [145]. Other, nuclide-specific problems have also been reported. The potential for ^{67}Cu may be limited as a result of trans-chelation with superoxide dismutase [161-162]. ^{90}Y lacks an imageable transmission, requiring dosimetry with ^{111}In for γ-Scintigraphy or Single Photon Emission Computed Tomography Imaging (gamma ray imaging).

Conversely, α emitters are complementary to β^- emitters in many respects. The α emitters have generally shorter half-lives, producing high-energy particles (4-9 MeV) that travel short distances (40-100 μm) (Table 1.1) with dense emission pathlengths of high LET, approximately 400X greater than β^-emitters [145]. Energy deposition for α emitters occurs at the decay site [160], exhibiting high cytotoxicity at a dose rate of 1 $cGy*hr^{-1}$, or 1 X 10^{-2} $J*Kg^{-1}*hr^{-1}$ [163]. Three α emitters, ^{212}Bi, ^{213}Bi, and ^{211}At are the subjects of increasingly, active study [164-165] and decay by both α and β^- emissions. However, ^{213}Bi may be better candidate than ^{212}Bi as the latter has an abundant high-energy γ – emission that is not shared by ^{213}Bi [166]. Additionally, ^{225}Ac may be a viable isotope, but may present clinical problems due to its longer half-life and may cause in vivo problems due to trafficking of decay products [167]. Nonetheless, these properties indicate that α emitters may be best suited for leukaemias, highly-vascularized tumors and metastatic disease.

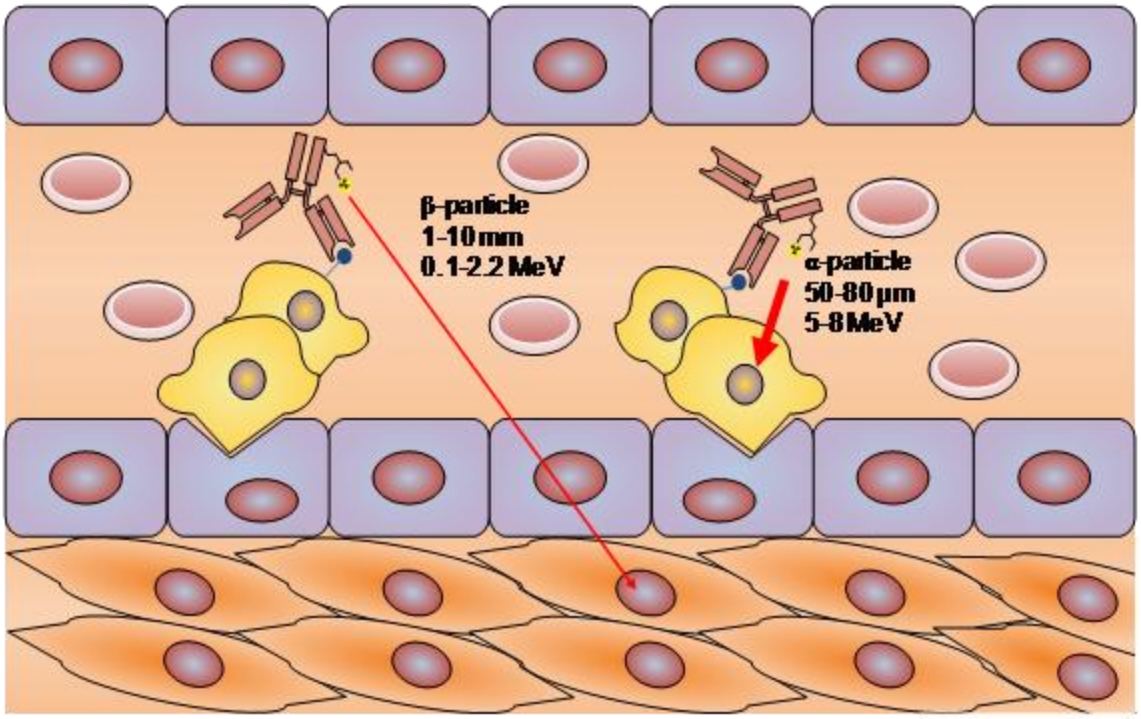

Figure 1.8 α- and β$^-$- particle emissions in antibody-targeted radiation therapy
Decay from the β$^-$- particle exhibits a longer path length with a narrower LET than the α-particle. Reproduced from Milenic [145].

Auger electrons (^{67}Ga, ^{195m}Pt, ^{123}I, ^{125}I) have received the least attention, despite reported extreme cytotoxicity. This form of decay is described by the emission of an electron from an atom which causes the emission of a second electron. When an electron is removed from a core level of an atom, an electron from a higher energy level may fall into the vacancy. The resulting energy may either be released as a photon, or transferred to a second electron. The γ emitters are considered unsuitable due to extremely long decay paths, so our focus will remain with the β$^-$ and α emitters, despite the fact that many of the β$^-$ emitters exhibit multiple decay paths that include γ emission (Figure 1.8).

Several major challenges remain to be overcome in this field, in order to deliver functional therapeutics capable of delivering the radionuclide to specific cells targeted for destruction. In addition to obvious considerations regarding the nature of the isotopes chemistry (i.e. – emission type, LET, half-life), complex stability between the radionuclide and the chelator is critical, yet complex formation with zero dissociation has proven to be a non-trivial problem [145]. Additionally, rapid binding kinetics are required, and as noted, are not necessarily achieved with current small molecule chelators. Another major challenge in radionuclide-based therapies is improving the therapeutic index (i.e. – benefit vs. risk) by devising means to focus cytotoxicity on the abnormal cell nuclei, thereby efficiently destroying cancerous cells while reducing radiation-induced DNA damage in adjacent healthy cells. The development of radioimmunoconjugates, radionuclide-chelating molecules capable of covalently bonding to antibodies, has demonstrated significant progress in this area.To address these challenges, we hypothesize that improved complex formation can be achieved based on rational protein design. Specifically, that metal-binding motifs with high selectivity and affinity for the target radionuclides can be designed based on rigorous understanding of the characteristics and properties associated with these motifs, which may then be either grafted directly onto the antibody

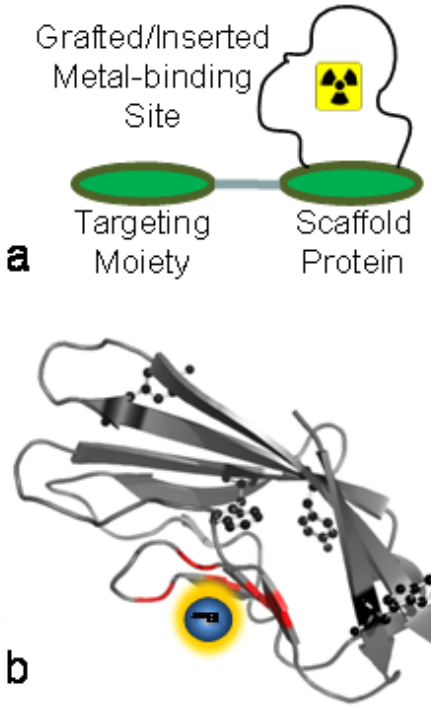

Figure 1.9 Proposed protein-based RNT agent
(**a**) As an alternative to mAbs, a metal-binding site capable of selectively chelating a radionuclide is grafted or inserted into a scaffold protein, which is in turn fused with a biomarker targeting moiety. (**b**) RNT model using CD2 as scaffold protein with Ca^{2+}-binding motif.

in regions distant from the recognition site, or may be synthesized in an engineered protein structure which will subsequently bind to the antibody.

Previous and continuing work in our laboratory has utilized site-directed mutagenesis and grafting methods to synthesize proteins with modified Ca^{2+} and Gd^{3+} binding sites in the development of sensors and MRI contrast agents [62, 168-175] similar to the model proposed in Figure 1.9. These existing constructs (CD2 and variants; N- and C-terminal calmodulin (CaM) domains; and several species of fluorescent proteins) will be utilized in preliminary testing to evaluate binding potential for the development of protein-based radioimmunotherapies.

Based on our current understanding of metal-binding properties with various metals, a sublist of potential radionuclides was selected for analysis which included 4 β^--emitters, 1 α-emitter and 1 γ-emitter (Table 1.1). These radionuclides were selected based on several criteria. First, their ionic radii are similar to either Ca^{2+} or Zn^{2+}, which is important for binding in sites specific to those metals. Second, they generally exhibit high electronegativity (EN) values, which may contribute significantly to binding affinity. Third, they are all commonly the subject of current research, and have either demonstrated some therapeutic efficacy, or, in the case of In^{3+}, are utilized in tandem with another radionuclide (Y^{3+}) for imaging purposes.

1.8 Cell adhesion molecule CD2 as scaffold protein for RNT agent

Domain 1 of cell adhesion molecule CD2 (CD2-D1) has been utilized previously in our laboratory as a scaffold protein for the design of MRI contrast agents (Figure 1.9). CD2-D1 is a 99-residue, predominately β-sheet protein that exhibits remarkable stability over a wide pH range (1-10), and reversibly refolds after both chemical and thermal denaturing. Various efforts have been made in our lab to design a metal binding site in CD2-D1, as summarized in Table 1.3.

Table 1.3 CD2-D1 designed metal-binding sites

				K_d (μM)	
Name	**Mutations**	**Ca(II) Site**	**Charge**	**Ca**	**Tb**
[a]CD2-DEEEE	I18D, F21E, G61E, V80E, I88E	D18, E21, E61, E80, E88	-5		21 ± 3
[b]CD2.Ca1	F21E, V78N, V80E, L89D, K91D	E21, N78, E80, D89, D91	-4	40 ± 10	3 ± 2
[c]CD2.6D15	N15D, N17D	D15, D17, N60, D62	-3	1400 ± 400	8 ± 2
[d]CD2.7E15	N15E, L58D, K64D	E15, E56, D58, D62, D64	-5	100 ± 50	0.4 ± 0.2

[a][118] [b][176] [c][62] [d][177]

1.9 Objectives of this dissertation

The objectives of this research are to understand the structural parameters associated with Ca^{2+}-binding proteins, determine the differences between binding of Ca^{2+} and toxic metals, particularly Pb^{2+}, and investigate the use of Ca^{2+}-binding sites to bind toxic metals with potential application in radiotherapy. The research presented here will focus on the following key objectives:

A. Analyzing Ca^{2+}-binding structures, applying statistical analysis to identify key structural parameters associated with Ca^{2+}-binding, and incorporating these parameters into prediction algorithms

To understand Ca^{2+}-binding in proteins, we will first summarize known data related to different types of Ca^{2+}-binding sites. Next, data for all Ca^{2+}-binding proteins identified in the PDB will be downloaded into a local database and analyzed with respect to charge, ligand type, coordination number, general coordination geometry (e.g., hull parameter), and distance and angle parameters associated with the Ca^{2+} ion, the coordinating ligand atom, and the atom covalently bound to the coordinating ligand atom. Once all statistics are compiled, the resulting values will be used as variables in the development of structure-based prediction algorithms to identify Ca^{2+}-binding sites.

B. Analyzing Pb^{2+}-binding structures comparatively with Ca^{2+}-binding structures

Pb^{2+}-toxicity is closely-linked with both Zn^{2+}- and Ca^{2+}-binding proteins. Our research focus is to analyze a potential route for Pb^{2+} toxicity in Ca^{2+}-binding proteins. In

order to understand Pb^{2+} toxicity from a molecular perspective, we will first analyze all of the structural data in the PDB associated with binding of Pb^{2+}, and then compare the results of this statistical analysis with those obtained from the analysis of Ca^{2+}-binding.

C. Investigating the potential molecular basis for Pb^{2+}-induced toxicity in the Ca^{2+}-binding protein calmodulin

The intracellular trigger protein calmodulin has been identified as a potential molecular target for Pb^{2+}-binding due to its four Ca^{2+}-binding sites. It has been assumed that the function of calmodulin may be disrupted by displacement of Ca^{2+} by Pb^{2+} in the metal binding sites. To investigate this, we will apply several experimental approaches to understand the binding modes of Pb^{2+} with calmodulin including fluorescence spectroscopy and multiple NMR approaches (e.g., 1D, 2D, 3D, relaxation and diffusion NMR experiments).

D. Potential applications of toxic metals in radiotherapy

Radionuclide therapy (RNT) is a growing field of study focusing on targeted delivery of radiation therapy to treat certain types of cancers. Many of the radioactive isotopes with known or potential applications in radiotherapy are toxic in their stable isotopes (e.g., Pb^{2+} and Lu^{3+}). To develop a protein-based chelators for targeted RNT, we will investigate binding assays and the chelating properties of fluorescent dyes for important RNT target metals. We will further investigate binding of these metals with Ca^{2+}-binding sites in scaffold proteins as a prelude to developing metal-specific protein-based RNT agents.

1.10 Significance of this dissertation

The research summarized in this work will **first** provide a comprehensive overview into the nature of Ca^{2+}-binding proteins and the structural characteristics associated with Ca^{2+}-binding. By analyzing these properties from a statistical

perspective, we can provide a set of structural parameters capable of more precisely defining a Ca^{2+}-binding site for computational efforts to predict or design Ca^{2+}-binding sites. Moreover, this approach can be extended to other metals, including Mg^{2+} and Zn^{2+}. Identifying potential metal binding sites provides us not only with insights into the functions of these metals in proteins, but directs us to regions in the proteins where mutations may result in metal-mediated dysfunction leading to diseased states.

Second, this work provides a first examination of the behavior of Pb^{2+} in proteins at a structural level. In the past, the behavior of Pb^{2+} with proteins was predicted based on interactions with small molecules. Our work reveals a more complicated level of interactions with different binding schemes from those previously assumed based on small molecule models.

Third, experimental work with Pb^{2+} and calmodulin reveals an opportunistic binding mode outside of well-defined Ca^{2+}-binding sites, which suggests that toxic metals may influence the behavior of proteins that do not normally bind metals, thus increasing the potential number of molecular targets that may be affected by metal uptake.

Fourth, our preliminary efforts to develop assays and analytical methods for toxic metals demonstrate that many of these metals exhibit unusual behavior compared with physiologically-relevant metals, which often complicates experiments and interpretation of data.

Chapter 2 in this dissertation summarizes the materials and methods used in these studies, including protein expression and purification, spectroscopic techniques (UV-VIS, fluorescence, NMR), methods to control free metal concentrations in samples and buffers, and statistical bases for analyses. All equations used in this study are summarized in this chapter.

Chapter 3 focuses on statistical analysis of EF-hand and non-EF-hand Ca^{2+}-binding sites in proteins for all structures in the PDB. The significance of water molecules in the coordination of non-EF-hand sites is discussed.

Chapter 4 summarizes the results of a statistical analysis of Pb^{2+}-binding sites in proteins, and compares the results against those obtained for Ca^{2+}-binding sites summarized in Chapter 3. A direct structural comparison of calmodulin bound with Ca^{2+} vs. Pb^{2+} is discussed, along with a proposed mechanism of opportunistic binding for Pb^{2+}.

Chapter 5 details experimental results for analysis of calmodulin binding with Ca^{2+}, Pb^{2+}, and the competition between these two metals. The binding affinities for both Ca^{2+} and Pb^{2+} are calculated for the N- and C-terminal domains of calmodulin. Structural changes and chemical exchange associated with metal binding in calmodulin are revealed through NMR HSQC spectra. Dynamic changes associated with metal binding are investigated through relaxation properties including T_1 (longitudinal), T_2 (transverse) and NOE data. These properties are further used to model protein dynamics and establish order parameters for residues in the protein. A mechanism for binding of Pb^{2+} to calmodulin in the Ca^{2+}-loaded state is proposed which includes opportunistic binding of Pb^{2+} outside of the known Ca^{2+}-binding sites.

Chapter 6 summarizes efforts to identify colorimetric and fluorescent dyes capable of binding of Pb^{2+}, Lu^{3+} and other toxic metals over a range of different affinities.

Chapter 7 presents a brief summary of the major conclusions presented in the dissertation.

2 Materials and methods

2.1 Ca^{2+}-binding protein statistics

Table 2.1 Summary of binding distance and angle values

	non-EF-Hand	EF-Hand
Total Binding Sites	1468	137
FC[a]	1 ± 1	3 ± 1
Mean CN[b] PLW[c]	6 ± 2	7 ± 1
Mean CN PL[d]	4 ± 2	6 ± 1
% In Hull	72	100
Bidentate Dihedral Angle	168.1 ± 9.7	170.6 ± 7.1
Mean Ca-O Distance (Å)		
MC[e] Carbonyl	2.4 ± 0.2	2.3 ± 0.1
SC[f]	2.4 ± 0.2	2.4 ± 0.2
Bidentate	2.6 ± 0.3	2.5 ± 0.2
Ca-O Distance Range (Å)		
MC Carbonyl	2.0-3.5	2.0-2.6
SC	1.6-3.5	1.8-3.5
Bidentate	1.8-3.5	2.2-3.5
Mean Ca-C Distance (Å)		
MC Carbonyl	3.5 ± 0.2	3.5 ± 0.1
SC	3.5 ± 0.2	3.4 ± 0.1
Bidentate	2.9 ± 0.2	2.9 ± 0.1
Ca-C Distance Range (Å)		
MC Carbonyl	3.0-4.6	3.1-3.9
SC	2.8-4.6	2.9-3.9
Bidentate	2.4-3.7	2.6-3.4
Mean Ca-O-C Angle (°)		
MC Carbonyl	151.5 ± 15.8	159.8 ± 12.5
SC	140.4 ± 15.2	136.7 ± 16.0
Bidentate	93.6 ± 11.3	92.9 ± 6.8
Ca-O-C Angle Range (°)		
Carbonyl	81-180	126-180
SC	56-180	116-170
Bidentate	61-140	66-120

[a]Negative Formal Charge. [b]Coordination Number.
[c]Protein and Water Ligands. [d]Protein Ligands.
[e] Mainchain. [f]Sidechain.

All data files were downloaded from the PDB, and relevant data were extracted using Matlab (MathWorks, Natick, MA). The PDB file ID and sequence ID for the Ca^{2+} ion associated with each binding sites are summarized in Table A.2. All statistical results were divided into two datasets (Table 2.1): One each for non-EF-Hand and EF-Hand proteins, where the non-EF-Hand protein data set contains 1468 binding sites and the EF-Hand protein dataset contains 137 calcium binding sites, respectively. The preponderance of non-EF-Hand proteins was attributable to the fact that more non-EF-Hand protein structures were available at or below the resolution cutoff of 2.0 Å. A number of EF-Hand proteins were

not identified as such by their SCOP classification, but were later identified using pattern motifs and related software developed in our laboratory [178], and less than 10% of sites classified as EF-Hand sites for the statistical analysis were Pseudo-EF-Hand sites belonging to the S100 family. Summarized values presented in Table 2.1 are discussed in the appropriate sub-sections below.

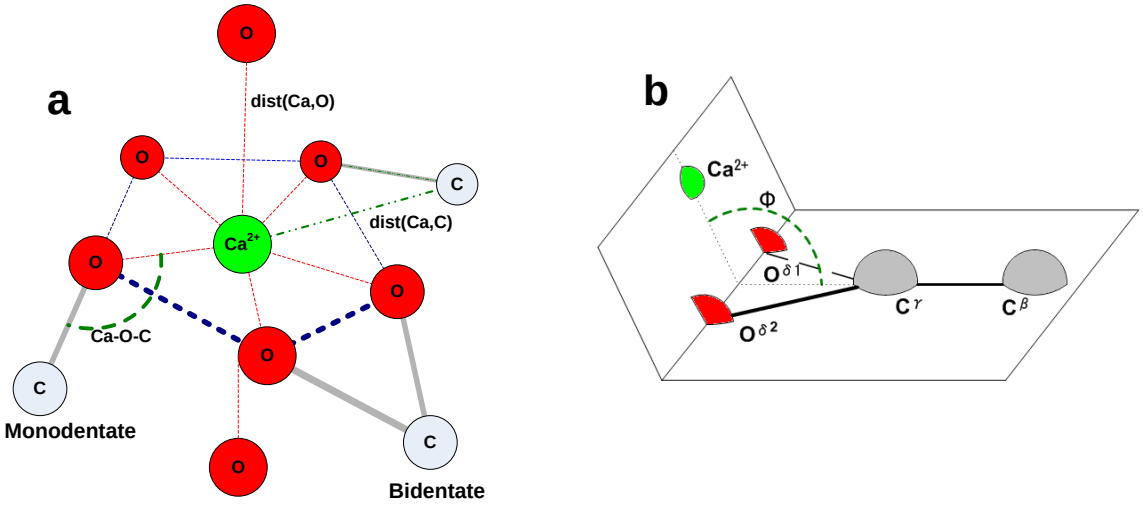

Figure 2.1 Illustration of key structural characteristics of Ca^{2+}-binding
(**a**) The physical relationships between the Ca^{2+} ion (Ca), the ligand oxygen (O), and the ligand oxygen atoms covalently-bound carbon (C) are defined by the angle Ca-O-C and distances dist(Ca,C) and dist(Ca,O). (**b**) Dihedral angle of bidentate ligands.

Structural parameters analyzed in this study are illustrated in Figure 2.1a. The cutoff distance of 3.5 Å was selected for several reasons. First, various studies have evaluated first shell Ca-O binding up to 4.0 Å, and reported a limited number of Ca-O bonds within the range 3.4-3.8 Å, although the majority of bond lengths falls within the range 2.2 – 2.9 Å [10, 179-180]. Dudev *et al* evaluated first-second shell interactions for metal binding with a second shell cutoff distance of 3.5 Å [181]. Additionally, Nayal *et al* reported statistical results using a cutoff distance of 3.5 Å [182], and previous work in our laboratory has demonstrated that this cutoff distance is valid for rapid and accurate prediction of Ca^{2+}-binding sites [183].

Parameter Analysis

The Mean Ca-O ($\overline{Ca-O}$) and Ca-C ($\overline{Ca-C}$) distance values were calculated as follows in Eq. 1 and Eq. 2, respectively.

$$\overline{Ca-O} = \frac{1}{k}\sum_{1}^{k} dist(Ca,O) \qquad \text{(Eq. 1)}$$

$$\overline{Ca-C} = \frac{1}{m}\sum_{1}^{m} dist(Ca,C) \qquad \text{(Eq. 2)}$$

In Eq. 1, *k* is the number of ligands in one site. In Eq. 2, *m* is the number of bonded carbon atoms, and $k \geq m$. When *k* equals *m* in a single binding site, it indicates that only monodentate ligands appear in this site, otherwise *k* must be greater than *m* for polydentate ligands.

Bidentate ligands commonly originate from residues Glu, and Asp, and to a lesser extent from Gln and Asn. The extent to which a sidechain residue is bidentate is dependent on the relative position of the metal ion to the ligand atoms. To our knowledge, previous statistical analyses identify bidentate ligands only on the basis of a cutoff distance, so to more accurately report coordination numbers for this analysis, bidentate ligands were identified based on a bidentate ligand propensity property L_β, as defined by Eq. 3 which predicts bidentate property as a function of deviation from an idealized symmetry.

$$L_\beta = (d_1/d_2) \qquad \text{(Eq. 3)}$$

To evaluate this, we first considered a theoretically-ideal, symmetrical bidentate ligand (Figure 2.2a) where the Ca-O distances (d_1, d_2) and Ca-O-C angles (θ_1, θ_2) for each potential ligand are equivalent: therefore $d_1/d_2 = 1$, and $\theta_1/\theta_2 = 1$.

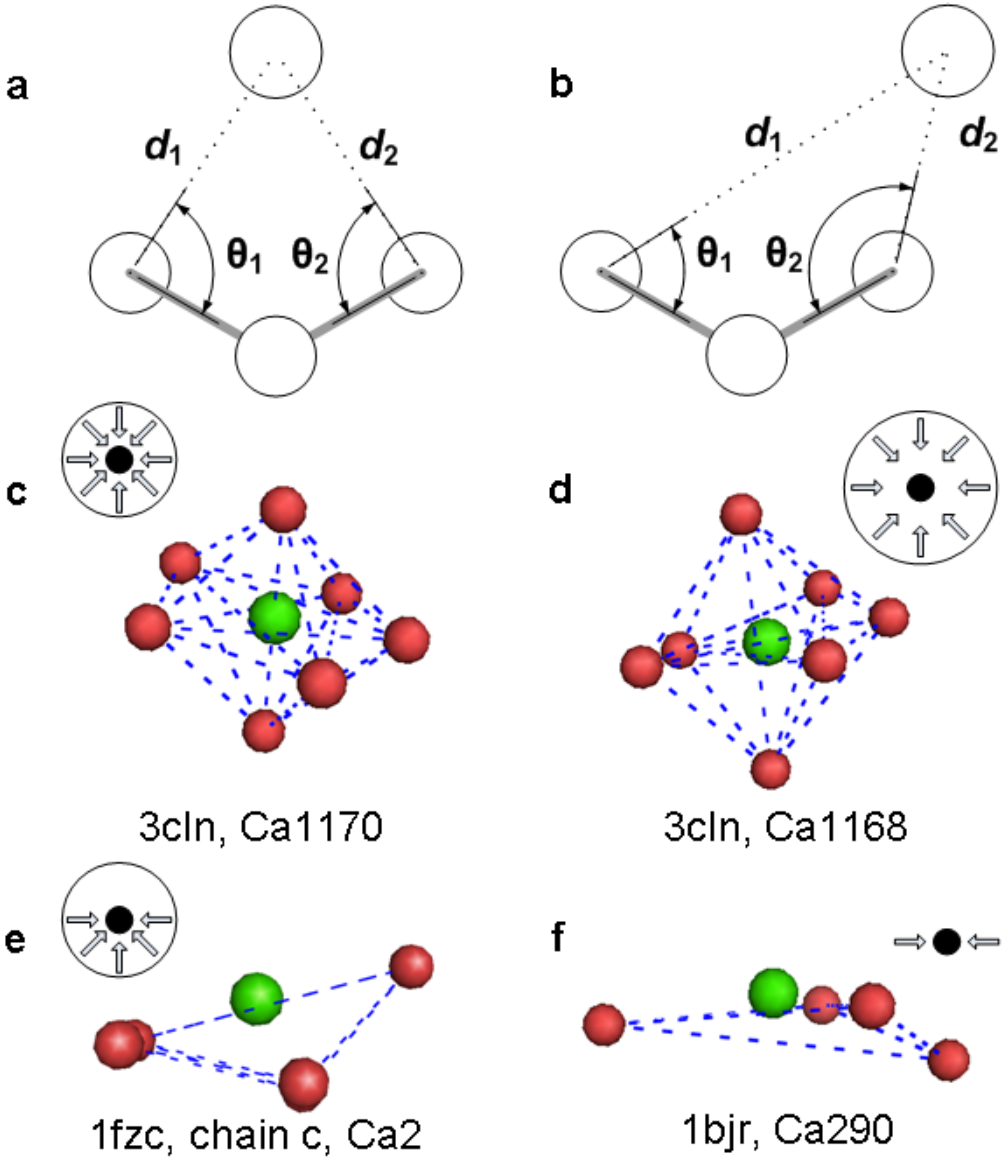

Figure 2.2 Bidentate ligands and calcium-binding
(**a**) Symmetrical bidentate structure and (**b**) monodentate structure where ion is bound to only 1 ligand atom. The relationship between each potential ligand oxygen and the Ca^{2+} ion is defined by distances d_1 and d_2, and angles θ_1 and θ_2. (**c**) Tight holospheric binding and (**d**) loose holospheric binding where the Ca^{2+} ion is enclosed in a volume defined by binding ligands. (**e**) Hemispheric binding where the Ca^{2+} ion is exposed on one hemispheric surface and (**f**) planar binding where the Ca^{2+} ion is bound in a ring structure with exposure above and below the plane.

A geometric relationship (described in supplementary materials) exists between these ratios which allows us to use d_1/d_2 as a measure of deviation from ideal symmetry. As the position of the metal ion shifts relative to the ligands (Figure 2.2b), the binding

character becomes increasingly monodentate, and the ratio d_1/d_2 increases or decreases proportionally, describing a range of valid values to distinguish bidentate from monodentate ligands. To establish a valid range for $\boldsymbol{L_\beta}$ to identify bidentate ligands, 61 potential bidentate pairs obtained from the Pidcock [61] dataset were visually inspected using Pymol (http://pymol.sourceforge.net/). From this dataset, a valid range of $\boldsymbol{L_\beta}$ for identified Ca^{2+}-binding bidentate ligand pairs was calculated at 1.07 ± 0.34. This range was then used as a filter to identify bidentate ligands for the EF-Hand and non-EF-Hand sites.

Dihedral angles were also calculated for bidentate ligands, defined as the angle between the plane formed by the sidechain carboxyl group (-COO), and the plane formed by the two carboxyl oxygen atoms and the Ca^{2+} ion (Figure 2.1b). Finally, an additional property Hull was examined to describe the spatial relationship of the Ca^{2+} ion to the interior volume of the inner shell binding ligands. This property functioned as a Boolean operator, indicating only whether or not the ion was enclosed in the defined volume.

Analysis of bimodal peak distribution for EF-hand ligands

An observed bimodal distribution of Ca-O-C angles for sidechain and mainchain EF-Hand ligands was further analyzed based on ligand distribution and protein family. Ligands comprising the Ca-O-C angle distribution were plotted for comparative analysis. The distribution of Ca-O-C angles was subdivided into two regions R1 and R2 corresponding to angle ranges 116.00° – 138.49° and 138.50° – 170.00° for sidechain, and 116.00° – 163.49° and 163.50° – 180.00° for mainchain, respectively.

The ligand contribution to these regions from each protein structure was determined. A multiple sequence alignment was conducted with ClustalW, using a gap open penalty of 10 and a gap extension penalty of 0.5 [184] for all chains of all EF-Hand

PDB structures. The resulting output file was edited to remove redundant chains, so the final data file contained only multiple chains from a structure if the chains were unique. This file was then read using TreeView software [185] to generate unrooted N-J phylogenic trees. Chains were further labeled on the phylogenic trees with their appropriate SCOP [186] family classifications using data from the Protein Data Bank, except for the Calmodulin-like SCOP families where the label was excluded to improve readability. Further detailed analysis was then performed to determine potential correlation between the ligands within the Ca-O-C angle data and protein family evolution based on ligand distribution in regions R1 and R2.

2.2 Pb^{2+}-binding protein statistics

A preliminary search of the Protein Data Bank (http://www.rcsb.org/pdb/) identified 27 PDB files for proteins known to bind Pb^{2+}. Six of these were discarded as they represented either duplicate structures or nucleic acid structures. From the remaining 21 PDB files, 20 of the 68 Pb^{2+} binding sites were eliminated due to redundancy associated with polymeric domains, or because the only binding ligands associated with the ion were water molecules, leaving 48 binding sites retained for the analysis (Appendix Table A.3).

Although possible Pb-O and Pb-N binding distances as long as 4.2 Å have been reported in the literature [187], we chose a shorter ligand inclusion cutoff distance of 3.5 Å from the Pb^{2+} ion for several reasons. First, 75% of the ligands identified by the analysis fell within the 3.5 Å cutoff distance, including all of the ligands where binding resulted from displacement of another ion. Second, work by Harding and others [180, 187] has suggested a variable region approximately between 3.2 – 4.0 Å where the distribution of ligands for certain metal ions decreases significantly, and begins to increase again near 4.0 Å. This corresponds with second shell interaction ranges reported by Dudev [181], where first shell interactions are constrained to 3.5 Å. This

cutoff distance is also frequently cited as the upper limit for Ca^{2+} binding; however, nearly all studies of Ca^{2+}, including a recent study completed in our laboratory, have demonstrated that Ca^{2+}-binding ligands are generally within 2.9 Å distance from the ion [5, 10, 180, 188]. In the case of Pb^{2+} which has a slightly larger radius than Ca^{2+}, we allowed for the possibility that the larger radius would result in minor increases in binding distance values, which is accommodated by the 3.5 Å cutoff.

Of the 177 ligand atoms retained for the analysis, only five have occupancy values less than 1 (i.e. - more than one stable set of coordinates was observed for the atom in the crystalline structure), and these atoms were not removed as their inclusion would not significantly alter the analysis. Two datasets were then constructed for evaluation: a final dataset (DS Final) comprised of all retained binding sites, and a subset comprised of higher resolution (DS HR) structural data (R less than 1.76 Å), to limit error inherent in structures with lower resolution [189].

Data from the Ligand Protein Contact Data Server (LPC) (http://bioportal.weizmann.ac.il/oca-bin/lpccsu) were obtained to verify binding ligands. Data from the PDB were selectively filtered using a custom, Visual Basic (Microsoft Corporation, Redmond, WA) program, then loaded into an Access relational database. Statistical data on binding ligands were extracted from the database using Structured Query Language (SQL) queries to identify all potential oxygen, nitrogen or sulfur ligand atoms within 3.5 Å of the target Pb^{2+} ions. Distance was calculated based on Eq. 4, where $(X_{Ligand} - X_{Pb})$ indicates the spatial difference between each component's numerical coordinate along the X-axis. The differences for each component along the Y and Z axis are calculated in the same manner.

$$\text{Distance} = \left((X_{Ligand} - X_{Pb})^{2} + (Y_{Ligand} - Y_{Pb})^{2} + (Z_{Ligand} - Z_{Pb})^{2}\right)^{1/2} \qquad \text{(Eq. 4)}$$

Additionally, 54 potential bidentate ligand pairs in the PDB files were inspected using Pymol [93], and 36 were visually-identified as bidentate pairs based on Eq. 3

where the bidentate ligand propensity property $\boldsymbol{L_\beta}$ was defined based on the ratio (d_1/d_2) where d_1 represents the distance between Pb^{2+} and either Asp OD1 or Glu OE1, and d_2 represents the distance between Pb^{2+} and either Asp OD2 or Glu OE2.

The L_β range determined for Pb^{2+}-binding was found to be 1.04 ± 0.29, which differs insignificantly from that calculated for Ca^{2+} (1.07 ± 0.34). The significance of this property is that it can be utilized in related analyses to predict bidentate ligands from structural data, without the necessity of viewing each individual model.

Comparative data for Ca^{2+}-binding was also obtained from the Protein Data Bank, where a total of 1605 binding sites from 558 PDB files with resolution R ≤ 2.0 Å were retained for the analysis, based on a cutoff distance of 3.5 Å as the maximum ligand distance for oxygen and nitrogen, and following removal of structures with greater than 90% sequence homology.

2.3 Expression and purification of CaM

Two variants of CaM were used in our research: wt-CaM and a mutant variant (CaM-Del) modified by the removal of residues 76-80 (MKDTD). Both were expressed and purified according to the same protocol, which will be described here for wt-CaM only.

Briefly, 1.0 µL pet20b/wt-CaM plasmid DNA was first added into 50 µL of BL21 (DE3) plysS competent cells. After mixing with the pipet tip, samples were placed on ice for 30 min following by immersion in 42 °C water bath for 45 s to heat shock the cell membrane and allow for entry of DNA plasmid. After the heat shock, samples were iced for 2 min, following which they were mixed with 1 mL LB media and placed in the incubator/shaker for 60 min at 37 °C. Samples were then plated on LB plates with 100 µg/mL ampicillin and incubated overnight at 37 °C. The transformed cells were then refrigerated at 4 °C the following day.

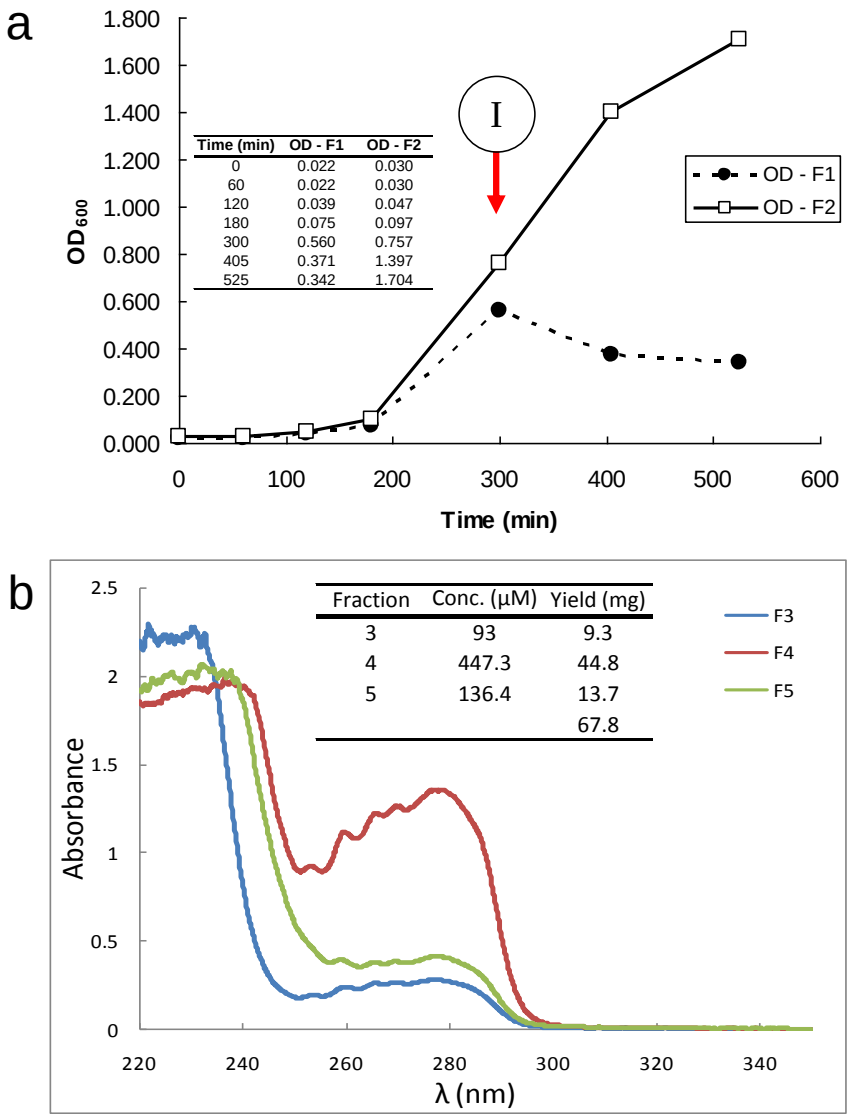

Figure 2.3 Expression and purification of CaM
(**a**) Growth curve for wt-CaM expression. OD-F2 appears to have died following addition of IPTG at 300 min. (**b**) Fraction concentration of wt-CaM and calculated yield in mg from 1 L cell cultures.

Single cell colonies were inoculated into 10 mL LB broth with 10 µL of 100 µg/mL ampicillin and placed in the incubator/shaker overnight at 37 °C. The incubated cells were then spun down in a centrifuge for 15 min at 8000 rpm (T=4 °C) and resuspended in 1 mL LB. Each 1 mL sample was then inoculated into 1 L LB with 100 µg/mL ampicillin. LB media was prepared by autoclaving three 1 L flasks of LB using cycle 4, 45 min, 121 °C. Cells were then incubated and shaken at 37 °C until OD_{600} = 0.6-0.7,

when cells were induced with 0.2 mM (200 µL of 1 M) Isopropyl-beta-D-thiogalactopyranoside (IPTG), and allowed to grow for 3-4 hours. An example of the associated growth curve can be seen in Figure 2.3a. Cells were collected after 525 min, centrifuged at 7500 rpm for 20 min, and the cell pellets stored at -20 °C for further purification.

Next, cell pellets were resuspended in 30 mL homogenization buffer (2 mM EDTA (Acros Organics, Geel, Belgium), 1 mM Dithiothreitol (DTT), 1 mM phenylmethylsulphonyl fluoride (PMSF), 50 mM Tris, pH 7.5). EMD Omnipur tris (hydroxymethyl)aminoethane (EMD Chemicals, Inc., Gibbstown, NJ) with a p*K*a of 8.06 at 25 °C was used as a buffering solution due to its working range from pH 5.0-8.6. PMSF (98.5%, Sigma), a serine protease inhibitor, was added to prevent protein degradation. Cells were broken using the French Press method at 16 k psi, passing the solution through twice. Cells were heated at 80 – 85 °C in a water bath for ~5 min then centrifuged at 17000 rpm for 40 min. 5 mM $CaCl_2$ was then added to the retained supernatant, which was filtered through a 0.45 µm pore size filter (Whatman, Florham Park, NJ). The sample was loaded onto a phenylsepharose column pre-equilibrated with Wash Buffer 1 (1 M $CaCl_2$, 1 M Tris, pH 7.5). Column was run at 1 mL/min at 4 °C, and then recycled overnight to ensure optimal binding to the column.

The following day, the column was washed with 5-10 column volumes of Wash Buffer 1. This was repeated with Wash Buffer 2 (Wash Buffer 1 with 5 M NaCl) at 2 mL/min. Protein was then eluted with Elution Buffer (0.5 M EDTA, 1 M Tris, pH 7.5) at 2 mL/min. Previous work with wt-CaM has demonstrated that all of the protein is eluted in the first 60 mL.

Collected fractions were then evaluated for absorbance at 278 nm (Trp) using a Shimadzu UV-1601 PharmaSpec UV-Vis spectrophotometer with UV Probe software (Shimadzu North America, Columbia, MD). Fractions with the highest absorbance were

then pooled and dialyzed 3-4 hours in 2 L of 50 mM Tris, pH 7.5, 4 °C. The dialysis buffer was then replaced and a 10 g Chelex 100 resin bag added for overnight dialysis to remove free Ca^{2+}.

An example of the final yield of purified wt-CaM can be seen in Figure 2.3b. Yield was calculated based on three collected fractions from a single 1 L flask of expressed and purified protein. Similarly, a yield of 134 mg of obtained for the CaM-Del variant (2L, data not shown). However, the yield for 2L wt-CaM expressed in SV media was only 82 mg. Despite later instances of slow cell growth or cell death following the same protocol, comparable yields were achieved (data not shown).

2.4 Expression and purification of isotopically-labeled CaM

For multidimensional NMR experiments, it was necessary to label our proteins with ^{15}N, or both ^{15}N and ^{13}C. The protocol for either double or single labeling is summarized below. For the transformation, add 1µl (~50ng/µl) of pET20b/Cam plasmid DNA into competent cells in 1.5 mL microcentrifuge tube, mix well and incubate on ice for 30 min. Next, heat shock the cells at 42 ^{o}C for 45-90 s, then add 1mL LB into the microcentrifuge tube and incubate at 37^{o}C for 1 hour with shake. Evenly spread ~ 50 µL of cells onto LB plate treated with 100µg/mL Ampicillin and incubate plate at 37^{o}C overnight. The next day, inoculate a single colony into a 50 mL disposable centrifuge tube containing 10ml LB broth with 100mg/mL (10 µL) Ampicillin. Incubate/shake at 37^{o}C for 6 hours. During this time period, prepare 30-35 mL of 20% Glucose for each 1 L of media. Glucose dissolves slowly, so for best results, mix in individual 50 mL tubes which leaves some headspace in the top. At this step, if the protein requires ^{13}C-labeling in addition to ^{15}N-labeling, prepare two solutions of Glucose: unlabeled (7.5 mL 20% Glucose/200 mL media) and ^{13}C-labeled (30-35 mL 20% Glucose/1 L media).

To maintain the isotopic enrichment, expression is done using SV (minimal) media, prepared as follows for 1 L: Add7.9 g K_2HPO_4 and 4.4 g KH_2PO_4 in 2.5 L flask, fill to 1 L with ddH_2O. Premix a concentrated solution of $MgSO_4 \cdot 7H_2O$ in ddH_2O, then add volume necessary for 0.05 g/L to media. Also, premix a concentrated solution of $(NH_4)_2Fe(SO_4)_2 \cdot 6H_2O$ in ddH_2O, then add volume necessary for 0.007 g/L to media. Autoclave 20 min

For expression, begin by spinning down the cells for 15 min, 8000 rpm at 20 ^oC. Resuspend cells in 1ml LB then inoculate into 200 mL SV media with 100mg/ml Amp (200 µL). To the 200 mL SV media, add the following: 7.5 mL 20% Glucose; 750 µL NH_4Cl (0.1g/5mL). Incubate/shake the cells overnight at 37^oC. Solubilize $^{15}NH_4Cl$ in ddH_2O at 0.5g/L. Filter dissolved $^{15}NH_4Cl$ with 0.45 µM membrane filter by syringe. 1g/4mL ddH_2O is adequate for solubilization. Following overnight incubation, add the following to each 1 L of media: 30-35 mL 20% Glucose/1 L media (**Note:** substitute ^{13}C-labeled Glucose at this step for double-labeling); 1 mL of 100mg/mL Ampicillin; 0.5 g/L $^{15}NH_4Cl$; 50 mL cell culture from original 200 mL sample. Record OD_{600} of sample in 1 L SV media.

Incubate/shake cells at 37^oC for 4 hours then record OD_{600} of sample in 1 L SV media. Continue to incubate/shake until OD_{600}=0.8,Cell growth can then be Induced with 0.2mM IPTG (200µl of 1M IPTG) and the cells allowed to grow for 3-4 hours. Cells are then collected by centrifugation at 7500 rpm for 20 min. Store the cells pellet at -20^oC or -80^oC.

Purifcation of the protein followed the same steps outlined in the previous section for unlabeled wt-CaM. The cell pellets were resuspended in 30 mL homogenization buffer (2 mM EDTA (Acros Organics, Geel, Belgium), 1 mM Dithiothreitol (DTT), 1 mM phenylmethylsulphonyl fluoride (PMSF), 50 mM Tris, pH 7.5). EMD Omnipur tris (hydroxymethyl)aminoethane (EMD Chemicals, Inc., Gibbstown, NJ) with a p*K*a of 8.06

at 25 °C was used as a buffering solution due to its working range from pH 5.0-8.6. PMSF (98.5%, Sigma), a serine protease inhibitor, was added to prevent protein degradation. Cells were broken using the French Press method at 16 k psi, passing the solution through twice. Cells were heated at 80 – 85 °C in a water bath for ~5 min then centrifuged at 17000 rpm for 40 min. 5 mM $CaCl_2$ was then added to the retained supernatant, which was filtered through a 0.45 µm pore size filter (Whatman, Florham Park, NJ). The sample was loaded onto a phenylsepharose column pre-equilibrated with Wash Buffer 1 (1 M $CaCl_2$, 1 M Tris, pH 7.5). Column was run at 1 mL/min at 4 °C, and then recycled overnight to ensure optimal binding to the column.

The following day, the column was washed with 5-10 column volumes of Wash Buffer 1. This was repeated with Wash Buffer 2 (Wash Buffer 1 with 5 M NaCl) at 2 mL/min. Protein was then eluted with Elution Buffer (0.5 M EDTA, 1 M Tris, pH 7.5) at 2 mL/min. Previous work with wt-CaM has demonstrated that all of the protein is eluted in the first 60 mL.

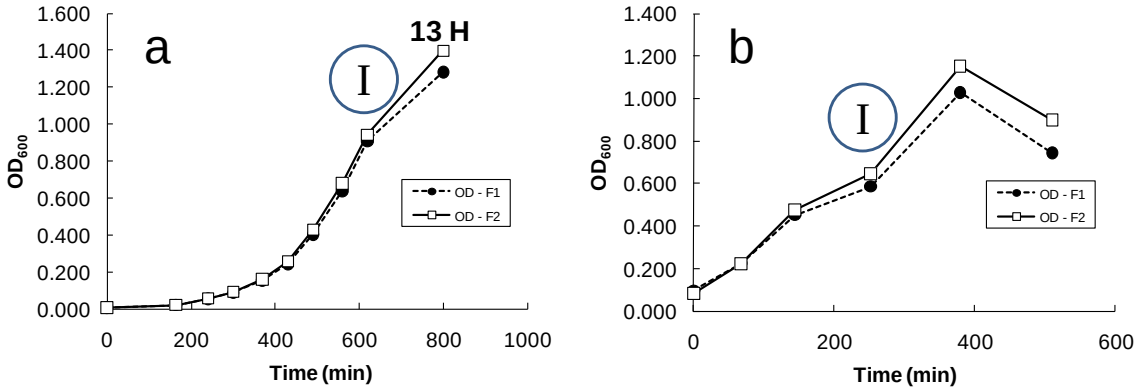

Figure 2.4 Expression of ^{15}N-labeled CaM
(**a**) Extremely slow cell growth observed following specified protocol. (**b**) Cell death observed 2H after induction with IPTG following modified protocol.

Collected fractions were then evaluated for absorbance at 278 nm (Trp) using a Shimadzu UV-1601 PharmaSpec UV-Vis spectrophotometer with UV Probe software (Shimadzu North America, Columbia, MD). Fractions with the highest absorbance were

then pooled and dialyzed 3-4 hours in 2 L of 50 mM Tris, pH 7.5, 4 °C. The dialysis buffer was then replaced and a 10 g Chelex 100 resin bag added for overnight dialysis to remove free Ca^{2+}.

Results using this method were inconsistent, however, producing variable yields and, in many cases, extremely slow cell growth (Figure 2.4) or cell death. Despite the slow growth observed in later expressions (Figure 2.4a), purification produced 47mg protein per 1 L expression. In an alternative approach, the original protocol was modified by inoculating multiple cell colonies into 10 mL LB media. After 6H growth, 4 colonies were transferred into 200 mL SV media. Cell death was observed 2H following induction with IPTG (Figure 2.4b). The resulting yield was less than 50% of that obtained from the original protocol, even in cases of slow growth.

2.5 Determination of CaM concentration

Following purification, proteins were concentrated using a Stirred Ultrafiltration Cell with a 3000 MWCO Ultrafiltration Membrane, under N_2 gas. Final concentration of the proteins were determined by measuring absorbance at 277 nm, and calculation based on the Beer-Lambert Law (Eq. 5):

$$A = \varepsilon bc \qquad \text{(Eq. 5)}$$

Where b = path length (1 cm), A is the measured absorbance, and ε is the molar absorptivity of 3030 $cm^{-1} * M^{-1}$.

2.6 Methods for controlling free Ca^{2+} in buffers and protein samples

Tris-Cl was treated with Analytical Grade Chelex 100 resin, 100-200 mesh Sodium Form (Bio-Rad Laboratories, Hercule, CA), hereafter referred to as Chelex. Two different methods were evaluated to determine optimal calcium removal. First, a 10 mM TRIS-Cl buffer was treated by dialysis on a stir plate at 4 °C with 10 g Chelex for three

days. Alternatively, 40 g of Chelex were packed into a 47 mL glass column. The TRIS-Cl buffer was pumped through the column and collected at 4 °C. For both methods, pH following treatment dropped from 7.4 to approximately 3.3 and had to be readjusted up to 7.4 with NaOH. For comparative purposes, the remaining background Ca^{2+} determined from the two Chelex treated buffers was evaluated in comparison with untreated ddH_2O, treated ddH_2O, and untreated TRIS-Cl. The background calcium present after treatment with Chelex was determined using 5,5',6,6'-tetrafluoro BAPTA dye (Molecular Probes, Eugene, OR). The remaining free calcium was calculated using Eq. 6.

$$[Ca^{2+}]_{free} = [Dye] * ((F_{EGTA} - F_{BAPTA})/(F_{EGTA} - F_{Ca^{2+}})) \quad \text{(Eq. 6)}$$

A calcium sponge column was also constructed comprised of 2g polystyrene BAPTA (Invitrogen). Protein samples are allowed to drip through the column via gravity flow.

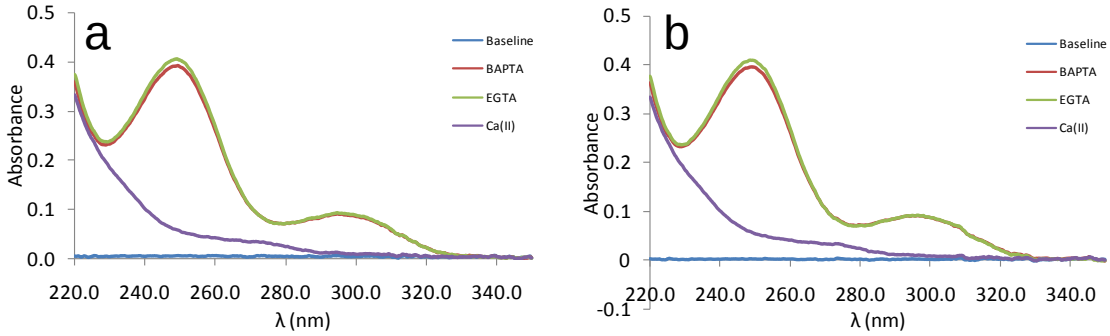

Figure 2.5 Calculating free calcium
Determination of $[Ca^{2+}]_{free}$ following treatment with (**a**) chelex-packed column and (**b**) chelex in dialysis.

Treatment with a Chelex 100 packed column method resulted in a $[Ca^{2+}]_{free}$ concentration of 1.51 µM (Figure 2.5a), while the dialysis method resulted in a concentration of 1.33 µM (Figure 2.5b). Based on data presented in Table 2.2 it can be seen that both methods reduce the available $[Ca^{2+}]_{free}$ in solution, but this reduction, compared to the $[Ca^{2+}]_{free}$ in the original buffer, is negligible. However, the Chelex 100

also removes other trace metals present, and ensures a quantifiable $[Ca^{2+}]_{free}$ value if variations of $[Ca^{2+}]_{free}$ should occur in either the Tris buffer or the ddH_2O.

Table 2.2 Free Ca^{2+} concentrations

	HOH Untreated	HOH Chelex Column	10 mM TRIS-Cl Untreated	10 mM TRIS-Cl Chelex Column	10 mM TRIS-Cl Chelex Dialysis
[Ca]free (µM)	2.68	1.08	2.52	1.51	1.33

Results from several early experiments had indicated that Ca^{2+} or other metals were still present in samples treated with Chelex100. Protein samples were subsequently treated by passing through a calcium sponge column. Although a quantitative assessment of the free metal in these treated samples has not yet been conducted, the qualitative difference between calmodulin treated with Chelex100 and with the calcium sponge methods can be seen in Figure 2.6 which shows the phenylalanine fluorescence for wt-CaM N-terminal before and after the addition of 200 µM EGTA. In this experiment, the addition of Ca^{2+} to CaM results in a decrease in Phe fluorescence. Following addition of EGTA to the Chelex100 treated sample, the fluorescence increases indicating that Ca^{2+} was still present in the sample. Conversely, the fluorescence decreased following addition of EGTA to the calcium sponge-treated protein sample.

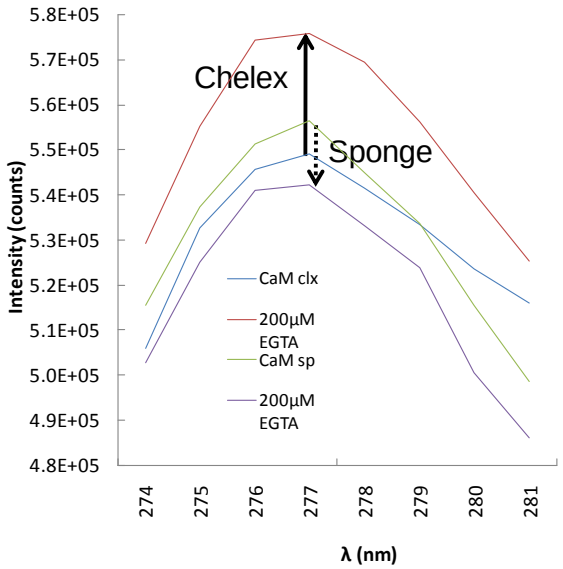

Figure 2.6 Removal of free calcium from protein samples
Phenylalanine fluorescence increases following addition of 200 µM EGTA in CaM treated with Chelex100, indicating the presence of residual Ca^{2+} in the sample. The converse is observed for the sample treated by passage through a calcium sponge column.

2.7 Fluorescence studies

Fluorometric spectral analyses of metals interacting with dyes and proteins were conducted using a PTI (Photon Technology International, Birmingham, NJ) Spectrofluorometer equipped with a 75 W xenon arc lamp and a model 814 Photomultiplier Tube (PMT) detector. Samples (0.8-1.0 mL) were evaluated in 1 cm pathway cuvettes. All analyses were conducted at 25 °C.

Table 2.3 Summary of buffers for fluorescence experiments

Buffer ID	Buffer	pH	Description	Purpose
HEPES EqT B1	50 mM HEPES 100 mM KCl 5 mM NTA 0.5 mM EGTA 5 µM protein	7.4-7.6	Equilibrium Titration	Very high affinity metal binding Tyr fluorescence
HEPES EqT B2	50 mM HEPES 100 mM KCl 5 mM NTA 15 mM M^{n+}	7.4-7.6	Equilibrium Titration	Very high affinity metal binding Tyr fluorescence
TRIS EqT B1	50 mM TRIS 100 mM KCl 5 mM NTA 0.5 mM EGTA 5 µM protein	7.4-7.6	Equilibrium Titration	Very high affinity metal binding Tyr fluorescence
TRIS EqT B2	50 mM TRIS 100 mM KCl 5 mM NTA 15 mM M^{n+}	7.4-7.6	Equilibrium Titration	Very high affinity metal binding Tyr fluorescence
TRIS BEX B1	10 mM TRIS 1 µM Fura-2 1 mM EDTA	7.4	Buffer Exchange Titration	Lower affinity metal binding
TRIS BEX B2	10 mM TRIS 1 µM Fura-2 1 mM EDTA 1 mM M^{n+}	7.4	Buffer Exchange Titration	Lower affinity metal binding
TRIS-DYE-M	10 mM TRIS 100 mM KCl 10 µM dye 10 µM M^{n+}	7.4	Competitive Titration	Metal binding affinity

To obtain Ca^{2+}-free conditions, all buffers were treated by overnight dialysis with 10g Chelex100. Buffer systems, including pH values, for the different experiments are summarized in Table 2.3. All metal standards were obtained from at least 99% pure sources. Protein samples in their respective buffer matrices were also treated by overnight dialysis with 10g Chelex100 followed by passing the sample through a Calcium Sponge (Invitrogen) column to remove all background metals.

Response of EGFP variants with grafted CaM EF-III motif to Pb^{2+}

The EGFPwtF protein and designed variants utilized for metal-binding and protease studies were developed via sub-cloning through polymerase chain reaction (PCR). Proteins were prepared for subsequent purification on a Ni^{2+} chelating sepharose column by addition of a 6x His-tag. These variants provide the scaffold for mutagenesis studies aimed towards designing proteins with high metal selectivity, and for development of a protease sensor. EMD Omnipur tris (hydroxymethyl)aminoethane (EMD Chemicals, Inc., Gibbstown, NJ), or TRIS, was utilized extensively as a buffering agent to maintain pH for the expressed proteins. LB media was prepared in a 2.8 L Erlenmeyer flask by combining 10 g Bacto-Tryptone (Becton, Dickinson and Co., Sparks, MD) with 5 g Bactone-yeast extract (EMD Chemicals, Inc., Gibbstown, NJ), 10 g NaCl, and then filling the flask to 1 L with ddH_2O. The pH was adjusted to 7.0 with 5 M NaOH (J.T. Baker, Phillipsburg, NJ).

Transformation

The Pet28A vector used for coding EGFPwtF and all variants was transformed into E. Coli cell line DE3. Cell colonies were grown on Agarose plates with Kanamycin. During preparation, 50 µL of the appropriate cell line were added to an autoclaved microcentrifuge tube, followed by 0.5 µL of DNA. Samples were incubated on ice for 30 min. Subsequent to incubation, the sample was subjected to heat shock for 90 s at 42 °C to allow DNA into the cell. The sample was replaced in ice for 2 min. After cooling the

sample, 50 µL of LB Media was added, and the sample was placed in an incubator for 30 min at 37 °C. Cell plates were labeled and dated. Steel coils were heated in an open flame and immersed in EtOH several times for sterilization. The cell culture was then added in drops onto the agarose plate, and spread across the surface with the sterilized coil. The plate was then covered and placed in an incubator overnight at 37 °C.

Inoculation

20 mL of LB media, pH 7.0, were pipeted into a 50 mL disposable centrifuge tube, followed by 12 µL of 50 mg/mL kanamycin, for a final concentration of 0.03 mg/mL kanamycin. Using an inoculation loop, a single cell colony was scraped from the agarose plate. The inoculation loop was swirled in the LB media in the centrifuge tube. The sealed tube was then placed in a large beaker and packed with paper towels to prevent movement of the tube. The beaker was then placed in an incubator-shaker overnight at 37 °C.

Expression

In 1 L of autoclaved LB media, 600 µL of 50 mg/mL kanamycin was added for a final concentration of 0.03 mg/mL. Optical density of the cell cultures was monitored using a Shimadzu UV-1601 PharmaSpec UV-Vis spectrophotometer with UV Probe software (Shimadzu North America, Columbia, MD).

Samples for the spectrophotometer were prepared in 1.0 mL plastic, disposable cuvettes. Two reference cuvettes were prepared for the baseline using 1.0 mL of the LB media/kanamycin. Using the Bunsen burner, the neck of the 2.8 L Erlenmeyer flask was rotated in the flame to prevent bacterial growth. Next, the cell culture in the 50 mL disposable centrifuge tube was poured into the 2.8 L flask. The flask was covered with Aluminum foil, and secured in the incubator-shaker set at 200 rpm, 37 °C. The optical density of the sample was checked in the UV-Vis spectrophotometer until the absorbance reached 0.6 ± 0.1, at 600 nm. This range was previously determined for

optimal induction. At the appropriate absorbance, 200 µL of Isopropyl-beta-D-thiogalactopyranoside (IPTG) were added to induce expression of the protein, and the temperature reduced to 20-25 °C, for optimal expression. Following induction, 1.0 mL samples were removed every hour for three hours, followed by a final sample on the following day, to evaluate protein expression using SDS-PAGE gels. Cell pellets were harvested the following day by centrifugation, and stored in a freezer at 4 °C until they could be purified.

Sample preparation

To the collected cell pellet, ~20 mL of extraction buffer (20 mM TRIS, 100 mM NaCl, 0.1% Triton x-100) was added, and the sample vortexed to dissolve. The dissolved cell pellet was poured into a 50 mL plastic beaker, and the beaker placed on ice. The sample was then sonicated six times to break the cell membranes, for 30 s periods, with ~5 min intervals between sonications. Following sonication, the cell pellet solution was centrifuged for 20 min at 17 x 10^3 rpm to separate the protein into the supernatant. The extracted supernatant was filtered with 0.45 µm pore size filter (Whatman, Florham Park, NJ) into a 50 mL plastic centrifuge tube. Concentrated solutions were diluted with the appropriate binding buffer prior to injection into the FPLC system.

Purification

Purification of EGFPwtF and variants was completed using an Aktaprime FPLC (Amersham Biosciences, Piscataway, NJ) equipped with a UV detector and a 280 nm optical filter. Preparation of the FPLC required rinsing of both pumps A and B with ddH_2O. Pumps were rinsed twice each.

Two different columns were utilized. For most purifications, a Hitrap 5 mL HP Chelating sepharose column was used. The binding Buffer A was comprised of 1 M

K_2HPO_4, 1 M KH_2PO_4, 250 mM NaCl, pH 7.4. The elution Buffer B was comprised of Buffer A and 0.5 M imidazole.

The column was first rinsed with EDTA (Acros Organics, Geel, Belgium) solution (100 mM EDTA, 1 M NaCl) to remove any metals, followed by ddH_2O. Following the EDTA rinsing step, the column was washed with 0.1 M $NiSO_4$, to bind Ni^{2+} onto the column, and rinsed again with ddH_2O to remove any unbound $NiSO_4$.

For additional purification, a Hitrap Q Ion Exchange column (GE Healthcare, Piscataway, NJ) was used. For the Q column, the binding Buffer A was comprised of 20 mM TRIS, pH 8.0. The elution Buffer B was comprised of 20 mM TRIS, 1 M NaCl, and pH 8.0.

Protein injections to load the binding column were limited to 5-8 mL. Once all of the protein was loaded onto the column, an elution method was run to elute the bound protein in 8 mL fractions. The collected fractions were further purified by dialysis in 2.0 L of 10 mM TRIS, 1 mM Dithiothreitol (DTT), (Inalco, Milano, Italy). The dialysis solution was changed every 24 hours for 72 hours to remove imidazole and other impurities. Protein fractions were sealed in dialysis bags (Spectrum, Rancho Dominguez, CA) with a molecular weigh cutoff value of 3,500 Da, and stirred on a stir plate. Following dialysis, samples were extracted from the collected fractions and the purity evaluated using SDS-PAGE gels. Protein concentration was determined using UV-Vis Spectrophotometry, based on the Beer-Lambert Law.

Fluorescence of aromatic residues

Three amino acid residues (tryptophan, tyrosine and phenylalanine) all include aromatic rings in their sidechains, and exhibit some level of intrinsic fluorescence. Standard wavelength values for light absorption, absorptivity, fluorescence emission and quantum yield of these residues are summarized in Table 2.4. The intensity of these

signals may increase, or decrease due to quenching, in the presence of a metal ion within ~ 15Å of the chromophore.

Previous work [190-191] has demonstrated that fluorescence associated with phenylalanine and tyrosine in calmodulin can be used to monitor binding of calcium ions in the N- and C-terminal domains, respectively. While this method cannot provide micromolecular binding constants for individual binding sites, it can provide both relative macromolecular constants for the individual domains as well as upper and lower limits. These published methods were modified for the analysis of Pb^{2+} binding using both wt-CaM and the CaM-Del variant, described in Figure 2.7.

Table 2.4 Fluorescent characteristics of aromatic amino acid residues

	Absorption		***Fluorescence***	
	λ (nm)	Absorptivity	λ (nm)	Quantum yield
Tryptophan	280	5,600	348	0.2
Tyrosine	274	1,400	303	0.14
Phenylalanine	257	200	282	0.04

Changes in tyrosine fluorescence associated with wt-CaM were initially evaluated with Ca^{2+}, Pb^{2+} and Gd^{3+} by equilibrium titration using buffers HEPES EqT B1 and HEPES EqT B2 (Table 2.3). In these experiments, aliquots of the B2 buffer were added directly to the B1 solution with 5 min equilibrium time between additions. The chelators EGTA and NTA (Figure 2.8) were present in the matrix to buffer the metal concentration. For emission scans, emission range was set at 290-350 nm. Integration was set over 0.2 s, with stepsize and averages values set at 1 nm and 1, respectively. Excitation passbands were both set at 0.8 nm, and emission passbands at 1.0 nm. Using this method, the concentration of metal ion was gradually increased over the course of the titration. Aliquot volumes were selected to obtain at least 20 points prior to saturation of protein by metal. Results of this initial set of titrations suggested some unusual

interaction between HEPES and Gd^{3+}, so TRIS was substituted for HEPES in subsequent buffers, as indicated in Table 2.3. However, both buffering systems produced erratic results, particularly with binding of Pb^{2+} to CaM.

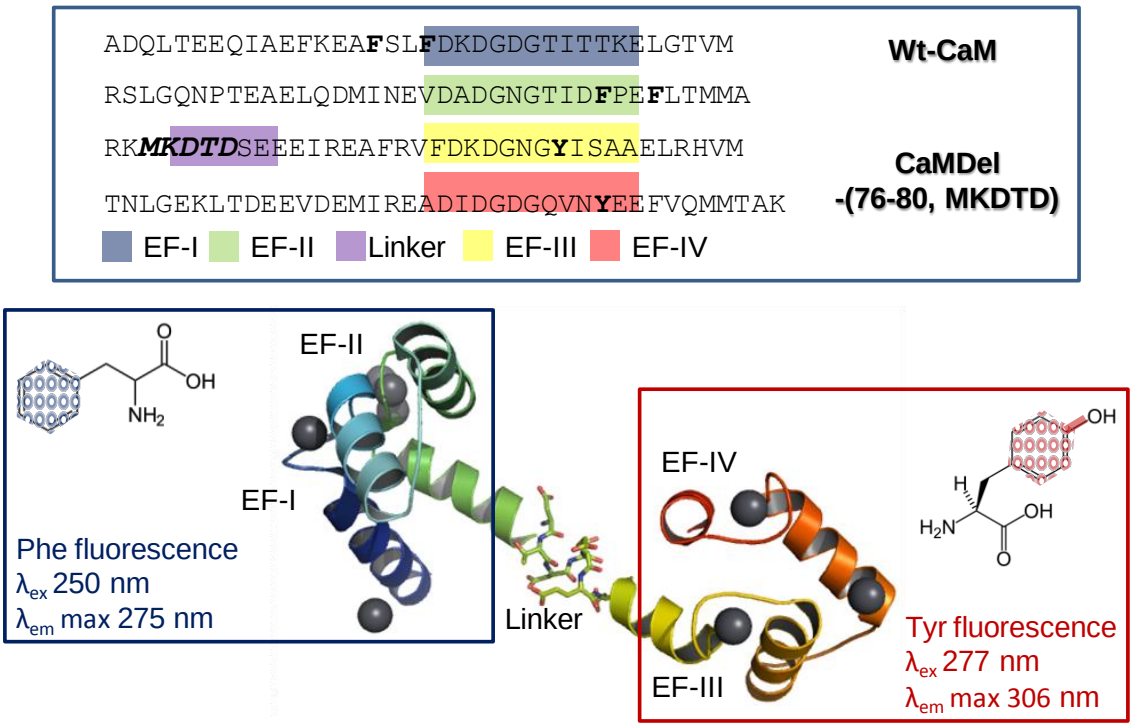

Figure 2.7 Aromatic fluorescence in CaM
Calmodulin sequence (**top**). Tyrosine and phenylaline residues highlighted in bold. Residues MKDTD, removed from the CaM-Del variant, are highlighted in italics. EF-hand sites I-IV and residues in the trans-domain linker region are color-coded. The crystal structure of Pb^{2+}-bound calmodulin (**bottom**, pdb file 2v01) showing phenylalanine and tyrosine fluorescent domains.

Next, direct titrations of Pb^{2+} to CaM and CaM-Delete were conducted. For tyrosine fluorescence, emission scans were monitored across an emission wavelength (λ_{Em}) range from 290 - 350 nm following excitation at 277 nm. Integration was set over 0.2 s, with stepsize and averages values set at 1 nm and 1, respectively. Excitation passbands were both set at 3 mm, and emission passbands at 4 mm.

For phenylalanine fluorescence, emission scans were monitored across an emission wavelength (λ_{Em}) range from 265 - 285 nm following excitation at 250 nm. Integration was set over 0.2 s, with stepsize and averages values set at 1 nm and 1,

respectively. Excitation passbands were both set at 7 mm, and emission passbands at 8 mm.

Proteins were prepared by passing through a Calcium-Sponge column as previously described. The proten was then diluted to a concentration of 10 μM in Chelex100-treated sample buffers comprised of 10 mM TRIS pH 7.4, 100 mM KCl. Titrations were conducted either by direct addition of Pb^{2+} to the protein, titration of Pb^{2+} to the protein pre-saturated with Ca^{2+}, or titration of Ca^{2+} to the protein pre-saturated with Pb^{2+}. Binding dissociation constant (K_d) values based on total metal concentration for direct titrations were calculated using a curve-fitting equation (Eq. 7), modeled on the quadratic equation (see Appendix for derivation), where $[P]_T$ is total protein concentration, $[M]_T$ is total metal concentration, and F is the fluorescence intensity.

$$F = \frac{([P]_T + [M]_T + K_d) - (([P]_T + [M]_T + K_d)^2 - 4[P]_T[M]_T)^{1/2}}{2[P]_T} \quad \text{(Eq. 7)}$$

$$K_{dM2} = (K_{app})(K_{dM1}) / ((K_{dM1}) + [M_1]_T) \quad \text{(Eq. 8)}$$

$$K_{dM1} = ([M_1]_T (K_{dM2})) / ((K_{app}) - (K_{dM2})) \quad \text{(Eq. 9)}$$

For competitive titrations involving pre-equilibration of the protein with one metal followed by titration with a second metal, the K_d in Eq. 7 becomes an apparent K_d (K_{app}). In Eq. 8, the K_d for a titrant metal (K_{dM2}) can be obtained based on K_{app} from Eq. 7, the known K_d for the pre-equilibrated metal ion (K_{dM1}) and the fixed, total concentration of the pre-equilibrated metal ion $[M_1]_T$ [192]. For titrations where the K_d of the titrant metal is known but not the pre-equilibrated metal, Eq. 8 is rearranged as Eq. 9.

Fura-2 fluorescence

The direct excitation responses of Pb^{2+}, Bi^{3+}, In^{3+}, Y^{3+}, and Lu^{3+} were evaluated with 2 μM Fura-2 (Molecular Probes, Eugene, OR) in chelex-treated 10 mM TRIS pH

7.4. The Fluorometer was set to evaluate an excitation wavelength (λ_{Ex}) 250-450 nm, with an emission wavelength (λ_{Em}) of 510 nm. Fura-2 produces two peak maxima over this excitation range at 335 and 355 nm. The maxima vary inversely, allowing for measurement of ratiometric fluorescence changes. Integration was set over 0.2 s, with stepsize and averages values set at 1 nm and 1, respectively. For Pb^{2+}, In^{3+} and Y^{3+}, excitation passbands were both set at 0.40 mm, and emission passbands at 0.50 mm. For Lu^{3+}, analyses were run in triplicate with excitation passbands set at 0.75 mm, and emission passbands at 2.50 mm. Excitation and emission scans were also run with Lu^{3+} in TRIS buffer only (same conditions) to verify that no fluorescence was observed in the buffer-metal matrix.

Another set of titrations involving a buffer exchange was conducted to evaluate the fluorescence response of Fura-2 binding with Pb^{2+}, Lu^{3+}, Gd^{3+}, and Ca^{2+}. For each point (20 or more) in the titration, a volume of buffer 1 (TRIS BEX B2) was exchanged by an equivalent volume of buffer 2 (TRIS BEX B2). This experiment was completed with both EDTA and NTA as chelators (Figure 2.8). Based on calculations of free metal in these experiments, binding affinity constants were established for the dye:chelator complexes.

When K_d between a dye and the metal is known, the apparent binding affinities (K_{app}) between a protein and the metal ion can be determined by competitive titration. Preliminary experiments were conducted to evaluate competitive binding between Fura-2 and CaM for Pb^{2+}, Gd^{3+} and Lu^{3+}. Samples were 800 µL in volume comprised of 10 mM TRIS pH 7.4, 100 mM KCl, 10 µM dye and 10 µM metal. The titrant was wt-CaM. The Fluorometer was set for the same parameters used to evaluate Fura-2 in previous experiments, with excitation passbands set at 0.2 mm, and emission passbands at 0.4 mm. The objective of these initial experiments was to identify a dye with a K_d similar to

that of the protein as indicated by gradual change in fluorescence intensity as a function of increasing protein concentration.

Fura-6F fluorescence

Fura-6F (Figure 2.9, Molecular Probes, Eugene, OR) also exhibits two peak maxima at or near 340 and 360 nm. Lu^{3+} binding with Fura-6F dye in competition with NTA was investigated using a buffer exchange assay, where a volume of the analyte Buffer A was removed, then replaced with an equivalent volume of Buffer B. Buffer A was comprised of 200 μM NTA, 1 μM Fura-6F, 100 mM KCl in 10 mM TRIS, pH 7.4. Buffer B was identical except that it included 200 μM Lu^{3+}. For the reaction, the metal ion bound to NTA is slowly transferred to Fura-6F. Excitation scans for Lu^{3+} were acquired with the following fluorometer settings: excitation wavelength 250-450nm; emission wavelength 510nm; stepsize 1; integration 0.2; averages 1; excitation passband 2 nm; and emission passband 2 nm. For each spectrum, a minimum of 20 points were collected with increasing concentration of Lu^{3+}. Although Fura-6F is reported by the manufacturer to have a single emission at 512 nm and two excitation wavelengths at 340 and 380nm, the numbers observed on our instrument were 510, 327 and 364 nm, respectively. For each point collected during the buffer exchange, $[Lu]_{free}$ was calculated based on application of the quadratic equation.

$$x = \frac{-b \pm \sqrt{b^2 - 4ac}}{2a} \qquad \text{(Eq. 10)}$$

In Eq. 10, x = $[Lu^{3+}]_{free}$; b = $[NTA]_{total}$-Volume Lu^{3+} added; a = K_d of Lu^{3+}-NTA complex; and c = $[Lu^{3+}]_{total}$. The K_d of Lu^{3+}-NTA was obtained from the NIST critical database, reported as 2.59 X 10^{-13} M.

The fluorescence ratiometric change of the two excitation wavelengths for each point as the fractional intensities at 327 and 364 nm are calculated with Eq. 11.

$$R = F_{327}/F_{364} \qquad \text{(Eq. 11)}$$

These data points are then normalized using Eq. 12.

$$\Delta R\,[0,1] = (R - R_{min})/(R_{max}-R_{min}) \qquad \text{(Eq. 12)}$$

The calculated values for $[Lu^{3+}]_{free}$ were then plotted against the normalized ratiometric change in fluorescence intensity (ΔR). Curve-fitting of the data was then accomplished using the Hill equation.

$$\Theta = \frac{[M]^n}{K_d + [M]^n} \qquad \text{(Eq. 13)}$$

Rhod-5N fluorescence

Rhod-5N (Figure 2.9, Molecular Probes, Eugene, OR) exhibits a single emission peak at or near 510 nm. Similar to competition assay for Lu^{3+} with Fura-6F, Pb^{2+} was evaluated with Rhod-5N. Fluorometer settings for the emission spectra at a single excitation wavelength of 550 nm were: emission wavelength 560-650nm; stepsize 1; integration 0.2; averages 1; excitation passband 3 nm; and emission passband 4 nm. For each spectrum, a minimum of 20 points were collected with increasing concentration of Pb^{2+}.

For each point collected during the buffer exchange, $[Pb^{2+}]_{free}$ was calculated based on application of the quadratic equation (Eq. 10), substituting Pb^{2+} for Lu^{3+}. The fluorescence intensity change was measured against the baseline with no added Pb^{2+}. By defining R_{min} as the baseline fluorescence intensity, Eq. 12 was again used to normalize Pb^{2+}-dependent changes in fluorescence intensity resulting from binding to dye. The calculated values for $[Pb^{2+}]_{free}$ were then plotted against the normalized ratiometric change in fluorescence intensity (ΔR). Curve-fitting of the data was then accomplished using the Hill equation (Eq. 13). K_d of Pb-NTA was obtained from the NIST critical database, reported as 3.31×10^{-12} M.

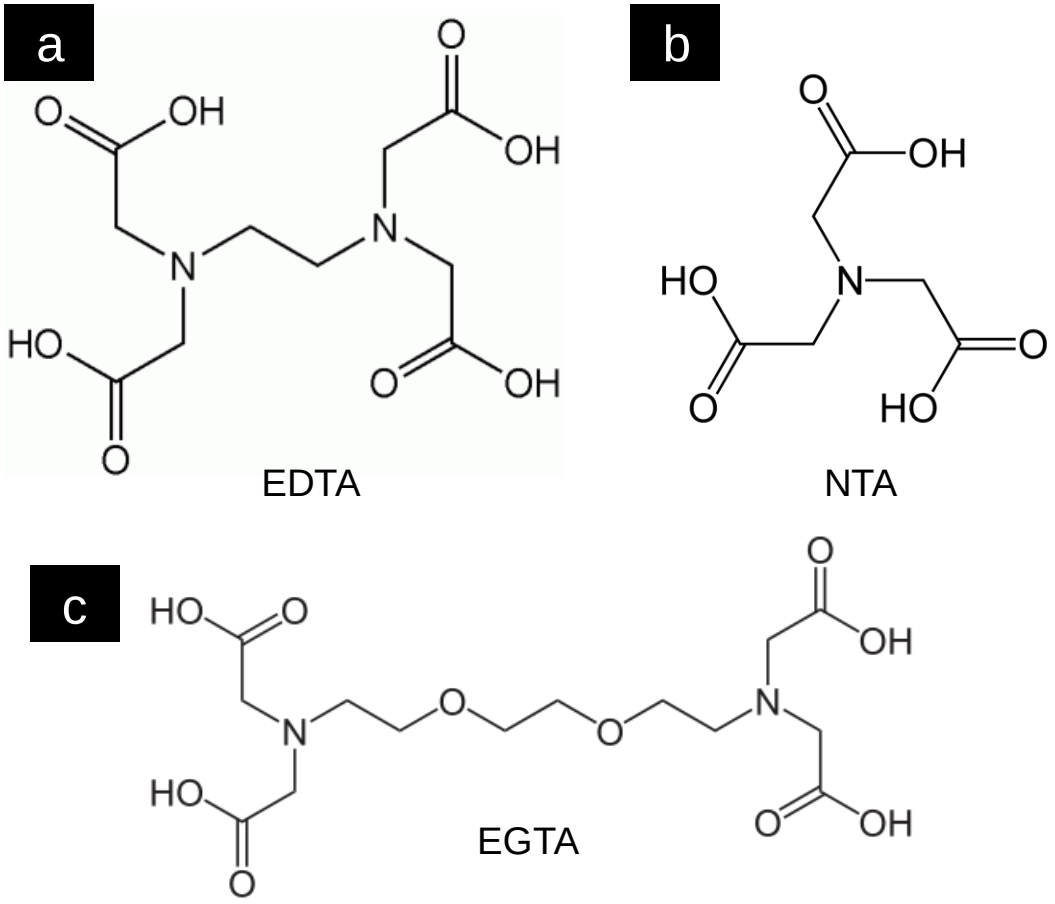

Figure 2.8 Chelating agents
(**a**) ethylenediaminetetraacetic acid (**b**) Nitrilotriacetic-acid (**c**) ethylene glycol tetraacetic acid.

FluoZin-1 fluorescence

FluoZin-1 (Figure 2.9, Molecular Probes, Eugene, OR) exhibits a single emission peak at or near 517 nm following excitation at 495 nm. Direct titrations of Pb^{2+}, Bi^{3+}, Lu^{3+}, Y^{3+} and Ca^{2+} to 2 μM FluoZin-1 were completed to evaluate fluorescence response. Samples were 800 μL in volume comprised of 10 mM TRIS pH 7.4, 100 mM KCl, and 10 μM dye. Metals were directly aliquoted into the sample and allowed to equilibrate for 3 min prior to analysis. Emission scans were acquired with the following fluorometer settings: excitation wavelength 495nm; emission wavelength 505-550nm; stepsize 1; integration 0.2; averages 1; excitation passband 2 nm; and emission passband 4 nm.

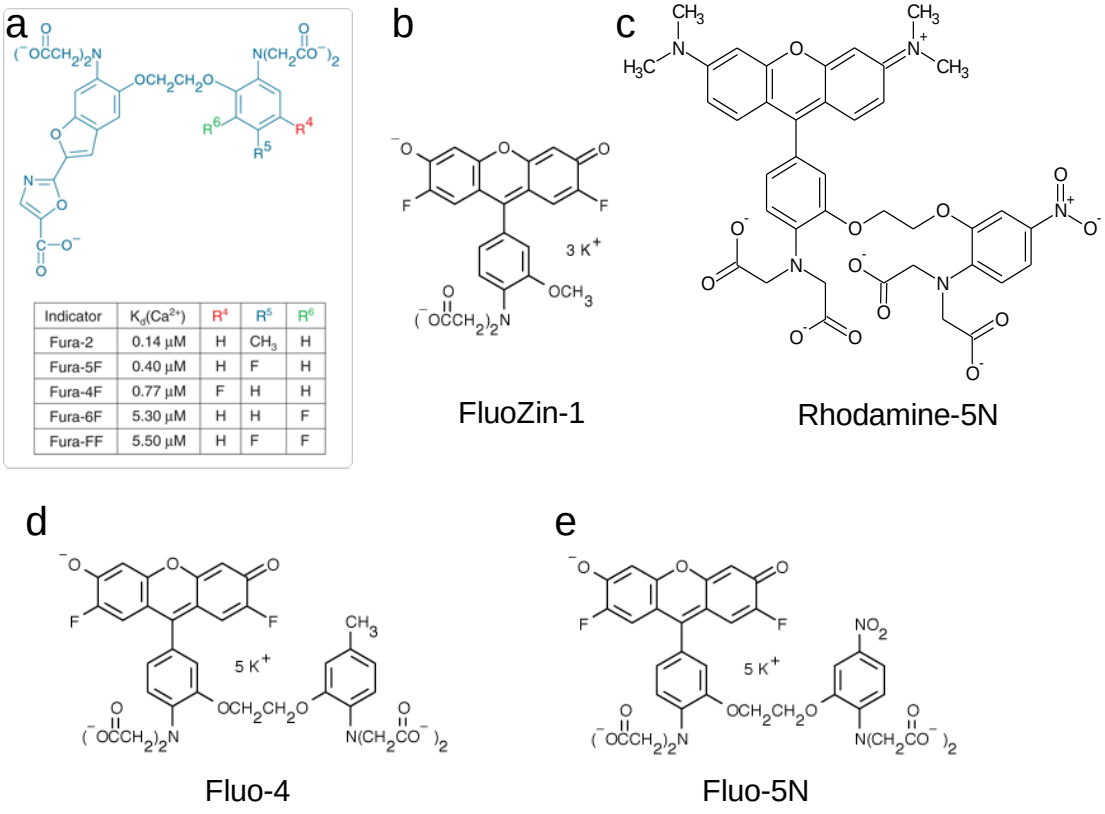

Indicator	$K_d(Ca^{2+})$	R^4	R^5	R^6
Fura-2	0.14 µM	H	CH_3	H
Fura-5F	0.40 µM	H	F	H
Fura-4F	0.77 µM	F	H	H
Fura-6F	5.30 µM	H	H	F
Fura-FF	5.50 µM	H	F	F

Figure 2.9 Fluorescent dyes
(**a**) Fura-2 and Fura-6F, (**b**) FluoZin-1, (**c**) Rhod-5N, (**d**) Fluo-4 and (**e**) Fluo-5N.

Fluo-4 fluorescence

Fluo-4 (Figure 2.9, Molecular Probes, Eugene, OR) exhibits a single emission peak at or near 517 nm following excitation at 495 nm. Direct titrations of Pb^{2+}, Bi^{3+}, Lu^{3+}, Y^{3+} and Ca^{2+} to 10 µM Fluo-4 were completed to evaluate fluorescence response. Samples were 800 µL in volume comprised of 10 mM TRIS pH 7.4, 100 mM KCl, and 10 µM dye. Metals were directly aliquoted into the sample and allowed to equilibrate for 3 min prior to analysis. Emission scans were acquired with the following fluorometer settings: excitation wavelength 495nm; emission wavelength 505-550nm; stepsize 1; integration 0.2; averages 1; excitation passband 2 nm; and emission passband 4 nm.

2.8 NMR studies

NMR Spectroscopy was utilized extensively in these projects to monitor structural changes in proteins related to metal binding events. NMR allows us to observe the effects of applied magnetic fields on the QM magnetic properties (spin) of different nuclei. A detailed discussion on the principles of NMR spectroscopy exceeds the scope of this work, but the interested reader is directed to the thorough online introduction to NMR spectroscopy provided by Horniak [193]. At the most fundamental level, a sample is first subjected to a constant magnetic field (B_0) which aligns the nuclear spin vectors (for nuclei with spin ½, i.e., ^{1}H, ^{13}C, ^{15}N) in one of two orientations (up or down) along a common (Z) axis, based on a Boltzmann distribution between higher and lower energy states. An oscillating radiofrequency (RF) pulse is then applied which reorients the nuclear spin along a different axis. Once the RF pulse is finished, the spin orientation of the nuclei will relax to their alignment in the constant field (H_0). This relaxation includes a longitudinal component (T1) and a transverse component (T2). The spin vectors are affected inhomogenously by the applied magnetic field(s) based on the proximity of other magnetic fields in the sample (e.g., other nuclei, electrons). Manipulation of the applied fields allows for separation of the resonances associated with different nuclei.

Proteins, which are typically much larger than organic molecules, require multidimensional NMR experiments to separate degenerate resonance signals. These experiments will be described in greater detail below.

All spectra were acquired on either a 500 or 600 MHz Varian NMR spectrometer. 1D FID data were processed using MestreNova (MestreLab, Escondido, CA) Software. Format conversion for FID files from Varian to Sparky formats were completed using NMRpipe [194] software. Peak assignment and area integration for 2D and 3D spectra were processed using Sparky [195] software. Data were analyzed or compiled in

Microsoft Excel (Microsoft, Redmond, WA), while curve-fitting was completed using Kaleidagraph software (Synergy Software, Reading, PA).

NMR sample tubes were purchased from Wilmad-Labglass (Vineland, NJ). For Pulsed Field Gradient (PFG) experiments, advanced microtubes and inserts were purchased from Shigemi, Inc., (Allison Park, PA). D_2O (99.96%) was purchased from Cambridge Isotope Laboratories (Andover, MA).

1D ^{1}H NMR

1D Proton spectra were acquired to compare differences in binding between Ca^{2+} and Pb^{2+} with wt-CaM. Binding of Pb^{2+} and wt-CaM was evaluated in both no-salt and high-salt environments, the latter being relevant to physiological conditions.

For 1D NMR, 500 µL samples were prepared with 100 µM wt-CaM, 50 µM EGTA to remove background Ca^{2+}, 10% D_2O, 10 mM TRIS, pH 7.1-7.4. The high-salt sample included 100 mM KCl. The Watergate pulse program was used to suppress the water peak in the spectra. Samples were evaluated at 37 °C. For all samples 128 scans were acquired covering spectral widths of 8384.9 Hz with 16384 complex data points.

Heternuclear Single Quantum Coherence (HSQC) NMR

Heteronuclear Single Quantum Coherence (HSQC) 2D spectra were evaluated for both Ca^{2+} and Pb^{2+}. Through-bond polarization transfer from ^{1}H to ^{15}N and from ^{15}N back to ^{1}H results in signal detection in two dimensions, allowing for identification of N-H pairs within the protein (Figure 2.10). The 500 µL samples were comprised of 253-400 µM ^{15}N-labeled CaM in 10 mM Bis-TRIS pH 6.5, 5 mM MES, 10% D_2O solvent, and 0.1 mM NaN_3 to inhibit bacterial growth. For 2D spectra, samples were analyzed on a 600 MHz Varian NMR spectrometer using pulse program gNHsqc (N15 Gradient HSQC) at 37 °C.

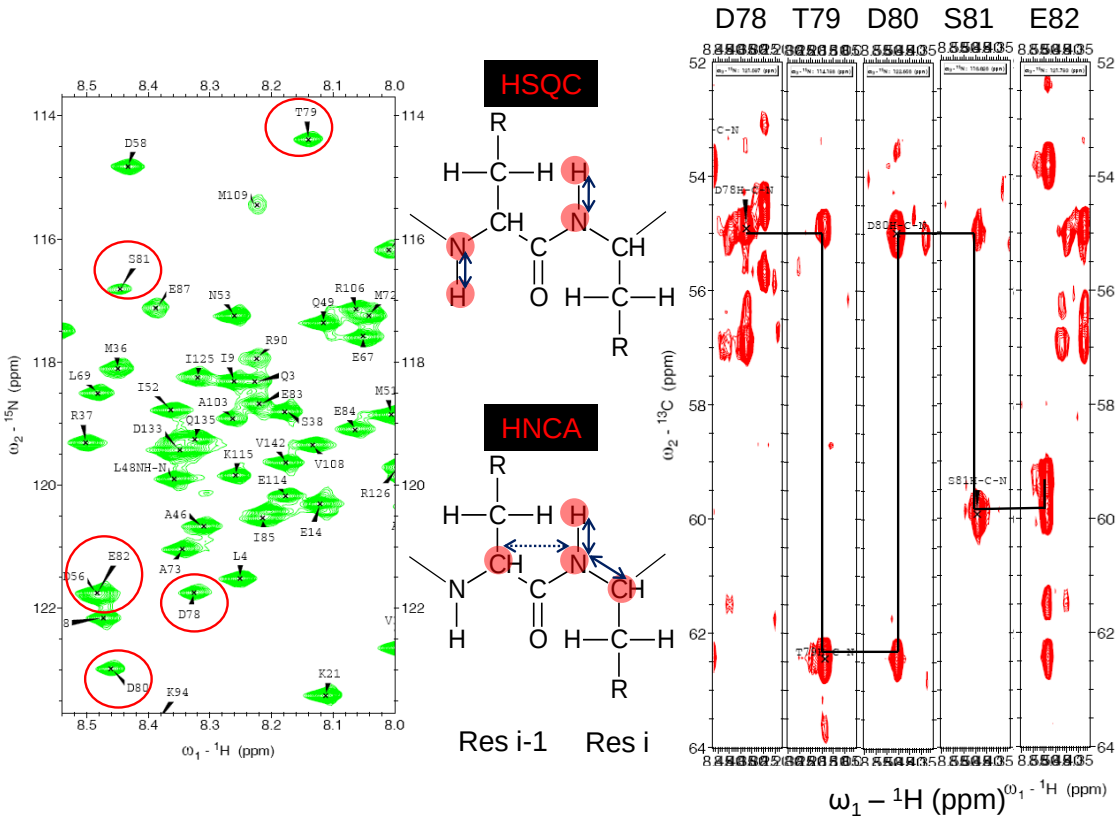

Figure 2.10 Multidimensional NMR spectra for CaM
NMR spectra for 2D HSQC (**left**). Red circles highlight residues corresponding to those identified in 3D HNCA (**right**). Black lines in HNCA connect the paired chemical shifts for identified residues. Polarization transfer schemes for HSQC (**top, center**) and HNCA (**bottom, center**). Blue arrows indicate direction of polarization transfer. The dotted blue arrow indicates weaker polarization transfer from N to C in HNCA.

Typically a total of 32 dummy scans and 32 acquisition scans were collected across a spectral width of 8384.9 Hz in the proton dimension, with 128 scans across a spectral width of 2000 Hz in the nitrogen dimension. Reference spectra for Ca^{2+}-free or Ca^{2+}-loaded CaM were acquired by treating samples first either with 10 mM EGTA or 20 mM Ca^{2+}. Three titration experiments were completed to monitor structural changes in CaM associated with metal binding. First, HSQC spectra were acquired for CaM with 0, 1, 2, 3, 4 and 6 molar equivalents (ME) of Ca^{2+}. Similarly, HSQC spectra were acquired for CaM with 0, 1, 2, 3, 4, 5 and 6 ME Pb^{2+}. Finally, HSQC spectra were obtained for the addition of 0.5, 1.0, 1.5, 2.0, 2.5 and 3.0 ME Pb^{2+} with CaM presaturated with 6 ME Ca^{2+}

to evaluate structural changes associated with competitive binding. Total chemical shift changes (Δδ) across both dimensions (^{15}N and ^{1}H) were weight-averaged based on Eq. 14.

$$\Delta\delta_{Total} = ((\Delta\delta_{NH})^2 + (\Delta\delta_N / 5)^2)^{1/2} \quad \text{(Eq. 14)}$$

HNCA NMR

3D HNCA spectra were evaluated for both Ca^{2+}-free and Ca^{2+}-loaded CaM. In HNCA, through-bond polarization transfer occurs reversibly between ^{1}H, ^{15}N and ^{13}C on residue ***i***, and between ^{15}N on residue ***i*** and ^{13}Cα at residue ***i***-1 (Figure 2.10). The resulting spectra include paired chemical shifts in the 2D plot of ^{13}C vs. ^{1}H. The (typically) less intense peak in the pair then corresponds to the more intense chemical shift in another pair of peaks at some different level in the ^{15}N dimension. This relationship is plotted by the black lines in Figure 2.10. The 500 µL samples were comprised of 780-1000 µM ^{15}N-^{13}C-labeled CaM in NaN_3 to inhibit bacterial growth, 100 mM KCl, pH 6.5, with 10% D_2O solvent. The 1 mM Ca^{2+}-loaded sample was prepared with 20 mM Ca^{2+}, and the 780 µM Ca^{2+}-free sample included 10 mM EGTA to remove all Ca^{2+}. Samples were analyzed using pulse program ghn_ca (Varian Protein-Pack) [196] at 37 °C. A total of 64 dummy scans and 48 acquisition scans were collected across a spectral width of 8384.9 Hz in the proton dimension, represented by 2048 complex data points, with 50 scans covering 4500 Hz and 32 scans covering 1700 Hz for the carbon and nitrogen dimensions, respectively.

Pulsed Field Gradient (PFG) NMR

In PFG NMR an increasing gradient pulse is applied, resulting in decreasing signal intensity due to dephasing of transverse magnetization. Translational motion (i.e., diffusion) in solution correlates with the hydrodynamic radius of the protein, based on the

Einstein-Stokes equation (Eq. 15). Details related to this method and applications have been previously summarized by Kay [197] and this method has been successfully applied in our lab in a related work by Lee [198]. PFG analyses of Pb^{2+} interacting with wt-CaM were acquired for [Pb]:[CaM] ratios 4:1 and 6:1 at 25 °C using a modified PG-SLED pulse sequence. Samples were 350 µL, 250 µM wt-CaM, 10% D_2O, 10 mM TRIS, pH 7.4. Spectra were referenced using the standard DSS (4,4-dimethyl-4-silapentane-1-sulfonic acid). A total of 320 dummy scans and 320 acquisitions were obtained over a spectral width of 8000 Hz in the ^1H dimension, represented by 8192 complex data points. The gradient strength (G) was arrayed over 40 steps covering a range from 0.2 G/cm to 31 G/cm. Results were compared with spectral data for the protein lysozyme which has a similar molecular weight to CaM (14.3 vs. 14.7 kDa) and a hydrodynamic radius of 20.1 Å. From analysis of data for the Pb:CaM complex, acquired under identical buffer and temperature conditions used for lysozyme, a close approximation of the hydrodynamic radius of the Pb:CaM complex can be obtained based on Equations 15-19, as detailed below.

$$D = k_B T / 6\pi a \eta \qquad \text{(Eq. 15)}$$

$$A = A_0 \exp[-(\gamma \delta G)^2 (\Delta - \delta/3) D] \qquad \text{(Eq. 16)}$$

$$[(\gamma \delta)^2 (\Delta - \delta/3) D] = m_1 \qquad \text{(Eq. 17)}$$

$$G^2 = m_0^2 \qquad \text{(Eq. 18)}$$

$$y = \exp[-m_1 * m_0^2] \qquad \text{(Eq. 19)}$$

Terms in Equations 15-19 are defined as follows: ***A*** is the integrated Area of resonance minus the baseline; ***G*** is Gradient Strength (G/cm); ***D*** is the Diffusion constant ($m^2\ s^{-1}$); **γ** is the Gyromagnetic ratio of the nuclei (rad $s^{-1}\ T^{-1}$); **δ** is the duration of each gradient pulse (ms); **Δ** is the Time between gradient pulses (ms); **η** is the solvent viscosity (in g $cm^{-1}\ s^{-1}$); ***α*** is the hydrodynamic radius (in Å) of the molecule and k_B is the Boltzmann constant (1.3807×10^{-23} J K^{-1}). The Diffusion constant D is defined by the

Einstein-Stokes Equation (Eq. 15). Constants from Eq. 16 are redefined as two new terms m_1 and m_0 respectively in Eq. 17 and Eq. 18, and then applied to a modified exponential decay function (Eq. 19) that returns a value for m_1 for CaM following curve-fitting. Coupling this value with the known values of m_1 and the hydrodynamic radius of lysozyme, the radius of CaM can be calculated from Eq. 20.

$$r_{CaM} = \frac{r_{Lys} m_{1_{CaM}}}{m_{1_{Lys}}} \qquad \text{(Eq. 20)}$$

Eq. 22, derived from Eq. 21, is used to calculate a theoretical dimeric hydrodynamic radius R for a monomer of radius r.

$$2 * \frac{4}{3}\pi r^3 = \frac{4}{3}\pi R^3 \qquad \text{(Eq. 21)}$$

$$R_{Calc} = 1.26r \qquad \text{(Eq. 22)}$$

T_1, T_2 and NOE relaxation studies

To compare dynamic properties of CaM complexed with either Ca^{2+} or Pb^{2+}, T_1, T_2 and ^{15}N-{^1H} NOE relaxation were collected and analyzed following the approach described by Seifert [199]. Samples were comprised of 1.14 mM ^{15}N-labeled wt-CaM prepared in 10 mM Tris pH 6.6, 100 mM KCl, 100 µM NaN_3, and 10% D_2O. For analysis of calcium-loaded CaM, 20 mM Ca^{2+} was added to the sample. For analysis of Pb^{2+}, 2 ME of Pb^{2+} was added to CaM pre-loaded with 4 ME Ca^{2+}. Both analyses were run at 37 °C.

For ^{15}N T_1 and T_2 experiments, spectra were acquired using Varian pulse program gNhsqc. T_1 (longitudinal relaxation) values were obtained for ^{15}N with the following relaxation delays (in s): 0.00, 0.01, 0.06, 0.13, 0.23, 0.34, 0.48, 0.74, 1.00, 1.50, and 0.00. T_2 (transverse relaxation) values were obtained for ^{15}N with the following relaxation delays (in s): 0.01, 0.03, 0.05, 0.07, 0.09, 0.11, 0.13, 0.15, and 0.01. Peak

intensity decreases with increasing relaxation time (Figure 2.11). Peaks for T_1 and T_2 spectra were integrated using Sparky software.

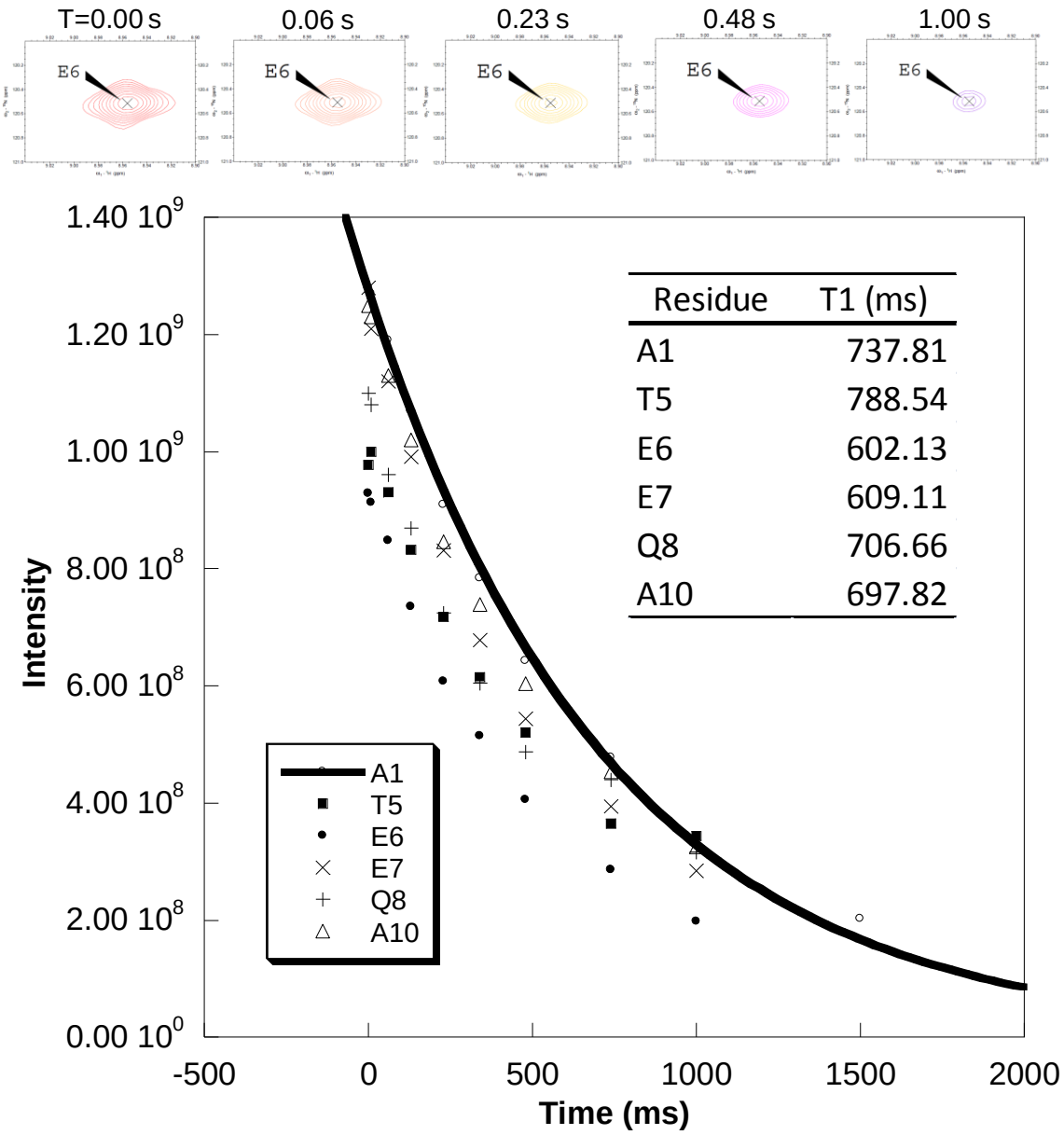

Figure 2.11 Determination of relaxivity values
(**Top**) Intensity of the HSQC peak decreases as relaxation time is allowed to increase. (**Bottom**) Plot of integrated peak areas of amide protons from multiple HSQC spectra with increasing relaxation times. T1 values are calculated using Eq. 23. T1 values for specified amide protons are summarized in inset.

Integrated peak values were plotted in Kaleidagraph as seen in Figure 2.11. T_1 and T_2 values for specific amino acids were calculated by curve-fitting the data with Eq. 23, where ***τ*** is time (ms), ***M₀*** is the signal integration at ***τ* = 0,** and ***T*ₓ =** T_1 or T_2 (ms).

$$Y = M_0 * \exp(\frac{-\tau}{T_X}) \quad \text{(Eq. 23)}$$

$$R_{NOE} = (\frac{t4}{t0}) \quad \text{(Eq. 24)}$$

For ^{15}N-{^{1}H} NOE data, two FID's were acquired with relaxation times of 0.0 and 4.0 s using pulse sequence gNnoe. Data for NOE were processed as a ratio (Eq. 24) where t4 and t0 are the integrated peak areas for relaxation times of 4s and 0s respectively.

Model free formalism and calculation of S^2 order parameters

The model free formalism first proposed by Lipari-Szabo is a means of relating molecular motions to NMR spectral densities [200]. The order parameters associated with motion of internuclear vectors do not depend on an explicit motional model, and the overall and internal motions are uncorrelated. From model free formalism, the function in Eq. 25 can be minimized to derive a general order parameter (S^2) and internal correlation time (τ_e) from T1, T2 and NOE data.

$$f(S^2,\tau_e) = [(T_{1,calc} - T_{1,meas})/T_{1,calc}]^2 + [(T_{2,calc} - T_{2,meas})/T_{2,calc}]^2 + [(NOE_{meas} - NOE_{calc})/2]^2 \quad \text{(Eq. 25)}$$

The order parameter S^2 indicates the degree of angular motion associated with internuclear vectors (i.e., the equilibrium distribution for the orientation of the magnetic moment vector, $\mu(t)$). This provides information on the relative flexibility of different regions in the protein [201], while τ_e represents the motions of $\mu(t)$ in a molecular reference frame.

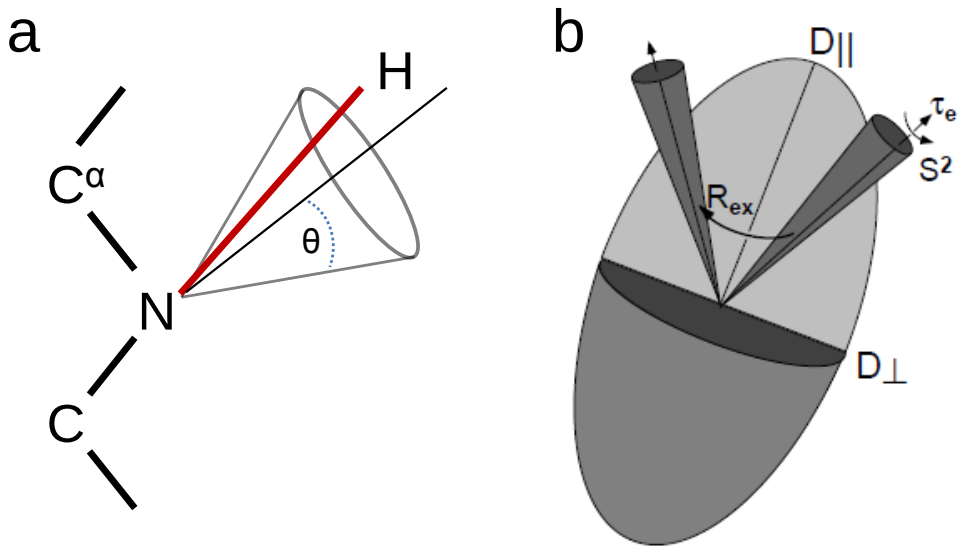

Figure 2.12 The S^2 order parameter
(**a**) S^2 is the square of the general order parameter for equilibrium distribution of orientation of $\mu(t)$ describes diffusion of the N—H bond vector in a cone of semi-angle θ. (**b**) ModelFree software parameters. $D_{\parallel}$ and $D_{\perp}$ are components of an axially symmetric diffusion tensor. R_{ex} accounts for contributions to spin-spin relaxation rate from chemical exchange processes. τ_e is the internal correlation time for motions of $\mu(t)$ in a molecular reference frame.

Both S^2 and τ_e , which represent librational motion of the N—H bond vector as it diffuses, or 'wobbles' within a cone of semiangle θ (Figure 2.12a) , may be calculated using ModelFree software [142-143], a freely-distributed software package for Unix/Linux systems for optimizing "Lipari-Szabo model free" parameters to heteronuclear relaxation data. ModelFree software parameters are illustrated in Figure 2.12b. Five different models can be run, each with different constraints, including constraints for chemical exchange (R_{ex}) and effective correlation time (τ_e) which requires a specific motional model. Files required for ModelFree processing are discussed below.

The **mfdata** file contains the R1, R2 and NOE relaxation values. An example of data from the mfdata file is presented below. Line 1 provides an input type (spin) and a sample ID (e.g., sample_1) for each residue in the protein. Columns 2-4 indicate the

frequency of the proton, R1 (in s) and the error. For our analysis, an averaged default error value was applied.

```
spin   sample_1
R1    599.863     1.355     0.030 1
R2    599.863     5.303     0.300 1
NOE   599.863     0.239     0.040 1

spin   sample_2
R1    599.863     1.268     0.030 1
R2    599.863     6.011     0.300 1
NOE   599.863     0.723     0.040 1
```

The **mfinput** file includes simulation input parameters. This file includes a set of command lines that control global options for running ModelFree. This file can be run with default settings, although the ***fields*** parameter needs to reflect the proton frequency, and the number of simulations can be set within this file.

The **mfmodel** file includes model setting for each residue. An example of data from the mfmodel file is presented below. This file includes a set of input model values for each residue in the protein. Column 4 specifies the type of simulation. In the example below, column 4 for S2s is set to 1, while all other values in this column are set to 0, specifying that this simulation is only for S2s.

```
spin   sample_1
M1 tloc  8.0   0   2    0.000  18.400 20  #       9.200
M1 Theta 0.0   0   2    0.000  90.000 20  #      55.304
M1 S2f   1.0   0   2    0.000   1.000 20  #       1.000
M1 S2s   1.0   1   2    0.000   1.000 20  #       0.929
M1 te    0.0   0   2    0.000 400.000 20  #      64.037
M1 Rex   0.0   0   2    0.000   0.000 20  #       0.000
```

The **mfparam** file includes Vector information, including the internuclear ^{1}H-^{15}N distance (1.02 Å) and the chemical shift anisotropy (CSA) tensor (-160 ppm) for ^{15}N. An example of data from the mfparam file is presented below. This file includes a set of parameters for each spin input (i.e., each residue). Each spin includes two lines of input data, which specify the spin to be analyzed in any single run.

```
spin  sample_3
constants 3 N15     -2.710     1.020     -160.00
vector N H

spin  sample_4
constants  4 N15    -2.710     1.020     -160.00
vector N H
```

The definitions of the keywords and parameters for each spin entry are as follows:

spin	*title*				
constants	*residue*	*nucleus*	*gamma*	*rxh*	*csa*
vector	*atom1*	*atom2*			

Where ***gamma*** is gyromagnetic ration of the spin in units of $T^{-1}s^{-1}/10^7$, ***rxh*** is bond length for dipole-dipole interaction (usually X-H bond length in Å), and ***csa*** is chemical shift anisotropy of the spin (in ppm).

The **mfpdb** file includes all ATOM records from a PDB coordinate file, modified by addition of H atoms and removal of everything else.

Running ModelFree

For the Ca:CaM complex, ModelFree software was used to calculate S^2 order parameters following model parameters reported by Yang *et al.*, [172] using as input the apparent R_1 ($1/T_1$), R_2 ($1/T_2$) and ^{15}N-{^1H} NOE values acquired for the Ca:CaM complex combined with the X-ray crystallographic structure of rat calmodulin (3cln.pdb). Calculations were optimized using the axially symmetric diffusion model based on Brent's implementation of Powell's multidimensional minimization method. Based on values reported by Palmer [202], the default input parameters for the internuclear ^1H-^{15}N distance and the chemical shift anisotropy (CSA) tensor for ^{15}N were preset at 1.02 Å and -172 ppm, respectively.

Models were run in succession, retaining the model for each residues that met a specific cutoff criterion, calculated from Eq. 26, Eq. 27 and Eq. 28.

$$\Gamma_{sum} = \left(\frac{(\exp - pred)^2}{(uncert)^2}\right)_{R1} + \left(\frac{(\exp - pred)^2}{(uncert)^2}\right)_{R2} + \left(\frac{(\exp - pred)^2}{(uncert)^2}\right)_{NOE} \quad \text{(Eq. 26)}$$

$$\alpha_{sum} = \left(\frac{(0.1 * pred)^2}{(uncert)^2}\right)_{R1} + \left(\frac{(0.1 * pred)^2}{(uncert)^2}\right)_{R2} + \left(\frac{(0.1 * pred)^2}{(uncert)^2}\right)_{NOE} \quad \text{(Eq. 27)}$$

$$\frac{\Gamma_{sum}}{\alpha_{sum}} \leq 0.50 \quad \text{(Eq. 28)}$$

Terms in Eq. 26 are derived from Eq. 25 and account for R1, R2 and NOE data. In this series of equations, ***exp*** represents the experimentally determined values, ***pred*** represents values predicted by ModelFree, and ***uncert*** represents predicted uncertainty. The value Γ_{sum} accounts for a percent relative error based on differences between the experimental results and the prediction model, while α_{sum} calculates the same error based on an allowable 10% deviation. If the ratio of the two values from Eq. 26 and Eq. 27 expressed in Eq. 28 meet the cutoff of 0.50, the model is considered acceptable and is retained for that residue. This process is repeated for the different models until acceptable values are obtained for all residues.

2.9 Equilibrium dialysis sample preparation

Another method to establish the stoichiometry of metal:CaM complex formation involved Equilibrium Dialysis. This method is a general process whereby two separated solutions containing different compounds are allowed to equilibrate over time via mixing through a semipermeable barrier that allows certain components to move freely between solutions while restricting one or more components to only one side of the barrier. The dialysis equipment consists of two reservoir molds (Figure 2.13) with a row of corresponding chambers in each mold. A layer of dialysis tubing is inserted between the molds, separating the reservoirs and providing a semipermeable barrier between the reservoirs once the molds are clamped together.

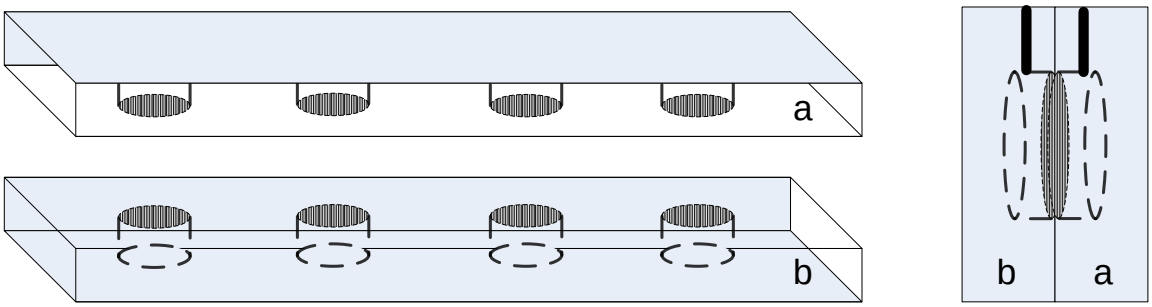

Figure 2.13 Dialysis reservoir molds
The four paired chambers from blocks *a* and *b* (**Left**) are separated by a layer of dialysis tubing (not shown). End-on view after clamping (**Right**). A vertical tube allows solutions to be added to each side of the bisected chamber (dark lines from top).

Once the molds are sealed together, a protein sample is introduced into one side of the bisected chamber, while a solution containing the target metal is introduced into the other side. After sealing the sample injection tubes at the top with parafilm, the apparatus is allowed to equilibrate for 48-72 h on a shaker at 4 °C.

For our first experiment, eight protein samples and eight corresponding metal solutions were prepared as follows: 3 X CaM (2 μM) corresponding to 3 X Pb^{2+} (18 μM); 3 X CaM-Delete (2 μM) corresponding to 3 X Pb^{2+} (18 μM); 1 X CaM (2 μM) corresponding to 1 X Ca^{2+} (12 μM), and; 1 X CaM-Delete (2 μM) corresponding to 1 X Ca^{2+} (12 μM). All sample volumes were 4 mL. Dialysis tubing used to separate the chambers had a MWCO of 3.5 kDa. Both protein and metal samples were prepared in 10 mM Tris pH 7.4, 100 mM KCl. Buffers were treated by overnight dialysis with Chelex100. Additionally, protein was treated by passing through a Calcium Sponge column to remove trace metals. After 66 h for equilibration, samples were transferred into 5 mL disposable centrifuge tubes.

In theory, the metal ions from the initial source reservoirs should have crossed the membrane and then become bound by the protein. At equilibration, the concentration of free metal in both the protein sample reservoir and the metal solution reservoir should have been equivalent, with the remainder of the initial metal bound to the protein. To

evaluate this, the final extracted samples were transferred to quartz cuvettes previously described for fluorescence. Rhod-5N dye was titrated directly into both the protein and metal buffer samples to compare changes in fluorescence as a measure of metal concentration.

2.10 Sub-cloning of CD2.7E15 variants

Several mutant variants of the protein CD2 have been previously developed in our lab [168, 177] to evaluate isolated EF-Hand Ca^{2+} binding sites. One of these, CD2.7E15, includes mutations (N15E, L58D, and K64D), coupled with two natural ligands (E56 and D62), to form a Ca^{2+} binding site based on the pentagonal-bipyramid structure of the EF-Hand motif.

Currently, we are modifying the CD2.7E15 plasmid DNA previously generated in our laboratory to introduce different charge mutations in the binding site microenvironment. This will allow us to further dissect the significance of charge associated with binding affinity for Ca^{2+} and other metals. The EENDN primer developed for the charge residue mutagenesis of CD2.7E15 is shown in Table 2.5.

Table 2.5 Primers for charge variants of CD2.7E15

Name	Sequence	bp changes	Tm
7E15-EEDDE	GCA AAT GGA GAC TTG GAG ATA AAG AAT CTG ACA AG	1	75.8
7E15-EEDDN	AC GCA AAT GGA GAC TTG AAC ATA AAG AAT CTG ACA AG	1	76.1
7E15-EEDDQ	AC GCA AAT GGA GAC TTG CAG ATA AAG AAT CTG ACA AGA G	2	75.9
7E15-EENDN	GCA TTT GAG ATC AAC GCA AAT GGA GAC TTG AAC ATA AAG AAT C	2	76.4
7E15-NENDN	CC CTG GGT CAT GGC ATC AAC CTG AAC ATC CCT AAC TTT C	2	80.1

The primer for mutation 7E15.EENDN (from EEDDD), designed by Ms. Ling Wei, was obtained from Invitrogen. The 7E15.EENDN primer was first phosphorylated. 1 µL (100 ng) primer was mixed with 1 µL 10X T4 polynucleotide kinase buffer, followed by 1 µL (1mM) ATP (pH 7.5), 6 µL ddH_2O and 1 µL (10U) T4 polynucleotide kinase. This solution was incubated at 37 °C for 60 min, then heated at 70 °C for 10 min. For the

polymerase chain reaction (PCR), 2.5 µL 10X QuikChange Multi Reaction Buffer was mixed with 17.5 µL ddH2O, 2 µL 30ng/µL pET20b/7E15 DNA, 1 µL 100 ng/µL Ⓟ-Primer, µL dNTP mix and µL QuikChange Multi enzyme blend. Samples were prepared in PCR microcuvettes and placed in PCR.

After overnight PCR cycling, 1 µL DpnI restriction enzyme was added directly to each PCR reaction. The reaction solution was mixed gently by pipetting up and down, then spun down for 1 min at maximum speed. The reaction was then immediately incubated at 37 °C for 60-120 min.

The next step was transformation. XL 10-Gold ultracompetent cells were thawed on ice for 10 min, and then aliquots of 22 µL were added to prechilled 15 mL polypropylene round-bottom tubes for each reaction. 1 µL of β-mercaptoethanol was added and mixed by swirling, followed by incubation of the cells on ice for 10 min, swirling every two min. 1.5 µL of the DpnI-treated DNA reaction was transferred to the ultracompetent cells, which was swirled to mix the transformation reaction, followed by incubation on ice for 30 min. Next, NZY^+ broth was preheated in 42 °C water bath, following which the reaction samples were heat-pulsed in 42 °C water bath for 30 s. The tubes were again incubated on ice, for 2 min, then 0.5 mL of the NZY^+ broth was added to the tube, which was then shaken/incubated at 37 °C for 1 hour 225-250 rpm. Aliquots of 20 µL and 50 µL were plated on LB plate with 100 µg/mL ampicillin. The transformation plates were then incubated overnight at 37 °C.

A single colony was extracted with an inoculation loop and stirred into 5 mL LB medium with 100 mg/mL ampicillin. Five samples were individually prepared in 50 mL falcon tubes. Samples were incubated 12-16 h at 37 °C with vigorous shaking, following which the bacterial cells were harvested by centrifugation at 8000 rpm for 5 min. Cells were refrigerated at 20 °C.

A QIAprep Spin Miniprep Kit (Qiagen) was prepared for plasmid DNA purification. The benchtop was cleaned thoroughly with ethanol and all pipets were also cleaned with ethanol. The bacterial cells were first resuspended in 250 µL Buffer P1 and transferred to a microcentrifuge tube. 250 µL Buffer P2 were added and mixed thoroughly by inverting the tube 4-6 times until the solution turned blue. Next, 350 µL of Buffer N3 was added and mixed thoroughly by inverting the tube 4-6 times until the solution becomes colorless.

Individual samples were then centrifuged 10 min at 13 000 rpm in a table-top microcentrifuge. The resulting supernatant was applied to the QIAprep spin column by pipetting and centrifuged for 30-60 s. Flow through from the column was discarded. The QIAprep spin column was washed by adding 0.5 mL Buffer PB and centrifuging 30-60 s at 13, 000 rpm, following which the flow-through was discarded. The spin column was washed again by adding 0.75 mL Buffer PD and centrifuging 30-60 s at 13, 000 rpm. The flow-through was discarded and the column centrifuged for an additional 1 min to remove residual wash buffer.

The QIAprep column was then inserted into a clean, autoclaved 1.5 mL microcentrifuge tube for elution of the plasmid DNA. 50 µL of Buffer EB was pipetted to the center of the QIAprep spin column. After allowing the column to stand for 5 min, it was centrifuged for 2 min at 13, 000 rpm. Samples were labeled and stored at 4 °C. Concentrations of the samples were first evaluated with Agarose gel. For the DNA samples, 1 µL of DNA was mixed with 2 µL 6X DNA dye and 7 µL ddH_2O. The marker was a mixture of 1 µL Super coiled marker, 2 µL 6X DNA dye and 7 µL ddH_2O. Based on the intensity of different samples observed with the agarose gel, two 5 uL samples were sent to the Georgia State Biology core facility for DNA sequencing to determine if the EENDN mutant was sub-cloned during mutagenesis.

3 Analyses of Ca^{2+}-binding in proteins

3.1 Ca^{2+}-binding proteins and Ca^{2+}-binding sites

Ca^{2+} is demonstrably one of the more relevant metal ions associated with biological functions. The significance of Ca^{2+} in biological systems first emerged with early efforts to understand biomineralization nearly 200 years ago. Since then, our knowledge regarding the roles of calcium in biological systems has increased drastically, and technological sophistication now allows us to study the activity of Ca^{2+} at a molecular level revealing complex systemic interactions related to cell life cycle, diverse protein structures and induced or modulated responses of intra- and extra-cellular proteins to changes in Ca^{2+} concentrations.

In the intracellular environment, Ca^{2+} is critical to a wide variety of functions related to muscle contraction, neurotransmitter release and enzyme activation [203-205]. Additionally, Ca^{2+} and Ca^{2+}-binding proteins (CaBPs) are involved in almost every aspect of the eukaryotic cell life cycle including cell differentiation and proliferation, membrane stability, apoptosis and intracellular signaling [206-209]. Control of these diverse functions is regulated by changes in cytosolic Ca^{2+} levels, which increase from ~10^{-7} M at rest to ~10^{-5} M when activated. This increase results either from influx of extracellular Ca^{2+} through Ca^{2+}-channels or by release of Ca^{2+} stored internally by CaBPs (e.g., calsequestrin in skeletal muscle cells) in the endoplasmic/sarcoplasmic reticulum (ER/SR). Surface receptors on the ER/SR, which regulate Ca^{2+} release, differ by cell type. Release of Ca^{2+} from the ER/SR in myocardial muscle cells is regulated by Ryanodine Receptor RyR2 channel protein, which itself may be in part regulated by binding with the intracellular Ca^{2+}-trigger protein calmodulin (CaM) [109-112]. The inositol 1,4,5 triphosphate receptor (e.g., IP_3R receptor) also regulates Ca^{2+} release from the ER/SR.

Intracellular CaBPs are generally of two types: sensors and buffers. In response to increased cytosolic Ca^{2+}, intracellular proteins such as calmodulin (CaM) and protein kinase C (PKC) bind Ca^{2+}. This alters their tertiary structure which allows them to bind and activate other enzymes which perform different functions within the cell. Other Ca^{2+}-binding proteins (CaBPs), including parvalbumin and $calbindin_{D9k}$ act as buffers to regulate cytosolic Ca^{2+}.

More recently, new functions for Ca^{2+} in the extracellular environment have been identified. Here, Ca^{2+} functions as a second messenger in signal transduction through binding with extracellular signaling molecules, including important membrane proteins in the family C of G protein-coupled receptors (GPCRs): (i) Metabotropic glutamate receptor 1 (mGluR1) [210] which performs multiple functions in neurological processes (e.g., memory, learning, pain and synaptic plasticity), and (ii) the Ca^{2+}-sensing receptor (CaSR) [211] which maintains extracellular Ca^{2+} homeostasis.

In the last decade, a number of studies have identified bacterial EF-hand-like Ca^{2+}-binding sites which may play important roles Ca^{2+}-signaling and Ca^{2+}-homeostasis. These binding sites exhibit variations in either the binding loop or the flanking sequences on either side of the loop which differentiates them from canonical EF-hand motifs, while simultaneously retaining a binding geometry similar to the pentagonal-bipyramidal coordination identified with EF-hand.

Additionally, new evidence demonstrates a role for Ca^{2+} in viral activity [212]. The complex intracellular machinery controlled by Ca^{2+}-mediated events presents diverse opportunities for viruses to utilize available Ca^{2+} to facilitate virion structure formation, cell entry, viral gene expression, replication and release. A Ca^{2+}-binding motif previously used to identify EF-hand Ca^{2+}-binding motifs in bacteria has identified nearly 100 putative Ca^{2+}-binding sites in viral proteins. A comprehensive treatment of this subject is presented by Zhou *et al* [213].

The cellular activities regulated by Ca^{2+}, while numerous, are all dependent upon the abilities of different proteins to bind Ca^{2+} selectively over other metals, and to do so with affinities consistent with the concentration of free Ca^{2+} available in any given environment.

Establishing a relationship between Ca^{2+}-binding site geometry and affinity is frequently problematic, and the literature remains relatively sparse with affinity data in comparison with the volume of available PDB structure files. A summary of some reported binding affinity values associated with CaBPs is available at http://structbio.vanderbilt.edu/cabp_database/. For many Ca^{2+}-binding proteins, particularly EF-hand proteins, the determination of binding affinity between Ca^{2+} ions and their binding sites is difficult for several reasons. First, the cooperative binding exhibited between pairs of Ca^{2+}-binding sites presents experimental challenges to determining affinity values for each of the sites as an isolated binding event. Affinity values for individual binding sites that function in cooperative pairs have been reported, but are typically calculated based on upper and lower limits derived from the relationship between macroscopic and microscopic binding constants as described by Linse *et al*. [139], or as relative affinities based on order of occupancy (i.e., higher affinity sites are populated first). Second, for higher affinity binding sites, analytical instruments lack sensitivity to analyze samples at concentrations comparable with their binding affinities, so experimental methods typically involve protein concentrations much higher than their metal-binding affinity, which precludes determination of binding affinity constants [214].

Different approaches have been made to circumvent the issue of cooperativity while trying to determine dissociation constants for single sites. Early efforts involved analyses of individual EF-hand motifs isolated as peptides. Another approach involved spectrofluorometric analysis, where the macroscopic Ca^{2+} affinities (expressed in dissociation constant K_d) for the N- and C-terminal domains of CaM, each comprising a

pair of cooperative binding sites (EF I and EF II in the N-terminal, and EF III and EF IV in the C-terminal), were determined by monitoring Phe and Tyr residues which exhibit fluorescence changes upon binding of metal ions [191]. The resulting values were found to be approximately 12 and 2 μM, respectively, for the N- and C-terminal domains, with initial occupancy observed in sites EF III and EF IV. These results are consistent with the current consensus that Ca^{2+} first occupies the higher affinity C-terminal sites with 6-fold higher affinity than the N-terminal sites. Additionally, NMR spectroscopy can provide data related to order of occupancy and affinity based on changes in chemical shift data in binding sites associated with Ca^{2+}-binding, however, this approach requires high-resolution NMR and significant time investment to collect data.

More recently, Ye *et al*. determined binding dissociation constants (K_d) for CaM EF-loops I-IV (34, 245, 185 and 814 uM, respectively) by grafting the loops into a scaffold proteins [173]. However, this approach, like the analyses of peptide fragments, fails to account for cooperative binding effects, and yields contradictory results compared with studies indicating that CaM EF-loops III and IV in the apo-protein exhibit higher binding affinity and bind Ca^{2+} before the N-terminal domain sites. Moreover, the results of this study, which show significant variance in binding affinity (> 20-fold) for EF-loops in the same protein (CaM), suggest that the binding site microenvironment does not exclusively control affinity, as these binding sites share high sequence similarity and all exhibit pentagonal bipyramidal geometry. Beyond the obvious influence of the binding site, additional structural parameters associated with binding affinity remain to be quantitatively assessed.

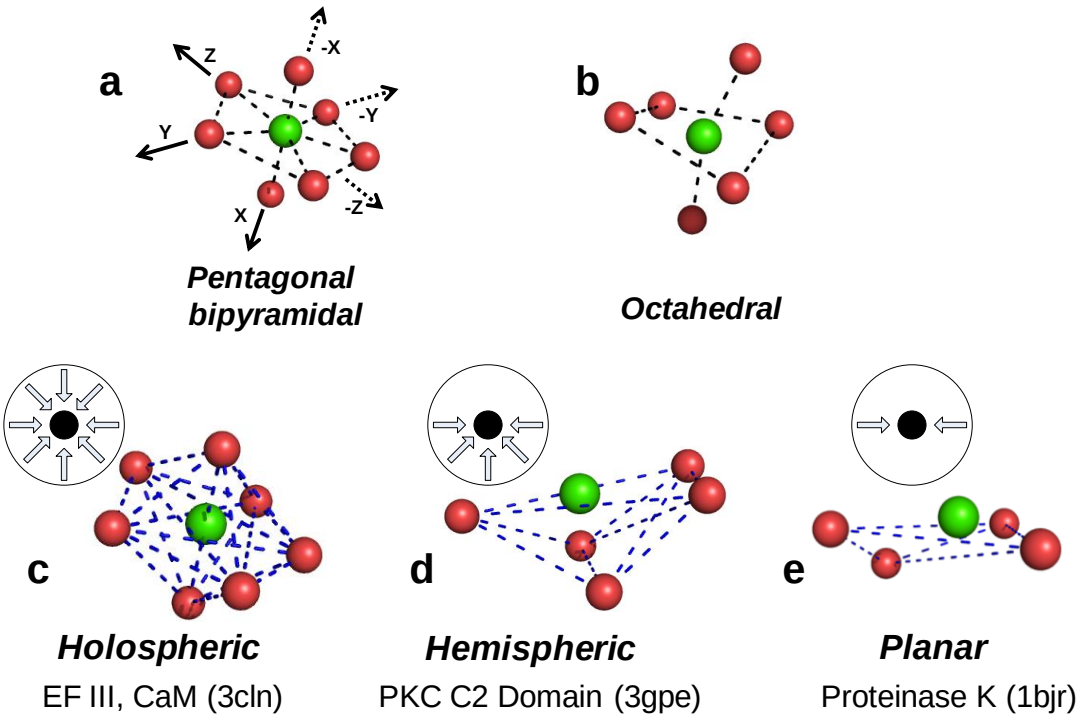

Figure 3.1 Metal binding sites
(**a**) Pentagonal-bipyramid geometry associated with EF-Hand binding motif. (**b**) Octahedral binding geometry for Ca^{2+} and Mg^{2+}. (**c**) Holospheric binding where Ca^{2+} is surrounded on all sides by oxygen ligands. This would include both pentagonal-bipyramid and octahedral geometries. (**d**) Hemispheric binding where the Ca^{2+} ion is exposed on one hemispheric surface. (**e**) Planar binding where the Ca^{2+} ion is bound in a ring structure with exposure above and below the plane.

The interface between Ca^{2+} and biological activity can be localized to the protein Ca^{2+}-binding sites; regions of the protein that have evolved to chelate Ca^{2+} and translate the binding event into a conformational change capable of inducing activity not observed in the Ca^{2+}-free state. Binding of Ca^{2+}, a hard Lewis acid, is almost exclusively coordinated in proteins by oxygen ligands which originate in sidechain carboxyl (Asp, Glu), carboxamide (Asn, Gln), and hydroxyl (Ser, Thr) groups. Carbonyl oxygen from the mainchain may also contribute to coordination, as well as oxygen from water molecules which are observed to form hydrogen bonds with Asp, Ser and Asn residues. Nitrogen, which binds Zn^{2+} and may associate with Ca^{2+} in small molecules, is only infrequently

observed in the structures of Ca^{2+}-binding sites, and then, observed mostly in cases where the site has no net negative charge.

Calcium-binding sites can be separated into three distinct classes [61, 215-217]. Class I sites are comprised of consecutive amino acids in the primary sequence which would include canonical EF-hand (discussed below), pseudo EF-hand (e.g., S100 proteins) and other noncanonical EF-hand (e.g., calpain) motifs. Class II sites include a similar stretch of consecutive amino acids, but also include a coordinating ligand that is close to the other binding ligands in the three-dimensional structure, but distant in the sequence (e.g., hcv helicase, PDB ID 1hei.pdb). Class III sites, the least commonly-observed, include multiple coordination ligands in close spatial proximity but still distant in the sequence (e.g., the C2 domain of the enzyme Protein Kinase C (PKC)). It should be emphasized that this classification scheme is based on the relationships between amino acids in the sequence, rather than structure. To understand Ca^{2+}-modulated protein function, metal selectivity and Ca^{2+}-binding affinity, and develop computational approaches for the prediction and identification of Ca^{2+}-binding sites, it is equally important to analyze structural changes associated with Ca^{2+}-binding.

Early work with Ca^{2+}-binding proteins observed examples of highly-organized coordination geometries [5, 17-19, 131, 179-180, 209, 218-220], including either pentagonal-bipyramidal (Figure 3.1a), where the ion is surrounded by a planar grouping of five oxygen atoms with additional oxygen atoms superior and inferior to the plane, or octahedral (Figure 3.1b), with similar ligand coordination above and below a planar ring of only four oxygen atoms. However, more recent analyses of Ca^{2+}-binding sites reveals much greater diversity in binding coordination geometries than previously assumed. The PDB currently includes structures for ~1500 CaBPs not classified as EF-hand or EF-like motifs, which suggests that a comprehensive structural classification scheme for Ca^{2+}-binding remains incomplete. To address the identification of Ca^{2+}-binding sites exhibiting

increasing diversity, a more generalized set of coordination geometries may be applied, based on similar classification of Pb^{2+}-binding [221] and a Hull property describing the spatial relationship of the Ca^{2+} ion to the interior volume of the surrounding binding ligands. Figure 3.1c describes a holospheric binding geometry where oxygen ligands surround Ca^{2+} on all sides, as would be observed in both the pentagonal-bipyramid and octahedral geometries. In Figure 3.1d, a hemispheric coordination scheme is observed with an open concavity (i.e., bowl structure) coordinating the ion. Finally, a more irregular binding site is described in Figure 3.1e, with as few as three coordinating ligands forming a plane around the ion without benefit of stabilization above or below the plane. These latter Ca^{2+}-binding sites, some of which lack well-structured and recognizable geometric configurations and include binding ligands sequentially distant from each other in the structure, present interesting challenges for determining functional implications, as well as establishing quantitative means of relating structure to both affinity and metal selectivity. This issue has been addressed in recent years by using a variety of different computational algorithms to identify or predict Ca^{2+}-binding sites. Some of these approaches utilize structural parameters associated with Ca^{2+} and its binding ligands, and statistical evaluation of different Ca^{2+}-binding sites has demonstrated that EF-hand and non EF-hand proteins are differentiable based on these parameters, including distance between the ligand and the ion, distance between ligands, and angles between the carbon covalently bound to the oxygen ligand, the oxygen ligand itself and the calcium ion. Although a discrete structural classification system for non EF-hand proteins remains to be developed, these emerging computational methods are providing a framework for viewing Ca^{2+}-binding beyond the limitations of sequence-based information [222].

3.2 EF-Hand superfamily

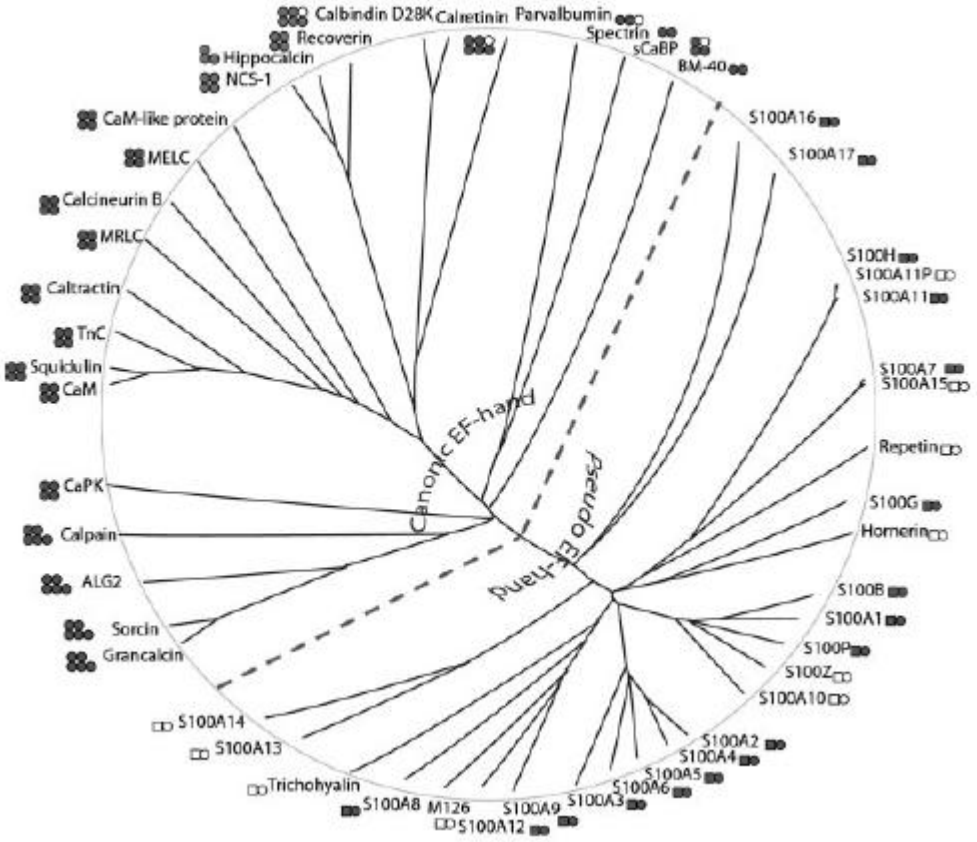

Figure 3.2 Phylogenic analysis of EF-hand protein family
The unrooted N-J tree (from Zhou, et al., [178]) was generated on the basis of multiple sequence alignments of 27 typical proteins containing pseudo EF-hand motifs and 22 proteins with canonical EF hand motifs. (Circle: canonical EF-hand; Square: pseudo EF-hand; Solid: bind Ca^{2+}; Open: do not bind Ca^{2+} or Ca^{2+} binding capability is unknown).

The increasingly populous superfamily of EF-hand proteins, comprising approximately 70 different genomic subfamilies, can be divided into two major groups based on Ca^{2+}-binding sites: The canonical EF-hand motif which is the most common and widely-recognized protein Ca^{2+}-binding structural domain, and; the more recently-characterized non-canonical EF-loops which include the pseudo EF-hands observed in the N-termini of S100 and S100-like proteins (Figure 3.2) [132, 178, 223-224]. Canonical EF-hand motifs are almost exclusively found in pairs ranging from 2-6 copies, while

pseudo EF-hand motifs are often paired with a C-terminal canonical EF-hand. Noncanonical EF-loops, including many recently identified in prokaryotic EF-hand-like proteins, exhibit more sequential diversity in or near the Ca^{2+}-binding loop, but still exhibit coordination properties similar to canonical EF-hand sites. Characteristics of the binding sites associated with the major EF-hand superfamily groups are summarized below.

3.3 Canonical EF-Hand binding motif

The canonical EF-Hand motif, first described by Kretsinger in the 1970's [225], is highly-conserved in both Eukaryotes and Prokaryotes. This sequential motif, described extensively in the literature, is 29 amino acids in length comprising a 12 residue loop surrounded by two flanking α-helices positioned in a relatively perpendicular orientation (Figure 3.3a). Analyses of meta-data from online databases (e.g., PFAM, ProSite) indicate that the length of the entering (E) and exiting (F) helices are typically 9 and 8 residues in length, respectively. Loop residues are assigned relative position numbers 1-12. Binding of Ca^{2+} is coordinated by residues in loop positions 1(*x*-axis), 3(*y*), 5(*z*), 7(-*y*), 9(-*x*) and 12(-*z*), forming a pentagonal bipyramidal geometry (Figure 3.1a).

The coordination number for Ca^{2+}-binding in proteins has been reported at 5-8 ligands, with an average between 6-7 [61, 217] . The mean Ca-O ligand binding distance has been reported, from different studies, as either 2.4 ± 0.1 Å, or 2.42 Å with a range of 2.01 – 3.15 Å [5, 10, 188, 204, 226-228]. Loops typically exhibit a negative charge between -2 and -4 [229], which likely represents an optimal charge configuration based on analyses of sequence homology and energy calculations for 276 EF-Hand loops [129, 218].

Ligands observed within the EF-Loop are typically Asp at position 1, Asp or Asn at position 3, Asp, Ser or Asn at position 5, a water molecule at position 9, and a

bidentate Glu at position 12 [218] which may initially anchor Ca^{2+} and thus initiate rotation of loop residues to form the binding site. The coordinating ligand from position 7 is usually a carbonyl oxygen, while the non-coordinating residue in position 6 is frequently a flexible Gly. The conserved hydrophobic residues in loop position 8 (Val, Leu or Ile) also play an important functional role related to the interaction between paired EF-loops. Binding of Ca^{2+} in paired EF-Hands is cooperative, and typically binding in one of the sites enhances the binding affinity of the second site (i.e., positive cooperativity). The hydrophobic residues in loop position 8 between paired EF-Hand sites (Figure 3.3b) form two short anti-parallel β-strands (Figure 3.3c) [230-231], and it has been suggested that this EFβ-scaffold governs Ca^{2+}-binding and the associated structural changes [232] and represents the structural basis for positive cooperativity between the

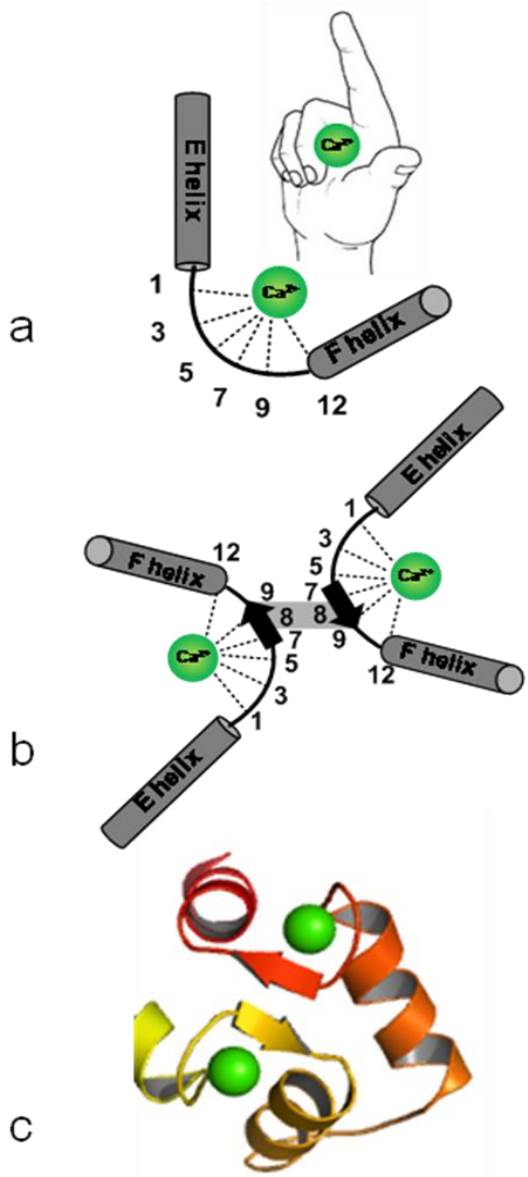

Figure 3.3 EF-Hand and cooperativity
(**a**) EF-hand motif. (**b**) Paired EF-hand motifs from Loops EF-III and EF-IV of CaM. Conserved hydrophobic residues in position 8 (Val, Leu or Ile). Cooperative binding between the two EF-hand motifs is related to formation of hydrogen bonds between residues in loop position 8 which create (**c**) two short anti-parallel β-strands.

sites [76-77]. Calmodulin, parvalbumin and troponin C all represent proteins with paired canonical EF-hand binding sites. See Gifford et al for recent review of EF-hand [233].

Instances of proteins with odd (i.e., unpaired) EF-loops have been identified, and in some cases, misidentified, as seen with the transmembrane protein STIM1. STIM1, found in the ER, responds to depletion of luminal Ca^{2+} by activating store-operated Ca^{2+} (SOC) channels on the plasma membrane and thereby facilitating extracellular Ca^{2+} influx into the cytoplasm. The N-terminal domain of STIM1 contains several functionally important regions including an ER signal peptide and a canonical EF-hand domain. Preliminary investigations on STIM1 had indicated that observed canonical EF-hand domain functioned as a solitary binding site for Ca^{2+}, but a second hidden EF-hand site was later revealed which was found to stabilize the canonical EF-hand through hydrogen bonding between the paired loops and to exhibit the cooperative binding effects associated with EF-hand pairs [234].

3.4 Pseudo EF-Hand binding motif

The pseudo EF-hand motif is found in the S100 and S100-Like proteins [132, 178, 223-224], including calbindin D_{9k} and calcyclin (S100A6). The S100 proteins generally are of lower molecular weight (~9-14 kDa). The full range of functions associated with S100 proteins remains unknown, but different S100 proteins have been identified with a substantial number of extracellular and intracellular activity, including regulatory activities related to phosphorylation, enzymes, and intracellular Ca^{2+} release associated with ryanodine receptor function, as well as increased expression in inflammatory responses and cancer metastasis [235]. In cells, these proteins may organize as covalently-bound homodimers or heterodimers, with some exceptions including calbindin D_{9k} which is a monomer. Dimerization of S100 proteins appears to directly relate to their biological activities, and the structural basis for this self-assembly is driven by binding with Ca^{2+}.

The pseudo EF-hand binding geometry is similar to the pentagonal bipyramidal conformation observed with the canonical EF-hand, but significant differences are observed in the binding loop. Rather than a 12-residue loop, pseudo EF-hand extends to 14 residues where the Ca^{2+} ion is coordinated predominantly with main-chain carbonyl oxygen atoms from residues occupying positions 1, 4, 6 and 9, with a water molecule coordinated by residue 11 and a bidentate (Asp or Glu) ligand in loop position 14 [236]. Because the majority of binding ligands originate from the backbone itself, the nature of the associated residue is less restricted than what is observed with canonical EF-hand binding sites. Additionally, where the canonical EF-loops typically have a formal charge between -2 and -4, less formal charge is observed in the pseudo EF-loops due to dominance of carbonyl oxygen binding ligands. An example of this can be seen with calprotectin (PDB ID 1xk4) which binds Ca^{2+} with zero formal charge in the binding site [237].

This motif is usually observed to be paired with, and to sequentially precede, a canonical EF-hand which exhibits higher binding affinity for Ca^{2+}. From the N-terminal, helices are labeled consecutively H1-H4. The pseudo EF-hand loop (L1) is flanked by H1 and H2, while the canonical EF-hand loop (L2) is surrounded by helices H3 and H4. The two motifs are separated by a flexible hinge region, while a short peptide extension appears at the C-terminal. Comparison of sequences indicates that the greatest homology is observed in the canonical EF-site, with the most variance observed in the hinge region and a C-terminal extension following the canonical EF-site.

The functional role of the pseudo EF-hand appears to be a more recent evolutionary feature producing lower affinity in the N-terminal domain and allowing significant Ca^{2+}-induced changes in the canonical EF-hand, which in turn expresses a hydrophobic cleft necessary for target recognition and peptide binding.

3.5 C2 domain

The C2 membrane-targeting domain is identified in cellular proteins that fulfill a role in signal transduction, including synaptotagmin I, phospholipase A and the β-isoform of protein kinase C (PKC) (PDB ID 1a25) [238]. C2 domains contain a core Ca^{2+}-binding region (CBR) where Ca^{2+}-binding, often accompanied with binding of additional cofactors as observed with certain isoforms of PKC, initiates conformational changes that allow the domain to identify membrane-attached targets, such as anionic phospholipids. C2 domain motifs diverge from the canonical EF-hand in several important ways. First, proteins with C2 domains exhibit β-sandwich architecture, compared to the predominantly α-helical nature of proteins with canonical EF-hands. Because of this architecture, a series of interstrand loops cluster at the end of the β-sandwich. In the C2 domain, a cleft is formed by these loops which are densely packed with aspartic acid residues.

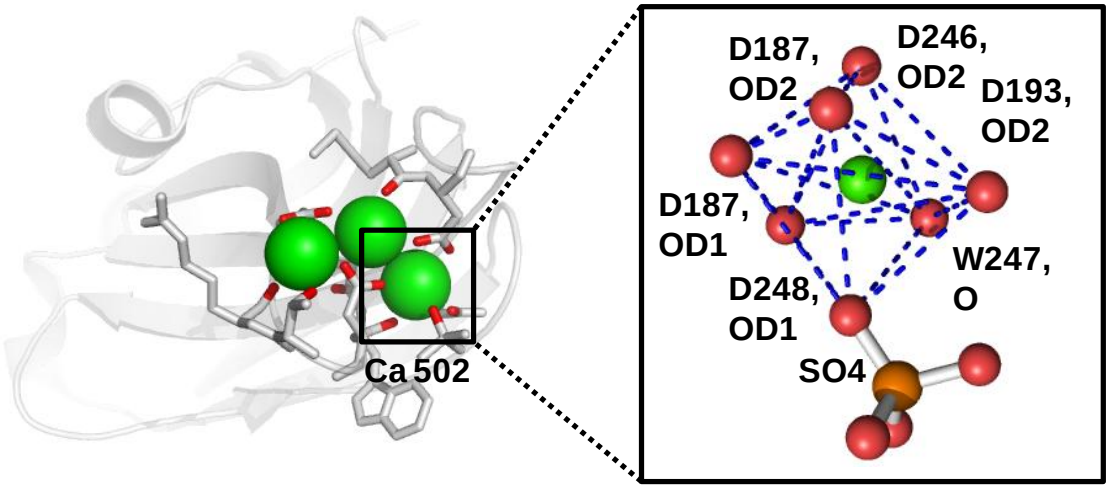

Figure 3.4 C2 domain from PKC
The coordination for the pentagonal-bipyramidal geometry for Ca-502 is completed with a sulfate ion.

This cleft accommodates binding of multiple Ca^{2+} ions as seen with PKC (Figure 3.4), which is presumed to be cooperative and necessary for stabilizing the structure in

order for the domain to recognize its molecular target [238]. Second, the binding ligands can originate from sequentially distant regions of the protein, as seen with Ca-502 in PKCα (PDB ID 3gpe) where the binding site is formed by ligands D187 (bidentate), D193, D246, W247 (carbonyl), D248, and SO_4. The overall geometry is holospheric (Figure 3.1c), conforming to a pentagonal bipyramidal geometry with oxygen from sulfate replacing the water molecule at the (-X) position. The crystal structure of PKCα shows binding of two additional Ca^{2+} ions. One of these is coordinated in a pentagonal-bipyramidal geometry, while the other occupies a hemispheric bowl geometry (Figure 3.1d). Unusually, several ligands appear to be shared between Ca^{2+} ions in the structure (Figure 3.2). Similar binding models in C2 domains are observed with: PKCβ (1a25.pdb); α-toxin, a phospholipase C enzyme from *Clostridium perfringens* (1qmd.pdb), and; cytosolic phospholipase A2 (cPLA2, PDB ID irlw).

3.6 Ca^{2+} and enzymes

The relationship between Ca^{2+} and the generation of trypsin from trypsinogen was being investigated as early as 1913 [239]. Today, we know that Ca^{2+} can stabilize the structures of different enzymes, including thermolysin [240], trypsin and proteinase K, which enables them to perform their catalytic activities. Many of these enzyme binding sites exhibit pentagonal-bipyramidal geometries, similar to canonical EF-hand sites but utilizing residues separated in the sequence, or octahedral geometries.

Trypsin contains a single high-affinity Ca^{2+}-binding site with an octahedral binding geometry where the superior and inferior apices are both water molecules. Binding of Ca^{2+} prevents autodegradation and is necessary for the structural integrity of the active enzyme. Proteinase K has two Ca^{2+}-binding sites: a higher affinity site exhibiting pentagonal-bipyramidal geometry comprised of four ligand atoms from amino acid residues (two in close sequential proximity with a bidentate ligand more distant in the

sequence) and four water molecules, and a second Ca^{2+}-binding site linked between residues in distant parts of the sequence (T16-O and bidentate D260) and bound with three water molecules [241]. As with trypsin, binding of Ca^{2+} in proteinase K is reported to stabilize the enzyme structure and facilitate structural changes necessary for catalytic activity.

Calcium-dependent Phospholipase A2 (PLA2) enzymes include cytosolic and extracellular isoforms. Cytosolic PLA2 (cPLA2), which plays a role in production of lipid mediators of inflammation, contains a C2 domain with two Ca^{2+}-binding sites. Both sites exhibit pentagonal bipyramidal geometry despite sequential separation of binding ligand residues. The roles of extracellular phospholipase A2 enzymes differ significantly from PLA2 in the cytosol. Extracellular PLA2 in venom help to immobilize prey, while pancreatic PLA2 plays an important role in the breakdown of phospholipids in dietary fat. Significant structural differences are also observed with extracellular PLA2 (PDB ID 3q4y), which incorporates a hemispheric Ca^{2+}-binding site. Residues comprising the site are summarized in Figure 3.2. This site includes a bidentate ligand D49 originating in an α-helix, similar to the bidentate anchoring ligand in the exiting helix of the canonical EF-loop. However, this ligand is sequentially distant from the other binding ligands. Additionally, binding ligands are not observed in either the region in the pentagonal plane corresponding to the –Y axis (EF-loop position 7), which is normally occupied by carbonyl oxygen in the canonical EF-hand, or in the -X axis space normally occupied by a water molecule. The resulting binding geometry in the crystal structure of phospholipase A2 therefore suggests an incomplete pentagonal-bipyramidal geometry.

Another example of pentagonal-bipyramidal geometry can be seen in MauG (PDB ID 3l4m). The Ca^{2+}-binding site in MauG includes a single-charged anionic ligand atom (N66-OD1), two carbonyl oxygen atoms (T275 and P277) and four water molecules. Despite the limited charge in the site, which differs significantly from

observations of canonical EF-hand sites, MauG apparently binds Ca^{2+} with relatively high affinity (K_d 5.3 μM) [242].

Table 3.1 Select CaBP's and characteristics of their binding sites

PDB ID	Protein/Enzyme/Assembly	Binding Site Ligands	Seq Class	Struct Class	Geometry
3gpe	PKC (Ca 501)	M186-O, D187-OD1, D246-OD2, D248-OD1, D248-OD2, D254-OD2, 1 H2O	III	holospheric	Pentagonal-Bipyramidal
3gpe	PKC (Ca 502)	D187-OD1, D187-OD2, D193-OD2, D246-OD1, W247-O, D248-OD1, PO_4	III	holospheric	Pentagonal-Bipyramidal
3gpe	PKC (Ca 503)	D248-OD2, D254-OD2, D254-OD2, R252-O, T251-OG1	I	hemispheric	Bowl
1hml	α-lactalbumin	K79-O, D82-OD1, D84-O, D87-OD1, D88-OD1, 2 H2O	I	holospheric	Pentagonal-Bipyramidal
1aui	calcineurin (Ca-500)	D32-OD1, E41-OE2, D30-OD1, E41-OE2, S36-O, S34-OG	I	holospheric	Pentagonal-Bipyramidal
1aui	calcineurin (Ca-501)	E68-O, N66-OD1, D64-OD1, E73-OE1, E73-OE2, D62-OD1	I	holospheric	Pentagonal-Bipyramidal
1alv	calpain (Ca 4)	D135-OD1, N226-OD1, D225-OD2, D225-OD1, D223-OD1, D223-OD2, 2 H2O	III	holospheric	--
1alv	calpain (Ca 1)	D110-OD1, E112-O, A107-O, E117-OE1, E117-OE2	I	holospheric	Pentagonal-Bipyramidal
1hqv	ALG-2 (apoptosis-linked gene-2, Ca-996)	N106-OD1, 3 H2O	--	Planar	--
1hqv	ALG-2 (apoptosis-linked gene-2, Ca-997)	D38-OD2, D36-OD1, V42-O, E47-OE2, S40-OG, E47-OE1, D38-OD1 1 H2O	I	holospheric	Pentagonal-Bipyramidal
1hqv	ALG-2 (apoptosis-linked gene-2, Ca-999)	D171-OD1, D173-OD1, D169-OD1, W175-O, 2H2O	I	holospheric	Pentagonal-Bipyramidal (incomplete)
1hz8	EGF (Ca-83)	E4-OE2, D18-OD1, E4-OE1, T2-O	II	?	?
1hz8	EGF (Ca-84)	N57-OD1, I42-O, E44-OE1, L58-O, D41-OD2, E44-OE2	III	holospheric	Pentagonal-Bipyramidal (incomplete)
3mi4	Trypsin	E70-OE1, N72-O, V75-O, E80-OE2, 2 H2O	II	holospheric	Octahedral
2prk	Proteinase K (Ca 280A)	P175-O, V177-O, D200-OD1, D200-OD2, 4 H2O	II	holospheric	Pentagonal-Bipyramidal
2prk	Proteinase K (Ca 281A)	T16-O, D260-OD1, D260-OD2, 3 H2O	--	hemispheric	--
1bci	Phospholipase A2 (cytosolic, C2 Domain, Ca 1950A)	T1041-O, N1065-OD1, D1043-OD1, D1043-OD2, D1040-OD1, MES 4000-O3S, 1 H2O	III	holospheric	Pentagonal-Bipyramidal
1bci	Phospholipase A2 (cytosolic, C2 Domain, Ca 1951A)	D1093-OD1, D1093-OD2, D1040-OD1, D1040-OD2, D1043-OD2, A1094-O, N1095-OD1, 1 H2O	III	holospheric	Pentagonal-Bipyramidal
3qfy	Phospholipase A2 (extracellular)	Y28-O, G32-O, G30-O, D49-OD1, D49-OD2	II	hemispheric	Pentagonal-Bipyramidal (incomplete)
3l4m	MauG (Ca 400 Chain A)	N66-OD1, T275-O, P277-O, 4 H2O	--	holospheric	Pentagonal-Bipyramidal
1qmd	alpha-toxin (phospholipase C, Ca 403)	A337-O, D269-O, D336-OD1, G271-O	--	hemispheric	Bowl
3mt5	Human BK K+ channel	D892-O, Q889-O, D897-OD2, D895-OD1	I	hemispheric	Bowl
2aef	Ca2+-gated K+ channel in Methanobacterium autotrophicum (Ca 602)	D184-OD1, D184-OD2, E210-OE2, E212-OE2, 3 H2O	II	holospheric	Pentagonal-Bipyramidal

The reason for this higher affinity is not clear, but this example suggests that charge is not the sole factor influencing binding affinity. Moreover, the structural similarity of these Ca^{2+}-binding sites in enzymes indicates Ca^{2+} can be coordinated with much greater flexibility than what is suggested by the highly-conserved, and more densely-charged canonical EF-hand loops.

3.7 Non-EF-hand binding sites

A significant proportion of Ca^{2+}-binding structures currently in the PDB are not sequentially or structurally identifiable as canonical EF-hand motifs, and may represent structural classes yet to be categorized. This group includes an increasing number of Ca^{2+}-binding sites structurally similar to EF-hands but with increasing variability in the loop or helices. The structural basis for the observed diversity in EF-hand CaBPs was recently reviewed by Grabarek who indicated that most changes in the loop occur in the N-terminal part, while the C-terminal part is more conserved [232]. Figure 3.1 summarizes many of the binding site examples discussed in this section.

Calpain, grancalcin and ALG-2 are classified in the Penta-EF-hand protein family. Penta-EF-hands have five binding sites. Not all sites are necessarily active, and may be characterized as either EF-hand sites or incomplete EF-hands. The incomplete EF-hands typically exhibit the helix-loop-helix structure of canonical EF-hand, but a reduction in the number of residues in the loop sequence result in incomplete pentagonal-bipyramidal geometry. ALG-2 (apoptosis-linked gene 2, PDB ID 1hqv) includes four Ca^{2+}-binding sites. The sites surrounding Ca-997 and Ca-998 are canonical EF-hand motifs, while the binding site chelating Ca-999 represents an incomplete pentagonal-bipyramidal geometry, comprising a short stretch of seven residues and water (Table I). The final binding site for Ca-996 includes a single sidechain ligand atom and water molecules, resulting in a planar binding structure.

Human low-density lipoprotein receptor contains two atypical Ca^{2+}-binding sites found in extended loop regions. The NMR structure of this protein (PDB ID 1hz8) does not include water molecules, so the structures appear incomplete. This is apparent in the binding site surrounding Ca-84 which exhibits a distorted, incomplete pentagonal bipyramidal geometry comprising six binding ligand atoms. However, these ligands span an unusually long region of the loop (17 residues), and the loop itself is partially restricted by the formation of a disulfide bond. The second binding site coordinating Ca-83 is comprised of only four ligand atoms which fail to surround the ion, although this may be due to the absence of water molecules in the PDB file.

Another example is α-lactalbumin, an extracellular protein from the C-type lysozyme family that participates in the formation of lactose synthetase, a precursor enzyme involved in lactose synthesis. The Ca^{2+}-binding site in α-lactalbumin consists of a short 4-residue N-terminal side helix, a 4-residue loop, and a longer (at least 12-residue) C-terminal side helix (PDB ID 1hml). Despite this significant variance from the canonical EF-hand loop, this site retains a pentagonal-bipyramidal binding geometry comprised of 5 protein ligand atoms and two water molecules. This site is also interesting because, with the exception of oxygen from the two water molecules and a single sidechain carboxyl oxygen from D82 in the loop region, the remaining binding ligand atoms are contributed by residues in α–helices.

3.8 Calcium in ion channels

Ion channels describe trans-membrane protein assemblies that allow the regulated movement of ions (Na^+, K^+, Ca^{2+}) across cellular compartments. Calcium channels, which facilitate the transfer of Ca^{2+} across membranes, may be either ligand-gated or voltage-gated. Examples of ligand-gated Ca^{2+} channels include IP_3 and ryanodine receptors. Voltage-gated calcium channels (VGCC) regulate the entry of Ca^{2+} into the cell following changes in the membrane potential. This Ca^{2+} influx in turn drives

diverse cellular functions including cardiac muscle contraction and neurotransmitter release. Voltage-gated calcium channels, through their Ca_v protein subunits, may be regulated through an indirect calcium feedback mechanism mediated by binding of Ca^{2+} to CaM which can interact with an isoleucine-glutamine (IQ) motif located in the N-terminal region of Ca_v.

Conversely, voltage-activated K^+ channels (e.g., BK or Slo1 channels) can be directly activated by increases in intracellular Ca^{2+} which provides a feedback mechanism where opening of these channels hyperpolarizes the membrane and initiates closing of Ca^{2+} channels, thereby reducing Ca^{2+} influx. A Ca^{2+} binding site identified in BK K^+ channel is believed to contribute to this Ca^{2+} regulatory mechanism. This binding site, identified as a 'calcium bowl' [243], is hemispheric, comprised of four binding residues (D892-O, Q889-O, D897-OD2, D895-OD1) originating in an Asp-rich sequence DQDDDDDPD, as seen in the PDB crystal structure for human BK (3mt5). Mutations or deletions of residues in this sequence have been shown to desensitize channel activity, however, further evidence suggests the existence of second Ca^{2+}-binding site that remains to be identified [243]. Similarly, the dimeric crystal structure of MthK Ca^{2+}-gated K^+ channel in Methanobacterium autotrophicum (PDB ID 2aef) reveals two symmetrical Ca^{2+}-binding sites believed to stabilize the RCK (regulate the conductance of K^+) domains. Unlike human BK, however, these binding sites conform to pentagonal-bipyramidal geometry with the addition of water molecules (Table I), and the residues comprising the binding sites span a longer region of the sequence than the BK K^+ channel binding site.

3.9 Statistical analysis of Ca^{2+}-binding sites

Coordination number and geometric configuration

Figure 3.5a summarizes mean coordination number (CN) values reported both with (PLW) and without (PL) contribution from water (HOH) oxygen ligands, where protein ligands may be oxygen or nitrogen. In all, 9507 ligands were identified, and of these, 2915 were water oxygen ligands. Interspersed within this group of identified ligands were 137 nitrogen atoms; approximately 42% of which fell within 2.9 Å of the Ca^{2+} ion.

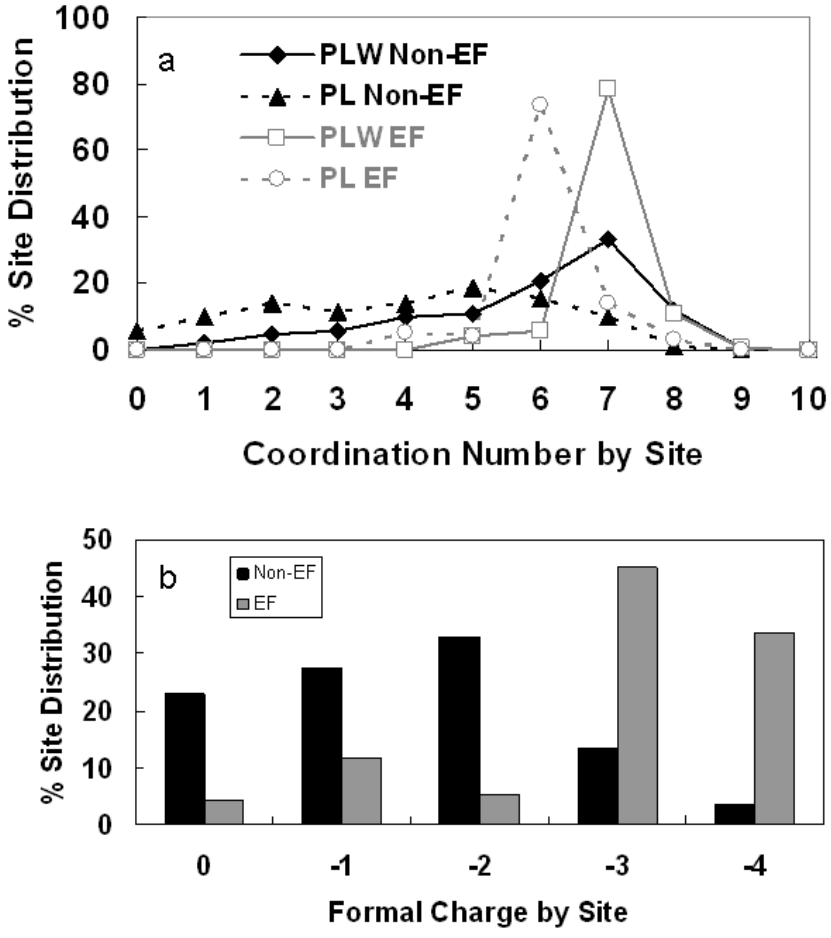

Figure 3.5 (a) Coordination number (CN) and (b) distribution of formal charge (FC) by site for Non-EF-Hand and EF-Hand protein classes

As seen in Table 2.1, the mean CN for EF-Hand sites, including water, was 7 ± 1, compared to 6 ± 2 for non-EF-Hand sites. All CN values were reported as whole integers only. When water was excluded, CN values for EF and non-EF sites were reduced to 6 ± 1 and 4 ± 2, respectively.

Figure 3.5a summarizes the % Site Distribution of CN values for EF and non-EF sites, both with and without water. It is evident that fewer protein ligands are involved in the coordination of the non-EF-Hand binding sites, which also coordinate with more water ligands. The significant impact of the water molecules in the non-EF-Hand proteins is clearly evident in Figure 3.5a, where the distribution of ligands reaches a maxima at CN=7 only with the inclusion of water.

On the other hand, the mean CN values reported in this study for EF-Hand proteins were consistent with previously published results indicating a CN of 6 to 8 ligands for Ca^{2+}-binding, with a mean of 7.3, or between 6-7 [5, 217]. Additionally, we identified 13 EF-Hand sites having fewer than 6 protein ligands (Figure 3.5a). Closer inspection of the PDB structures associated with these sites revealed that they are either S100 type sites classified as EF-Hands, or included an additional HOH oxygen ligand, although the binding sites were still located within a flexible loop region flanked by two helices.

The space defined by edges connecting the ligand vertices of each binding site, termed Hull, was examined to determine the relative position of the Ca^{2+} ion to the binding site center of volume. EF-Hand proteins tend to have well-defined pentagonal-bipyramid geometric structure, as seen in Figure 3.1a. However, the results of this analysis indicated a wider variety of low coordination structures associated with Ca^{2+}-binding in non-EF-Hand proteins. In Figures 3.1c-3.1e, three generalized structures of Ca^{2+}-binding sites are described. Figure 3.1c shows a holospheric site, with the ion enclosed in the Hull volume, and closer ligands interactions between the ion and the first

shell. Figure 3.1d describes a hemispheric site, with the Ca^{2+} ion partially- or full-removed from the defined volume, whereas Figure 3.1e describes a roughly planar binding site. The results of the statistical analysis (Table 2.1) indicated that 72% and 100% of evaluated ions were positioned within the Hull, for non-EF-Hand and EF-Hand, respectively. These results suggest that most Ca^{2+}-binding involves a holospheric coordination geometry, which corresponds to an increasing CN value. This geometric configuration may contribute to strong metal selectivity for calcium over other metal ions.

Ligand type

Ligand distribution is summarized in Figure 3.6. Figure 3.6a and Figure 3.6b illustrate major differences in ligand type between EF-Hand sites and non-EF-Hand sites. Sidechain groups account for the highest proportion of ligands in both classes, but represent a much higher percentage for EF-Hand (65.3%) than for non-EF-Hand (42.9%). For EF-Hand, the ligand distribution follows the order *sidechain Asp* > *sidechain Glu* > *mainchain Carbonyl*, with the percentage of Asp and Glu nearly equivalent (29.7% and 26.6%, Figure 3.6a). For non-EF-Hand, HOH is the dominant ligand comprising 33.1%, followed by sidechain Asp (24.5%), mainchain carbonyl (23.9%) and sidechain Glu (10.4%). It can be seen that the ratio of Asp:Glu for non-EF-Hand (23.9:10.4) is nearly identical to that reported by Pidcock (2.4:1) but not so for EF-Hand (29.7:26.6). Moreover, as seen in Figure 3.6a and Figure 3.6b, the presence of sidechain hydroxyl and amide groups (Asn, Gln, Ser, Thr, Tyr) is minimal in both classes.

Consistent with previous analyses on the canonical EF-hand motifs based on either sequence or structure [61, 218], Glu is much more common to EF-Hand binding sites than the non-EF-Hand sites, but differs significantly from Falke's reported ligand preferences of 65% and 21% for Asp and Glu, respectively, based on 567 canonical EF-Hand sequences analyzed [244]. This common presence of Glu within EF-Hand sites is

likely due to its strategic importance as a bidentate, anchoring ligand for Ca^{2+} [245], and it's strong propensity towards helical formation.

In our analysis, we have shown that EF-Hand proteins, including both canonical and pseudo EF-hand motifs, have similar distributions of Asp and Glu sidechains. The presence of carbonyl oxygen ligands is similar for EF-Hand (21.4%) and non-EF-Hand (23.9%), so the major contributor in non-EF-Hand to replace the missing carboxyl ligands comes from the increasing presence of available water oxygen atoms, as previously noted.

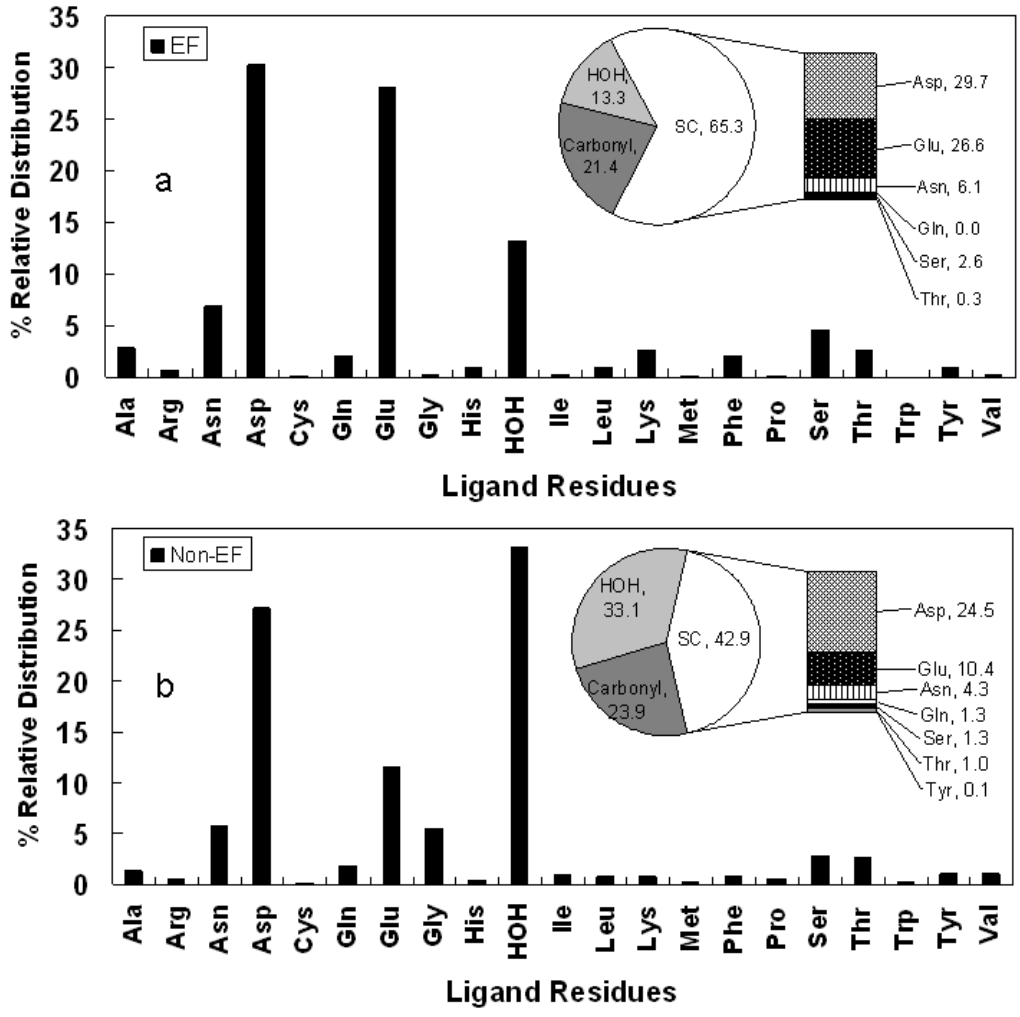

Figure 3.6 Frequency distribution of ligand residues
Distribution for (**a**) EF-Hand and (**b**) Non-EF-Hand proteins. The pie graphs (*inset*) show the distribution between water, carbonyl and sidechain residue oxygen ligands.

The data for EF-Hand sites follow the trends reported by Dudev and Lim, (*carboxylates* > *carbonyls* > *water* >> *hydroxyl* atoms) [219], but vary for the non-EF-Hand proteins, due to the increased presence of water. In fact, the 33.1% distribution of water oxygen ligands for non-EF-Hand sites is much higher than values reported by McPhalen (20%) [219], and Dudev (22.4%) [181]. In the case of Dudev, this difference may in part be attributed to the shorter distance cutoff constraint in their study (2.9 Å vs. 3.5 Å). When water oxygen ligands with Ca-O distances between the range 2.9 – 3.5 Å are eliminated from our statistics, the % distribution of water oxygen ligands drops to 25.0%, which is only a modest increase from the value reported by Dudev, but still significantly different than the 13.3% reported for EF-Hand sites (Figure 3.6a) which all fall within 2.9 Å.

Charge analysis by site

Formal Charge (FC) by site was simplified to account only for negatively-charged sidechain carboxyl groups (-1) from Glu and Asp [218]. Mean negative FC values of 1 ± 1 and 3 ± 1 were found for non-EF-Hand and EF-Hand sites, respectively. The difference in distribution between FC in non-EF-Hand and EF-Hand sites is shown in Figure 3.5b, with increased negative charge (3 to 4) more apparent in the case of EF-Hand sites. The charge data for EF-Hand sites are consistent with previous studies of Ca^{2+} indicating that a microenvironment containing 3-4 negative charges likely represents an optimal charge configuration [129, 218], however, it is surprising that only a small percentage of non-EF-Hand sites exhibit negative charge greater than 2 (Figure 3.5b).

Calcium binding sites with high negative formal charges are likely located in flexible loop regions of the protein. Figure 3.7 shows examples of canonical EF-hand proteins and non-EF-hand proteins with -4 formal charge values. Figure 3.7a shows the

EF-Hand binding site with a helix-loop-helix from the crystal structure of coelenterazine-binding protein from *Renilla muelleri* (2hq8.pdb) formed by the sidechains of D112, D114, D116 and E123 and mainchain of Y118. Figure 3.7b shows Ca^{2+}-binding in a flexible loop region between two β–strands from family 9 carbohydrate-binding module of *Thermotoga maritime xylanase* 10A (1i8a.pdb). Figure 3.7c shows Ca^{2+}-binding between two loop regions discontinuous in the primary sequence from calcium-binding domain 2B (1uow.pdb) [246].

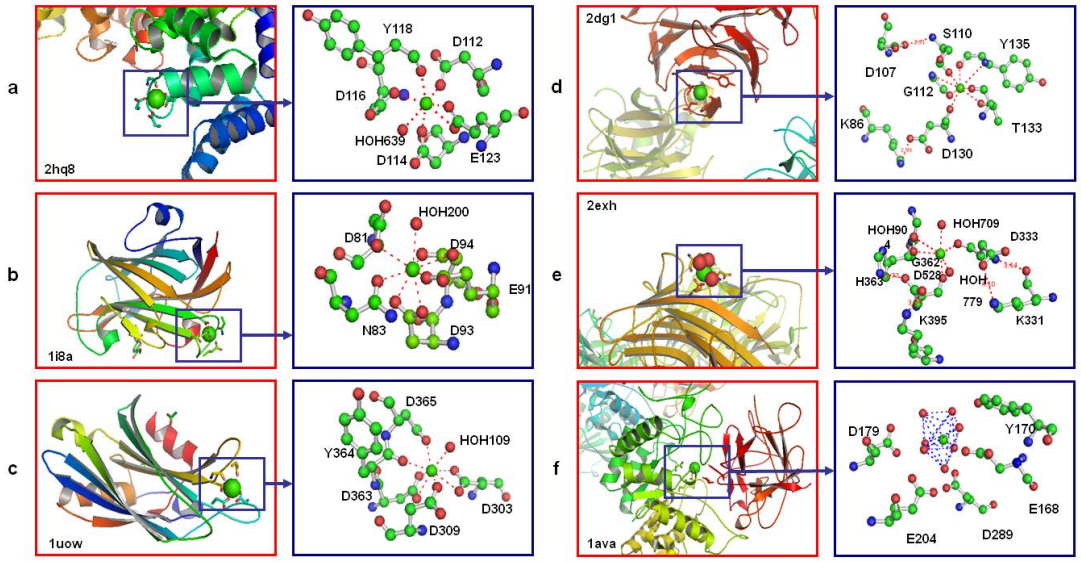

Figure 3.7 Comparison of EF-Hand Ca^{2+}-binding sites
(**a**) Canonical EF-Hand binding site from coelenterazine-binding protein from *Renilla muelleri*. (**b**) C-terminal module of the thermostable *Thermotoga maritima xylanase* 10A (1i8a.pdb). Four negative charges are found in the site. (**c**) Synaptotagmin I C2B domain (1uow.pdb). Four negative charges are found in the site. (**d**) Binding site (PDB Sequence ID 3012) of Drp35 (2dg1.pdb). Ca^{2+} is bound with 5 mainchain and 1 hydroxyl oxygen atom, and 2 nitrogen atoms from loop region of chain F. FC in site is zero. (**e**) Binding Site (PDB Sequence ID 2003) from beta-Xylosidase (2exh.pdb). Ca^{2+} is coordinated by 3 protein ligands and 3 water oxygen ligands. FC in site is zero. (**f**) Binding site (PDB Sequence ID 503) from 1ava.pdb. The hydrated Ca^{2+} is bound between Barley alpha-amylase and its endogenous protein inhibitor BASI. Formal charge is zero.

Binding sites without formal charge were identified within both classes. For the EF-Hand proteins, 6 binding sites were identified which had zero FC in the binding site, all from the protein calprotectin (1xk4.pdb) [237]. These are S100/pseudo EF-Hand sites

predominantly binding with mainchain carbonyl oxygen atoms. Surprisingly, over 20% of the non-EF-Hand binding sites (338 sites from 153 proteins) had reported FC values of zero.

Detailed structural analyses of the protein environments of these charge-deficient sites reveals that charge-charge stabilization beyond the chelated metal ion leads to the exclusion of available negatively-charged sidechain residues and facilitates the binding of Ca^{2+} with carbonyl oxygen atoms. Figure 3.7d shows the Ca^{2+}-binding site (Ca^{2+} sequence ID 3012) of Drp35 (2dg1.pdb), a protein induced by cell wall-affecting antibiotics or detergents, which possesses calcium-dependent lactonase activity [247]. Ca^{2+} is bound with 6 oxygen and 2 nitrogen ligands from a loop region in chain F. Binding ligands for this site are summarized in Appendix Table A.4. It is interesting to note that, except for OG1 of THR133, all other protein oxygen ligands are from the mainchain, despite the apparent availability of sidechain oxygen atoms from TYR135, ASP130 and SER110. A closer examination (Figure 3.7d) of the structure reveals several probable charge interactions (Appendix, Table A.5) between ASP130 OD2 and LYS86 NZ; SER110 N and ASP107 OD2. These interactions with ligands beyond the second shell likely stabilize the holo-protein and account for the use of mainchain carbonyl oxygen ligands in the binding site. These types of interactions are even more apparent with the structure from 2exh.pdb, a family43 beta-Xylosidase from *Geobacillus stearothermophilus* [248]. Ca^{2+} site 2003 from 2exh is coordinated by 3 mainchain oxygen ligands, 2 from Asp residues 333 and 528, where 528 originates in a β-strand, and 3 water oxygen ligands (Figure 3.7e). As was observed with 2dg1 of Drp35, charge interactions are apparent between ASP333 N and LYS331 O, ASP333 OD2 and LYS331 NZ, ASP528 OD2 and LYS395 NZ, and ASP528 OD1 and HIS363 NE2 (Appendix, Table A.4). For these residues, both sidechain and mainchain charge interactions with

ligands in the second shell would stabilize the structure, enabling the observed Ca^{2+} coordination by available mainchain oxygen atoms.

244 of these sites lacking charged ligand residues had fewer than 3 protein ligands. The absence of charge and low coordination number is unusual for Ca^{2+}-binding sites, and may represent incidental effects of crystallization, rather than naturally-occurring binding sites. As such, data collected from these sites, while still meaningful with respect to individual ligand interactions, are less desirable for characterization of the total binding site. An example of a very unusual site (Ca^{2+} 503 from 1ava.pdb) is shown in Figure 3.7f. This site shows a hydrated Ca^{2+} ion bound between Barley alpha-amylase and its endogenous protein inhibitor BASI [249]. As seen in Figure 3.7f, no protein ligands are associated with the Ca^{2+} ion, however, the hydrated ion is surrounded by a outer shell of protein ligand oxygen atoms orientated towards the hydrated ion: Probably as a result of hydrogen-bonding with the inner shell of water molecules.

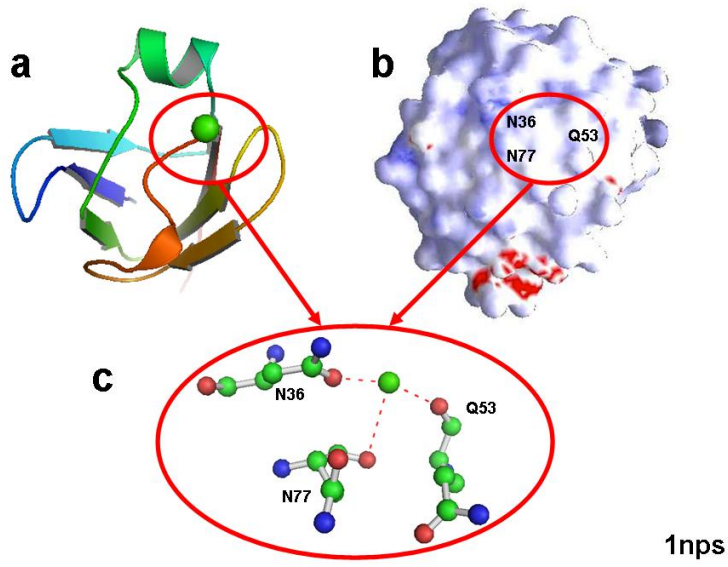

Figure 3.8 (a) Ca^{2+} binding site for protein S from Myxococcus xanthus (1nps.pdb)
The binding site around calcium 145 has zero assigned formal charge. (**b**) Electrostatic potential map for 1nps showing neutral charge (gray and white contours) in the site. (**c**) Expanded view of binding site protein ligands.

As shown in Figure 3.8a, the non-EF-Hand site (Site 145) from the isolated N-terminal domain of protein S from *Myxococcus xanthus* (PDB ID 1nps) is

coordinated by three protein ligands, ASN36, ASN77 and GLN53 (Figure 3.8c), with three additional water oxygen ligands. The absence of charge in this region is illustrated in the electrostatic potential map (Figure 3.8b) generated using DelPhi and GRASP [250-254], where the surface region corresponding to the binding site appears neutral (i.e. – surface area represented in gray and white contours, with no red contouring indicating the presence of negative charge). Ca^{2+}-binding was not shown to increase protein stability in the case of the isolated N-terminal domain of protein S, although the intact protein was reported by Wenk *et al*. to be very stable across a wide pH range (2 to 10), and resistant to both urea and thermal unfolding [255]. Wenk also reported an unfolding intermediate where the N-terminal domain remains folded during unfolding of the C-terminal domain. Cooperativity between these domains contributes to the overall stability, and it is evident from their study that the absence of charge in the binding site (site 145) has no apparent correlation with stability. Studies of Ca^{2+} have indicated higher binding affinities are observed in the presence of a net negative charge within 5-15 Å of the ion [256-257], However, the relationship between charge and thermal stability is less easily evaluated. Vogt *et al* [258] presented a summary of studies related to thermal stability where charge interaction and metal-binding were cited as factors contributing to increased stability. Recent work in our laboratory has suggested that increasing the number of localized charge residues in a relatively constrained calcium binding site, while increasing both metal binding affinity and stability of the calcium-loaded form, also leads to decreased stability of the apo-form [168, 177]. It is clear that such effects are context dependent; i.e. strongly depend on the protein environment. Consequently, no attempt was made to evaluate thermal stability with respect to charge availability based on the data presented in this study.

Nitrogen, which is associated with Ca^{2+}-binding in studies of small molecules, was not observed to any appreciable extent in the protein structures analyzed. Of the

137 nitrogen ligands identified in the study, only 2 were found within EF-Hand binding sites. Interestingly, 85 of the 135 nitrogen ligands identified in non-EF-Hand binding sites are reported in the zero-charge sites. This suggests that nitrogen may potentially play a secondary role in Ca^{2+} binding, and that this role may increase in the absence of negative charge, possibly due to a reduction in charge repulsion forces.

Distance parameters

Mean distance parameters are summarized in Table 2.1 and in Figure 3.9a-d. The ranges of reported Ca-O and Ca-C distances are also summarized in Table 2.1, based on a 0.1 Å interval bin.

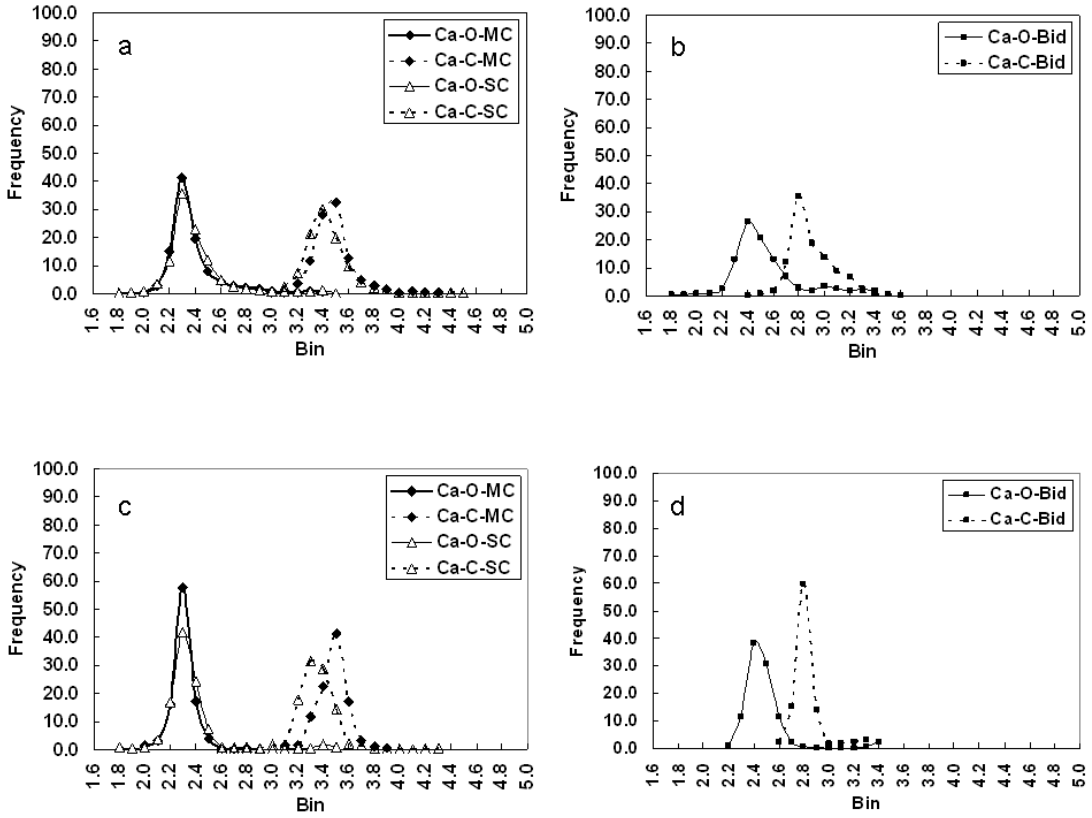

Figure 3.9 Ca-O distance comparisons
(a) Non-EF carbonyl and sidechain oxygen, **(b)** non-EF bidentate oxygen, **(c)** EF carbonyl and sidechain oxygen, and **(d)** EF bidentate oxygen.

A clear delineation between these distances is apparent for both carbonyl and sidechain ligands in the non-EF-Hand and EF-Hand datasets (Figure 3.9a and Figure 3.9c) at or near 3.0 Å.

The mean Ca-O distance values reported in this study for EF-Hand and non-EF-Hand indicate little difference between carbonyl and sidechain oxygens, and between the different classes (Table 2.1) for each ligand type. These results are identical to previously cited studies, however, our data separate bidentate ligand distances, which are slightly longer for both EF-Hand (2.5 ± 0.2 Å) and non-EF-Hand (2.6 ± 0.3 Å) than for the carbonyl and sidechain ligands, in their respective classes. Moreover, a more pronounced change was observed for the bidentate mean Ca-C distances, which were 0.5-0.6 Å shorter than the distances found for carbonyl and sidechain ligands oxygen atoms, resulting in overlap between the Ca-O and Ca-C shells (Figure 3.9b and Figure 3.9d). Also, the majority of reported Ca-O distance values for carbonyl and sidechain oxygen ligands, as seen in Figure 3.9a (non-EF-Hand) and Figure 3.9c (EF-Hand) indicate a narrower range of ligand distances (2.0-2.8 Å and 2.1-2.6 Å, respectively) than previously reported values approximately between 2.0 – 3.2 Å [219].

These effective binding ranges suggest that our cutoff of 3.5 Å may be arbitrarily long for structural parameterization, given the narrow distributions seen in Figure 3.9a-c. Additionally, nearly 60% of the identified nitrogen ligands fell within the range 2.9-3.5 Å, and because nitrogen is accepted as only a marginal binding ligand for Ca^{2+}, it is probable that some of these identified ligands do not interact with the Ca^{2+} ion. However, only 7% of the non-EF ligands, and 1% of the EF ligands, fell within the range 2.9-3.5 Å, and these data did not significantly alter the statistical results, except in the case of water molecules for non-EF-Hand proteins, where approximately 25% of the water oxygen ligands were identified in this range. It is likely that not all of these identified water oxygen atoms are ligands, however, it is clear from Figure 3.5a that binding in the

non-EF-Hand sites with 7±1 ligands is possible only with inclusion of the water molecules, including those greater than 2.9 Å from the Ca^{2+} ion. We conclude from this that the longer cutoff of 3.5 Å, while valid for this large statistical analysis, can likely be reduced to 2.9 Å for future studies without loss of relevant data, with a possible exception for the special case of water.

Analysis of bond angles

The mean Ca-O-C angles (Figure 2.1a) are summarized in Table 2.1, where differences are observed between carbonyl, sidechain, and bidentate oxygen ligands. The carbonyl Ca-O-C angles (°) were largest (151.5 ± 15.8 and 159.8 ± 12.5), followed by sidechain (140.4 ± 15.2 and 136.7 ± 16.0) and bidentate (93.6 ± 11.3 and 92.9 ± 6.8) for non-EF-Hand and EF-Hand, respectively.

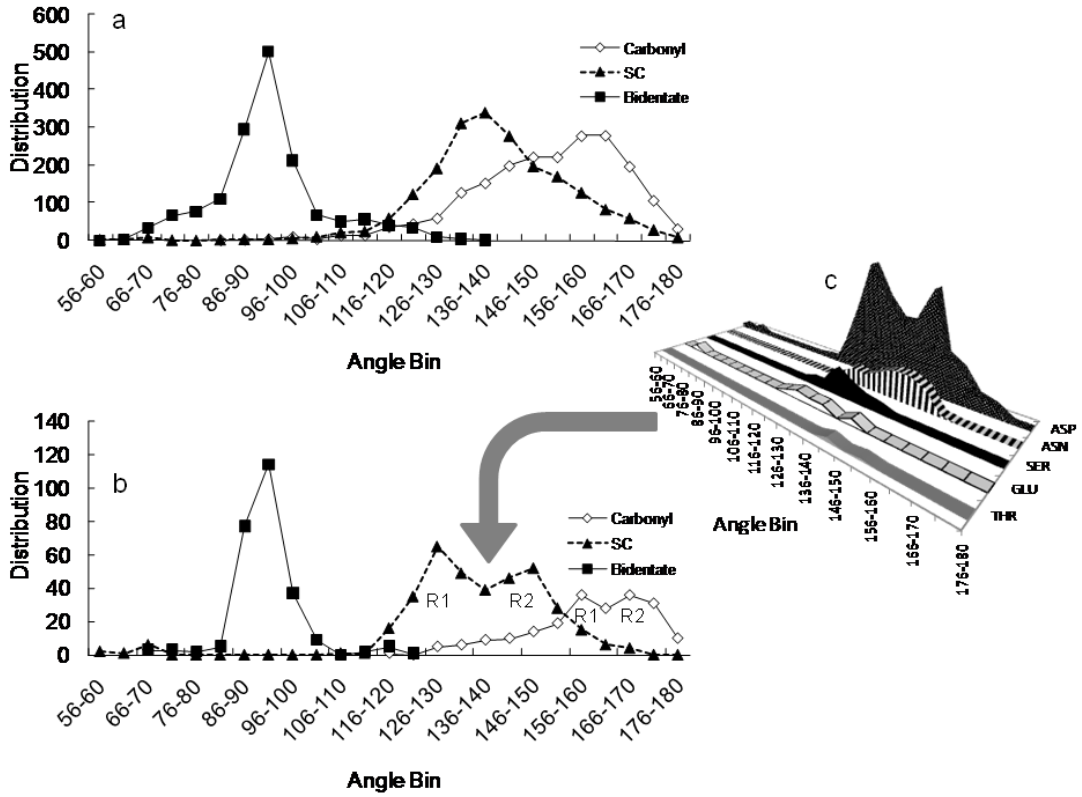

Figure 3.10 Ca-O-C angles
Distribution for (**a**) non-EF-Hand and (**b**) EF-Hand binding sites. (**c**) Ligands comprising bimodal sidechain distribution for EF-Hand.

Figure 3.10a and Figure 3.10b show the distribution of Ca-O-C angles for non-EF-Hand and EF-Hand Ca^{2+}-binding ligands, respectively. It can be seen that a Gaussian distribution of angle values is associated with non-EF-Hand ligands, and the range values for both classes are nearly identical for carbonyl, sidechain and bidentate (Table 2.1). For the bidentate ligands, the mean and standard deviation values for dihedral angles are also summarized in Table 2.1. For non-EF-Hand and EF-Hand these values were found to be 168.1 ± 9.7 and 170.6 ± 7.1, respectively.

To understand the observed bimodal distribution associated with Ca-O-C angles for sidechain, and to a lesser extent, mainchain EF-Hand ligands in Figure 3.10b, two additional analyses were performed. Results of these analyses are summarized in Figure 3.10c and Appendix Table A.5. In Figure 3.10c, the ligands represented by the angle data in Figure 3.10b were further divided by residue type. The majority of these ligands (262/366) originated from Asp, and it is clear that the bimodal distribution seen in Figure 3.10b mirrors the distribution of Asp in Figure 3.10c. A similar analysis (not shown) of the data for mainchain carbonyl residues associated with the Ca-O-C angles in Figure 3.10a did not reveal a residue-specific origin for the apparent bimodal mainchain distribution.

Table A.5 (Appendix) summarizes data for the EF-Hand ligands comprising the Ca-O-C angle distribution in Figure 3.10b, and the associated protein families. From the data presented in Table A.5, protein structures were identified where a majority of the ligands were contributed preferentially to one peak region or the other. These regions, mapped to the unrooted N-J phylogenic trees in Figure 3.11, indicated two major phylogenic branches where the peak region sidechain Ca-O-C angle distribution correlated with related protein families. In Figure 3.11a, peak region R1 angles corresponded with the highly-conserved Parvalbumin and Penta-EF SCOP families (shaded oval), while angles from peak region R2 corresponded with the S100 family of

proteins (shaded rectangle). However, no consistent trends were observed along the Calmodulin-like SCOP branches.

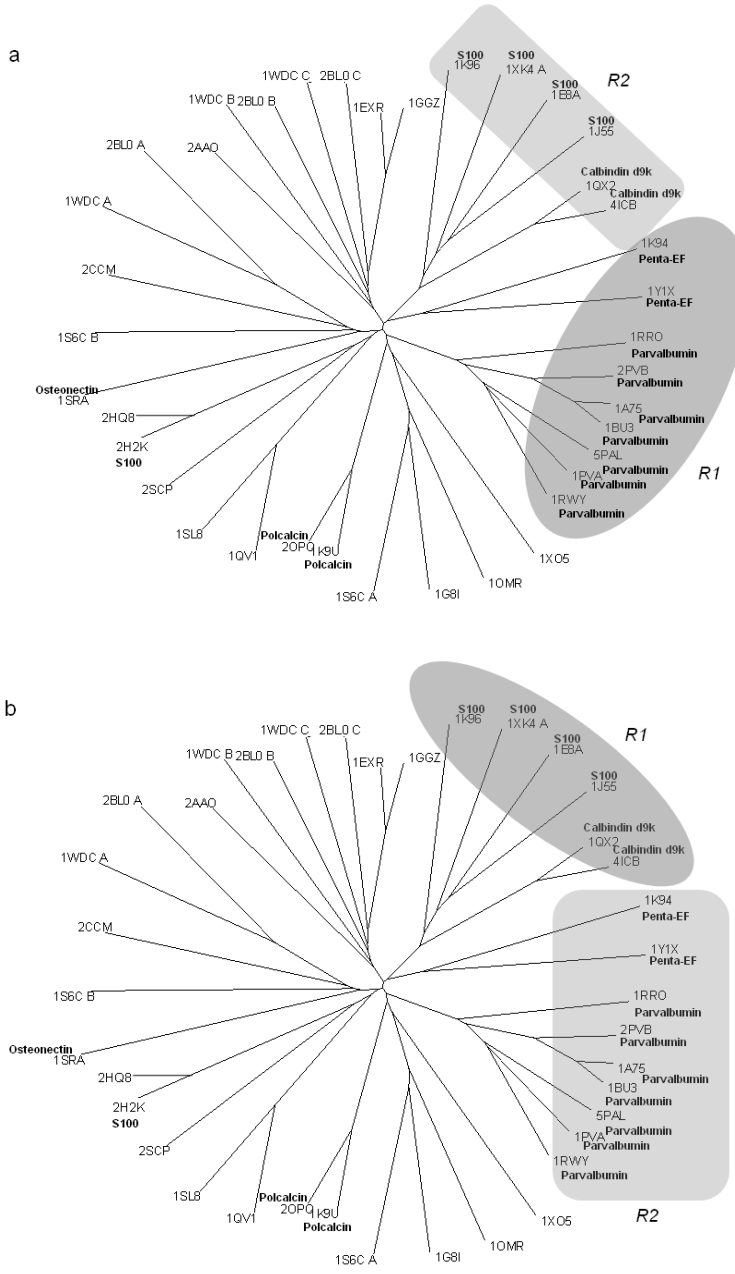

Figure 3.11 Unrooted N-J phylogenic tree for EF-Hand proteins
Unlabeled chains are all in the family of Calmodulin-like proteins. (a) For sidechain residues, the Parvalbumin and Penta-EF families contribute the majority of their ligands to the first observed peak (R1) in Figure 3.10b, whereas the S100 proteins contribute the majority of their ligands to peak 2 (R2). (b) This distribution appears reversed for the mainchain carbonyl Ca-O-C angles.

Interestingly, the data in Table A.5 suggests an inverse correlation between the sidechain and mainchain angles and the related protein families, where the shorter sidechain angles in peak region R1 (shaded oval in Figure 3.11a) are coupled, by protein chain, with longer mainchain angles in peak region R2 (shaded rectangle in Figure 3.11b) and vice-versa. However this reversal was not observed in all cases (Table A.5), so the correlation is considered weak.

These results suggest two possible explanations for the observed sidechain bimodal distribution in Figure 3.10b. First, the emergence of two quasi-discrete peaks for Asp may result from charge interactions between the Ca^{2+} ion and the non-ligand carboxyl oxygen from Asp, such that proximity of the second oxygen, while outside the ligand cutoff distance of 3.5 Å, is sufficient to effectively reduce the Ca-O-C angle of the primary oxygen ligand. Second, based on the data presented in Table A.5, it is possible that discrete angles are conserved along evolutionary lines. A third possibility is that the observed bimodal distribution relates to different secondary properties associated with the ligand residues, and further work is in currently in progress to evaluate this.

3.10 Conclusions

Data presented in this study are based on the most comprehensive statistical analysis of higher resolution Ca^{2+}-binding structures available to date. While certain data presented here with respect to EF-Hand proteins are generally consistent with previously reported studies, a clear distinction can be made between EF-Hand and non-EF-Hand proteins, based on the physical properties assessed. It is apparent from the data that non-EF-Hand CaBPs coordinate with fewer ligands, on average, than the EF-Hand proteins, and with a higher proportion of bound water molecules. Less formal charge is evident in the non-EF-Hand binding sites, which is expected given the lower proportion of charged sidechain ligands. It remains to be seen whether these properties can be

correlated with binding affinities. The EF-Hand sites additionally exhibit a bimodal distribution of sidechain Ca-O-C angles, which may be due to the abundant presence of Asp as a chelating ligand residue, which in turn may be conserved along evolutionary lines. In both classes, the majority of Ca^{2+} ions are surrounded by a holospheric binding geometry. In the case of EF-Hand proteins, this frequently involves a pentagonal-bipyramid geometry, whereas the non-EF-Hand binding sites exhibit less regular structure. The Ca-O Bond lengths for both classes were generally equivalent, but discrete differences were apparent in the bond angles, and in both cases the range of bond angles was narrower than previously assumed (Table 2.1). Additionally, the dihedral angles for non-EF-Hand and EF-Hand binding sites were generally equivalent, with low standard deviations, indicating that these values (168.1 ± 9.7 and 170.6 ± 7.1) may be utilized as input parameters for computational design.

The significant differences between ligand types (carbonyl, sidechain, bidentate), demonstrate the necessity of classifying these angles separately. Moreover, the small standard deviation in each case provides a narrower range of ideal angles for each ligand type, thus improving our input parameters used to design proteins with specific Ca^{2+}-binding characteristics.

The physical parameters and key characteristics associated with Ca^{2+}-binding in different classes of CaBPs identified from our analysis have two-fold significance. First, structural parameters derived from a more current, comprehensive data set provide a more accurate representation of Ca^{2+}-binding, particularly between different classes of CaBPs. Second, these data will provide input parameters to both improve the accuracy of prediction algorithms and facilitate the design of engineered CaBPs with high selectivity and affinity for Ca^{2+}. The data compiled in this analysis have been directly applied to define weighted coefficients used in a graph theory-based prediction algorithm developed in our laboratory which can predict Ca^{2+} binding sites, within 0.20 of the

documented site, with 94% sensitivity and 93% selectivity [222]. The algorithm also correctly identifies only those ligands comprising the binding site in 45 out of 48 test sites. These results are in part attributable to refinement of the algorithm based on the availability of more precise structural parameters obtained from the statistical analysis reported in this manuscript.

Due to the ubiquitous presence of CaBPs in biological processes, and the roles of Ca^{2+} imbalance in different diseases, the ability to predict and identify Ca^{2+}-binding sites using computational methods can accelerate our understanding of these processes and problems, and subsequently improve our ability to alter Ca^{2+}-dependent functions for therapeutic purposes, and design CaBPs with tailored functions for medical diagnostics.

4 Statistical analyses of Pb^{2+}-binding in proteins

4.1 Pb^{2+}-binding protein statistics

Table A.6 (Appendix) lists the binding sites retained for analysis, their PDB identifiers, and resolution of the crystal structure. Table A.1 (Appendix) summarizes the PDB data by binding site for retained sites, including coordination number (CN) values both with (PLW) and without (PL) water molecules, formal charge (FC), and binding mode (D – displacement, O – opportunistic, or U - unknown) by site. As seen in Table S6, approximately 1/3 of the Pb^{2+}-binding sites were identified as sites of ionic displacement, indicating that these sites are also known to bind physiologically-relevant ions, as listed in the Binding column. Statistical analysis of these two separate binding modes was not performed in this study due to limited data for each of the different metals listed.

Binding sites from the high-resolution dataset (DS HR) are identified by an asterisk preceding the PDB_ID. A charge of (-1) was assigned to acidic side-chain ligands Glu and Asp, and the Cys thiol [218]. Table 4.1 presents a summary of all statistical data from the analysis. A comparison of the values reported for DS HR and DS Final show little difference in ligand distance values, coordination number, and charge, indicating that resolution did not significantly alter the results. Consequently, unless otherwise specified, results from only the DS Final dataset are discussed from the analysis. These statistical results for Pb^{2+} are then compared with data recently compiled for Ca^{2+} to emphasize differences in binding characteristics exhibited by the two metals.

Table 4.1 Pb^{2+}-binding statistics

	DS HR	DS Final
Total PDB proteins in study	7	21
Total Pb binding sites evaluated	27	48
Total target ligand atoms	105	177
Total O_{aa} ligands	86	118
Total O_{HOH} ligands	16	36
Total N ligands	3	10
Total S ligands	0	13
Total sites with N ligands	3	9
Mean CN, PLW	3.9 ± 2.3	3.7 ± 2.0
% CN 2-5	77.8	77.1
% CN 6-9	22.2	16.7
Mean CN, PL	3.3 ± 2.0	2.9 ± 1.7
% CN 2-5	70.4	72.9
% CN 6-9	14.8	8.3
Mean charge by site	-1.8	-1.7
Total identified bidentate pairs	24	36
Total sites with bidentate ligands	21	30
% Sites with bidentate ligands	77.8	62.5
Mean distance, Pb-O_{aa}, (Å)	2.7 ± 0.4	2.7 ± 0.4
Mean distance, Pb-O_{HOH}, (Å)	2.8 ± 0.3	2.8 ± 0.4
Mean distance, Pb-N (Å)	2.7 ± 0.3	2.6 ± 0.4
Mean distance, Pb-S (Å)	---	3.2 ± 0.3

DS HR: High resolution dataset (R ≤ 1.76 Å), 3.5 Å ligand-atom distance cut off. **DS Final:** Summary dataset, no restriction on resolution, 3.5 Å ligand-atom distance cut off, refined for bidentate ligands. **CN:** Coordination Number. **PLW:** Ligands from protein and water. **PL:** Ligands from protein only. **O_{aa}**: Amino acid oxygen ligand. **O_{HOH}**: Water oxygen ligand.

4.2 Ligand coordination by binding site

The coordination numbers presented in Table 4.1 are differentiated based on the inclusion or exclusion of water oxygen ligands. For the DS Final dataset, mean CN values were reported as 2.9 ± 1.7 and 3.7 ± 2.0 for the exclusion (PL) and inclusion (PLW) of water ligands, respectively. As reported in this study, ligands (e.g. – carboxyl

groups) are monodentate unless specifically identified as bidentate; i.e. comprising two ligand atoms. Water occupancies in the crystalline structures are considered approximations. The distribution of CN by site (Figure 4.1a) indicates that binding was most commonly observed with two, or to a lesser extent, four ligands. Interestingly, nine sites were reported with only a single amino acid ligand atom for coordination when water was excluded, and three of these were unchanged even with the inclusion of oxygen ligands from water.

The distribution of CN values in Table 4.1 is further divided into percentages falling between the ranges of 2 to 5 ligands (77.1%) and 6 to 9 ligands (16.7%). The CN range of 2 to 5 was selected for two reasons. First, previous studies have indicated that Pb^{2+} may adopt a binding structure similar to Zn^{2+} , using 4 to 6 binding ligands, as a result of ionic displacement [50-51]. Second, a study of crystalline structure data in the Cambridge Structural Database by Shimoni-Livny *et al.* [221] observed two general geometries for Pb^{2+}-binding: a holodirected, spherical geometry comprised of 9 to 10 ligands (Figure 3.1c); and a hemidirected geometry where 2 to 5 coordination ligands occupy only half of a sphere (Figure 3.1d). It is notable that a hemidirected or planar geometry was also observed in nearly 28% of the Non-EF-Hand Ca^{2+} binding sites surveyed in our recent statistical analysis [229], indicating that this geometry is not confined to Pb^{2+}-binding.

Alternatively, the CN range of 6 to 9 was selected for comparison with Ca^{2+}-binding (6 to 8 ligands) [245] and because previous studies with small molecules suggested a coordination number of 6.9 for Pb^{2+} [5]. The results of this analysis indicate that binding coordination of Pb^{2+}, based on number of ligands, is more closely-related to that of Zn^{2+} than Ca^{2+}. This is particularly apparent with respect to the EF-Hand Ca^{2+}-binding sites which average 6 to 8 ligands in well-ordered structures. These results, which conflict with conclusions reported from studies of small molecules, are however,

consistent with hard-soft acid models for metals. Ca^{2+} is classified as a hard Lewis acid (Appendix, Table A.7) with an ionic radius of 0.99Å - 1.12 Å for a typical coordination number of 6 to 8 based on studies of small molecules [5, 208]. Conversely, Pb^{2+} has a reported ionic radius of 1.12 Å – 1.19 Å for similar coordination. Both Pb^{2+} and Zn^{2+} are classified as borderline acids, exhibiting properties of both hard and soft acids, so it is reasonable to assume that Pb^{2+} may share more similar binding features (e.g., polarizability) with Zn^{2+} than Ca^{2+}.

4.3 Charge by binding site

The Relative % Distribution of charge between the two datasets is shown in Figure 4.1b, indicating a range from 0 to -4 in the binding site, with a mean negative charge of 1.7 ± 1.1 for DS Final (Table 4.1). The mean and net charge values reported for the metal binding sites do not reflect positive charge contribution from the divalent cation. Previous studies of Ca^{2+} have indicated that higher binding affinities are found with a net negative charge within 5-15 Å of the ion [256-257], and a microenvironment containing 3-4 negative charges likely represents an optimal charge configuration [129, 218]. However, a more recent study in our laboratory indicates that this is representative of the more highly-structured EF-Hand proteins. The mean integer net negative charge for Pb^{2+}-binding sites (2 ± 1) falls between the structurally more diverse Non-EF-Hand proteins (1 ± 1) and the EF-Hand proteins (3 ± 1). Charge interactions for Pb^{2+} are likely stabilized due to the higher electronegativity (Appendix, Table A.7) and increased potential for partial covalent bond formation of Pb^{2+}, compared with Ca^{2+}.

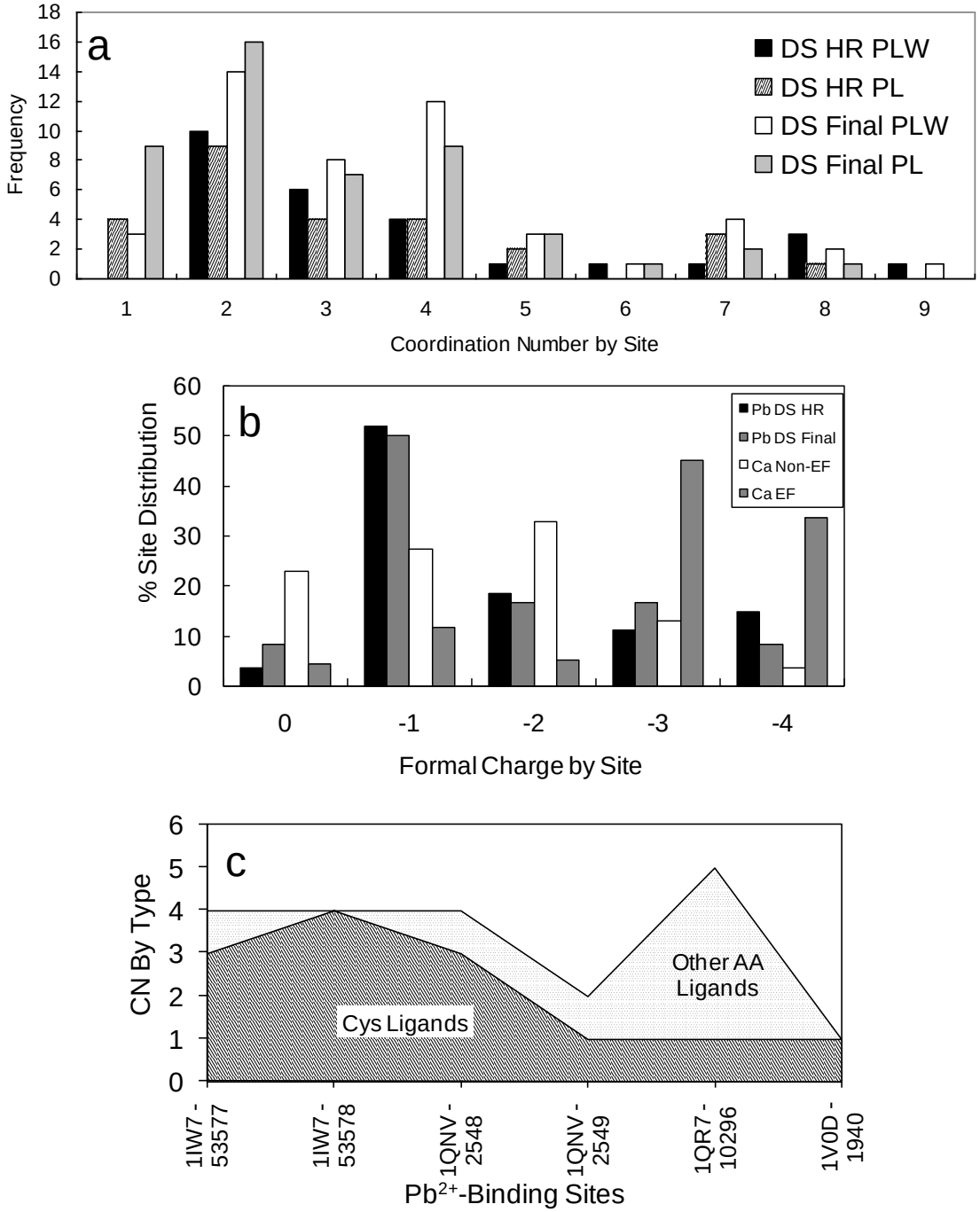

Figure 4.1 Select Pb^{2+}-binding statistics
(**a**) Frequency distribution of CN values, with and without water, for DS HR and DS Final. (**b**) Relative % distribution of charge values for Pb^{2+}-binding sites from DS HR and DS Final, and Ca^{2+}-binding sites for Non-EF-Hand and EF-Hand proteins. (**c**) Distribution of CN values by type for six Pb^{2+}-binding sites containing sulfur ligands. Other AA in the figure represents ligand atoms other than sulfur from amino acids.

4.4 Binding ligands

Oxygen atoms from amino acids represent the major binding ligand for Pb^{2+} (118), followed by oxygen from water (36), sulfur (13) and nitrogen (10) (Table 4.1). The % Relative Distribution of ligand atoms shown in Figure 4.2a indicates that binding ligand preference for Pb^{2+} followed the order sidechain Glu (38.4%) > sidechain Asp (20.3%) = water (20.3%) > Sulfur (7.3%). For comparison, the distributions of ligand preference for EF-Hand and Non-EF-Hand Ca^{2+}-binding proteins are presented in Figures 4.2b and 4.2c, respectively. From these figures, it can be seen that Pb^{2+} differs in several significant ways from Ca^{2+}-binding. The increased use of sidechain Glu by Pb^{2+} (38.4%) followed by sidechain Asp (20.3%) contrasts sharply with trends observed in both the highly-structured EF-Hand sites (sidechain Asp, 29.7%; sidechain Glu 26.6%) and the more structurally-diverse Non-EF-Hand sites (sidechain Asp, 24.5%; sidechain Glu, 10.4%). The presence of water in the Pb^{2+} sites falls roughly in the middle of the two Ca^{2+}-binding classes, but utilization of carbonyl oxygen atoms by Pb^{2+} is considerably lower than both the EF and Non-EF Ca^{2+}-binding classes (Figure 4.2).

Table 4.1 also summarizes the mean binding distance values determined from the analysis. The Pb-O distance (for amino acids) was found to be 2.7 ± 0.4 Å, which is slightly higher than the mean of 2.4 ± 0.2 Å reported for Ca-O. The mean distances reported for Pb-O (water), Pb-N and Pb-S were 2.8 ± 0.4 Å, 2.6 ± 0.4 Å, and 3.2 ± 0.3 Å, respectively. Except for Pb-S, these values were nearly identical despite expectations that Pb-N would exhibit a longer binding distance based on a comparison with data from Sarret *et al*. [187], where ranges for Pb-O, Pb-N and Pb-S were reported as 2.2-4.2 Å, 3.0-4.2 Å, and 2.6-3.4 Å, respectively.

Nitrogen is generally accepted as a binding ligand for Pb^{2+}, and marginally for Ca^{2+}, with small molecules; however, in our detailed statistical analysis of protein

calcium binding sites, less than 1% of all identified potential ligands were nitrogen atoms, and the limited contribution by nitrogen to bind Pb^{2+} in proteins is clear in Figure 4.2a. Only ten nitrogen atoms were identified as potential ligands within a cutoff distance of 3.5 Å. Nine of these were from side-chains, with six from His, two from Lys and one from Gln. Although the low pK_a (6.0) for His makes it a suitable binding ligand, Lys is unlikely to function as a binding ligand as its pK_a is significantly higher than physiological pH. For Gln, and presumably Asn, it is more likely to assume that binding of Pb^{2+} would occur with the polar, uncharged $–CO(NH_2)$ functional group, rather than the isolated sidechain nitrogen, due to the conjugated π–bond system and the planar structure of the group resulting from resonance. It can be inferred from these data that nitrogen plays a more limited role in the binding of Pb^{2+} to proteins than what has been reported in the case of small molecules.

Additionally, since Pb^{2+} was previously reported by Magyar and Andersen [49, 259] to bind in a thiol-rich site with a tendency to adopt a three ligand, trigonal pyramidal geometry, we attempted to evaluate the limited data available for sulfur ligands. As shown in Figure 4.1c, data were available for only six Pb^{2+}-binding sites which included sulfur ligands, where coordination number values reported were 1, 2, 4 and 6, with binding by 4 ligands apparent in three of the six sites. A trigonal pyramidal geometry for Pb^{2+} was not observed in our study; however this may be due to fact that the structures in our limited dataset were not identical to those reported by Magyar and Andersen.

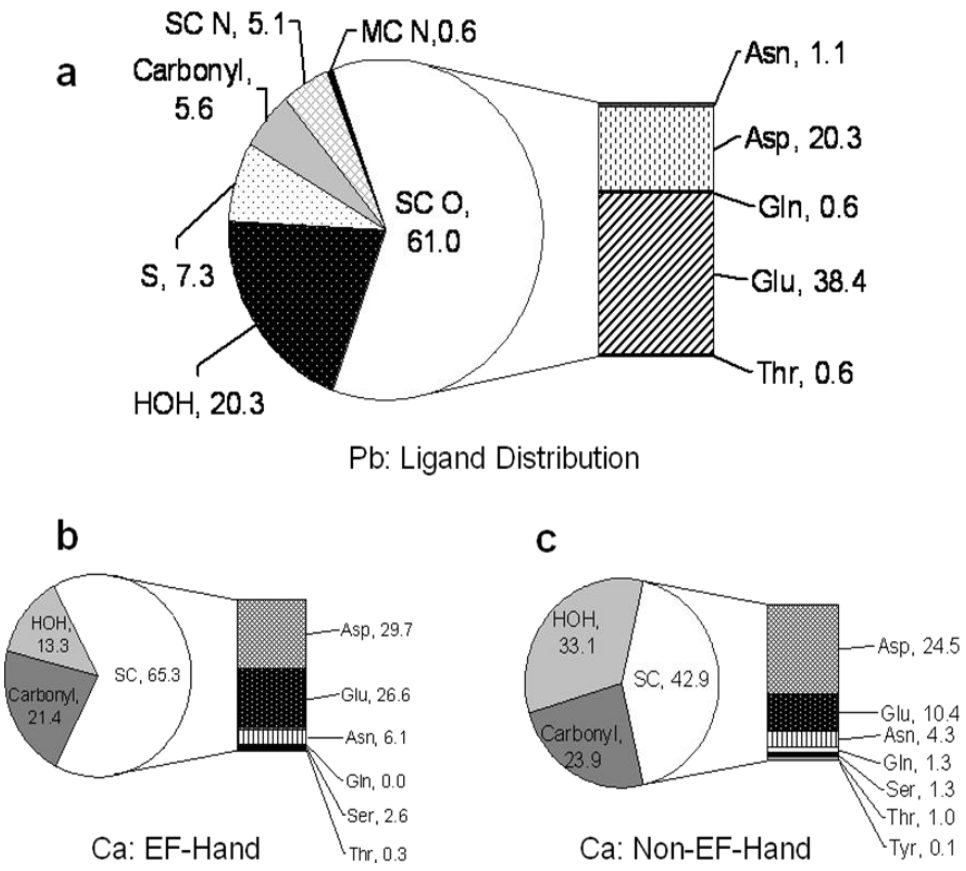

Figure 4.2 Comparison of ligand distributions between Pb^{2+} and Ca^{2+}
Percent distribution of ligands for (**a**) Pb^{2+}, (**b**) EF-Hand Ca^{2+} and (**c**) Non-EF-Hand Ca^{2+} binding sites, where: SC indicates sidechain; MC indicates mainchain; O, N, S indicates oxygen, nitrogen, and sulfur, respectively, and; HOH represents ligand oxygen from water.

4.5 Structural analysis

Next we evaluated structural changes associated with the displacement of Ca^{2+} by Pb^{2+} in the EF-Hand protein CaM. CaM, like most EF-Hand proteins, exhibits an irregular pentagonal-bipyramidal geometry (Figure 3.1a), with 5 planar ligands at -Z, Y, Z, and –Y, where –Z is a bidentate ligand. Ligands at X and –X are typically oxygen atoms from a side-chain carboxyl group and a bound water molecule, respectively. CaM also has high sequence similarity between species. An alignment for PDB proteins 3cln, 1exr, and 1n0y using ClustalW (http://www.ebi.ac.uk/clustalw/) indicates that the Ca^{2+}-

and Pb^{2+}-bound complexes of CaM (1exr.pdb and 1n0y.pdb) share 100% sequence similarity except for an additional Ala at the N-terminal, and a Lys at the C-terminal in 1n0y, and both are 88% homologous to 3cln (Appendix, Figure A.1). The structures of Ca^{2+} -CaM (1exr) and Pb^{2+} -CaM (1n0y, Figure 1.4e), were compared by Wilson *et al.* [134], who reported a C^{α} RMSD of 2.1 Å in the N-terminal domain compared with 1.1 Å in the C-terminal domain, with the most apparent deviation occurring between the N-terminal helix A and the C-terminal half of helix D/E. Additionally, Figure 1.4e shows that 14 Pb^{2+} ions are bound in the crystalline structure of CaM (1n0y), such that Pb^{2+} ions have not only replaced Ca^{2+} ions in the binding pockets, but have also become bound to surface ligands.

The pronounced global conformational changes observed in Figure 1.4e for Pb^{2+} bound CaM indicate new folding that is not observed in the Ca^{2+} bound form. An electrostatic potential surface map of protein 1n0y generated using DelPhi and GRASP (Figure 1.4f) [250-251, 253-254] shows an area of concentrated negative charge in the folding groove between Chains A and B where the 4 Pb^{2+} ions appear bound in the structure. However, the backbone RMSD comparing sites EF-I through EF-IV in the two structures, calculated using Sybyl software (Tripos, St. Louis, MO), indicated RMSD values ranging from 0.12 in EF-III, to 0.35 in EF-IV (Table 4.2). This suggests minimal disruption of the site due to ion displacement. To further validate this, a Ramachandran plot generated by VADAR [260] for 1n0y revealed that all dihedral angles fall within allowed regions, indicating no apparent strain on the backbone associated with binding of Pb^{2+}. The limited perturbation in the binding sites and the secondary binding of Pb^{2+} coincident with regions of high electrostatic potential strongly suggest that the observed conformational changes are independent of ion displacement, but related instead to our proposed mechanism of opportunistic binding which would imply much stronger binding

affinity for the Pb^{2+} ions than what is typically observed with low affinity, non-specific binding of metals at high concentrations.

Table 4.2 Summary of angle/distance values for 1exr and 1n0y

	EF-I	EF-II	EF-III	EF-IV	Mean
1EXR total Ca^{2+} ligands	6	6	6	6	6
1N0Y total Pb^{2+} ligands	7	8	6	7	7
Mean sum Δ Binding Distance Ca→ Pb (Å)	0.14	0.08	0.01	0.08	0.08
Mean sum Δ CLI Angle Ca→ Pb (°)	-8.67	-5.38	-1.34	-4.62	-5.00
RMSD by site	0.28	0.28	0.12	0.35	0.26 ± 0.10
Ca^{2+} planar monodentate LIL angles (°)	78.14 ± 3.34	78.05 ± 3.08	77.07 ± 1.75	78.76 ± 1.59	78.00 ± 2.37
Pb^{2+} planar monodentate LIL angles (°)	78.95 ± 5.86	75.80 ± 4.74	77.12 ± 2.00	78.70 ± 5.89	77.64 ± 4.57
Ca^{2+} planar bidentate LIL angles (°)	53.01	51.48	52.30	52.35	52.29 ± 0.63
Pb^{2+} planar bidentate LIL angles (°)	50.84	46.49	51.77	48.99	49.52 ± 2.33
Ca^{2+} Ion Dihedral (°)	4.91	4.12	7.43	0.23	4.17 ± 2.98
Pb^{2+} Ion Dihedral (°)	20.76	26.03	21.10	11.79	19.92 ± 5.93
Distance of Ca^{2+} ion out of bidentate plane	0.24	0.21	0.37	0.01	0.21 ± 0.15
Distance of Pb^{2+} ion out of bidentate plane	1.01	1.36	1.02	0.61	1.00 ± 0.31

CLI: Carbon-Ligand-Ion. **LIL**: Ligand-Ion-Ligand.

Consistent with this, a comparison of paired models (Figure 4.3: ab, cd, ef, gh) corresponding to EF sites I-IV for Ca^{2+}-binding and Pb^{2+}-binding indicates that the basic geometry for binding of Ca^{2+} is conserved upon binding with Pb^{2+}, and the same binding ligands, with minor exceptions, are used by both ions (Appendix, Table A.8). A comparison of distance and angle values for binding ligands utilized by both ions (Table A.8) shows a negligible, mean net increase in the binding distance (0.08 Å) and a corresponding mean sum decrease in the C-Lig-Ion angle (-5.00 º) for Pb^{2+}, but the monodentate and bidentate carbon-ligand-ion angles were nearly identical, and in both cases, the mean differences fall within the range of the standard deviation, so they are in all probability not statistically different.

The data associated with the bidentate dihedral angles for Ca^{2+}-binding, as summarized in Table 4.2, correlate well with research reported by McPhalen [219] that indicated a mean distance of 0.4 Å for the Ca^{2+} ion out of the carboxlyate plane, with a φ angle under 30°. For Pb^{2+}, however, the mean average distance for the ion increases to 1.00 ± 0.31 Å from 0.21 ± 0.15 Å observed for Ca^{2+}, and the mean bidentate ligand dihedral (φ) angle was much larger for the Pb^{2+} ion (19.92 ± 5.93º) than for Ca^{2+} (4.17 ± 2.98º) (Figure 4.4a).

Mean values of 6 and 7 coordination ligands (excluding water) were found for Ca^{2+} and Pb^{2+} respectively (Table 4.2), indicating that Pb^{2+} may take advantage of additional proximate ligand oxygen atoms when available, without disruption to the binding site. Nitrogen atoms potentially available as sidechain ligands in the binding loop sequence (Asn60 and Asn97; Figure 4.4d and Figure 4.4f, respectively) do not appear to be involved in binding, although there are no apparent barriers restricting rotation of the amide group around the Cγ-Cβ bond. This may, however, be due to mislabeling of atoms in the original structure.

For comparative purposes, two structures of yeast 5-aminolaevulinic acid dehydratase (ALAD) from *Saccharomyces cerevisiae* bound with Zn^{2+} (1eb3.pdb) and Pb^{2+} (1qnv.pdb) were also evaluated for changes associated with ionic displacement by Pb^{2+}. ALAD is a 280-kDa protein comprised of eight identical subunits that each bind a single Zn^{2+} ion. A single subunit from Chain A is presented in PDB files 1eb3 and 1qnv. Previous work by Bergdahl identified ALAD as the protein binding Pb^{2+} in human erythrocytes, where 99% of free Pb^{2+} concentrates in the blood [261], and the relationship between Pb^{2+} toxicity and human ALAD has been well-established [262].

Data from a structural analysis are summarized in Table A.9 (Appendix), which demonstrates strong similarity to changes observed in the EF-Hand binding sites for CaM. Distortion of the binding site is observed based on a mean increase in the binding distances of the three Cys thiol ligands (0.54 Å) and decreasing carbon-ligand-ion (CLI) angles for Cys133 and Cys135 (Table A.9) which is consistent with the larger radius of Pb^{2+}.

Additionally, the carbonyl oxygen of Ser179 which does not appear to be a binding ligand for Zn^{2+} (Figure 4.4d, top) is reoriented 0.9 Å to interact with the Pb^{2+} ion (Figure 4.4d, bottom). The binding site is formed in a deep pocket where interestingly, a second Pb^{2+} ion is bound 4.40 Å from the ion occupying the binding site, sharing the SG sulfur ligand from Cys143, whereas only a single Zn^{2+} ion is bound in the 1eb3 ALAD structure. Generation of an electrostatic potential map with Sybyl did not indicate dense charge clustering in this region, possibly due to the buried nature of the site.

Erskine *et al*., who deposited the structure 1qnv.pdb, reported a RMSD value of 0.4 for 326 matched C^{α} atoms [263]. Calculations with Sybyl for the resolved structural region indicated a backbone RMSD of 0.58 for the structure comprising residues 133-179 and a backbone RMSD value of 1.43 for the structure comprising residues 1-219.

As was seen with the displacement of Ca^{2+}, disruption of the backbone in the binding site microenvironment appeared minimal as a result of Pb^{2+}-binding.

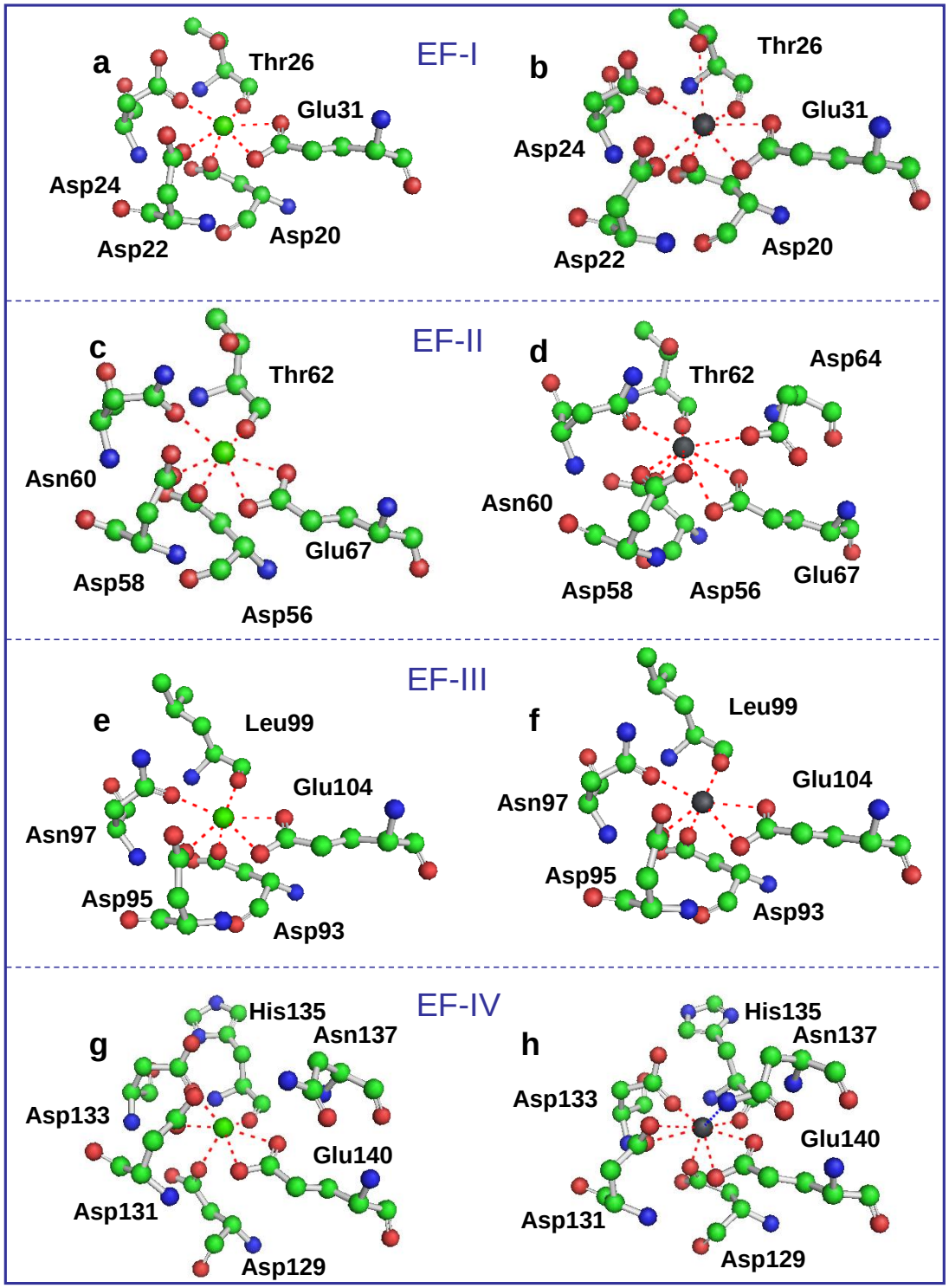

Figure 4.3 Paired binding sites EF-I (ab) EF-II (cd) EF-III (ef) and EF-IV (gh) for PDB proteins 1exr (left) and 1n0y (right)

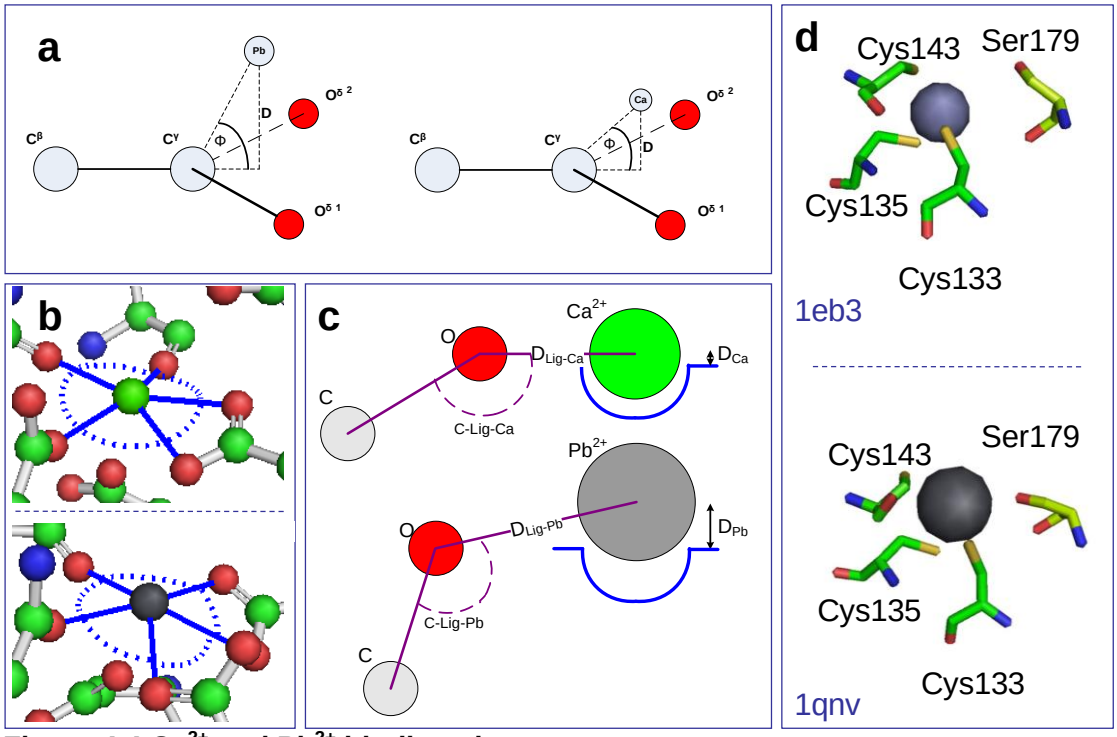

Figure 4.4 Ca^{2+} and Pb^{2+} binding site occupancy
(**a**) Illustration of position of the Pb^{2+} ion (left) and the Ca^{2+} (right) with respect to the carboxlyate bidentate plane. D and φ indicate distance and angle of ion relative to plane formed by C^{γ}, $O^{\delta 1}$ and $O^{\delta 2}$. (**b**) Positions of Ca^{2+} ion (top) and Pb^{2+} ion (bottom) with respect to pentagonal plane. (**c**) Example illustrating comparison of Ca^{2+}- and Pb^{2+}-binding characteristics with respect to the pentagonal plane. D_{Ca} and D_{Pb} indicate ion distance out of pentagonal plane. (**d**) Comparison of a binding site from ALAD protein showing Zn^{2+}-binding in 1eb3.pdb (top) and Pb^{2+}-binding in 1qnv (bottom) where one additional ligand (Ser179) is provided for binding of Pb^{2+}. For the color scheme, red is oxygen, blue is nitrogen, yellow is sulfur, and green is carbon. In (c), the small, red spheres indicate water molecules.

Based on the results of our analysis, Figure 4.4 illustrates characteristics of a proposed model showing the differences between Ca^{2+} and Pb^{2+} during binding. In this model, which includes parameters that may be extensible to Zn^{2+}-binding sites, the slightly larger ionic radius of Pb^{2+} is accommodated by small changes in sidechain ligand orientations, increased displacement of the ion (D_{Pb}) relative to the Ca^{2+} occupancy (D_{Ca}) of the site (Figure 4.4c), and more pronounced reorientation of the Glu anchor at –Z

(Figure 4.4a). This would account for the apparent minimal distortion in the pentagonal plane (Figure 4.4b) and more significantly, the backbone. This proposed model accounts for the larger ionic radius of Pb^{2+}, minor rotation of the side-chains, the net increase in binding distance and net decrease in bond angles when binding Pb^{2+} (Table 4.2), and the increase observed in the bidentate ligand dihedral (φ) angle for the Pb^{2+} ion. It is also consistent with previously-noted observations indicating that Pb^{2+} initially activates then deactivates CaM with increasing Pb^{2+} concentration, where activation of CaM results from ionic displacement, followed by strong opportunistic binding to effect conformational changes.

4.6 Conclusions

It is apparent from both the structural and database analyses of Pb^{2+}-binding sites that oxygen is the dominant binding ligand for Pb^{2+}, or sulfur in the case of Zn^{2+}-binding sites, with only negligible interaction between Pb^{2+} and nitrogen. The Pb^{2+} binding sites were significantly different from those observed for EF-Hand proteins, requiring fewer coordinating ligands and less negative charge, but sharing more structural similarity with the more disordered Non-EF-Hand sites. Conversely, the increased utilization by Pb^{2+} of Glu (38.4%) over Asp (20.3%) reverses the trend observed for Non-EF-Hand CaBPs (10.4% and 24.5%, respectively), indicating differences in the two binding models not accounted for solely by ionic charge and atom type. Moreover, the significant structural alterations in CaM appear to be due to binding of Pb^{2+} in regions of high surface negative charge potential (Figure 1.4f), rather than exchange of Ca^{2+} with Pb^{2+}, which is supported by the low RMSD values reported for ionic displacement (Table 4.2). The combination of these results, and previous studies citing the initial activation and subsequent inhibition of CaM as a function of toxic metal concentration [83, 85-86, 88, 137-138], argues that strong opportunistic binding, either

coupled with, or independent of, ionic displacement, has several important ramifications with respect to toxicity. First, proteins may bind both opportunistically and by ionic displacement, resulting in activation or inhibition of the protein as a function of metal concentration. Studies of CaM showing initial activation followed by inhibition in response to increasing concentration of metal ion (e.g. – Pb^{2+}) suggests that initial binding in the active sites may first activate the protein as if bound with Ca^{2+}, but the subsequent deactivation may result from more pronounced conformational changes resulting from additional opportunistic binding. Second, strong non-specific or opportunistic binding can potentially increase solubility and facilitate transport and diffusion of toxic metals, as may be the case with ALAD from human blood erythrocytes, which may potentially bind multiple Pb^{2+} ions in a site normally occupied by a single Zn^{2+} ion.

Furthermore, the apparent, promiscuous binding of Pb^{2+} is suggested by the variety of ions it can displace (Table A.1), its adaptability to different coordination geometries, and the wide range of coordination numbers and charge values associated with opportunistic binding in the absence of well-defined binding sites. Additionally, recently reported studies indicate that bacterial proteins encode different binding motifs in sensors capable of detecting Pb^{2+}. CmtR, a Cd^{2+}/Pb^{2+} regulator expressed in *Mycobacterium tuberculosis*, binds Pb^{2+} with three Cys thiols, more typical of Zn^{2+} binding [264]. However, in *Ralstonia metallidurans* strain CH34, a Cys ligand is replaced by two Glu residues, resulting in a binding motif more similar to that of Ca^{2+} [23]. It is presumed that the ability of Pb^{2+} to bind opportunistically may extend to non-metalloproteins, thus increasing the number of potential target proteins whose function may be altered due to the introduction of toxic metals.

5 Investigation of Pb^{2+}-toxicity via Ca^{2+}-binding proteins

5.1 Fluorescent response of Pb^{2+}-binding in isolated EF-hand Ca^{2+}-binding site

Previous work in our laboratory had produced unusual results with respect to binding of Pb^{2+} with Enhanced Green Fluorescent Protein (EGFP) and several engineered variants with grafted Ca^{2+}-binding sites [265]. Changes in signal intensity were observed during titrations of Pb^{2+} with EGFP and variants, regardless of whether a metal-binding site was grafted to the construct. Additionally, during competitive titrations where Pb^{2+} was added in µM concentrations in the presence of mM concentrations of Ca^{2+}, changes in fluorescence intensity were coupled with small but persistent red-shifts in the spectra, as seen in Figure 5.1 through Figure 5.4. These results were consistent with our proposed hypothesis concerning opportunistic binding as a potential avenue of molecular toxicity for Pb^{2+}.

Using EGFPwtF as a scaffold, several variants were produced by grafting the calcium-binding loop III (sequence DKDGNGYISAAE) and it's flanking E (sequence EEEIREAFRVF) and F (sequence LRHVMTNL) helices from calmodulin onto one of three targeted, solvent-exposed loops on EGFPwtF (Figure 5.5), designated herein as A, B and C (not shown in Figure 5.5). This grafting approach has been used to evaluate EF-hand Ca^{2+}-binding motifs [173, 175], and previous work in our lab has demonstrated that Ca^{2+} binding motifs maintain their binding properties when grafted onto non-Ca^{2+}-binding proteins [174, 266]. The E-III-F segments were variously combined as indicated in Figure 5.5, and will be referenced as sub-variant types 1-4 (e.g, EGFP-C2 indicates sub-variant 2, the E Helix and Loop III only, grafted onto EGFP at site C).

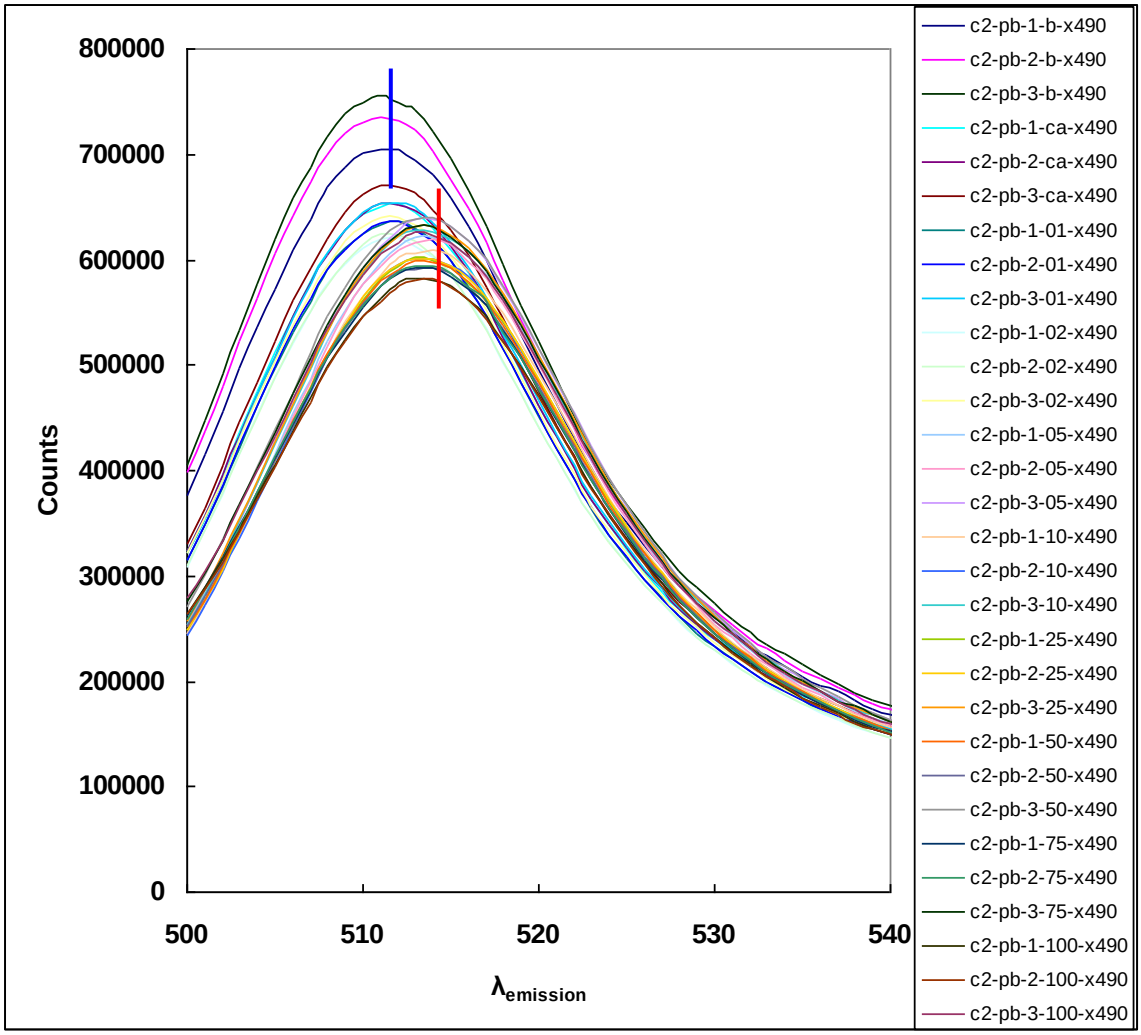

Figure 5.1 490 nm fluorometric emission scans of 1 µM EGFP-C2 variant
Competitive titration between 1 mM Ca^{2+} and 0-100 µM Pb^{2+} in 10 mM chelexed TRIS-Cl buffer, pH 7.4. Red-shift observed at 5 µm Pb^{2+} from 511 nm to 513 nm.

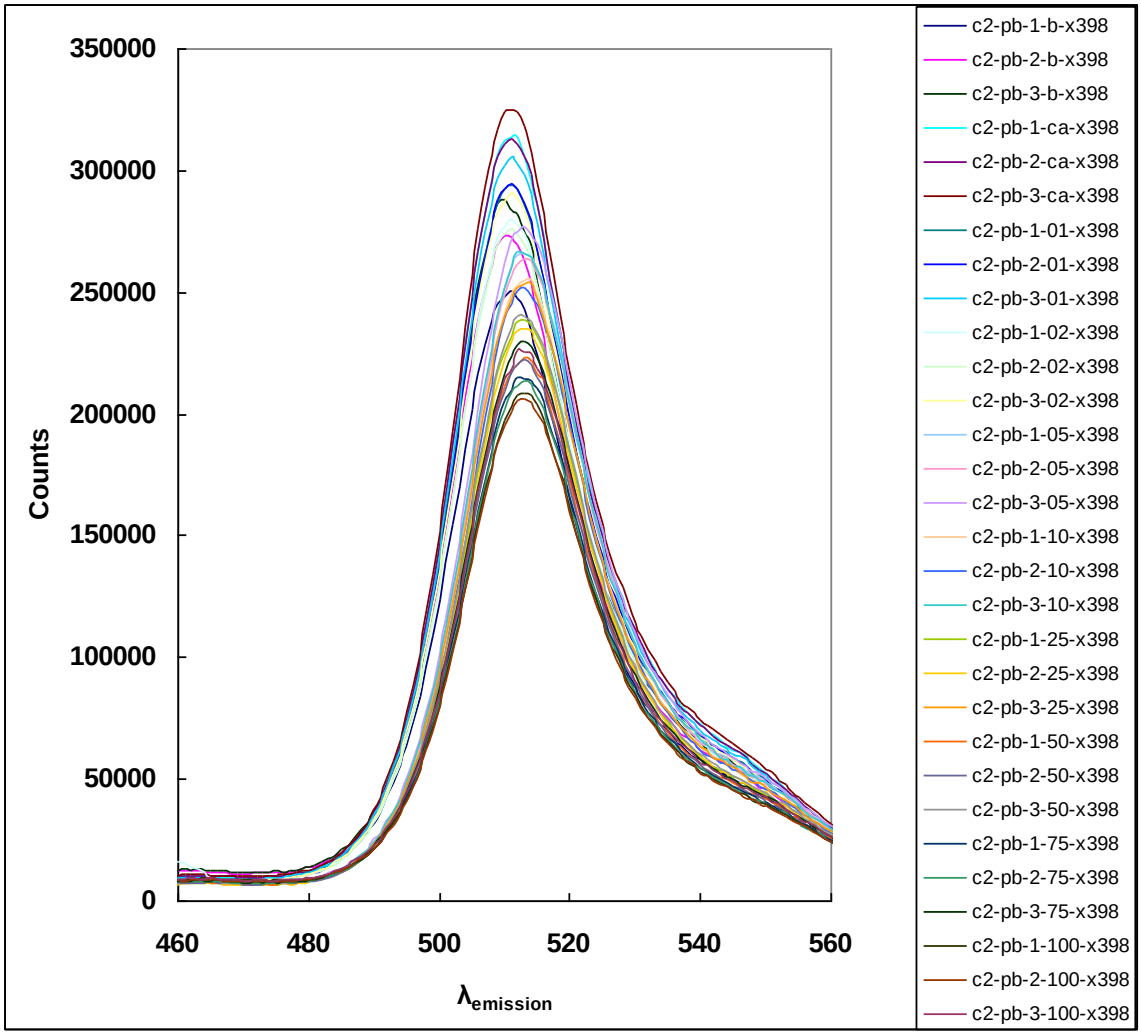

Figure 5.2 398 nm fluorometric emission scans of 1 µM EGFP-C2 variant
Competitive titration between 1 mM Ca^{2+} and 0-100 µM Pb^{2+} in 10 mM chelexed TRIS-Cl buffer, pH 7.4. Red-shift observed at 5 µm Pb^{2+} from 511 nm to 513 nm.

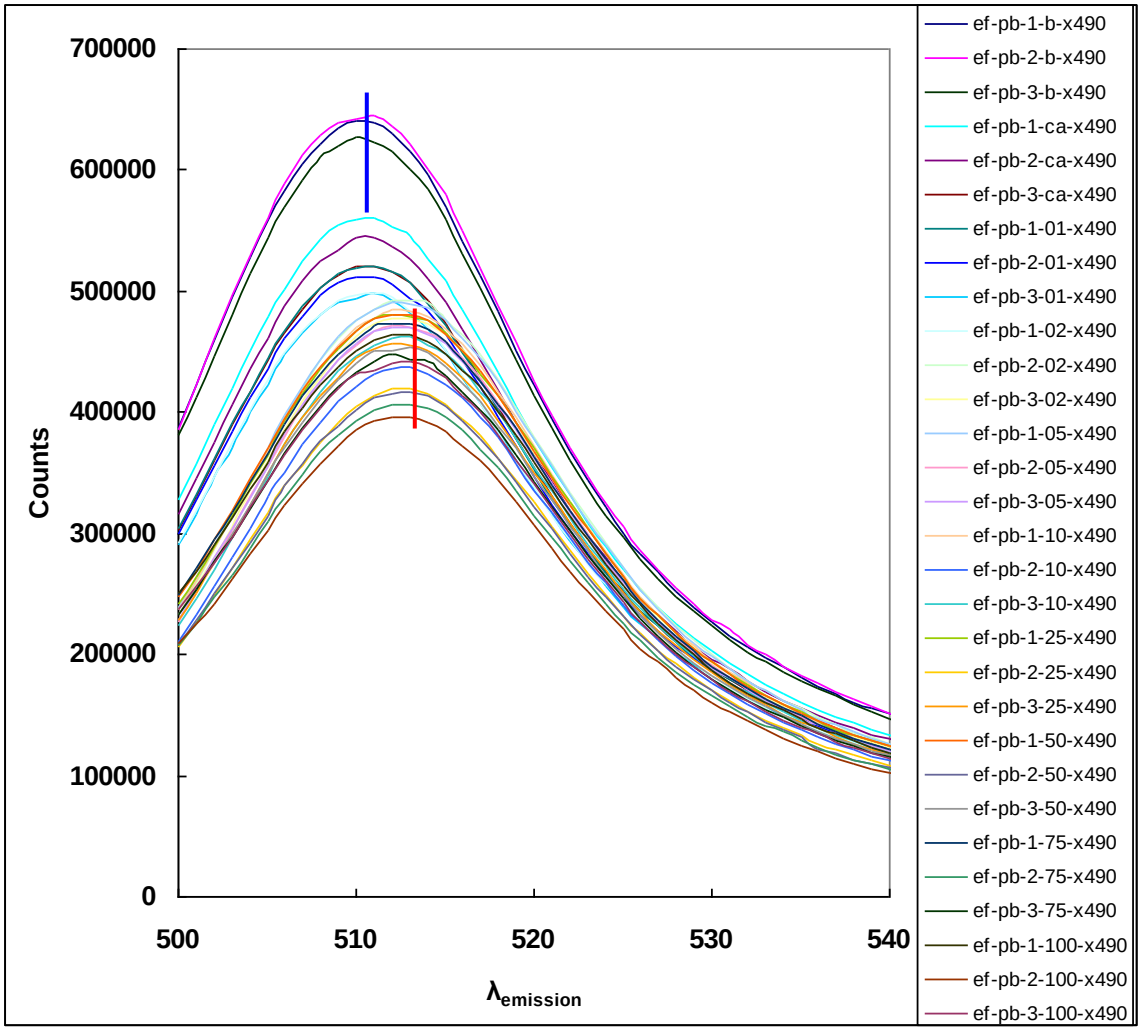

Figure 5.3 490 nm fluorometric emission scans of 1 µM EGFPwtF EF172 variant Competitive titration between 1 mM Ca^{2+} and 0-100 µM Pb^{2+} in 10 mM chelexed TRIS-Cl buffer, pH 7.4. Red-shift observed at 5 µm Pb^{2+} from 511 nm to 513 nm.

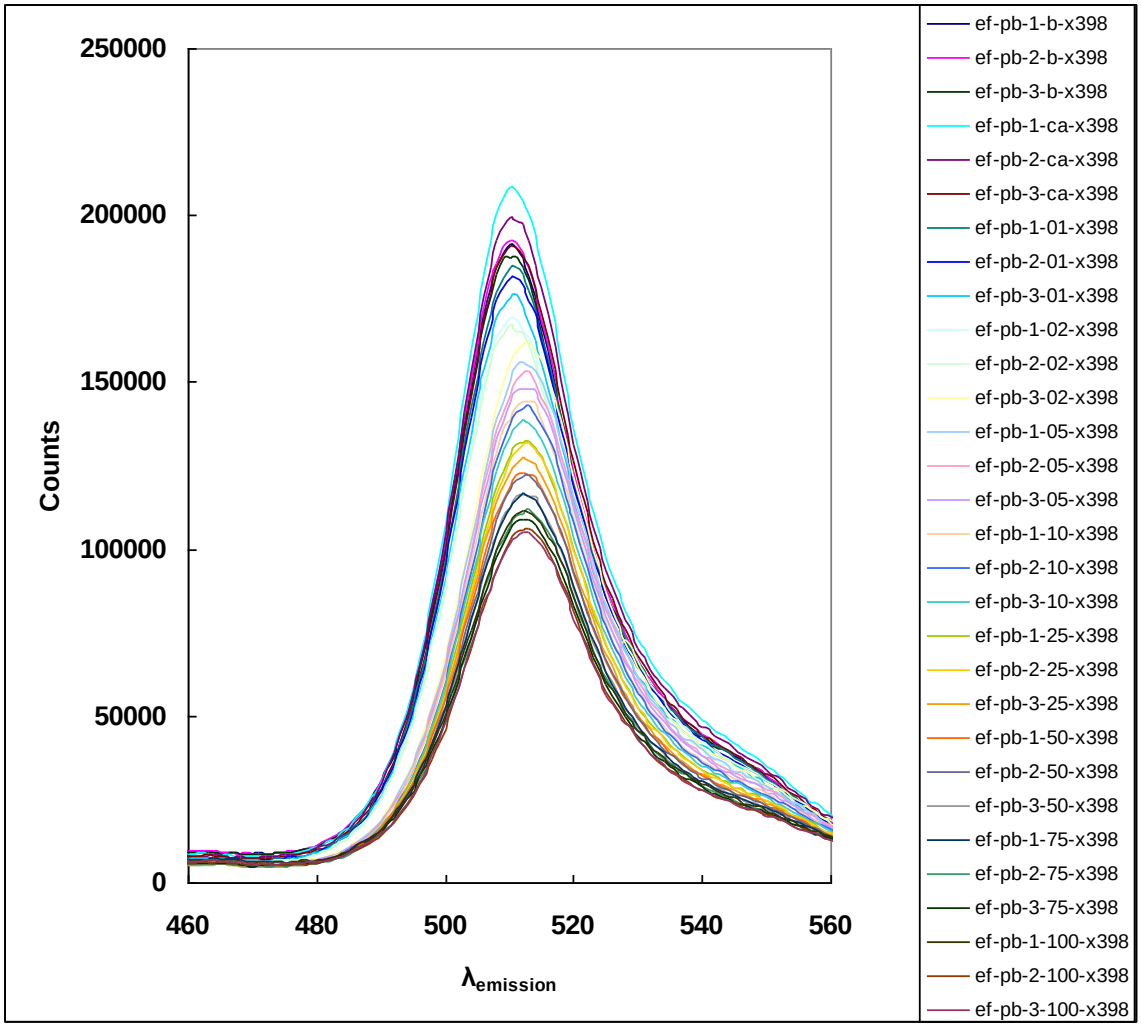

Figure 5.4 398 nm fluorometric emission scans of 1 µM EGFP-C-4 variant
Competitive titration between 1 mM Ca^{2+} and 0-100 µM Pb^{2+} in 10 mM chelexed TRIS-Cl buffer, pH 7.4. Red-shift observed at 5 µm Pb^{2+} from 511 nm to 513 nm.

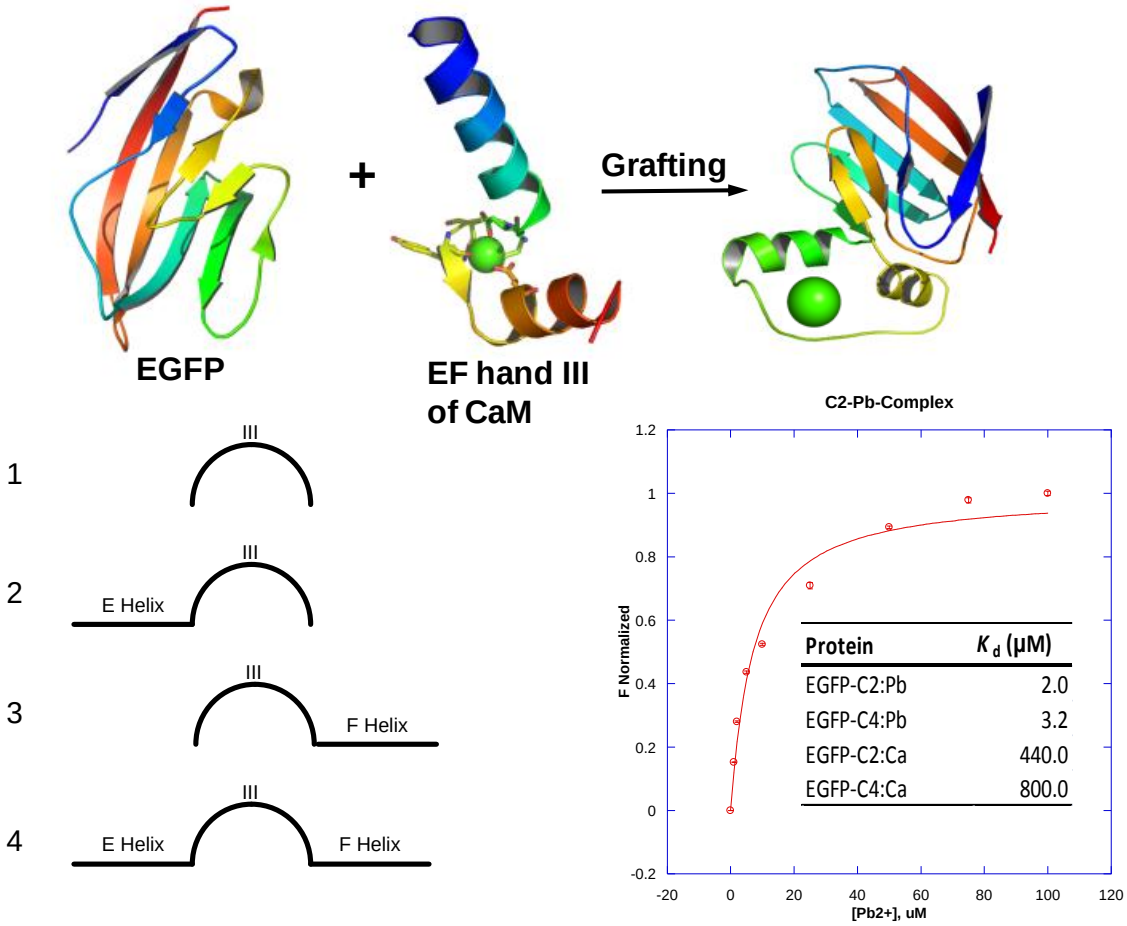

Figure 5.5 Grafting approach to protein engineering
(Top) Grafting approach to incorporate all or part of the EF-III binding motif from CaM into EGFP at solvent-exposed loops. (Bottom left). Coding for partial or complete EF-III components grafted into EGFP. (Bottom right) Calculation of K_d for Pb^{2+} binding to a Ca^{2+}-binding site with 1 μM EGFP-C2 in chelex-treated 10 mM TRIS buffer, pH 7.4. Fluorescence changes were measured with addition of Pb^{2+} at 398 nm and 490 nm. Changes in the ratio F398/F490 were plotted against Pb^{2+} concentration. Curve-fitting of data indicated the binding affinity of Pb^{2+} for our modified EGFP variants was over 200-fold greater than that of Ca^{2+} (inset).

Normalized data for variants C2 and C4 were plotted and K_d values were calculated by curve-fitting with Eq. 7. The results indicated that Pb^{2+} has 200-fold or higher affinity for CaM EF-III than Ca^{2+} (Figure 5.5).

5.2 CaM tyrosine fluorescence response to binding of Pb^{2+}, $Gd^{3+}$and In^{3+}

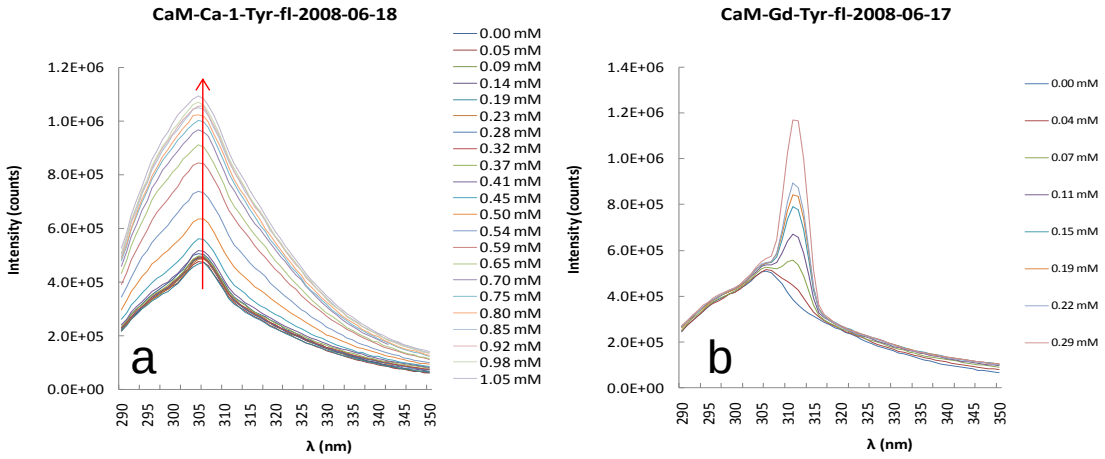

Figure 5.6 CaM tyrosine fluorescence
Equilibrium titration with wt-CaM and (a) Ca^{2+} , and (b) Gd^{3+}

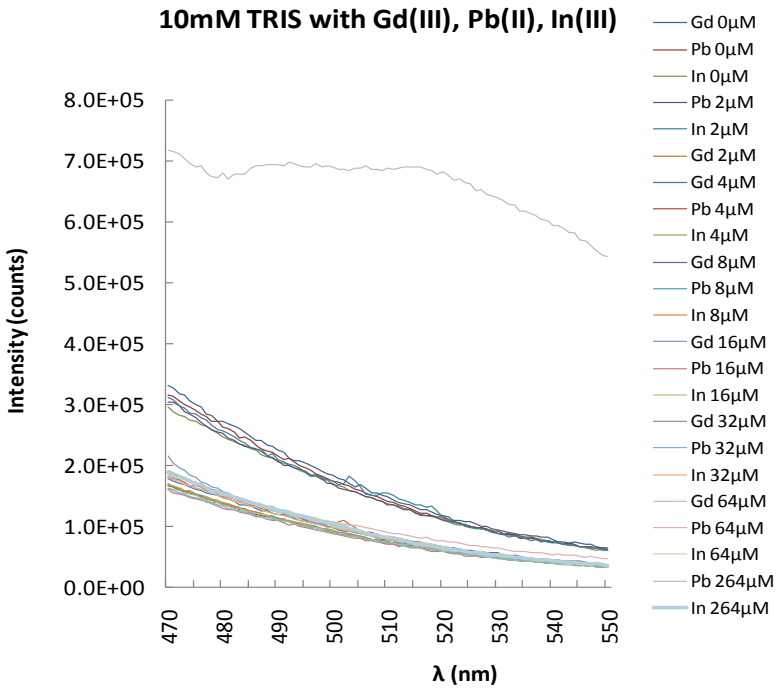

Figure 5.7 Fluorescent response of Gd^{3+}, Pb^{2+} and In^{3+} in 10 mM TRIS

Tyrosine in CaM exhibits a change in its fluorescence emission at ~304 nm as a result of metal binding. A series of titrations were conducted to measure the tyrosine response to Ca^{2+} and Gd^{3+} (Figure 5.6). The binding affinity for calcium to the C-Terminal of CaM, based on tyrosine fluorescence, was previously calculated to be 2 μM

(data not shown). Additionally, we observed in Figure 5.6b a second peak emerging at 312 nm that rapidly obscured the tyrosine fluorescence peak. It is believed that this second peak is a result of Gd^{3+} interaction with the buffering system, but to date, this has not been established. It was apparent from these preliminary data, however, that a different buffering system was required to evaluate Gd^{3+}. TRIS was then evaluated as an alternative to HEPES, with no apparent interaction (Figure 5.7). It should be noted that Gd^{3+} precipitates in solutions at some point after 64 µM concentration, as seen in the isolated spectral line at the top of Figure 5.7.

5.3 Determining K_d for Ca^{2+} and Pb^{2+} binding with CaM by intrinsic fluorescence

Methods for establishing K_d values for Ca^{2+} binding to the N- and C-terminal domains of CaM based on metal-induced changes to the intrinsic fluorescence of Phe and Tyr residues were previously detailed by VanScyoc [191]. The distribution of Tyr residues in the C-terminal domain and Phe residues in the N-terminal domain are highlighted in bold in Figure 2.7. This delineation allows for monitoring of domain-specific, metal-induced fluorescent changes. Effective K_d values for Ca^{2+} binding to the N- and C-terminal domains were found to be $1.15 \pm 0.68 \times 10^{-5}$ M and $2.04 \pm 0.02 \times 10^{-6}$ M, respectively (Table 5.1). The calculated K_d values are consistent both with reported values for Ca^{2+} [267] and with known Ca^{2+} intracellular concentrations in the µM range.

Table 5.1 Domain-specific binding dissociation constants for CaM

	K_d (M)	
	Ca^{2+}	Pb^{2+}
N-terminal (EF-Hand I & II)	$1.15 \pm 0.68 \times 10^{-5}$	$1.40 \pm 0.30 \times 10^{-6}$
C-terminal (EF-Hand III & IV)	$2.04 \pm 0.02 \times 10^{-6}$	[a] $7.34 \pm 0.95 \times 10^{-7}$
C-terminal (EF-Hand III & IV)	--	[b] $6.69 \pm 0.63 \times 10^{-7}$
C-terminal (secondary)	--	$1.93 \pm 0.32 \times 10^{-6}$

[a] Direct titration
[b] Competitive titration with Ca^{2+}

Direct titration of Pb^{2+} to CaM produced a decrease in Phe fluorescence (Figure 5.8b), similar to the response observed with Ca^{2+} (Figure 5.8a). Curve-fitting of data, based on Eq. 7, produced a calculated K_d of 1.40±0.30 X 10^{-6} M for binding of Pb^{2+} in the N-terminal domain (Table 5.1).

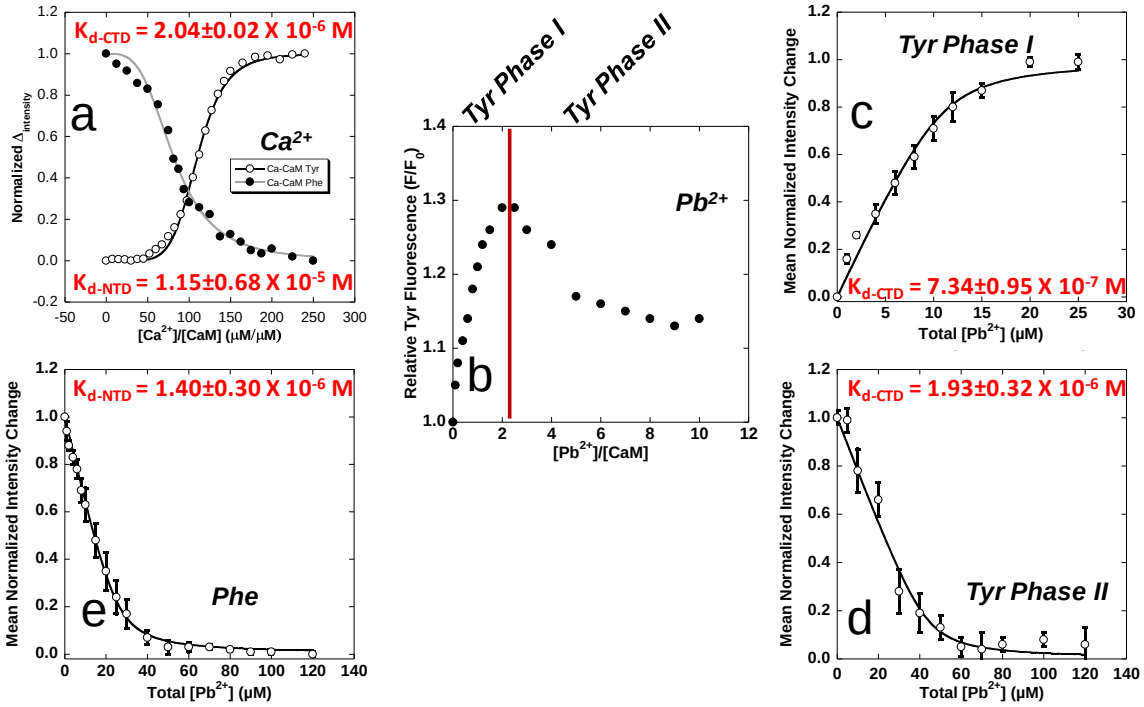

Figure 5.8 CaM fluorescence with binding of Ca^{2+} and Pb^{2+}
(**a**) Mean normalized Tyr and Phe fluorescence changes as functions of the ratio $[Ca^{2+}]/[CaM]$. (**b**) Relative Tyr fluorescence as a function of Pb^{2+}:CaM complex formation for CaM (open circles) and CaMDelete (filled circles). The observed biphasic fluorescent response is divided into (**c**) Phase 1 with a calculated K_d of 7.34 ± 0.95 X 10^{-7} M and (**d**) Phase 2 with a calculated K_d of 1.93 ± 0.32 X 10^{-6} M. (**e**) Mean normalized Phe fluorescence change as a function of total $[Pb^{2+}]$ for the N-terminal domain. The calculated K_d of 1.40 ± 0.30 X 10^{-6} M was equivalent to the value calculated in (**d**) for Phase 2 of the Tyr fluorescence associated with the C-terminal domain sites.

Different from the increase in Tyr fluorescence upon addition of Ca^{2+} (Figure 5.8a), the direct titration of Pb^{2+} produced a biphasic response characterized by a rapid initial increase in fluorescence intensity up to ~2:1 molar equivalents of Pb^{2+}/Protein, followed by a hyperbolic decrease in intensity reaching a minima below 10 molar equivalents of Pb^{2+} (Figure 5.8b). The initial increase (Phase 1, Figure 5.8c) which

mimics the Ca^{2+} response and peaks at ~2 ME of Pb^{2+}, was interpreted as binding of Pb^{2+} in one of the two binding sites EF-III and EF-IV, while the subsequent decrease (Phase 2, Figure 5.8d) was interpreted as binding in the other C-terminal domain site. Curve-fitting of data, based on Eq. 7, produced a calculated K_d of 7.34 ± 0.95 X 10^{-7} M for Phase 1 and a K_d of 1.93 ± 0.32 X 10^{-6} M for Phase 2 (Table 5.1). Interestingly, this value and the associated curve of the second phase in the tyrosine titration (Figure 5.8d) are nearly identical to the corresponding curve and calculated K_d observed for the Phe signal change for the N-terminal domain (Figure 5.8e). These results are consistent with a single higher affinity Pb^{2+}-binding site in the C-terminal domain and nearly equivalent affinity for the three remaining sites.

Precipitation was typically observed at or beyond 10 ME Pb^{2+}. Except for a higher observed fluorescence intensity, the same biphasic response was observed for both CaM and CaM-Delete (not shown), indicating that fluorescent changes were independent of activity in the deleted subset of residues from the central linker region (76-80).

Competitive titrations to analyze changes in Tyr fluorescence were also conducted. CaM was first presaturated with Ca^{2+} followed by titration with Pb^{2+}, however, no change in fluorescence intensity was observed using this approach and the samples precipitated with increasing Pb^{2+} concentration (data not shown). Based on this preliminary evidence, and results from NMR studies suggesting that Pb^{2+} does not readily displace Ca^{2+} in the C-terminal domain sites, we instead equilibrated 10 µM CaM with different concentrations of Pb^{2+} followed by titration with Ca^{2+}. At 20 µM equilibration (Figure 5.9a), the addition of Ca^{2+} produced a plot similar to that observed for direct titration of Pb^{2+}, indicating rapid displacement of Pb^{2+} by Ca^{2+} in the two C-terminal EF-Hand sites. However, at 50 µM Pb^{2+} equilibration (Figure 5.9b), a biphasic curve was observed, similar to the response observed with direct Pb^{2+} titration (Figure 5.8c), which

peaked near 20 µM (2 ME Pb^{2+}), followed by decreasing fluorescence. Assuming that the first phase of the curve represents binding in the EF-hand sites, we concluded that the decreasing fluorescence observed from 20-50 µM resulted from binding in the lower affinity C-terminal domain site. Finally, at 100 µM Pb^{2+} presaturation (Figure 5.9c), sample precipitation became apparent after addition of the first 2 ME Ca^{2+}. This latter result suggested that Ca^{2+} displaced Pb^{2+}, followed by precipitation of free Pb^{2+}. Collectively, these results indicated that the C-terminal EF-Hand sites bind Ca^{2+} selectively even in the presence of high concentrations of Pb^{2+} and despite the apparent higher binding affinity of CaM for Pb^{2+} as calculated based in a Ca^{2+}-free environment (Table 5.1). This would indicate also that binding of Pb^{2+} does not conform to the same model of positive cooperativity between paired sites as Ca^{2+}, consistent with observations from our HSQC NMR data.

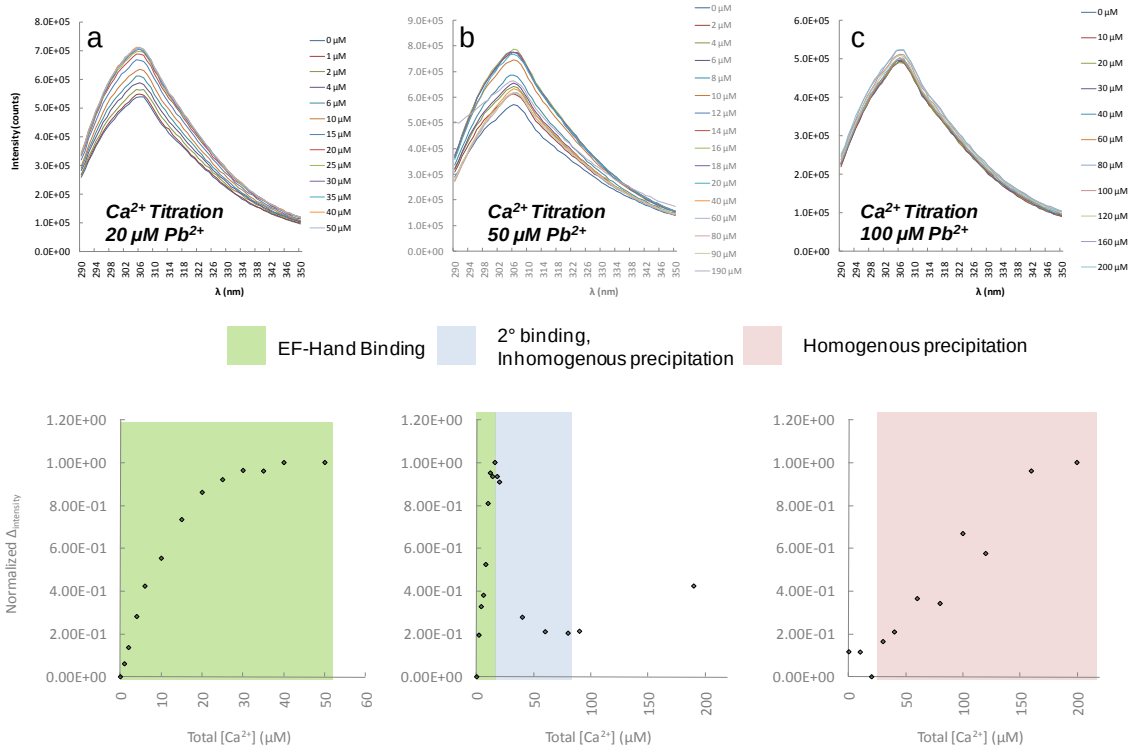

Figure 5.9 Calcium titrations with 10 µM wt-CaM presaturated with Pb^{2+}
Samples were prepared in 10 mM Tris pH 7.4, 100 mM KCl, presaturated with (**a**) 20, (**b**) 50 and (**c**) 100 µM Pb^{2+}, respectively.

Based on these preliminary results, 10 µM samples of Ca^{2+}-free CaM were pre-equilibrated with 20 µM Pb^{2+}, assuming that all Pb^{2+} was binding to sites EF-III and EF-IV, followed by titration of Ca^{2+}. The resulting data is still fit with Eq. 7, but the K_d value returned for Pb^{2+} is calculated by rearranging Eq. 8 into Eq. 9, and solving for K_{dm1} based on the known K_d for Ca^{2+} (K_{dm2}), K_d from Eq. 7 which becomes K_{app}, and the total, fixed concentration of Pb^{2+} pre-equilibrated with the protein $[M_1]_T$. Results indicated a K_d (K_{dm1}) of 6.7±0.6 X 10^{-7} M (Table I), which overlaps the standard deviation reported for results obtained by direct titration of Pb^{2+} (Figure 5.8d).

These results were interpreted to indicate that Pb^{2+} initially binds in the known EF-Hand sites, followed by binding of one or more additional ions in either the C-terminal domain or the linker region. However, aside from a marginal increase in fluorescence intensity in the wt-CaM titration, the same trends were observed with the CaM-Del variant, which did not support binding of Pb^{2+} in the Linker region of the protein, but was consistent with the possibility of an additional site in the C-terminal domain.

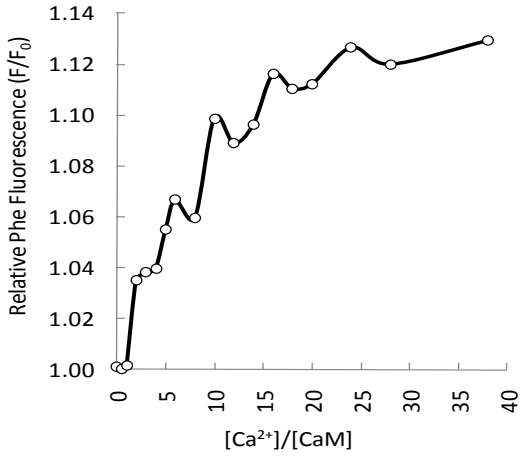

Figure 5.10 CaM Phe fluorescence
Addition of Ca^{2+} to 10 µM CaM presaturated with 50 µM Pb^{2+} results in an oscillating fluorescent response.

5.4 Effect of Ca^{2+} titration on Phe fluorescence in Pb^{2+}-bound CaM

A competitive titration was also conducted where 10 µM CaM was presaturated with 50 µM Pb^{2+} prior to titration with Ca^{2+}. This resulted in an oscillating fluorescence response (Figure 5.10) which may be due to rapid exchange between two metal ions, although kinetics have not been investigated as part of this study, to date.

5.5 1D NMR Spectra of Pb^{2+}- and Ca^{2+}-CaM complexes

The 1D NMR spectra presented in Figure 5.11 indicate changes in the chemical shifts as a consequence of adding Pb^{2+} to 100 µM wt-CaM in a salt free environment. Changes were apparent up to 6:1 molar equivalents (ME) of Pb^{2+}/wt-CaM, however, precipitation was observed beginning at 8:1 (data not shown). At 6:1 ME, peak intensity has decreased and signals have become obscured with increased peak broadening. These same trends were observed in the parallel analysis in 100 mM KCl (Figure 5.12), indicating that the presence of high salt did not significantly inhibit the response due to metal-protein interactions, but did result in increased line broadening. No attempt was made to assign the proton spectra due to extensive overlapping of chemical shifts observed with proteins. This information is more readily acquired through multidimensional NMR experiments described later in this chapter.

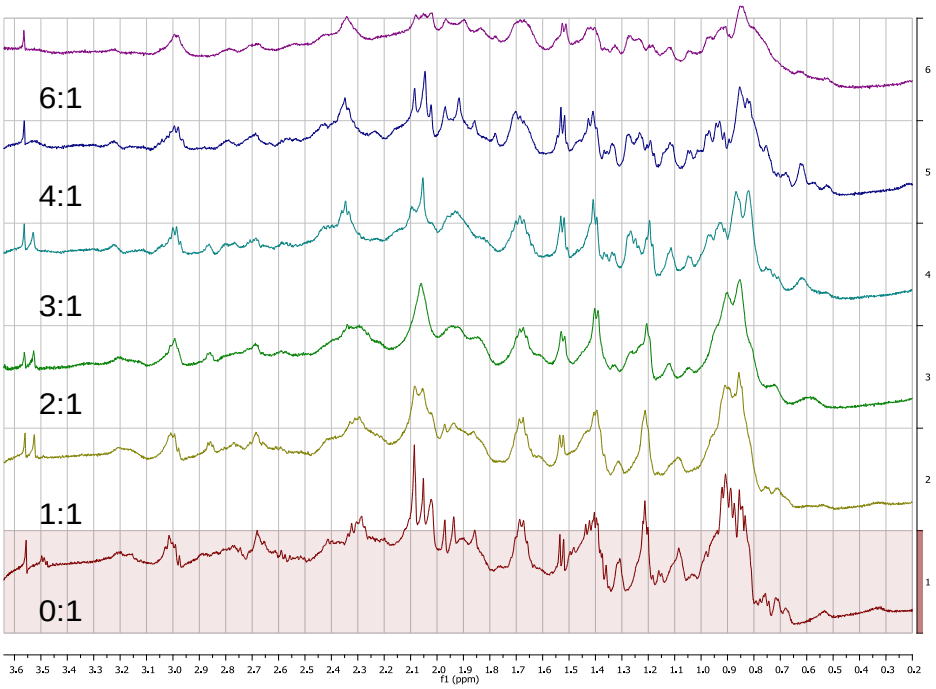

Figure 5.11 ^{1}H spectrum of sidechain region of CaM in salt-free buffer for titration of Pb^{2+} (0-6ME)

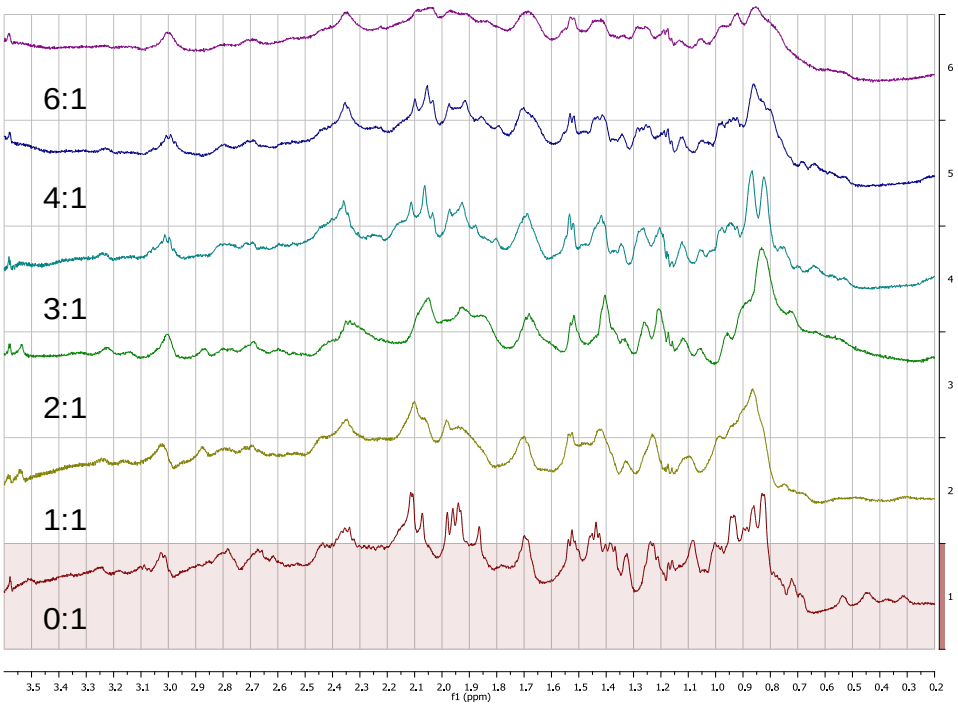

Figure 5.12 ^{1}H spectrum of sidechain region of CaM in 100 mM KCl buffer for titration of Pb^{2+} (0-6ME)

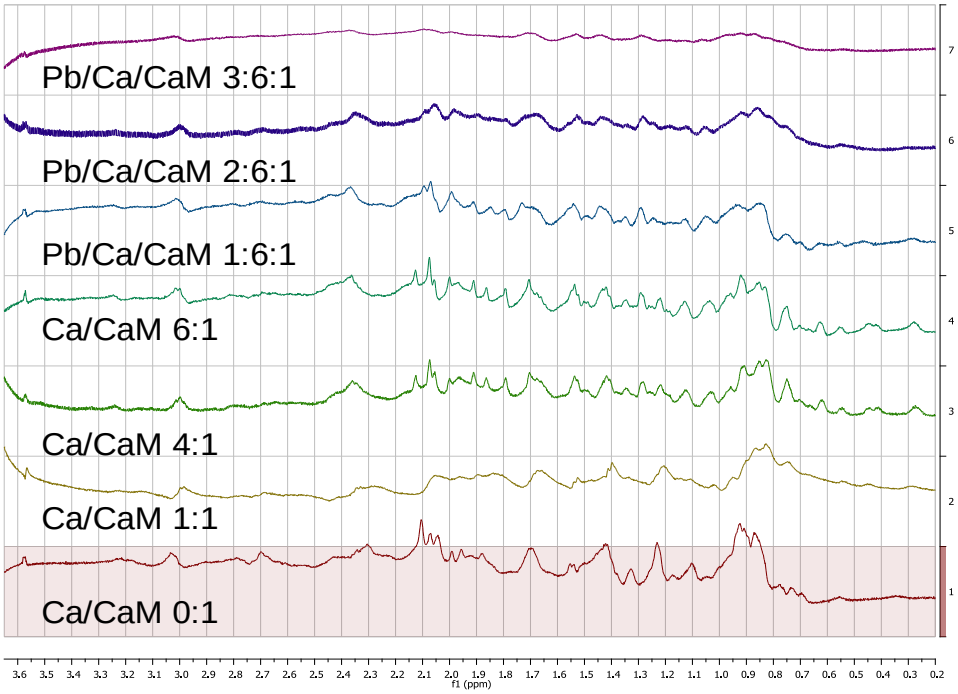

Figure 5.13 Competitive titrations between Ca^{2+} and Pb^{2+}, spectra from 0.2-3.6 ppm

In Figure 5.13 we observe the competitive effects between Ca^{2+} and Pb^{2+}. For consistency, Ca^{2+} was added up to 6:1 ME with wt-CaM, followed by the addition of Pb^{2+}.

Interestingly, precipitation was observed after 3 ME of Pb^{2+} was added, at which point 9 ME of metal had been titrated with the protein. We conclude from this and other results that CaM may only bind a maximum of 3 ME of Pb^{2+} in the Ca^{2+} -loaded, which would indicate that Pb^{2+} cannot displace all of the Ca^{2+} in the binding sites.

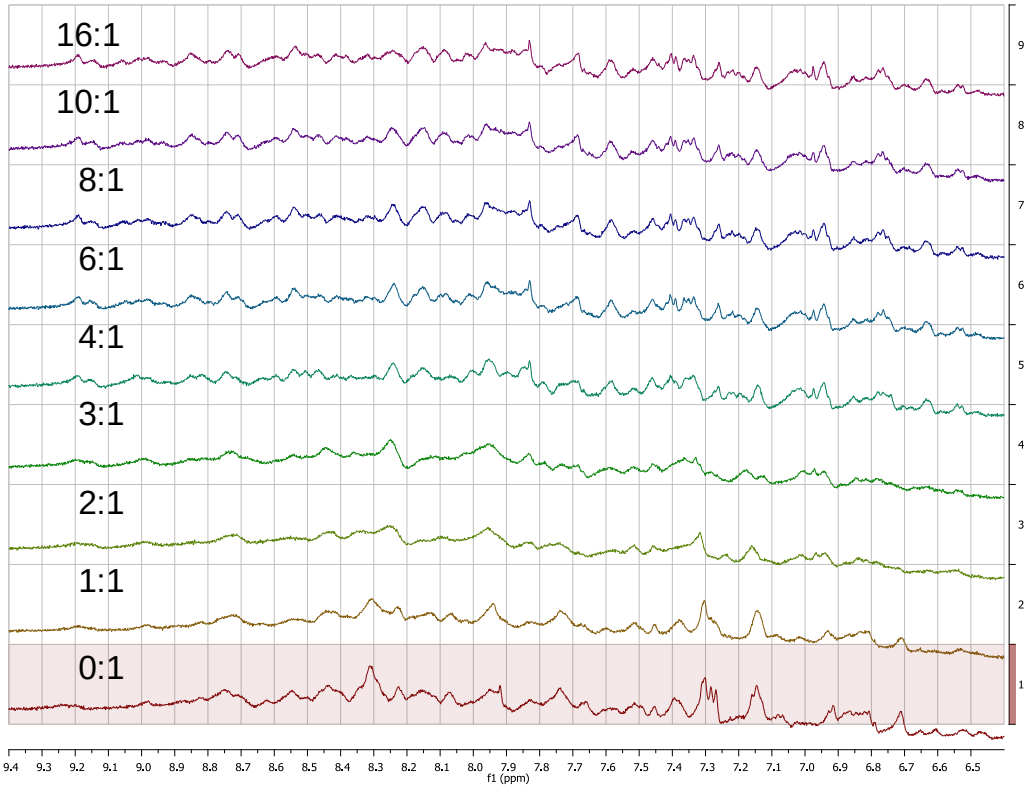

Figure 5.14 Ca^{2+} titration with 100 µM wt-CaM
The spectrum appears unchanged following addition of 4 ME Ca^{2+}, corresponding to binding in the four known EF-Hand binding sites.

It can be seen in the 1D spectrum for titration of Ca^{2+} with CaM (Figure 5.14) that chemical shift changes occur with the addition of 1-4 ME of Ca^{2+}, following which no further changes are observed up to 16 ME of Ca^{2+}. In contrast, chemical shift changes are observed with Pb^{2+} up to 6 ME of metal (Figure 5.12), which suggests that conformational changes occur with further addition of Pb^{2+}. These preliminary data suggest that Pb^{2+} binds not only in the known EF-Hand binding sites, but binds

opportunistically in secondary sites resulting in conformational changes not observed with the Ca^{2+}-bound state of CaM.

5.6 Assignment of CaM HSQC chemical shifts

From our HNCA spectra using ^{15}N-^{13}C-labeled CaM and HSQC assignments reported by Kuboniwa [268] we were able to assign most of the HSQC chemical chemical shifts for apo-CaM at pH 6.5 (Figure 5.15) and pH 7.4 (Figure 5.16, see Appendix for full list of assignments). From these spectra it can be seen that the pH difference had no significant impact on the chemical shifts observed.

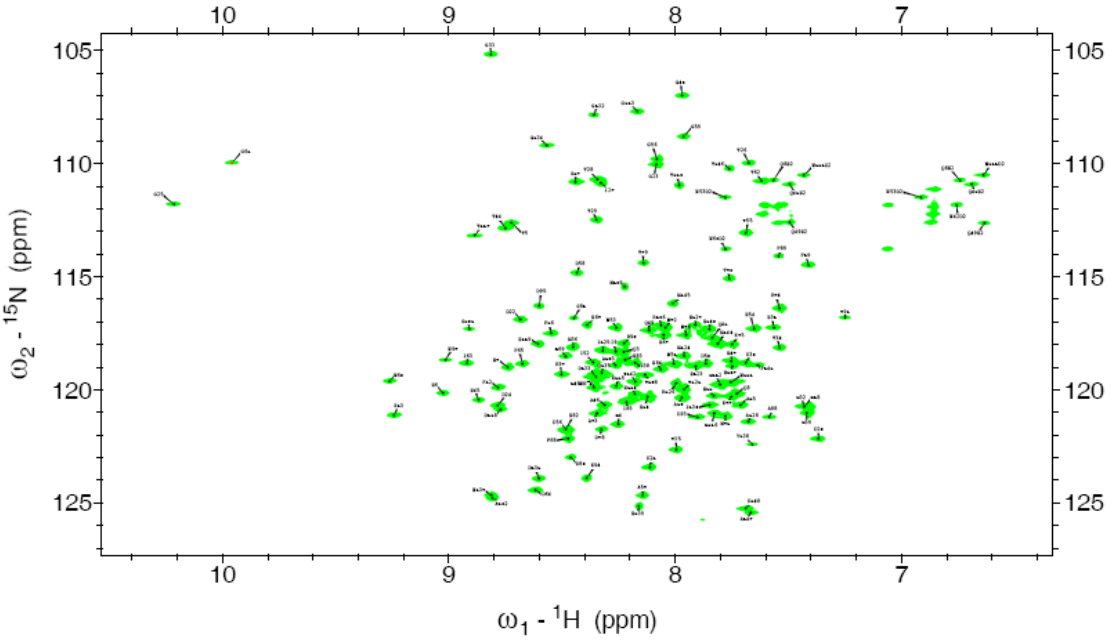

Figure 5.15 HSQC assignment of 1.0 mM apo-CaM at 37 °C, pH 6.5
Samples prepared in 0.1 mM NaN_3, 100 mM KCl, 10% D_2O, 10 mM EGTA

The chemical shifts for CaM presaturated with 6 ME Ca^{2+} (Figure 5.17), were assigned based on both HNCA experiments in our laboratory and assignments published by Torizawa [269]. Chemical shifts for glycine and hydrophobic residues that move downfield as a result of Ca^{2+}-binding in the EF-hand sites are circled in the spectrum of Figure 5.17.

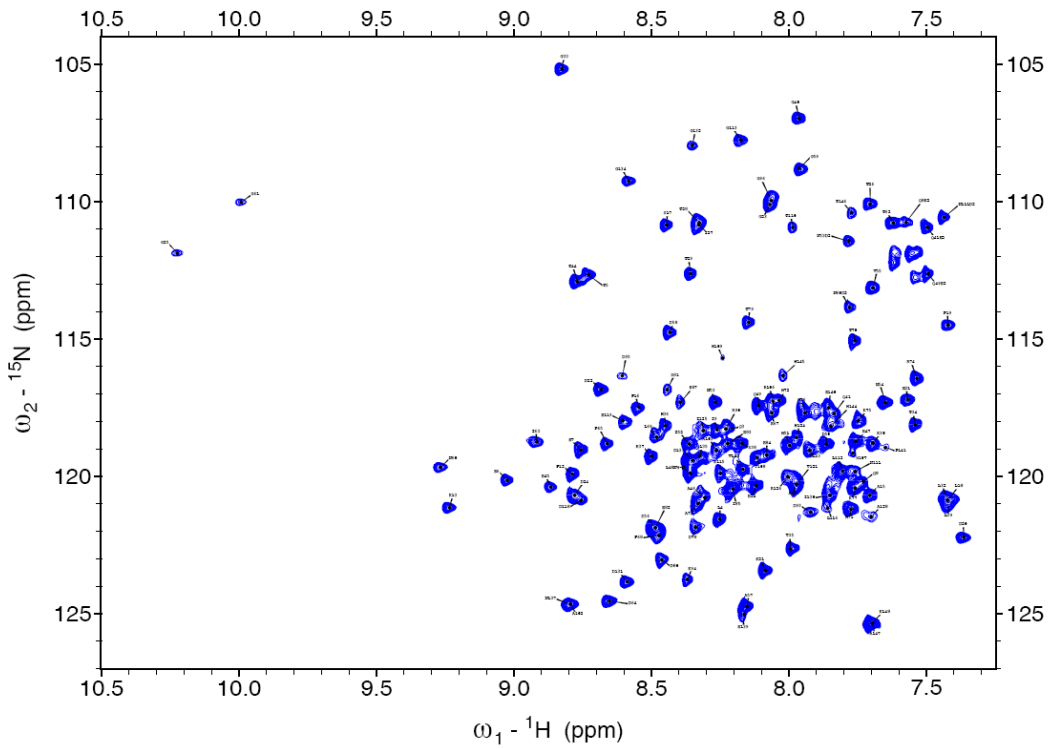

Figure 5.16 HSQC assignment of 1.0 mM apo-CaM, 37 °C, pH 7.4
Samples prepared in 10 mM TRIS, 100 mM KCl, 10% D_2O, 10 mM EGTA

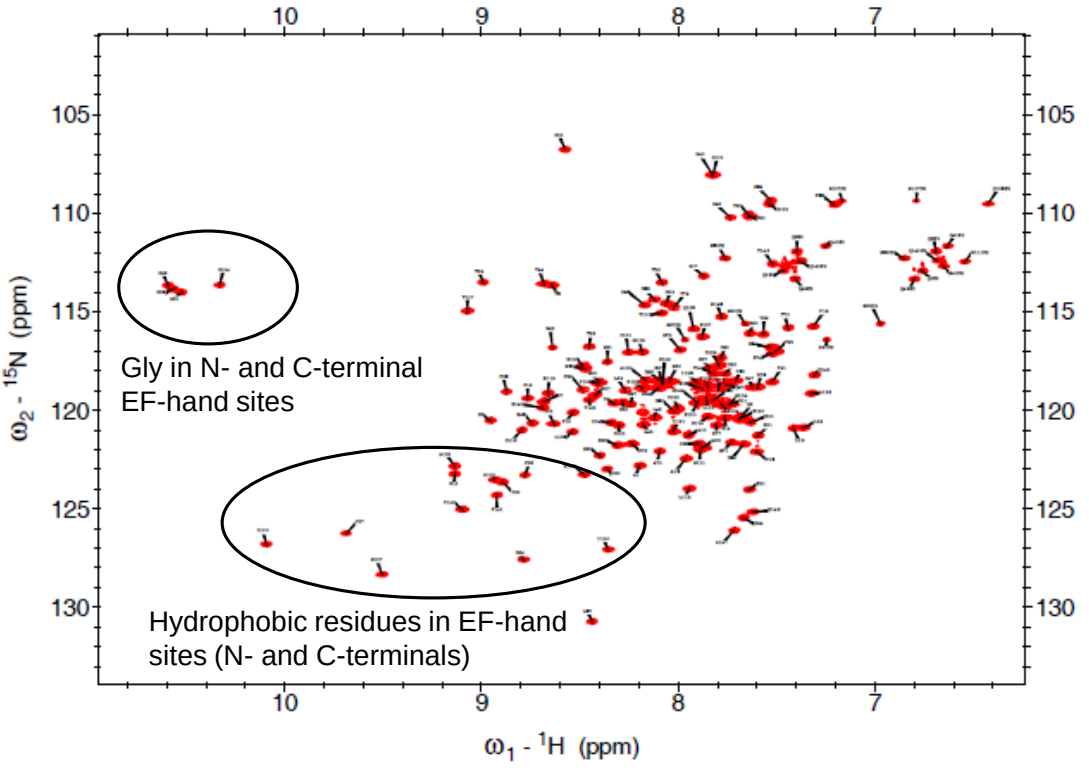

Figure 5.17 HSQC assignment of 400 µM Ca:CaM Complex (6:1), 37 °C, pH 6.6
Samples prepared in 10 mM Bis-TRIS, 0.1 mM NaN_3,100 mM KCl, 10% D_2O, 10 mM EGTA

5.7 HSQC spectra for CaM binding with Pb^{2+} and Ca^{2+}

Two sets of ^{15}N-HSQC Titrations were completed. In the first series, Pb^{2+} was directly titrated into CaM, up to 6 Molar Equivalents (ME). In the second series, Ca^{2+} was added to CaM up to 6 ME, followed by 3 additional ME of Pb^{2+}. Changes in the proton chemical shifts (Δδ) were calculated after all spectra were superimposed, referenced to a stable residue E6. A change in the chemical shift is considered significant if Δδ ≥ 0.050.

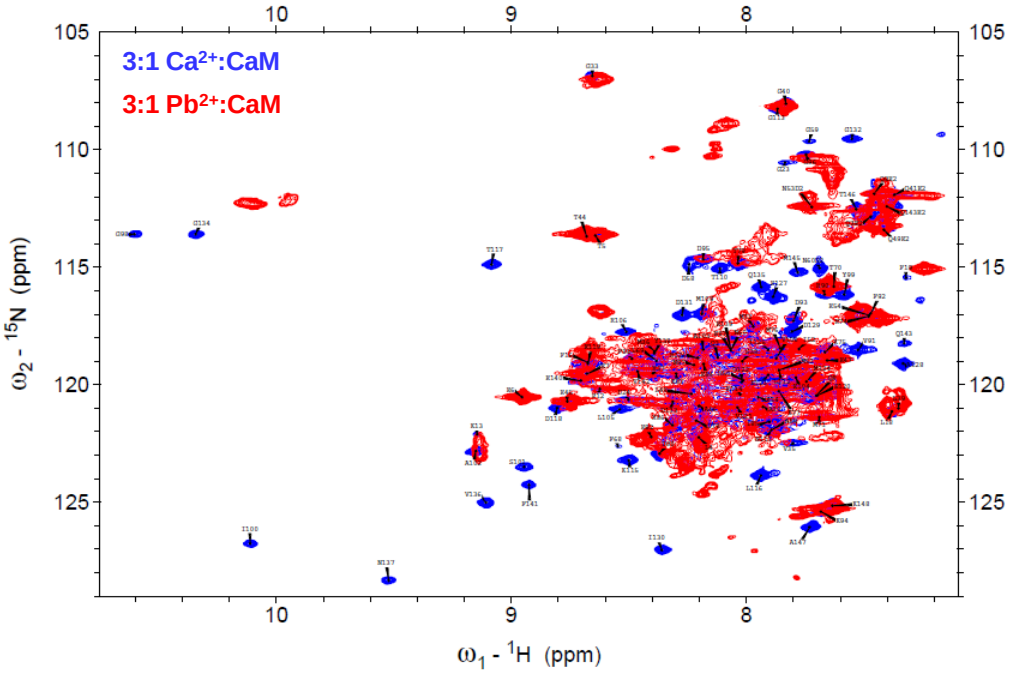

Figure 5.18 Overlaid HSQC spectra for CaM with 3 ME Ca^{2+} and 3 ME Pb^{2+}
Lack of structural homology between the Ca^{2+}- and Pb^{2+}-bound states is evidenced by the number of C-terminal domain residues in the Ca^{2+} spectrum lacking a corresponding peak from the Pb^{2+} spectrum.

Comparison of spectra for the addition of Ca^{2+} to apo-CaM, the addition of Pb^{2+} to apo-CaM, and the addition of Pb^{2+} to CaM presaturated with Ca^{2+} suggests that all three structures differ from one another. Overlaid spectra for CaM with 3 ME Ca^{2+} and 3 ME Pb^{2+} show significant loss of shift data, almost exclusively for residues in the C-terminal domain (Figure 5.18). Additionally, the overlaid spectra for holo-CaM with 3 ME Pb^{2+}, and apo-CaM with 3 ME Pb^{2+}, reveals that while Pb^{2+} alters the structural

conformation of holo-CaM, it does not produce structural changes identical to those observed in the absence of Ca^{2+} (Figure 5.19).

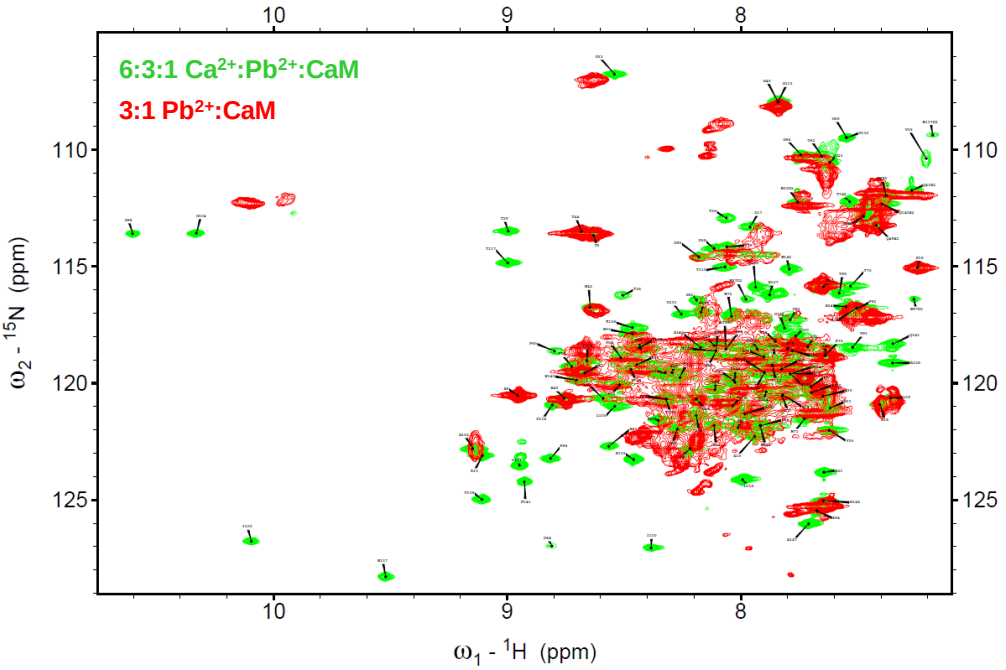

Figure 5.19 Overlaid HSQC spectra for CaM bound with 6 ME Ca^{2+} followed by addition of 3 ME Pb^{2+}
Lack of structural homology between Pb^{2+}-bound states in the presence and absence of Ca^{2+} is evidenced by the number of C-terminal domain residues in the dual ion spectrum lacking a corresponding peak from the Pb^{2+} spectrum.

5.8 Chemical exchange with addition of Ca^{2+} to apo-CaM

Analyses of spectra for the titration of Ca^{2+} to apo-CaM indicates a domain-specific differentiation in chemical exchange, consistent with results published by Jaren *et al.* for paramecium CaM [73].

At low concentrations of Ca^{2+} we observe both peak loss due to broadening associated with intermediate chemical exchange, and the emergence of coupled peaks as a result of slow chemical exchange (Figure 5.20a). These changes in the spectra contrast sharply with fast chemical exchange as seen with G59 and G23 (Figure 5.20b) indicating single, averaged peaks transient in the spectra in response to Ca^{2+}-binding. In Figure 5.20c we color-label the residues based on fast (blue), intermediate (purple) or

slow (red) chemical exchange, which demonstrates that slow and intermediate exchange occur almost exclusively in the C-terminal domain, with fast exchange observed primarily in the N-terminal domain. A summary of residues and their associated chemical exchange can be found in Table A.10 (Appendix).

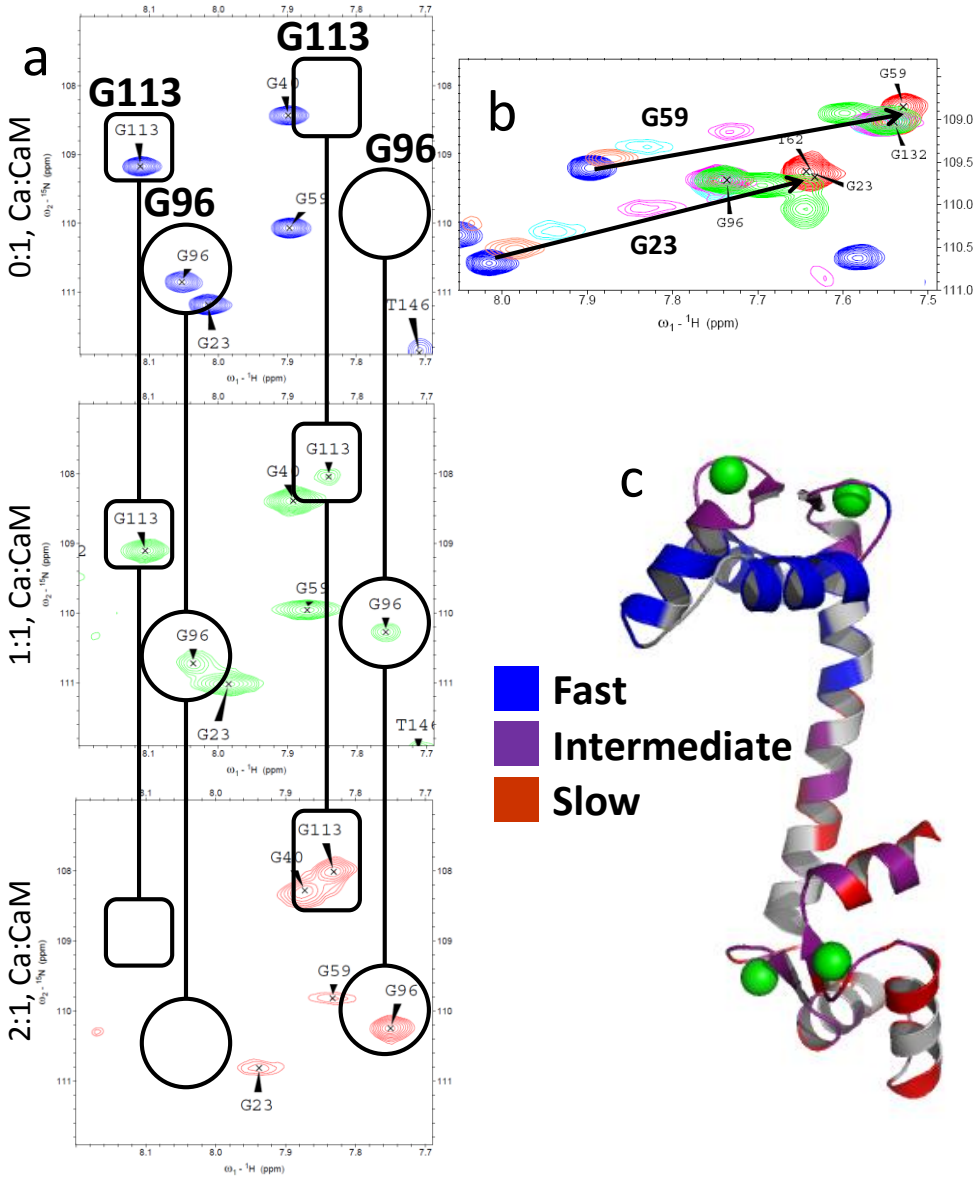

Figure 5.20 NMR chemical exchange in CaM
(**a**) Slow chemical exchange for G113 (rounded rectangle) and G96 (circle). Both residues display a single peak at 0 ME Ca^{2+}, with emergence of a second peak at 1 ME Ca^{2+}. At 2 ME Ca^{2+}, the original shift in each pair is undetectable. (**b**) Fast chemical exchange for G23 and G59. (**c**) CaM (3cln.pdb) with residues color-labeled to indicate fast (blue), intermediate (purple) and slow (red) chemical exchange.

The Jaren study [73] reported three important conclusions supported by our results: (1) The largest conformational changes associated with binding of Ca^{2+} were observed in the four EF-hand Ca^{2+}-binding sites; (2) the initial, slow exchange in the C-terminal domain sites indicated high affinity binding of Ca^{2+} occurred first in sites EF-III and EF-IV in the C-terminal domain; and (3) the variable exchange observed in the trans-domain linker region provided evidence of domain coupling.

5.9 HSQC chemical shifts reveal where Ca^{2+} and Pb^{2+} bind with CaM

By comparing the spectra from the Ca^{2+}-free to the Ca^{2+}-loaded states, the magnitude of the absolute chemical shift change (i.e., change in total distance across both the ^{1}H and ^{15}N dimensions from the initial δ values) reveals that the most significant changes occur for residues within the Ca^{2+}-binding sites (Figure 5.21a), while comparatively small changes are observed in the linker region. For the titration of Pb^{2+} to CaM, some loss of data is observed as a number of peaks observed in the Ca^{2+} spectrum fail to reappear following addition of Pb^{2+}. However, from the peaks that are assigned, it is clear that the same trend is observed with addition of Pb^{2+}, with the most significant changes observed only in the canonical EF-Hand sites (Figure 5.21b). We can also establish a relative order of occupancy for Ca^{2+} by (1) comparing total Δδ across both dimensions for successive points in the titration (Figure 5.22) or (2) plotting the order in which chemical shifts disappear relative to ME of Ca^{2+} added (Figure 5.23).

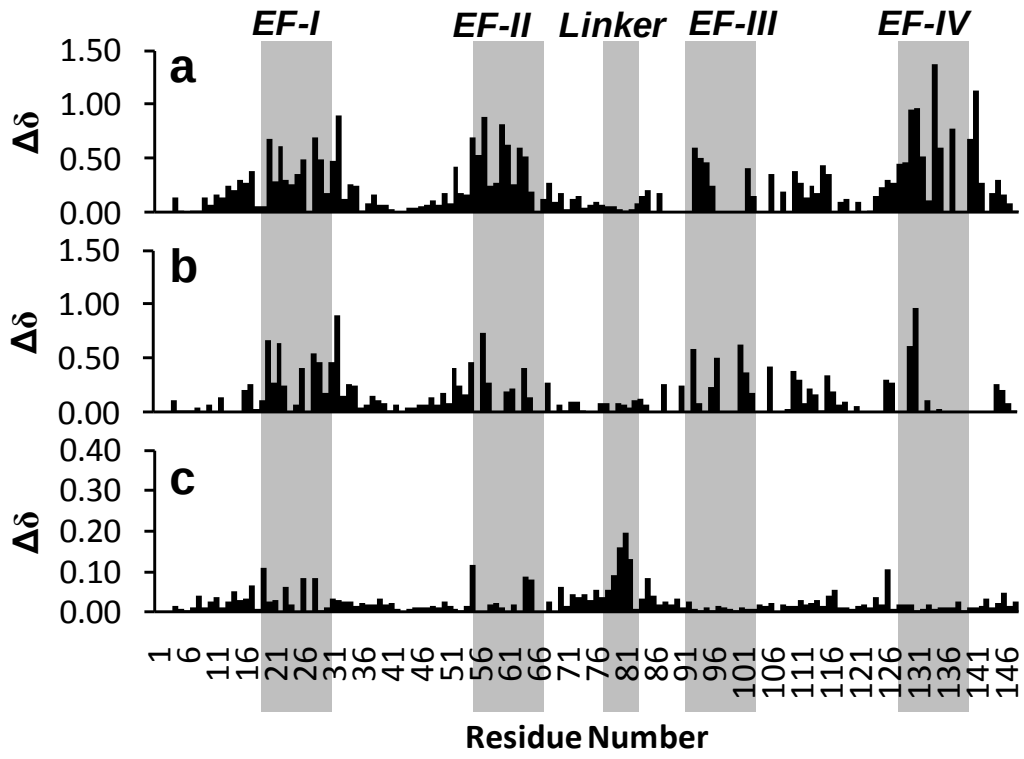

Figure 5.21 Weight-averaged Δδ in ^{15}N HSQC spectra for CaM titrations
The EF-Hand sites and the linker region in the sequence are highlighted in gray. (**a**) Titration of Ca^{2+} to apo-CaM. (**b**) Titration of Pb^{2+} to apo-CaM. Some loss of data is observed in (**b**) for addition of Pb^{2+}, however, in both graphs the highest magnitude Δδ is clearly observed for residues within the four EF-Hand Ca^{2+}-binding sites, with minimal change observed in the linker region. (c) Titration of Pb^{2+} to Ca^{2+}-loaded CaM. In (**c**) Pb^{2+} displaces Ca^{2+} in sites EF-I and EF-II, while the most significant structural changes occur in the linker.

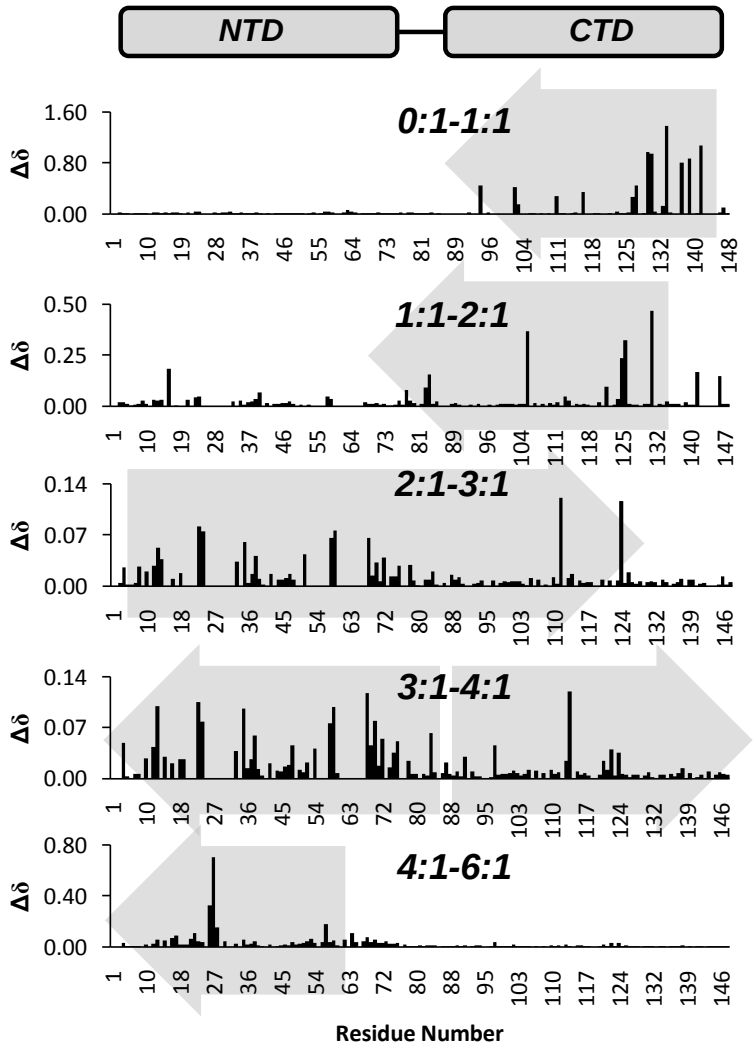

Figure 5.22 Absolute changes in δ between successive points in the titration of Ca^{2+} to CaM

Changes are expressed in molar ratios of Ca^{2+}:CaM (0:1-6:1). Viewed from top to bottom, Δδ values indicate binding of Ca^{2+} first in the C-terminal domain, followed by the N-terminal domain. Additionally, binding in one domain affects structural changes in the other. The gray arrows indicate direction of changes.

Based on the relative magnitude of the chemical shift changes between points in the titration in Figure 5.22, we can observe that Ca^{2+} first binds in the C-terminal domain followed by the N-terminal domain sites. Moreover, binding of Ca^{2+} in one domain is accompanied by structural changes in the opposite domain (i.e., domain coupling): Chemical shift changes from 0-2 ME Ca^{2+} (Figure 5.22), corresponding to binding in the C-terminal domain, also produces structural changes in the N-terminal domain.

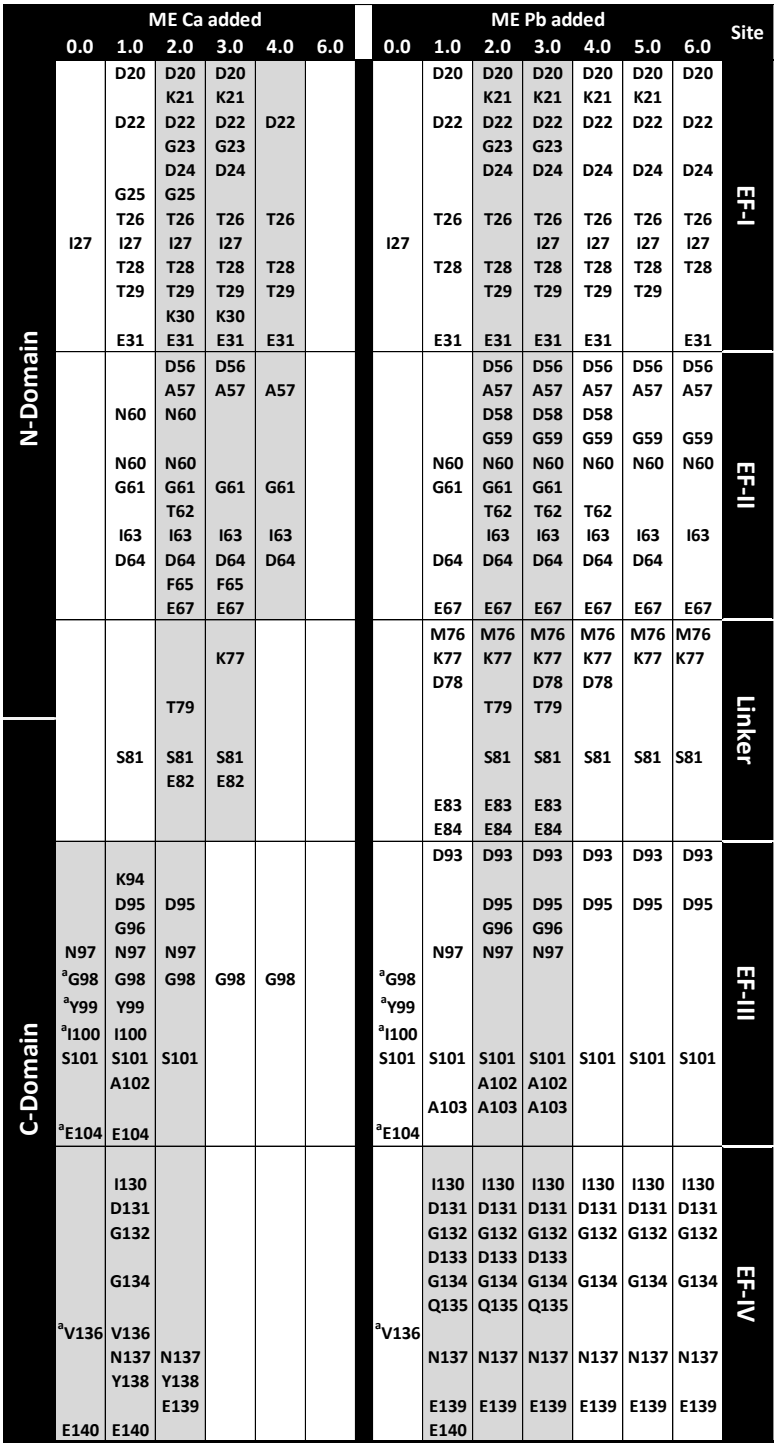

Figure 5.23 Chemical exchange effects by binding site

The order in which chemical shifts disappear and reappear as a function of metal concentration. For Ca^{2+}, δ peaks highlighted in gray disappear first in the C-terminal domain followed by the N-terminal domain, then reappear with increasing concentration of Ca^{2+}, showing the same trend observed with Δδ. For Pb^{2+}, δ peaks disappear first in site EF-IV, followed by concurrent disappearances in Sites EF-I through EF-III.

From 2-3 ME Ca^{2+}, more restructuring is observed in the N-terminal domain due to binding in either site EF-I or EF-II, but is still accompanied with changes in the C-terminal domain. From 3-4 ME Ca^{2+}, chemical shift changes indicate restructuring in both domains. Interestingly, the final, Ca^{2+}-saturated state of the protein was not observed until the addition of 6 ME of Ca^{2+}, as determined by comparison with a reference spectrum obtained for 400 μM CaM in 20 mM Ca^{2+} (Figure 5.17). Similarly, the disappearance of critical residues in each of the binding sites occurred in a domain-specific order (Figure 5.23) with δ peaks (highlighted in gray) disappearing first in the C-terminal domain followed by the N-terminal domain.

For Pb^{2+}, however, the order of occupancy could not be determined by analysis of Δδ which exhibited simultaneous changes in both domains (data not shown). However, from Figure 5.23 we observe the most significance disappearance of peaks first in site EF-IV, followed by nearly-concurrent disappearance of peaks for residues in sites EF-I through EF-III. This is consistent with results of fluorescence analysis indicating a single higher affinity Pb^{2+} site in the C-terminal domain with equivalent affinity for the three remaining sites.

5.10 Disappearance of chemical shifts associated with cooperative Ca^{2+}-binding

The addition of Ca^{2+} sufficient to saturate CaM produces a number of significant changes in the locations of chemical shifts. Shifts for I27, I63, I100 and V136 have been observed to move 4-8 ppm downfield in the spectra, and this shift movement (Figure 5.17) is related to cooperative binding between the paired binding sites in each domain [270]. While these changes are observed in our spectrum for Ca^{2+}-loaded CaM, they were not observed for binding of Pb^{2+}, which suggests that Pb^{2+} occupancy in the Ca^{2+}-binding sites may disrupt this intradomain cooperativity.

5.11 Pb^{2+} partially displaces Ca^{2+} in CaM, binds in secondary site in linker

Titrations of Pb^{2+} to CaM presaturated with 6 ME of Ca^{2+} produced changes in the chemical shifts not observed with direct addition of Pb^{2+} to apo-CaM. Overlaying the HSQC spectra reveals significant movement for key residues in or adjacent to the trans-domain linker region, specifically residues D78, D80, S81, E82, E83 and R86 (Figure 5.24a). Analysis of absolute Δδ values (Figure 5.21c) indicate displacement of Ca^{2+} by Pb^{2+} only in sites EF-I and EF-II, but not sites EF-III and EF-IV, as seen for residues G25 and G61 in Figure 5.24b, which disappear following the addition of 0.5 ME Pb^{2+}.

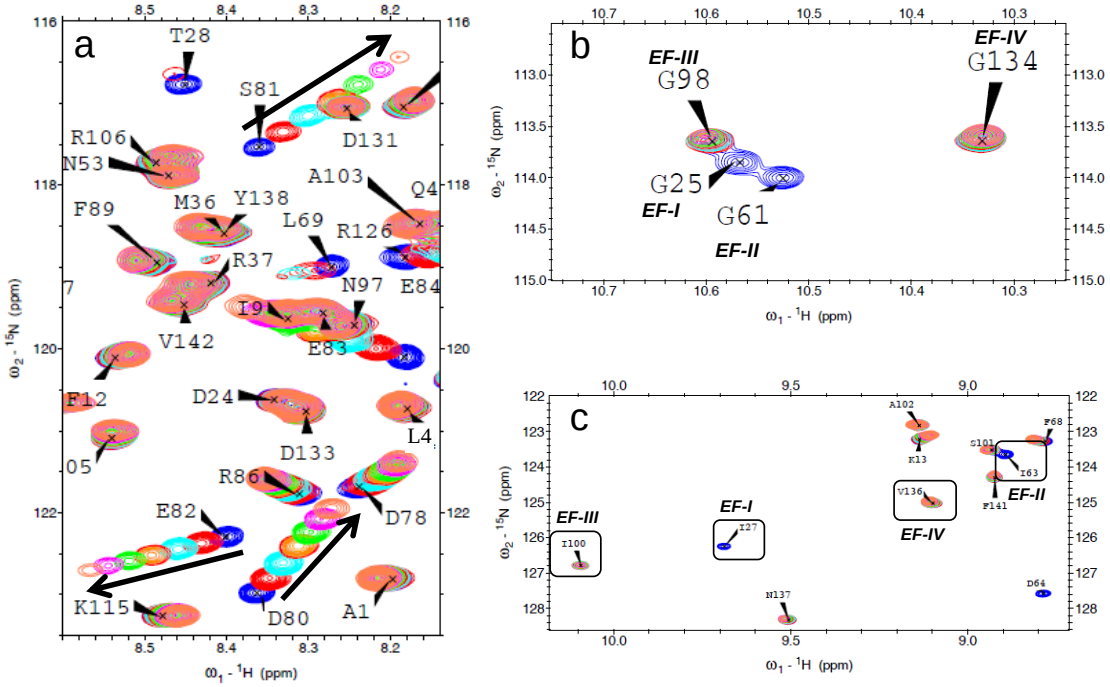

Figure 5.24 (a) Movement of HSQC chemical shifts for CaM bound with 6 ME Ca^{2+}
Pb^{2+} was titrated into Ca^{2+}-bound CaM in 0.5 ME increments up to 3 ME. Residues in the C-terminal domain exhibit stable chemical shifts, while significant changes are observed for residues D78, D80, S81, E82, E83 and R86, which suggests a potential Pb^{2+}-binding site in the linker region (74-82). (**b**) Residues in sites EF-I and EF-II, but not EF-III and EF-IV, disappear with addition of Pb^{2+} to Ca^{2+}: CaM complex. (**c**) Similar results are observed for residues I27 and I63 occupying position 8 in the EF loop regions of sites EF-I and EF-II only.

Additionally, chemical shifts for I27 and I63 disappear following addition of 0.5 ME Pb^{2+}, indicating loss of interdomain cooperativity (Figure 5.24c). However, shifts for

I100 and V136 remain visible in the spectrum. These results strongly indicate that Pb^{2+} displaces Ca^{2+} only in the N-terminal domain sites EF-I and EF-II.

5.12 Calculation of order parameter for CaM from relaxation studies

^{15}N-{^{1}H} NOE data acquired for Ca^{2+}-saturated CaM (Figure 5.25a) followed the same trends reported previously by Barbato et al [271] with increasing flexibility (i.e., less ordered secondary structure) apparent in the end termini, the central helix, and the small loop region separating sites EF-III and EF-IV.

Comparison of our NOE data between Ca^{2+}-loaded CaM in the absence (Figure 5.25a) or presence (Figure 5.25b) of 2 ME Pb^{2+} indicate increased flexibility in sites EF-I and EF-II, but loss of flexibility in the linker region. Additionally, NOE values for residues in sites EF-III and EF-IV, while exhibiting more variance in the Pb^{2+}-bound protein, do not indicate any significant change in these regions, further indicating that Pb^{2+} does not displace Ca^{2+} in these sites.

The calculated S^2 values for Ca^{2+}-loaded CaM in the absence (Figure 5.25c) or presence (Figure 5.25d) of 2 ME Pb^{2+} , are generally consistent with the NOE data. The absence of significant changes in residues in the C-terminal domain suggest that Pb^{2+} does not displace Ca^{2+} ions in the canonical binding sites. However, the disappearance of residues within sites EF-I and EF-II indicate dynamic changes associated with Pb^{2+} binding. A direct comparison of residues in the important linker region could not be made using the calculated S^2 values due to the loss of chemical shift data for either T_1, T_2 or NOE relaxation data.

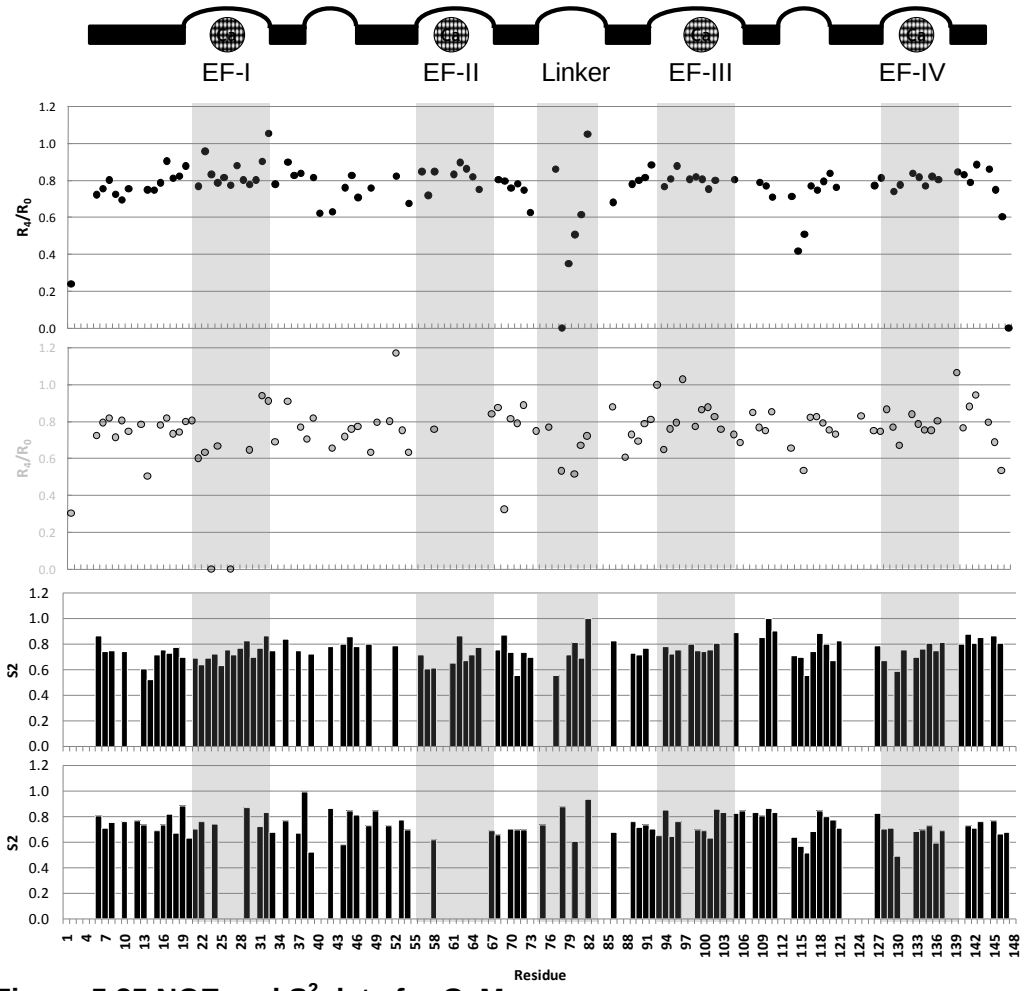

Figure 5.25 NOE and S^2 data for CaM
Comparison of NOE data for (**a**) Ca-CaM and (**b**) Ca-CaM with the addition of 2 ME Pb^{2+}. Helices, loop regions and Ca^{2+}-binding sites are identified above the plots. Pb^{2+} appears to displace Ca^{2+} in the N-terminal domain but not the C-terminal domain, with additional binding in the linker region. Comparison of S^2 data for (**c**) Ca-CaM and (**d**) Ca-CaM with the addition of 2 ME Pb^{2+}.

5.13 Discussion: CaM binding with Pb^{2+}

While previous studies have reported that CaM exhibits a relatively higher binding affinity for Pb^{2+} compared with Ca^{2+}, our data quantitatively distinguish between the two metals, clearly showing a much higher relative affinity (~8-fold) for Pb^{2+} over Ca^{2+} in the N-terminal domain with a smaller comparative increase (~3-fold) in the C-terminal domain (Table 5.1). The calculated K_d values are consistent both with reported values for Ca^{2+} and with known Ca^{2+} intracellular concentrations in the μM range.

Additionally, we report a previously unobserved biphasic response in the tyrosine fluorescence change associated with Pb^{2+}-binding. The initial tyrosine increase (Figure 5.8c), which resembles the Ca^{2+} response (Figure 5.8a) is interpreted as binding of Pb^{2+} in one of the two C-terminal domain EF-Hand sites, while the decrease in Phase II (Figure 5.8d) is interpreted as a structural change unique to Pb^{2+}-binding in the other site. This interpretation is consistent with our NMR chemical shift data suggesting initial occupancy of site EF-IV by Pb^{2+}, followed by concurrent occupancy of sites EF-I through EF-III, and with reports by Aramini [135] and Ouyang and Vogel [133] indicating that Pb^{2+} occupies all four EF-Hand sites concurrently and with equal high affinity.

Results of the analysis of HSQC data for Ca^{2+}-binding to CaM are consistent with previously published results, indicating cooperative pairwise binding of Ca^{2+} first in the C-terminal domain, followed by the N-terminal domain. Comparing our results with those reported by Jaren *et al.* for paramecium CaM [73], we observe a similar differentiation between fast and slow chemical exchange in the N-terminal domain and C-terminal domain, respectively.

For the direct titration of Pb^{2+} to Ca^{2+}-free CaM, we observe from the HSQC $\Delta\delta$ values that Pb^{2+} binds in the four EF-Hand binding sites, which was also reported in both the Aramini and Ouyang studies, and is observed in PDB crystal structures 1n0y.pdb and 2v01.pdb (Figure 1.4e and Figure 1.4g). The study by Ouyang and Vogel [133] reporting equivalent, high binding affinity between Pb^{2+} and the four EF-Hand sites was based on the disappearance of chemical shifts for G23, G59, G96 and G132 following addition of 1 ME of Pb^{2+}, and the disappearance of G25, G61, G98 and G134 at 2 ME of Pb^{2+} [133]. Comparing our results with those reported by Ouyang, we observed the disappearance of G61, G132 and G134 at 1 ME Pb^{2+}, followed by G23, G59, and G96 at 2 ME Pb^{2+} (Figure 5.23). However, shifts for residues G23, G61, and G96 reappeared in the spectra with increasing Pb^{2+} concentration, while shifts for residues G25 and G98

remained visible across the spectra. Additionally, only shifts for G25 and G61 disappeared following the addition of Pb^{2+} to Ca^{2+}-loaded CaM. The initial disappearance of residues G132 and G134 along with the majority of the loop residues (Figure 5.23) at 1 ME Pb^{2+} suggests binding first in site EF-IV, followed by a concurrent distribution of Pb^{2+} across sites EF-I through EF-III.

Although Pb^{2+} does occupy the EF-Hand Ca^{2+}-binding sites, it is also clear from the spectra (Figure 5.20) that Pb^{2+}-bound CaM exhibits structural differences compared with Ca^{2+}-bound CaM, as evidenced by the significant loss of spectral data for residues in the C-terminal domain. The extent to which the structure of Pb^{2+}-bound CaM deviates from Ca^{2+}-bound CaM is not yet known, however we can make some predictions based on our observations and results presented by others. A study by Chao *et al*. reported that Pb^{2+} exhibited a biphasic effect on the amount of phosphate transferred from [γ-^{32}P] ATP into MLCK, with stimulation observed at low concentrations followed by inhibition at higher concentrations [85]. Similarly, Habermann who observed that Pb^{2+}-bound CaM initially activates PDE with higher potency than Ca^{2+}, but increasing Pb^{2+} concentration subsequently inhibited CaM-dependent phosphorylation [88]. From these functional assays and our structural data, we suggest that at low concentrations of Pb^{2+}, the nearly-equivalent binding affinity of CaM for Pb^{2+} likely results in multiple complex conformers, one or more resembling the Ca^{2+}/CaM complex in form and function. With increasing Pb^{2+} concentration, CaM eventually adopts a conformation which inhibits the proteins function. The potential for complex speciation at low levels of Pb^{2+} is consistent with both Aramini [135] and Ouyang and Vogel [133] who observed binding in four EF-Hand sites at a 2:1 ratio of Pb^{2+}:CaM, while the inhibitory effects with increasing concentration are consistent with results reported by both Chao and Hambermann.

While useful information is acquired by addition of Pb^{2+} to Ca^{2+}-free CaM, the behavior of Pb^{2+}-binding to CaM in the presence of Ca^{2+}, as would be observed in a

cellular environment, provides us with more relevant data to understand the mechanism of Pb^{2+} toxicity at a molecular level. From our data we observed that the binding of Pb^{2+} in Ca^{2+}-loaded CaM results in the disappearance of residues exclusively in sites EF-I (D22, G25 and I27) and EF-II (D56, A57, G61, I63, and E67). Conformational change due to binding is further revealed in the movement of δ in the spectra (Figure 5.21), particularly in sites EF-I, EF-II, and the linker region, as plotted in Figure 5.21c. These results are closely-correlated with our analyses of NOE data and calculated S^2 parameters which indicate that the addition of Pb^{2+} to Ca^{2+}-loaded CaM results in a rapidly changing environment (e.g., increasing flexibility) in sites EF-I, EF-II, coupled with loss of flexibility in the linker region (Figure 5.25), while residues in sites EF-III and EF-IV appear unperturbed. Together, these data suggest that Pb^{2+} displaces Ca^{2+} only in the N-terminal domain sites EF-I and EF-II, and we can speculate that the positive cooperativity associated with Ca^{2+}-binding between the paired sites EF-III and EF-IV [76-77] in the C-terminal domain is sufficient to inhibit translocation of Pb^{2+} into the sites, while the 8-fold higher affinity of CaM for Pb^{2+} compared with Ca^{2+} in the N-terminal domain is sufficient for Pb^{2+} to displace Ca^{2+}.

The disappearance of δ for residues I27 and I63 (Figure 5.24c) may also indicate that binding of Pb^{2+} in sites EF-I and EF-II disrupts the intradomain cooperativity observed with Ca^{2+}-binding. These residues occupy position 8 in the EF-loop sequence. Previous NMR studies reported by Biekofsky *et al*. [270] indicated that Ca^{2+} binding with the loop position 7 ligand results in observed deshielding (+4 to +8 ppm) of the mainchain nitrogen in position 8 due to polarization of the O(7)=C(7)-N(8) amido group, which was used to monitor occupancy of Ca^{2+} in CaM, and provide evidence of cooperativity between the paired EF-Hand sites. This intradomain cooperativity observed between CaM EF-Hand binding site pairs in the presence of Ca^{2+} [76-77] is believed to be due to the formation of a short β-sheet between residues in position 8 of the paired

EF-Loops joining EF-I with EF-II, and EF-III with EF-IV [230-231]. In our HSQC spectra for titration of Pb^{2+} to Ca^{2+}-loaded CaM, peak loss for residues I27 and I63 due to intermediate chemical exchange is observed immediately upon addition of Pb^{2+}. A structural basis for this minor conformational change may be observed in the crystal structures of Pb^{2+}-bound CaM (1n0y.pdb and 2v01.pdb), where the T26 O^{γ} oxygen appears to rotate inward, placing it close enough (~3.5 Å) to the Pb^{2+} ion to serve as an active coordinating ligand in addition to the carbonyl oxygen utilized in binding of Ca^{2+} (Figure 5.26). This may be associated with changes in the orientation of I27 which alters the distance between atoms in I27 and I63 (Table 5.2) which could alter the hydrogen bonding network and disrupt the formation of the anti-parallel β-sheets between residues in position 8 of the EF-Loop joining EF-I with EF-II. From these data we infer that minor conformational changes associated with binding of Pb^{2+} in site EF-I could disrupt the intradomain cooperativity between the paired EF-Hands as well as reducing binding affinity [141].

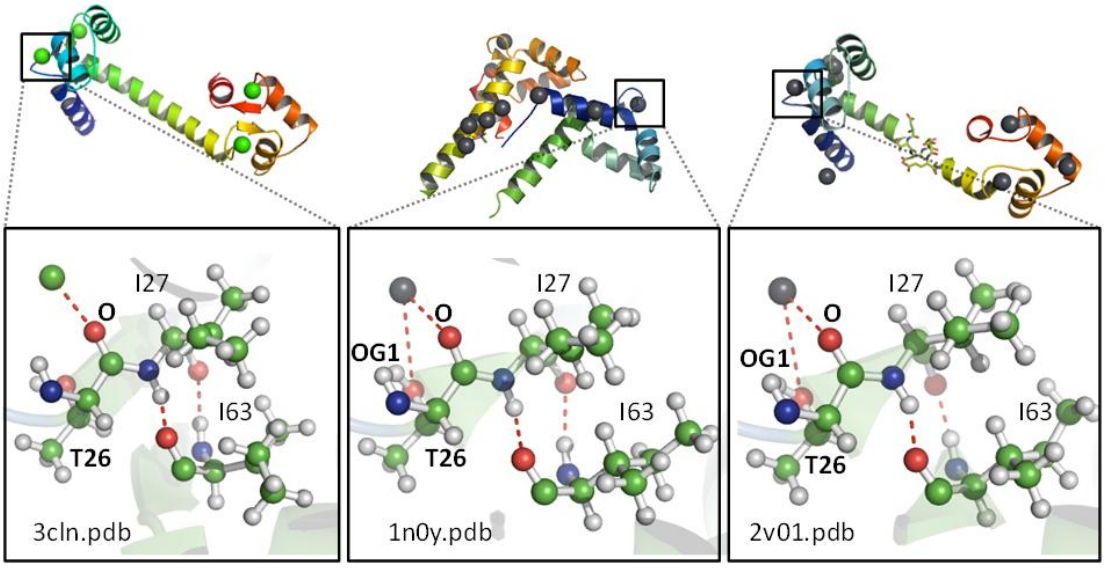

Figure 5.26 Crystal structure variations with CaM site EF-I
(**a**) Ca^{2+} is coordinated by the T26 carbonyl oxygen (red dashed line). PDB structures for Pb^{2+}-bound CaM (**b**) 1n0y and (**c**) 2v01 suggest that the T26 OG1 oxygen participates in the coordination of Pb^{2+} along with the T26 carbonyl oxygen, which may account for chemical shift differences seen with T26.

In addition to binding in the EF-Hand sites, the crystal structures of Pb^{2+}/CaM indicate binding of Pb^{2+} in regions of high electrostatic potential, including the trans-domain linker. This functionally-important region of CaM contains a string of oxygen-rich sidechains (DTDSEEE) in position 78-84. Results of our study demonstrate significant δ movement due to fast chemical exchange for residues in the linker with the addition of Pb^{2+} to the Ca^{2+}-bound protein (Figure 5.21c), but not with the addition of Pb^{2+} to Ca^{2+}-free CaM. This argues for a unique binding mode observed only when CaM initially adopts an active Ca^{2+}-induced conformer which prevents structural degradation in the C-terminal domain due to ionic displacement. Furthermore, Δδ values for residues in the linker exceed changes observed in sites EF-I and EF-II (Figure 5.21c), which suggests the potential for opportunistic binding of Pb^{2+} in this region of oxygen-rich sidechains.

Table 5.2 Calculated hydrogen bond and metal to ligand distances for CaM EF-I

		PDB ID		
		3CLN	**1N0Y**	**2V01**
Distance (Å)	**T26O-M**	2.45	2.67	2.56
	T26OG1-M	4.13	3.49	3.57
	I27O-I63NH	2.02	2.26	1.96
	I27NH-I63O	1.63	2.20	1.84

The potential for binding of Pb^{2+} in this region was summarized in a previous statistical analysis conducted in our laboratory which reported that Pb^{2+} can bind to carboxyl and hydroxyl groups in regions lacking defined binding geometries [136]. Although to date little evidence has been presented demonstrating metal-binding in this region, Kursula and Majava [272] reported a Ca^{2+}-binding site in the linker chelated by residues R74 and D78 in the crystal structure of Pb^{2+}-bound to human CaM. Additionally, two different prediction algorithms recently developed in our lab have predicted a Ca^{2+}-binding site in this region. An analysis of CaM with MUG^{SR}, which predicts Ca^{2+}-binding sites based on oxygen clusters with high sensitivity, revealed a potential site comprising

residues D80, E83, and E84 [273]. A similar analysis with MUG^{C}, a variation of MUG^{SR} which predicts Ca^{2+}-binding sites based on refined carbon clusters suggested a potential site comprising residues D2, M76, K77, and D80, which would be possible if the two domains were brought together. Further support is provided by Bertini *et al* [90] who reported a potential metal-binding site in this region based on the disappearance of chemical shifts in the linker (78-81) following addition of 0.3 equivalents of Yb^{3+}, and Raos and Kasprzak who suggested the existence of two secondary binding sites occupied by Ni^{2+} in the Ca^{2+}-bound state [274].

Arguments for this unique, Ca^{2+}-potentiated binding mode for Pb^{2+} are provided by Mills and Johnson who reported that Pb^{2+} and other metals may bind to Ca^{2+}-bound CaM in secondary sites forming an allosterically potentiated conformer [59]. Additionally, Kern *et al* demonstrated that inorganic Pb^{2+} and Ca^{2+} can interact positively to activate CaM [83] while Shirran and Barran reported that Pb^{2+} affinity for CaM increases relative to other divalent cations in the presence of Ca^{2+} [84]. These results suggest that this observed opportunistic binding of Pb^{2+} is dependent upon Ca^{2+}-induced restructuring of CaM, as would be observed in an intracellular environment.

It is also possible that the observed changes in the linker only reflect structural changes induced by binding in some region of the protein more distant from the linker. The Pb-CaM structure reported by Kursula and Majava [272] depicts binding of Pb^{2+} between sidechain carboxyl groups from D118 and D122 (Figure 5.27), and significant chemical shift changes (>0.05δ) are observed in our data for residues T117 and R126 (Figure 5.21c) as a result of Pb^{2+}-binding. The sequence 117-123 comprised of residues TDEEVDE (Figure 1.4a) also represents a grouping of carboxyl-rich sidechains that could potentially bind Pb^{2+}. However, unlike the proposed binding sites in the linker, these residues are all found in an α–helical structure. If binding were confined to residues D118 and D122, the secondary structure could remain intact, but it is not clear

how binding in this region would induce major conformational changes in the linker region unless the helix itself were to lose its structure, which was not indicated in the analysis of our dynamic NMR data. Also, the biphasic fluorescent response observed (Figure 5.8d) could relate to binding of Pb^{2+} in a secondary site in the C-terminal domain, however, this can only be clarified with further study.

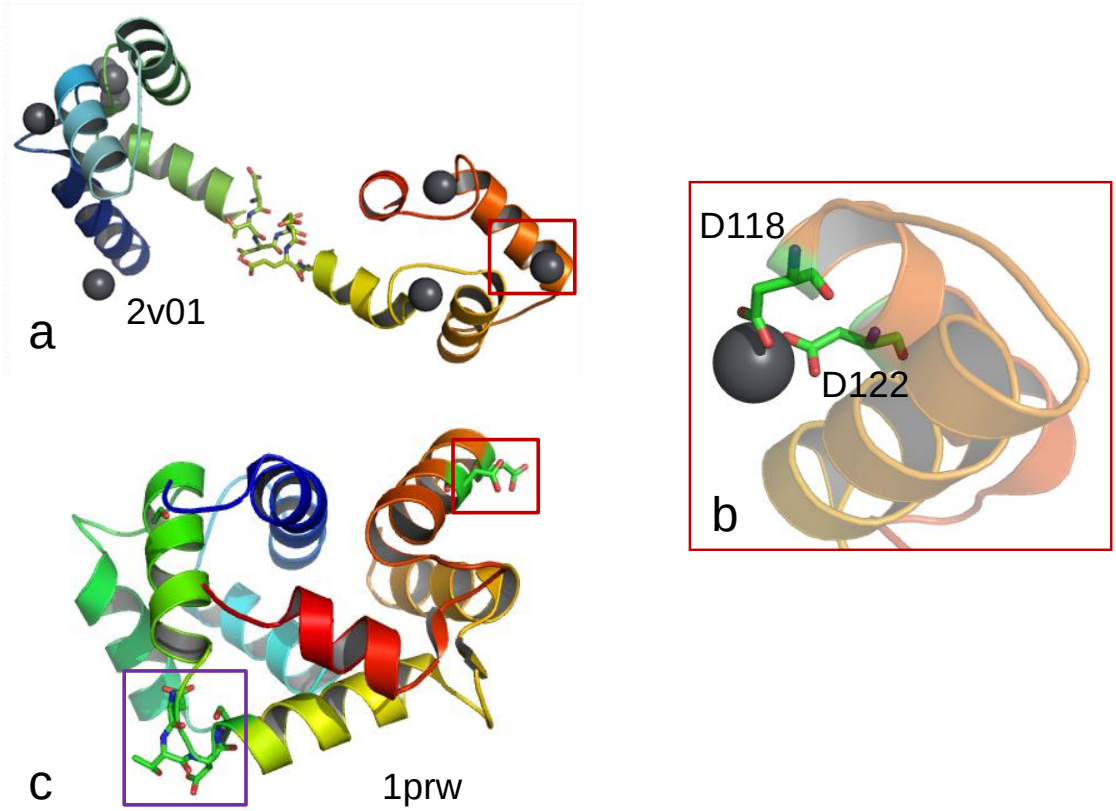

Figure 5.27 Potential Pb^{2+} site in CaM C-terminal
(**a**) Binding of Pb^{2+} ions in CaM (2v01.pdb). The additional C-terminal binding site is highlighted in the red box. (**b**) Closer view of binding site showing orientation of carboxyl groups from D118 and D122. (**c**) Position of binding site ligands (red box) relative to trans-domain linker region (purple box) in the compact structure of CaM.

5.14 PFG Diffusion NMR reveals dimerization of Pb^{2+} CaM at 6 ME Pb^{2+}

Translational motion of the protein in solution was evaluated for Pb^{2+}:CaM complexes using PFG NMR. The calculated hydrodynamic radius (r_{CaM}) for the Pb^{2+}:CaM complex at 4:1 was 22.0 Å (Figure 5.28). This was not significantly different than values

similarly measured in our lab for Ca^{2+}-free CaM (22.4 ± 0.3 Å) and Ca^{2+}-loaded CaM (22.8 ± 0.5 Å). However, it is possible that CaM bound with 4 ME Pb^{2+} adopts a more compact structure which would be consistent with results published by Dowd for Pb^{2+}-binding with the Ca^{2+}-binding protein osteocalcin [275], and with a recently-reported compact structure of CaM [276] (Figure 5.29).

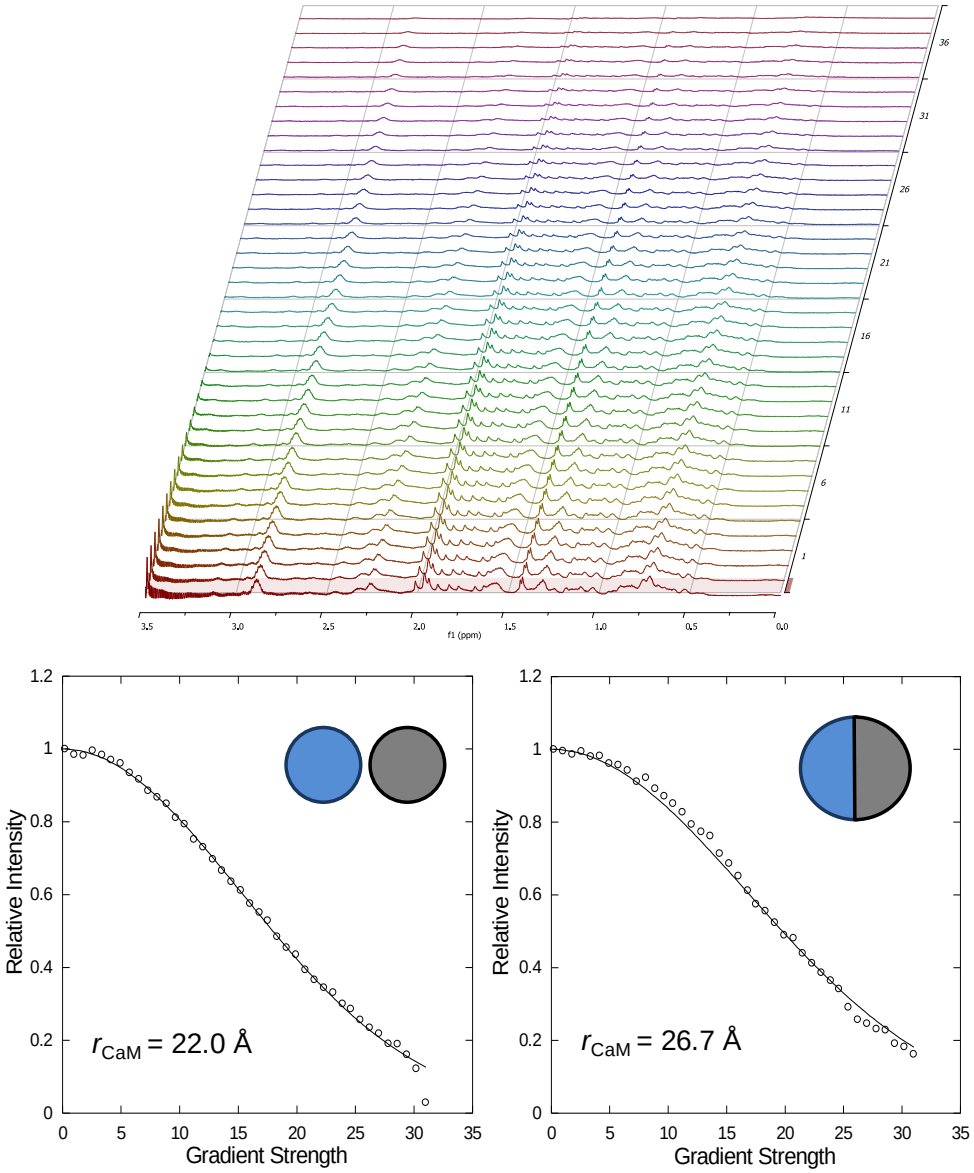

Figure 5.28 PFG experiment
(Top) PFG spectrum for Pb-CaM at 25 °C. (Bottom Left) Diffusion plot based on Eq. 19 for CaM with 4 ME Pb^{2+} (Bottom Left), and 6 ME Pb^{2+} (Bottom Right).

Additionally, for the Pb^{2+}:CaM complexes at 6:1 (Figure 5.28), r_{CaM} was calculated to be 26.7 Å. The theoretical value for the radius *R* of a dimer using Eq. 22, with r_{CaM} = 22.0 Å was 27.7 Å, indicating that Pb^{2+}:CaM oligomerizes at 6:1, likely in the form of a dimer. This is consistent with line broadening observed in both 1D and 2D HSQC spectra at 6-8 ME Pb^{2+} added to CaM, and could be explained by loss of flexibility in the linker region and the resulting compaction of the tertiary structure.

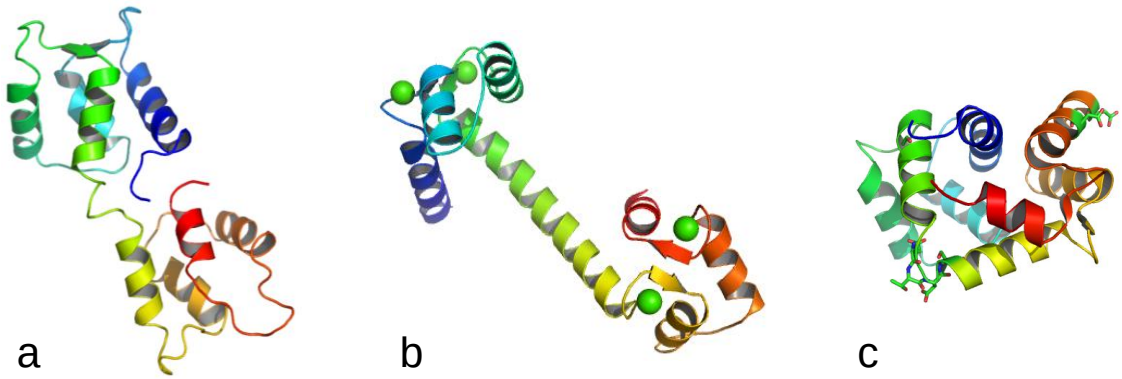

Figure 5.29 Comparison of CaM structures
(a) Apo form (1cfc.pdb), **(b)** calcium-loaded form (3cln.pdb), and **(c)** Compact form (1prw.pdb) of CaM. Binding of Pb^{2+} suggests a structure more similar to that seen in **(c)** than in **(b)**.

These data and calculations support the conclusion that Pb^{2+} causes CaM to oligomerize at 6 ME of Pb^{2+}. While this has not been verified in the case where Pb^{2+} is added to Ca^{2+}-loaded CaM, it does suggest a potential mechanism by which the introduction of Pb^{2+} may induce toxicity at the molecular level when present in low concentrations.

5.15 Opportunistic binding of Pb^{2+} to Ca^{2+}/CaM complex

Based on our current results, we propose a mechanism to explain binding of Pb^{2+} to Ca^{2+}-loaded CaM (Figure 5.30) as would be observed in an intracellular environment. In Figure 5.30 we initially illustrate the cooperative pairwise binding of Ca^{2+} in the C-terminal domain, following by similar response to increasing Ca^{2+} in the N-terminal

domain. In this state, the central linker region interconverts between a random coil and an extended helix, and this flexibility allows CaM to interact with target ligand molecules.

The introduction of Pb^{2+} in this environment results in displacement of Ca^{2+} in sites EF-I and EF-II, followed by opportunistic binding which alters the conformation of the central linker region, thus inhibiting the ability of CaM to bind other molecules.

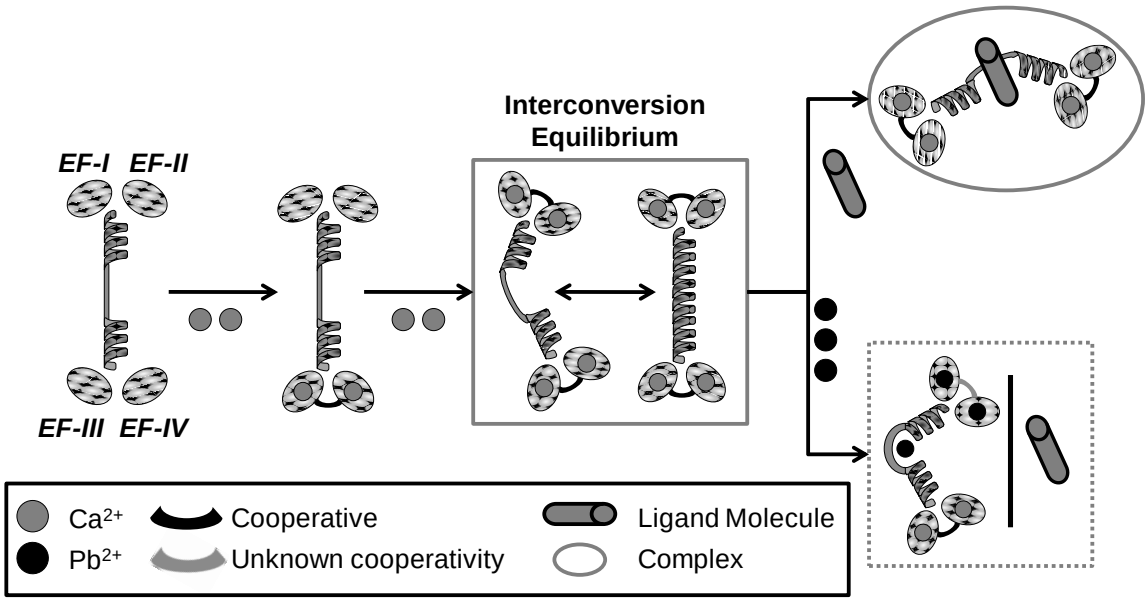

Figure 5.30 Model of Pb^{2+}-binding to holo-CaM
Calcium binds with intradomain cooperativity first in the C-terminal domain sites, followed by the N-terminal domain. The linker region of Ca^{2+}-loaded CaM interconverts between a flexible random coil and an extended helix. Pb^{2+} added to Ca^{2+}-loaded CaM binds in the N-terminal domain sites and potentially the linker region. Conformational changes in the linker region inhibit the ability of CaM to bind target ligand molecules.

5.16 Conclusions: CaM binding with Pb^{2+}

In the Ca^{2+}-free state, CaM appears to bind Pb^{2+} with an ~8-fold higher affinity than Ca^{2+} in the N-terminal domain. The biphasic Tyrosine fluorescent response suggests that one of the paired EF-Hand sites in the C-terminal domain binds with 3-fold higher affinity than Ca^{2+}, and that the affinity of the second site is very similar to that for the N-terminal domain sites. This conclusion is further supported by analysis of HSQC δ values which indicated binding of Pb^{2+} in site EF-IV followed by concurrent binding in

sites EF-I through EF-III, based on the disappearance of peaks due to broadening effects related to chemical exchange.

More importantly, the addition of Pb^{2+} to Ca^{2+}-bound CaM does not follow an exclusive displacement mechanism. While Ca^{2+} appears to be retained in the C-terminal domain sites, the addition of low concentrations of Pb^{2+} initiates replacement of Ca^{2+} in the N-terminal domain sites resulting in more pronounced conformational changes, as indicated by changes in NMR HSQC chemical shifts and NOE data analysis. These changes in the trans-domain linker region may be coupled with binding of Pb^{2+} in the oxygen-rich linker itself. The biphasic Tyr fluorescence response suggests either the presence of one or more secondary Pb^{2+}-binding sites in the C-terminal domain, or may be related to the same changes observed by phenylalanine fluorescence in the N-terminal domain.

This mechanism results in significant conformational changes to the linker, observable at low concentrations of Pb^{2+} in the HSQC spectrum. If binding of Pb^{2+} produces similar effects to those observed with osteocalcin [275], increasing Pb^{2+} concentration presumably produces a more compact or dynamically-restricted conformer incapable of binding properly with target ligand molecules. The apparent dimerization of CaM in the presence of increasing Pb^{2+} concentration further supports this conclusion.

Moreover, our NMR results indicate that while Pb^{2+} may displace Ca^{2+} in site EF-I in the N-terminal domain, there is no indication that Ca^{2+} is displaced in either site in the C-terminal domain, suggesting that positive cooperativity between these paired sites for Ca^{2+} sufficiently inhibits translocation by Pb^{2+}, despite the apparent higher binding affinity for Pb^{2+} relative to Ca^{2+}.

Furthermore, the NMR results indicate that binding of Pb^{2+} in secondary binding sites, either alone or in conjunction with binding in site EF-I and possibly EF-II, allosterically produce conformational changes sufficient to alter the function of CaM.

These changes are apparent with the addition of 1-2 ME Pb^{2+} in Ca^{2+}-saturated states, and coupled with the apparent stable occupancy of Ca^{2+} in the C-terminal domain sites, would explain results reported by both Chao [85] and Habermann [88] showing a concentration-dependent activation followed by inhibition of CaM relative to downstream enzyme activity, as well as results reported by Kern [83] showing that Pb^{2+} and Ca^{2+} can interact positively to activate CaM.

The positive cooperativity reported between EF-Hand sites in each CaM domain as a result of Ca^{2+}-binding is not apparent for binding of Pb^{2+}, while the equivalent affinity model proposed by Ouyang [133] does not account for an additional, induced binding sites. The role of CaM in Pb^{2+} toxicity requires further clarification, however, the results of this study demonstrate that Pb^{2+} can adversely impact the conformation of CaM even in the Ca^{2+}-bound state, and provides evidence that molecular toxicity may be induced in CaM or other proteins as a result of binding opportunistically in secondary sites outside of known metal-binding sites. This allosteric mechanism suggests that the nature of Pb^{2+} allows for multiple molecular targets and by extension offers a comprehensive explanation for the resulting systemic pathology of Pb^{2+} toxicity.

6 Preliminary investigations of RNT metals

6.1 Selection of metals

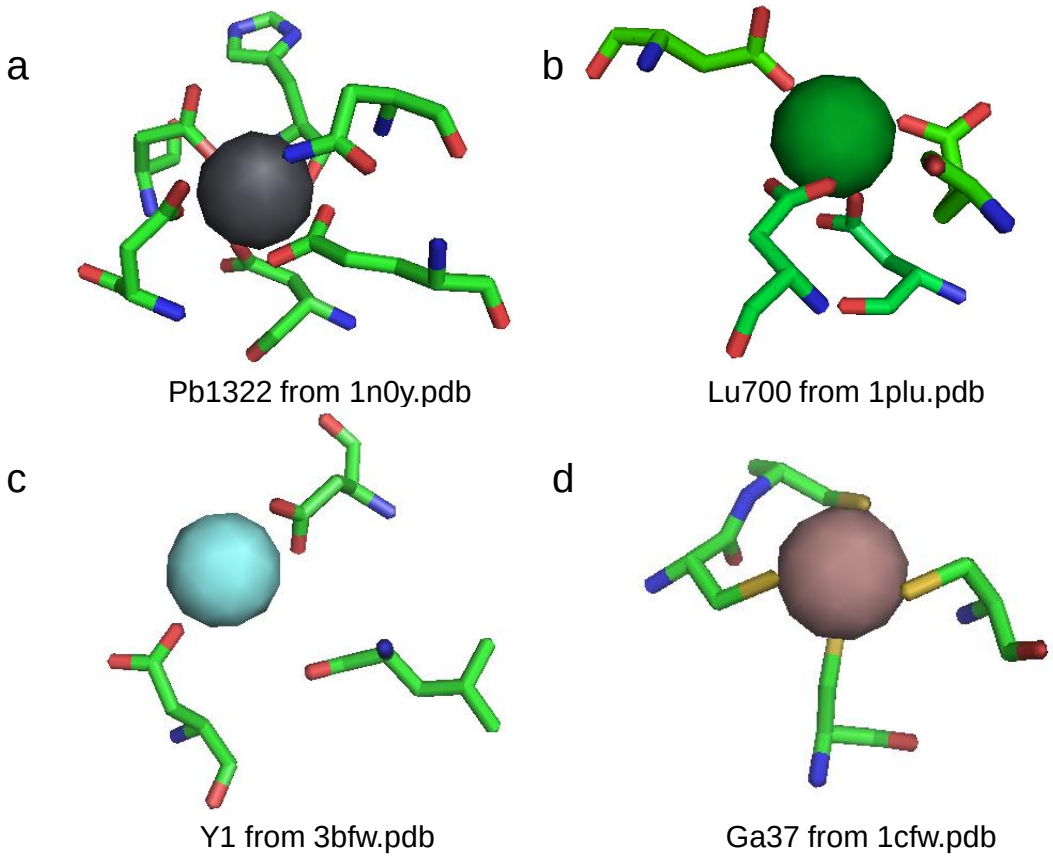

Figure 6.1 Binding sites of non-essential metals
(**a**) Pb^{2+} binding in a Ca^{2+}-binding site from calmodulin (1n0y.pdb). (**b**) Lu^{3+} is expected to behave similarly to Gd^{3+} and Tb^{3+}, binding in oxygen-rich sites as seen in 1plu.pdb. (**c**) Binding of Y^{3+} in 3bfw.pdb appears to involve less structure than the other metals. (**d**) Ga^{3+} from 1cfw.pdb occupies a a Cys-rich site consistent with observed Zn^{2+} sites.

Of the ions identified as potentially useful radionuclides in our preliminary review of the literature, significant data was obtained from the PDB only for Pb^{2+}. While the molecular toxicity of Pb^{2+} renders it less than ideal as a candidate for beneficial therapy, the strong binding affinity of Pb^{2+} for Ca^{2+} binding sites is clearly advantageous, and it is likely that it can be further enhanced to form stable complexes with rapid binding kinetics, based on previous observations reported in our laboratory. Of the remaining metals, data was available only for Lu^{3+}, Y^{3+} and Ga^{3+}. Examples of protein binding for

these four ions are seen in Figure 6.1. Despite its potential for metal toxicity, Pb^{2+} is an attractive candidate for radioimmunotherapy for several reasons, assuming the ions can be rapidly removed from the patient following therapy. This can most likely be achieved with current EDTA therapies, although further research is necessary to validate this assumption. For Pb^{2+} (Figure 6.1a), previous research completed in our laboratory has demonstrated that that Pb^{2+} will readily displace Ca^{2+} and occupy Ca^{2+} binding sites with high affinity in an isolated binding site on a scaffold protein (Figure 5.5), exhibits high EN (Table 1.1), and exhibits nearly-instantaneous binding kinetics. Additionally, Pb^{2+} radioisotopes may act as both β^- - and α-emitters, which suggests it may be possible to develop radionuclide "cocktails" capable of providing simultaneous, dual decay therapy. However, in additional to the primary risk associated with radiation and the secondary risk of molecular toxicity, the potential for opportunistic binding of Pb^{2+} in regions outside the binding motif on the targeting structure or with incidental contact between other proteins may be a concern.

With the exception of La^{3+}, several lanthanides studied in our laboratory have been observed to occupy Ca^{2+}-binding sites, albeit with affinities lower than that observed for Pb^{2+}. The binding site for Lu^{3+} (Figure 6.1b) is consistent with behavior observed for Gd^{3+} and Tb^{3+}, suggesting the engineered proteins already developed in our laboratory may be modified to provide a strong chelator for this β^- -emitting radionuclide.

Data available for Y^{3+} was limited in the PDB, and the few structures available suggested incidental binding, rather than occupancy of a well-structured site, as seen in Figure 6.1c. This β^- -emitting radionuclide is non-imageable, requiring the concurrent use of In^{3+} dosimetry if imaging is required. Despite this limitation, Y^{3+} is also a good candidate for protein-based radioimmunotherapy due to its previously-noted capacity to deliver high dosage radiation, and its chemical properties noted in Table 1.1.

Data from the PDB suggests that Ga^{3+} can occupy Cys-rich sites in a geometry similar to some Zn^{2+}-binding sites, and as seen in Table 1.1, the ionic radius of Ga^{3+} is closer to that of Zn^{2+} than Ca^{2+}. To evaluate this, the design of grafted Zn^{2+} motifs is proposed, again using protein constructs developed in our lab.

No protein data was available for Bi^{3+}, the only α-emitter listed in Table 1.1. However, as seen in Table 1.1, Bi^{3+} exhibits strong EN (2.02) and has an ionic radius very similar (1.03 Å) to that of Ca^{2+} (0.99 Å). Based on its physical and chemical properties, it is reasonable to assume binding of Bi^{3+} will be similar to that of Pb^{2+}. Unlike Pb^{2+} which appears to bind very rapidly, complex formation between Bi^{3+} and current radioimmunotherapy chelators is nearly as long as the half-lives, as previously discussed. In this respect, it is possible that a protein-based chelator may provide a more stable complex for Bi^{3+} with improved binding kinetics.

6.2 PAR assay

To establish the stoichiometry of metal:CaM complex formation, work was completed to develop a modified colorimetric assay using 4-(2-pyridylazo)resorcinol (PAR) (Sigma-Aldritch, St. Louis, MO) for the detection of Pb^{2+} and various lanthanides. As reported by McCall and Fierke [277], this method provides a rapid means for quantifying micromolar concentrations of transitions metals, when PAR forms a 2:1 complex with the metal, resulting in a decrease in the dye's absorbance at 410 nm.

Carbonic anhydrase (CA), a Zn^{2+}-binding protein with a single binding site was used to first bind the transition metal. Following removal of free metal ions in solution, the protein was digested with protease K, and PAR was then added to the solution to complex with the available ion of interest. Comparison with a standard curve of the PAR:metal complex provides a cost-effective and rapid method for determining the metal concentration in solution.

PAR was selected for optimization of a colorimetric assay to evaluate the stoichiometry associated with the binding of Pb^{2+}, Gd^{3+} and other toxic metals to CaM. A 5 mM solution of PAR was prepared according to procedures described by Hunt and Ginsburg [278]. Briefly, solid PAR was dissolved in ddH_2O while adding 1 N KOH to maintain pH at 8.8. It should be noted that some particulate remained in solution.

As the control, 29 mg of bovine CA (92% pure, Sigma, from bovine erythrocytes, MW = 28980 g/mol), was dissolved in 10 mL ddH_2O to a final concentration of 100 µM. CA has an apparent extinction coefficient of 56, 000 cm^{-1} M^{-1}.

The response of PAR to both Zn^{2+} and Pb^{2+} was first evaluated, and linear regression analyses conducted to determine standard curves. The analytical matrix was comprised of 10 mM Tris (pH 7.4, treated with chelex to remove background metals), 1.0 mg protease K, and 5 mM IAM (Sigma Ultra Iodoacetamide (Sigma-Aldritch, St. Louis, MO)). Zn^{2+} and Pb^{2+} were obtained from analytical grade $ZnCl_2$ and $PbCl_2$, respectively.

From the procedures described by McCall, several modifications were introduced to work with CaM. DTT, used to prevent disulfide bond formation in CA, was found to interfere with CaM in preliminary testing, and had to be removed. Iodoacetamide also appeared to exert an inhibitory effect, but it was negligible compared to DTT, and did not prevent quantitation of the metal ions.

To evaluate Zn^{2+} and Pb^{2+} using PAR, solutions of 50 µM protein were prepared in 10 mM Tris buffer, pH 7.4. CaM, which is treated with $CaCl_2$ during purification, was first dialyzed in 2 L 10 mM Tris, pH 7.4 with 100 mM EGTA to remove Ca^{2+}, followed by dialysis in Chelex-treated 10 mM Tris to dilute the EGTA to less than 1 µM. CA and CaM were then equilibrated with both Zn^{2+} and Pb^{2+}, respectively, in the ratios Metal:CA, 2:1, and Metal:CaM, 8:1. Equilibration was accomplished by slow shake overnight at 4 °C, followed by dialysis in 3 L Chelex-treated 10 mM Tris-Cl, pH 7.4. Final concentrations of CaM and CA were determined by UV-Vis absorbance. CaM exhibits a tyrosine

absorbance at 274 nm, and CA exhibits a tyrosine absorbance at 274 nm and a tryptophan absorbance at 278 nm. Molar absorptivity values for CA and CaM are 54000 cm^{-1} M^{-1} and 3030 cm^{-1} M^{-1}, respectively.

For CA and CaM, three 1 mL samples were prepared in autoclaved microcuvette tubes to obtain concentrations of protein-bound metals in the range 5-15 µM, based on linear response of PAR. The target protein concentration for CA and CaM was 50 µM. 100 µL of protease K (1 mg/mL) was added, and the sample filled to 600 µL. Samples were placed in a water bath at 56 °C for 30 min, and shaken every 5 min to ensure mixing of the protein with protease K. Following digestion of the protein, 100 µM PAR was added, followed by 5 mM IAM, to a final volume of 1 mL. Absorbance of the complexes was measured using UV-Vis. The calculated concentration values for Zn^{2+} and Pb^{2+} were then compared with the previously-established standard curves.

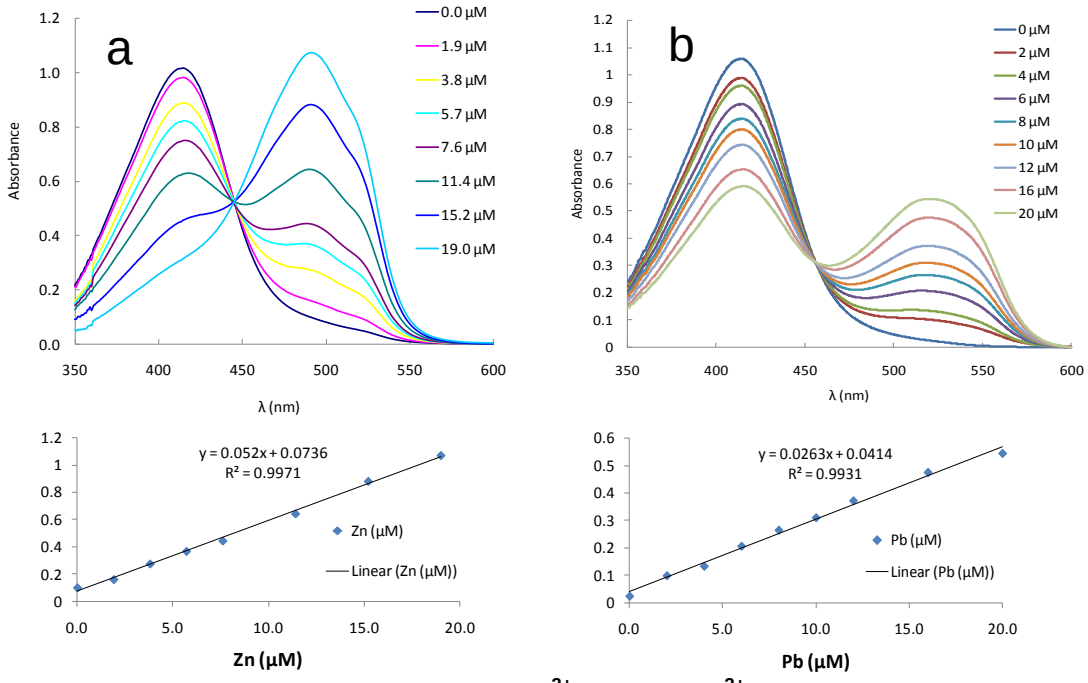

Figure 6.2 Absorbance spectra for (a) Zn^{2+} and (b) Pb^{2+}, with linear regression analyses

As seen in Figure 6.2, the response to Pb^{2+} and the isosbestic point both appear red-shifted approximately 20-25 nm compared with Zn^{2+}. Additionally, the dynamic range

is reduced by about 50%, although a standard curve with good linearity is still achieved. The observed red-shift may result from complex formation between Pb^{2+}:PAR where the stoichiometry is greater than the 2:1 observed with Zn^{2+}. In this case, the larger complex would produce a more extensive conjugated π electron network, thereby increasing the absorbance wavelength.

While the results for the Zn-CaM analysis appear consistent with those reported by McCall and Fierke [277], several difficulties were encountered while attempting to quantify Pb^{2+} bound to CaM. Protease K, a Ca^{2+} binding protein, appears to strongly interact with Pb^{2+}, as seen in Figure 6.3a, and in comparison with the absorbance data in Figure 6.2b. Additionally, the activity of Protease K was apparently inhibited by the presence of Pb^{2+} as seen in Figure 6.3b, and summarized in Table 6.1. This inhibitory effect was not observed in the presence of Zn^{2+} (Figure 6.2a). Figure 6.3b also suggests that Zn^{2+} may still be present in solution for CA, as evidenced by the peak absorbance at 490 nm.

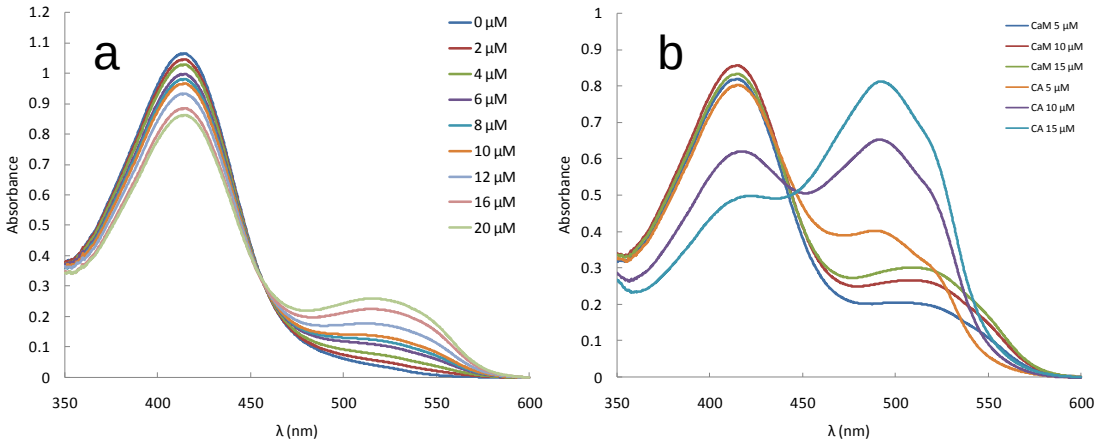

Figure 6.3 Reduced absorbance of PAR-Pb^{2+} in the presence of protease K
(**a**) The reduced dynamic range observed for Pb^{2+} is likely due to competition between PAR and Protease K for Pb^{2+}. (**b**) Absorbance of PAR-Pb^{2+} complex for CA and CaM following digestion with Protease K.

Table 6.1 Pb^{2+} complexed with PAR following protease K digestion of CA and CaM

[Protein] µM	CA (492 nm)	CA [Pb2+] (µM)	CaM (509.4 nm)	CaM [Pb2+] (µM)
5	0.4001	32.3	0.2029	15.0
10	0.6530	54.5	0.2660	20.5
15	0.8113	68.4	0.3008	23.6

PAR assay conclusions

These efforts to modify the PAR assay for detection of Pb^{2+} were unsuccessful apparently due to interactions between protease K and Pb^{2+}. Future efforts will be directed towards investigating different methods to decomplex Pb-CaM, such as heat denaturation or addition of Urea.

6.3 Response of fluorescent dyes to target metals

Fluorescent dyes with high affinity for different metals can be utilized competitively with proteins to establish binding affinities between the metals and the proteins. To be useful, the dyes need to have affinities for the metals similar to those of the proteins, and binding needs to produce a dynamic range sufficiently large enough to curve-fit data representing incremental changes between the unsaturated and saturated states of the dye. Here we summarize the responses of different dyes to target RNT metals.

Fura-2

The fluorescence response of Fura-2 dye was evaluated with different metals. For the emission scans (Figure 6.4), spectra were collected for four conditions: (1) TRIS buffer only; (2) Addition of 1 µM Fura-2; (3) Addition of 2 µM M^{n+}; (4) Addition of 50 µM M^{n+}. For the excitation scans, a fifth condition was included: addition of 168 µM EGTA to chelate the metal ions.

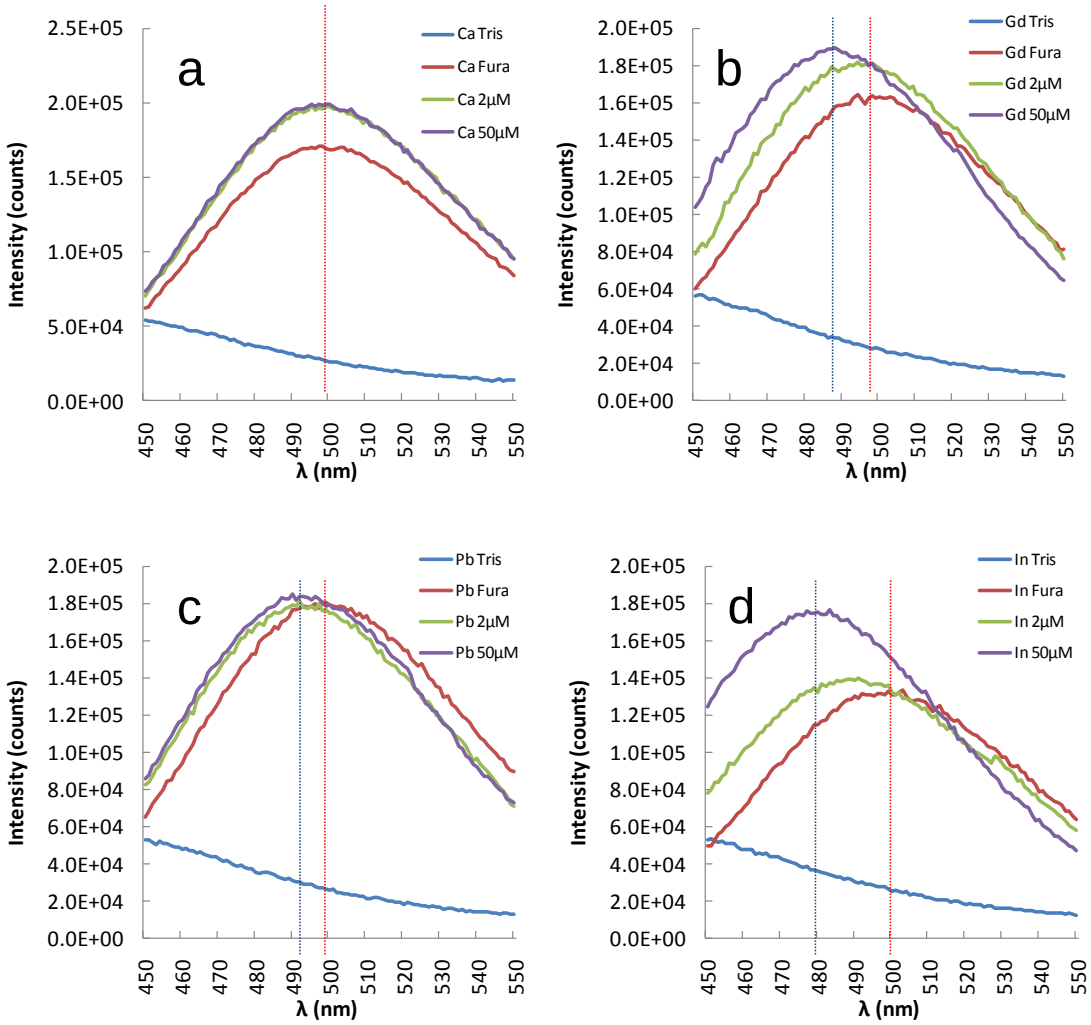

Figure 6.4 Fluorescent emission scans, 1 uM Fura-2 dye pH 7.4
Spectra for addition of (**a**) Ca^{2+}. (**b**) Gd^{3+} (**c**) Pb^{2+} and (**d**) In^{3+}

As seen in Figure 6.4, a blue-shift was observed following addition of all metals, except Ca^{2+}. This appears most pronounced in the case of In^{3+} (Figure 6.4d), however, the peak for Fura-2 in the In^{3+} spectrum was unusually low compared with the other spectra, indicating the concentration of Fura-2 was probably lower than the other experiments, suggesting this experiment will need to be repeated due to random error.

The decreasing fluorescence following addition of EGTA strongly suggests that sufficient background Ca^{2+} was present at the beginning of the experiment to increase the Fura-2 signal before additional Ca^{2+} was added, despite pre-treatment of the buffers.

Also, the apparent high binding affinity of Fura-2 for Pb^{2+}, which remains to be quantified, suggests that it may be an effective, competitive chelator for protein titration experiments, although EDTA should be used to remove Pb^{2+} in future experiments.

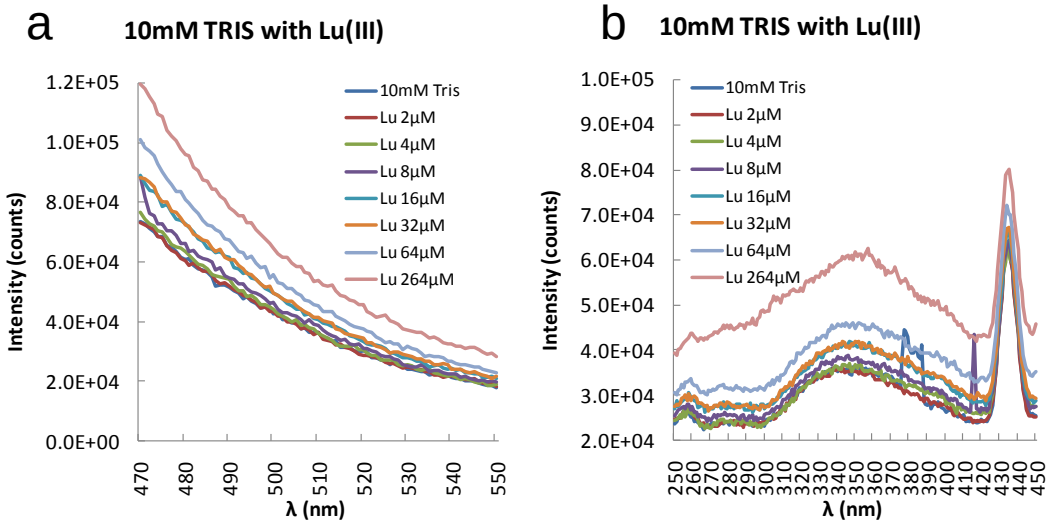

Figure 6.5 Lu^{3+} fluorescence scans
(a) Emission and **(b)** excitation scans of Lu^{3+} in 10 mM TRIS, pH 7.4.

Results of the emission and excitation scans for 10 mM TRIS pH 7.4 with Lu^{3+} can be seen in Figure 6.5, which clearly indicate that the selected buffering system has no apparent interaction with Lu^{3+} that would interfere with the signal intensity. Fluorescent excitation scans of the direct addition of Pb^{2+}, In^{3+} and Y^{3+} to Fura-2 followed by chelation of metal ions with EGTA are shown in Figure 6.6. These results suggest that all 3 metals exhibit high response to binding with Fura-2, with apparent higher binding affinity for In^{3+} based on the increased concentration of EDTA (400 µM) required to remove the background free metal. Results for In^{3+} suggest some unusual binding effects not apparent with the other metals. The addition of In^{3+} resulted in a significant decrease in fluorescence that was almost completely restored with the addition of EGTA. However, only a single maxima was observed at 340 nm, and this maxima exhibited an unexpected concavity at the apex which remains to be explained.

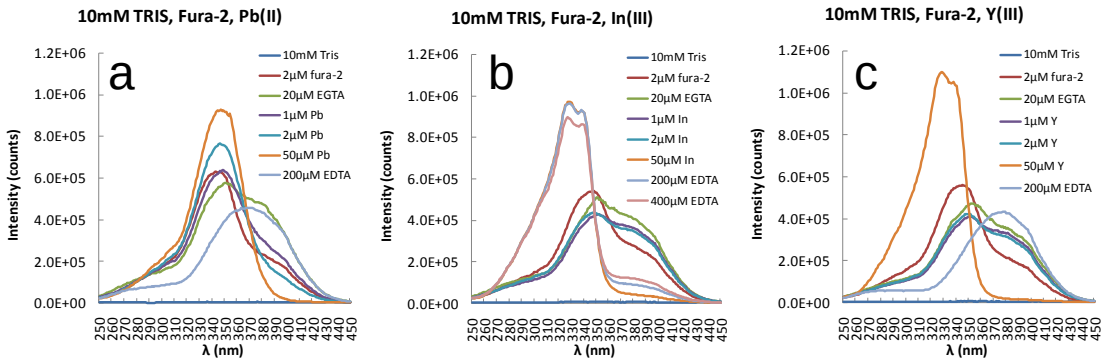

Figure 6.6 Excitation scans with Fura-2
Metals analyzed were (a) Pb^{2+}, (b) In^{3+} and (c) Y^{3+} in 10 mM TRIS, pH 7.4.

We evaluated direct titration of CaM into buffer matrices comprised of 10 μM concentrations of Pb^{2+}, Gd^{3+} and Lu^{3+} with Fura-2 (Figure 6.7). Results indicate that all 3 metals bind with relatively higher affinity to the dye compared with the protein, thus rendering this method undesirable due to the high concentration of protein required for analyses.

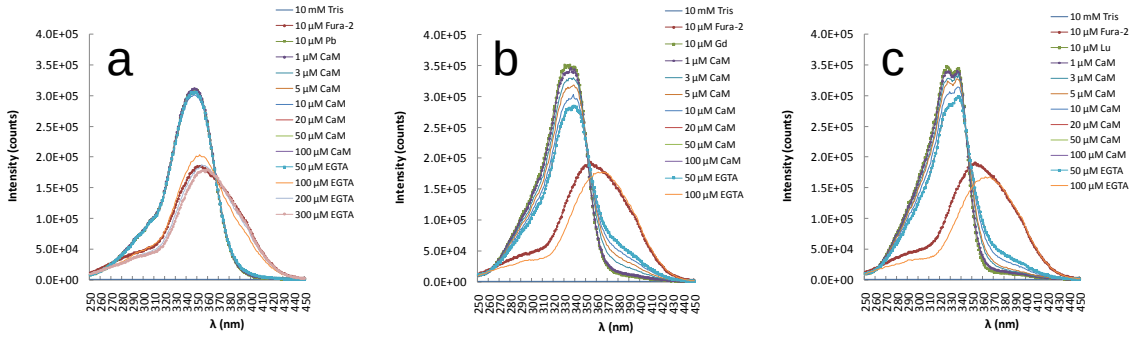

Figure 6.7 Competitive titration of CaM with Fura-2
Samples contained 10 μM concentrations of (**a**) Pb^{2+} (**b**) Gd^{3+} and (c) Lu^{3+}. Very high concentrations of CaM were required to produce changes in spectra.

Spectra for a second series of excitation scans for 2 μM Fura-2 binding with Pb^{2+}, Bi^{3+}, Lu^{3+} and Y^{3+} are presented in Figure 6.8. The addition of 100 uM EDTA at the end of these titrations demonstrated that metals were present in the initial samples, either the buffer or the dye itself, prior to the experiment. This is evident based on the observed peak at or near 370nm following addition of the chelator. Had the sample been metal-

free prior to the titration, this peak would have emerged with the first titration point, prior to addition of metal.

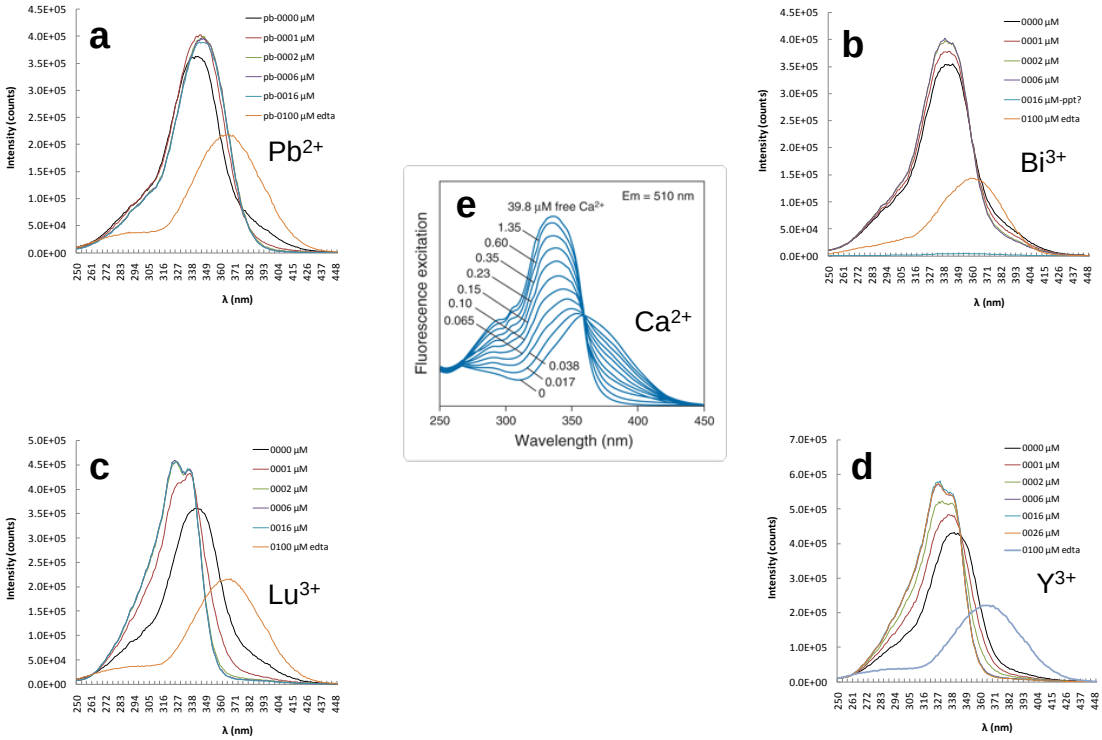

Figure 6.8 Changes in Fura-2 fluorescence with different metals
Spectra analyzed following addition of (a) Pb^{2+} (b) Bi^{3+} (c) Lu^{3+} and (d) Y^{3+}. Spectra for (e) Ca^{2+} [279] included for comparison. Except for Bi^{3+}, metals evaluated wavelength shifts that differed from observed Ca^{2+} response. All samples also appeared to have been contaminated by metals prior to experiment.

Spectra for Pb^{2+}, Lu^{3+} and Y^{3+} also suggest that Fura-2 is not a suitable dye for analysis of these metals. When comparing these spectra with Ca^{2+} (Figure 6.8e) we do not observe an isosbestic point indicating the transition between the peak maxima, but rather we observe gradual shifts in the wavelength suggesting additional conformational changes in the dye, possibly due to binding in ratios exceeding 1:1. Bismuth may be an exception to this (Figure 6.8b), as the wavelength shift observed for the other metals is not immediately apparent in this spectra, but this will have to be further evaluated by repeating the experiment in such a way as to eliminate the background metal effects (e.g., increasing the dye concentration so that the background metal contamination

becomes negligible), and using a buffering system to chelate the metal ions during the titration to allow for the observation of more points during the transition, as the rapid changes observed in the spectra suggest high affinity binding.

Fura-6F

We evaluated direct titration of CaM into matrices comprised of 10 µM concentrations of Pb^{2+}, Gd^{3+} and Lu^{3+} with Fura-6F. Results of these direct addition titrations are presented in Figure 6.9. An observable transition between peak states for both Gd^{3+} and Lu^{3+} suggested that this dye may be suitable as a competitive chelator for quantitative analysis of complex formation between CaM and these metals.

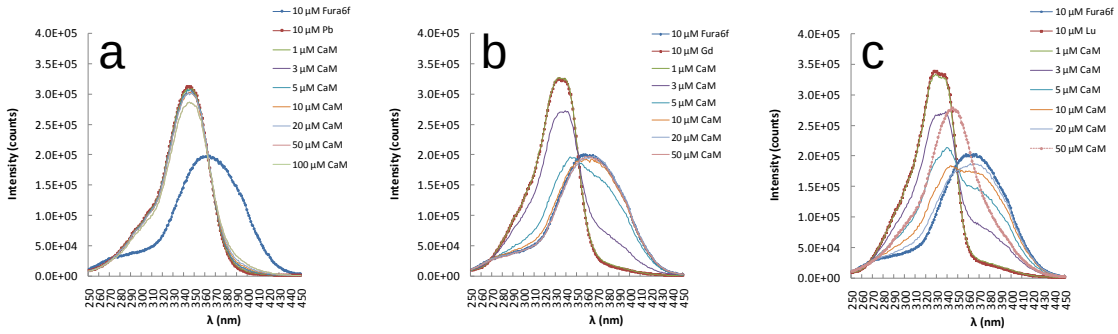

Figure 6.9 Competitive titration of CaM with Fura-6F
Samples contained 10 µM concentrations of (a) Pb^{2+} (b) Gd^{3+} and (c) Lu^{3+}. Response for matrices containing Gd^{3+} and Lu^{3+} suggest Fura-6F may be suitable for competitive titration analyses with CaM.

Another set of titrations involved the controlled addition of Lu^{3+} to Fura-6F using a buffer exchange system. From the curve-fitting presented in Figure 6.10, a constant K_d for Lu^{3+} dissociation from Fura-6F was calculated at 9.41 X 10^{-13} M, which was close to the NIST Critical database value of 7.59 X 10^{-13} M for NTA- Lu^{3+}. However, the hill coefficient *n* calculated during the curve-fitting was 3.45, suggesting positive cooperativity which would imply some complex with multiple Lu^{3+} ions binding to a single molecule of dye. Evidence to support this type of complex formation has not yet been discovered in the literature.

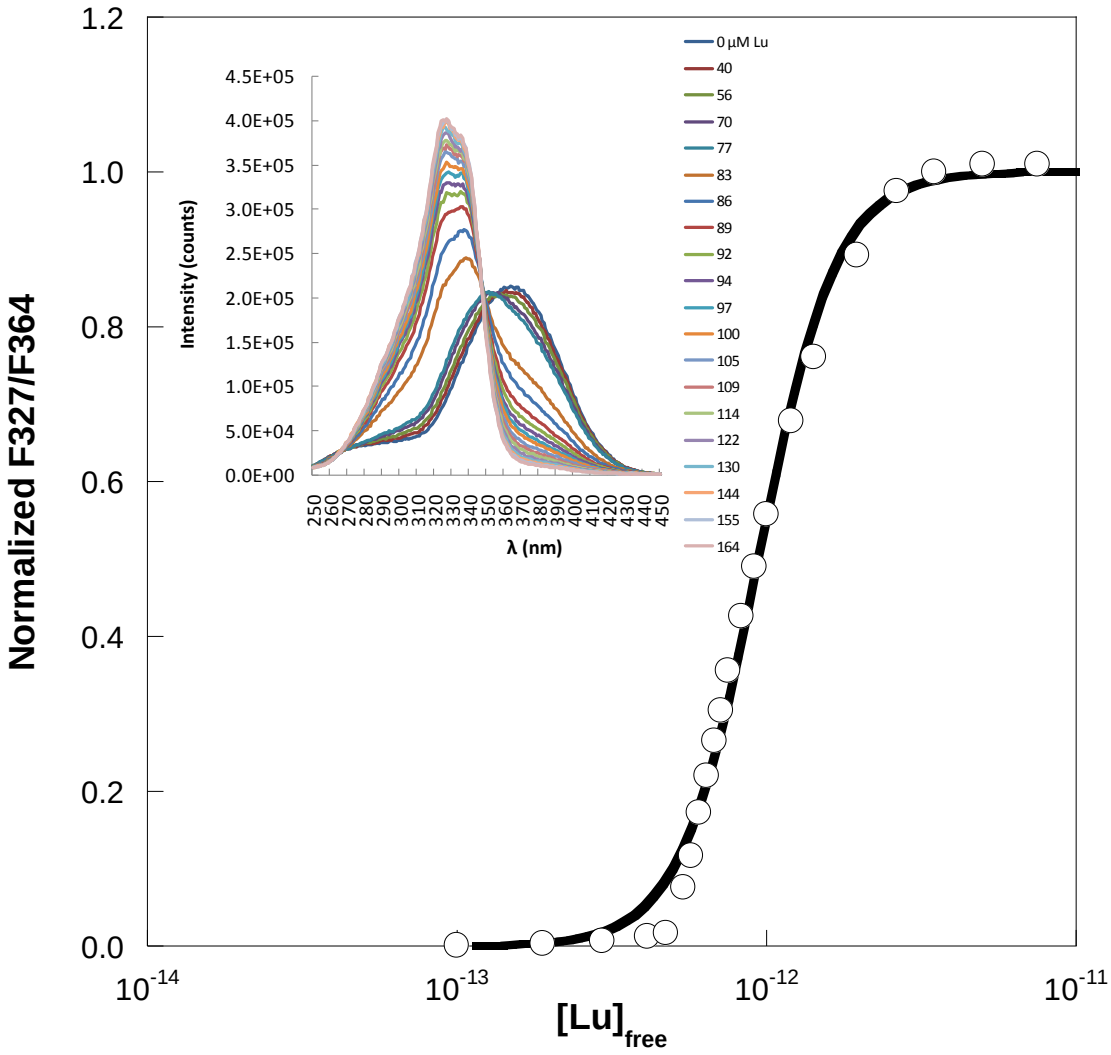

Figure 6.10 Fitting of calculated free Lu^{3+} for titration of Lu^{3+} with Fura-6F Rhod-5N

We evaluated direct titration of CaM into a matrix comprised of equimolar concentrations of Pb^{2+}, Gd^{3+} and Lu^{3+} with Rhod-5N. Results of these direct addition titrations are presented in Figure 6.11. Comparison of these spectra suggested that Rhod-5N affinity for Pb^{2+} was similar enough to CaM that Rhod-5N would be a viable chelator for further competitive titration experiments (Figure 6.11a). For both Gd^{3+} and Lu^{3+}, the addition of CaM resulted in more rapid decrease in fluorescence intensity, suggesting that these metals have higher affinity for CaM than the Rhod-5N. These latter

results indicate that Rhod-5N may be a good competitive chelator for these metals in the presence of proteins with weaker metal binding affinities.

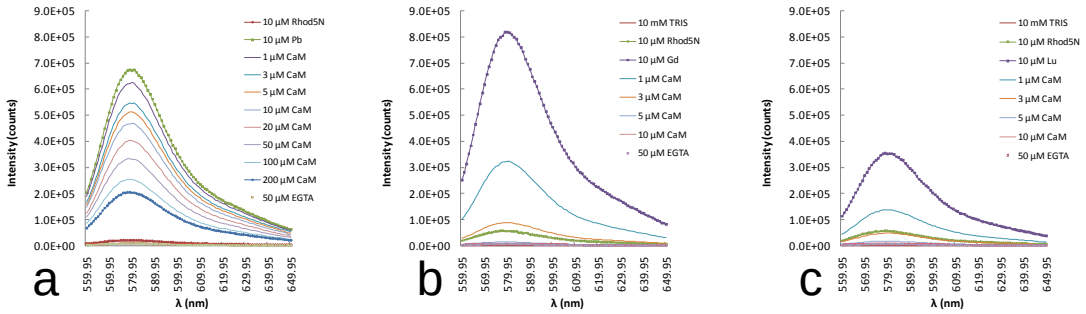

Figure 6.11 Competitive titration of CaM with Rhod-5N
Samples contained 10 uM of (a) Pb^{2+} (b) Gd^{3+} and (c) Lu^{3+}. Results suggest similar affinity between Rhod-5N and CaM for Pb^{2+} and higher CaM affinity for Gd^{3+} and Lu^{3+} relative to Rhod-5N.

In a related experiment, Pb^{2+} was titrated directly against Rhod-5N (inset, Figure 6.12). Changes in signal intensity at the observed peak maxima were normalized against the baseline scan. The plot in Figure 6.12, averaged over three trials, was fit with a quadratic equation, yielding a K_d value 1.82 X 10^{-6} M. However, it is clear that the data do not fit the curve. In this experiment, the binding affinity between Pb^{2+} and Rhod-5N is too strong for this experimental method.

Next, a buffer (NTA) exchange experiment was conducted, involving the controlled addition of Pb^{2+} to Rhod-5N, as seen in Figure 6.13. A dissociation constant K_d for Pb^{2+}, based on mean and standard deviation for three trials, was calculated at 1.14 X 10^{-11} M using a quadratic equation for curve-fitting. This was close to the NIST Critical value of 3.31 X 10^{-12} M for Pb^{2+}-NTA. The fitting in Figure 6.13 had a calculated R value of 0.999. Therefore, the K_d calculated from the buffer exchange experiment will be used as the assumed correct value.

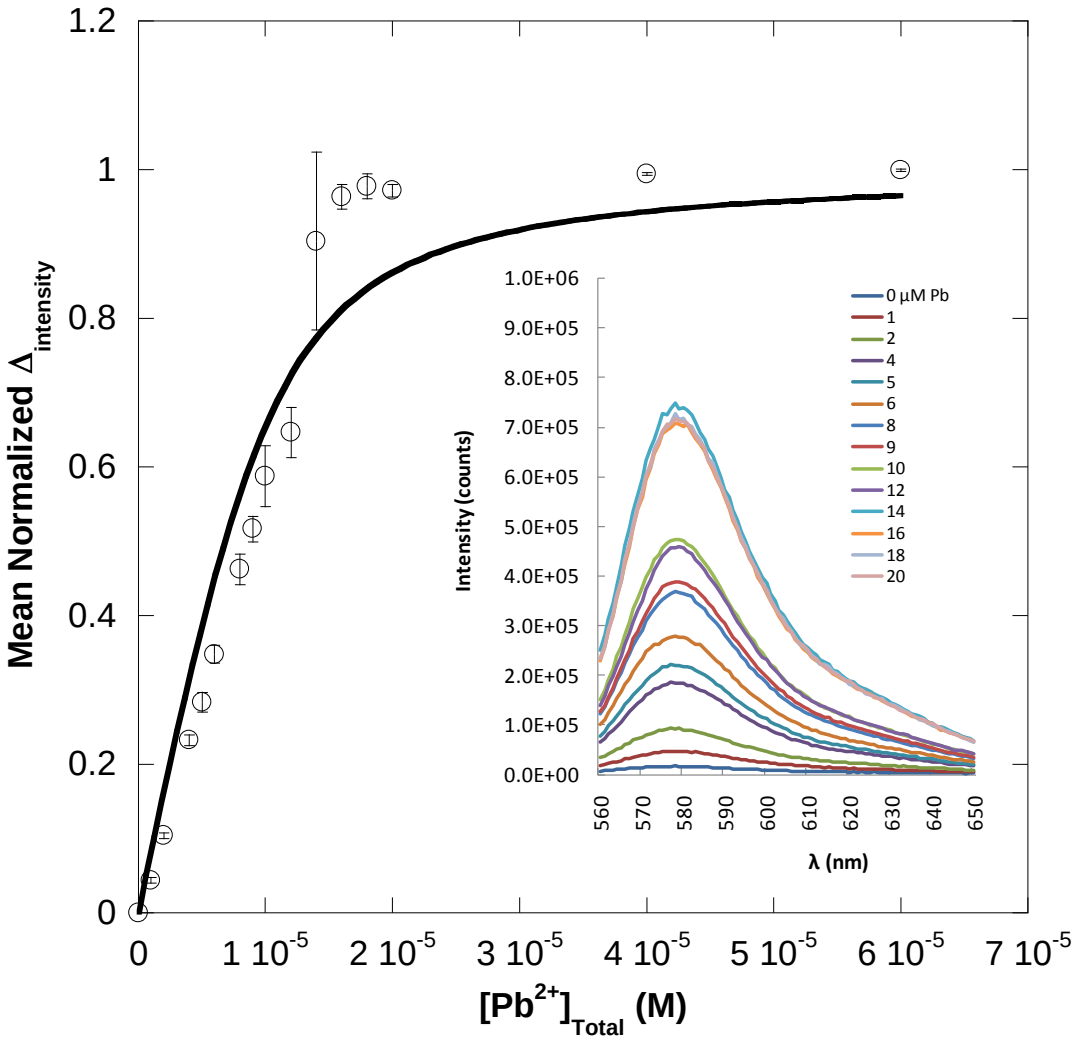

Figure 6.12 Binding of Pb^{2+} to Rhod-5N via direct titration
Titrations done in triplicate. Curve was fit with Hill equation.

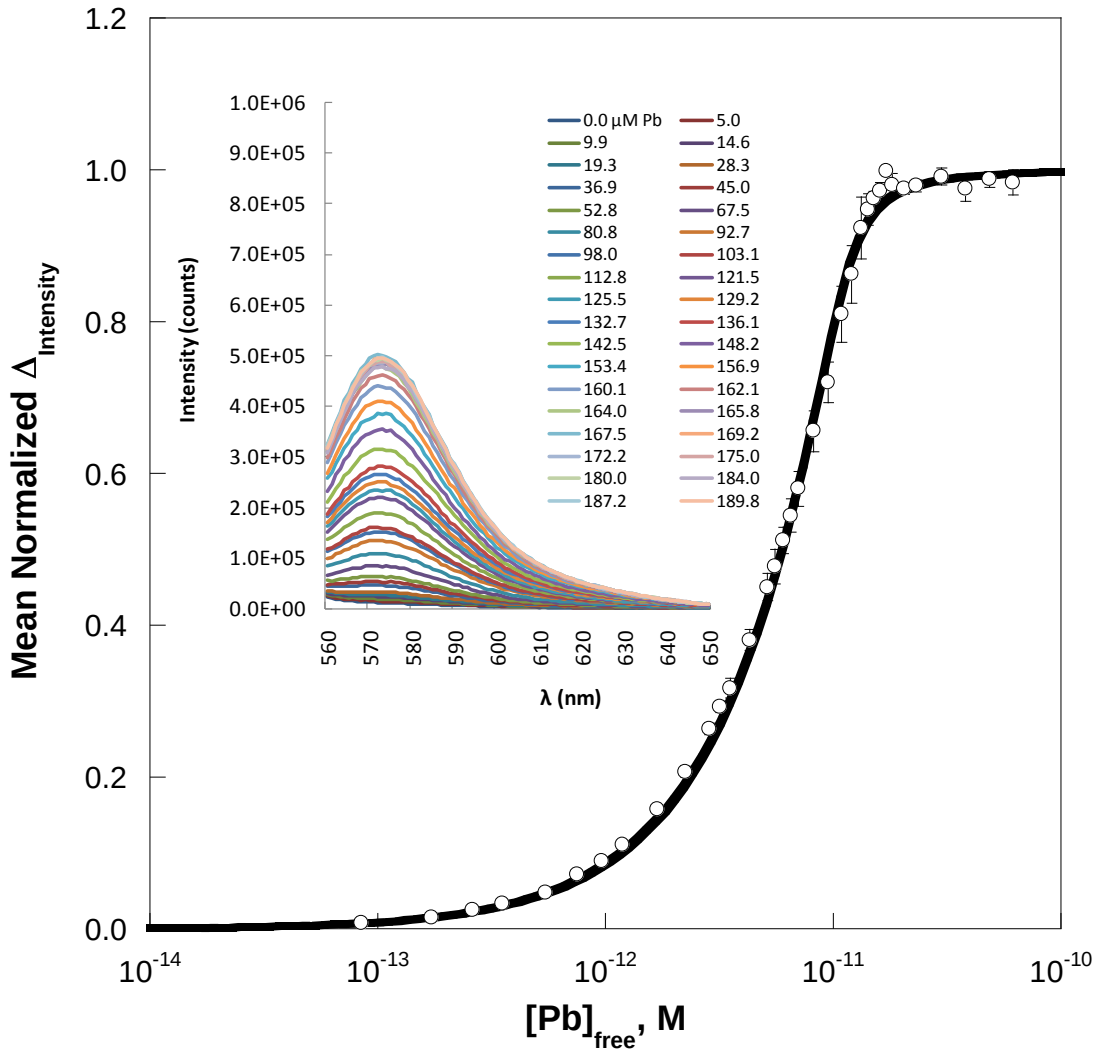

Figure 6.13 Fluorescence changes in Rhod-5N due to binding of Pb^{2+}
Fitting of calculated free Pb^{2+} in sample to normalized change in fluorescence intensity was completed using quadratic equation.

FluoZin-1

The fluorescence responses of 2 µM samples of FluoZin-1 binding to Pb^{2+}, Bi^{3+}, Lu^{3+}, Y^{3+} and Ca^{2+} were investigated by direct titration. The addition of Pb^{2+} resulted in an initial increase in fluorescent intensity followed by a decrease that is attributed to either binding of multiple ions resulting in inhibitory quenching, and/or precipitation (Figure 6.14a). This response makes the use of FluoZin-1 problematic for analysis of Pb^{2+} due to the biphasic trend preventing reasonable curve-fitting of the data. Additionally, only Pb^{2+} produced any measurable change in intensity (Figure 6.14b)

similar to the observed fluorescent changes reported by the manufacturer, Invitrogen (Figure 6.14c, http://products.invitrogen.com), which indicates that FluoZin-1 is unlikely to be suitable for use with the other target metals for fluorescent analyses.

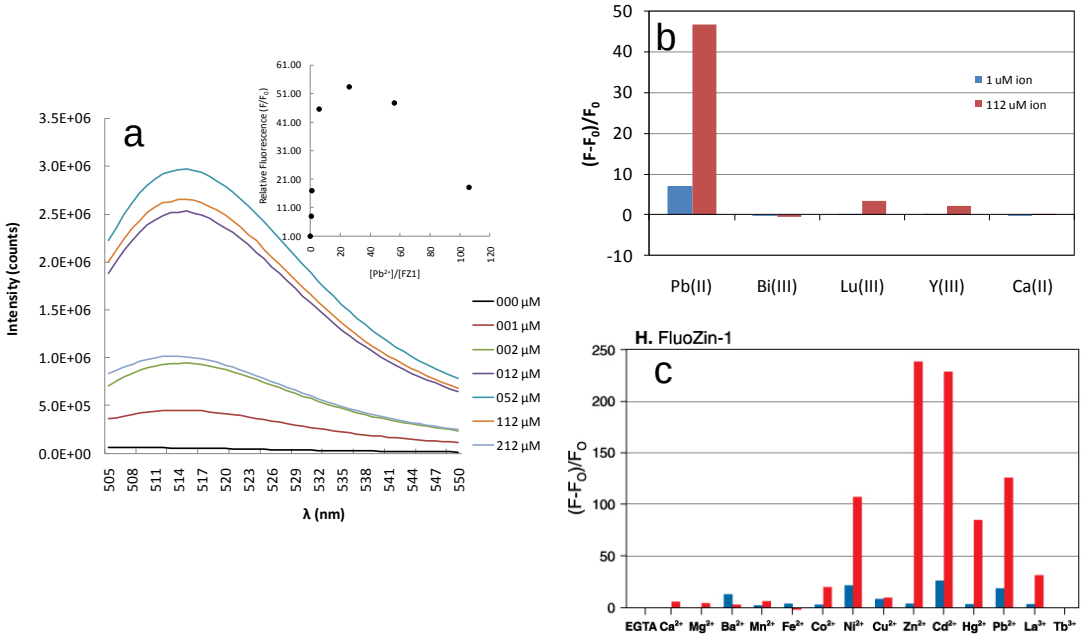

Figure 6.14 Direct titration of Pb^{2+}, Bi^{3+}, Lu^{3+}, Y^{3+} and Ca^{2+} into 2 µM FluoZin-1
Spectra for **(a)** Pb^{2+} were characterized by an initial increase followed by a decrease (inset) possibly due to binding of multiple ions and/or precipitation. **(b)** Comparison of fluorescence changes following addition of 1 µM ion (blue bar) and 112 µM ion (red bar). Data for each ion are plotted as (F-F0)/F0 for comparison with (**c**) the manufacturers (Invitrogen) reported values at 1 and 100 µM, respectively.

Fluo-4

The fluorescence responses of 2 µM samples of Fluo-4 binding to Pb^{2+}, Bi^{3+}, Lu^{3+}, Y^{3+} and Ca^{2+} were also investigated by direct titration. As seen in Figure 6.15a, all metals except for Ca^{2+} produced a fluorescent response as a result of binding to Fluo-4. These preliminary results suggest that dissociation constants may be calculated with further experimentation. However, the results also demonstrate a serious problem with this experiment. The fluorescence observed for Pb^{2+} in Figure 6.15a differs from that reported by the manufacturer as seen in Figure 6.15b. Consistent with this, the addition

of EDTA to both the Pb^{2+} and Bi^{3+} complexes resulted in elimination of the fluorescence signal, indicating that the initial dye sample was probably contaminated with metal.

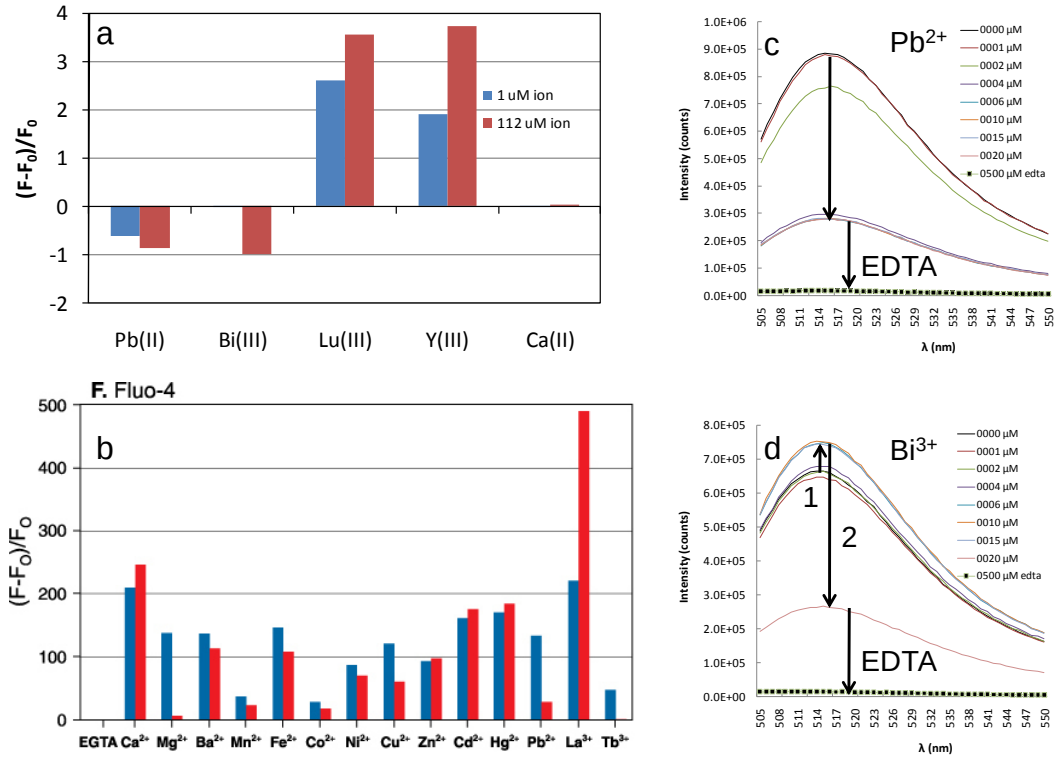

Figure 6.15 Direct titration of Pb^{2+}, Bi^{3+}, Lu^{3+}, Y^{3+} and Ca^{2+} into 2 µM Fluo-4
Spectra indicated fluorescent responses to all metals except Ca^{2+}. Comparison of **(a)** the response from both Ca^{2+} and Pb^{2+} differ from **(b)** results reported by the manufacturer. The addition of EDTA to both samples titrated with **(c)** Pb^{2+} and **(d)** Bi^{3+} indicate the initial dye samples were contaminated with metal prior to initiation of the experiment.

7 Significance and conclusions

The results of our statistical and structural analyses confirm that Pb^{2+} exhibits greater flexibility than Ca^{2+} in binding with respect to ligand type and number, charge, and geometry. This behavior more closely resembles that exhibited by the less structured Non-EF hand Ca^{2+}-binding proteins. These features appear to increase the binding promiscuity of Pb^{2+}, allowing for opportunistic binding in the absence of well-defined binding sites. Our results suggest that Pb^{2+} may bind to proteins both opportunistically in regions of high surface negative charge and by ionic displacement, resulting in activation or inhibition of the protein as a function of metal concentration. Pb^{2+} binding in CaM does not appear to follow the same order of occupancy described for Ca^{2+}. However, the significant structural alterations in CaM revealed by NMR appear to be due to opportunistic binding of Pb^{2+} resulting in an induced secondary binding site (i.e., residues 78-82) rather than as a result of displacement in known binding sites. Moreover, this region appears to exhibit rapid conformational change with the addition of Pb^{2+} after CaM has been saturated with Ca^{2+}, suggesting that in the Ca^{2+}-bound form, Pb^{2+} does not readily displace Ca^{2+}. Additionally, CaM appears to dimerize with the addition of 5-6 ME Pb^{2+}. After that, the protein precipitates. The significance of this dimerization has not yet been established, however, the picture that is emerging, with respect to toxicity, is that CaM activity even in the holo-form may be disrupted by low concentrations of Pb^{2+}. This again supports our hypothesis that the characteristics of Pb^{2+} may allow it to bind to non-metalloproteins as well as known metal-binding proteins and alter their activity or function through a subtle mechanism involving weak opportunistic binding in charged regions where physiologically-relevant cations fail to bind.

8 References

1. Ibers, J.A. and R.H. Holm, *Modeling coordination sites in metallobiomolecules.* Science, 1980. **209**(4453): p. 223-35.
2. Bertini, I., A. Sigel, and H. Sigel, *Handbook on metalloproteins*. 2001, New York: Marcel Dekker. xxvii, 1182 p.
3. Holm, R.H., P. Kennepohl, and E.I. Solomon, *Structural and Functional Aspects of Metal Sites in Biology.* Chem Rev, 1996. **96**(7): p. 2239-2314.
4. Tainer, J.A., V.A. Roberts, and E.D. Getzoff, *Protein metal-binding sites.* Curr Opin Biotechnol, 1992. **3**(4): p. 378-87.
5. Glusker, J.P., *Structural aspects of metal liganding to functional groups in proteins.* Adv Protein Chem, 1991. **42**: p. 1-76.
6. Silva, J.R.R.F.d. and R.J.P. Williams, *The biological chemistry of the elements : the inorganic chemistry of life*. 1991, Oxford [England] New York: Clarendon Press ; Oxford University Press. xxi, 561 p.
7. Lippard, S.J. and J.M. Berg, *Principles of bioinorganic chemistry*. 1994, Mill Valley, Calif.: University Science Books. xvii, 411 p.
8. Yamashita, M.M., et al., *Where metal ions bind in proteins.* Proc Natl Acad Sci U S A, 1990. **87**(15): p. 5648-52.
9. Bagley, S.C. and R.B. Altman, *Characterizing the microenvironment surrounding protein sites.* Protein Sci, 1995. **4**(4): p. 622-35.
10. Dudev, T. and C. Lim, *Principles governing Mg, Ca, and Zn binding and selectivity in proteins.* Chemical Reviews, 2003. **103**(3): p. 773-787.
11. Babu, C.S., et al., *A combined experimental and theoretical study of divalent metal ion selectivity and function in proteins: application to E. coli ribonuclease H1*. J Am Chem Soc, 2003. **125**(31): p. 9318-28.
12. Dudev, T. and C. Lim, *Effect of carboxylate-binding mode on metal binding/selectivity and function in proteins.* Acc Chem Res, 2007. **40**(1): p. 85-93.
13. Chakrabarti, P., *Geometry of interaction of metal ions with histidine residues in protein structures.* Protein Eng, 1990. **4**(1): p. 57-63.
14. Chakrabarti, P., *Geometry of interaction of metal ions with sulfur-containing ligands in protein structures.* Biochemistry, 1989. **28**(14): p. 6081-5.
15. Chakrabarti, P., *Interaction of metal ions with carboxylic and carboxamide groups in protein structures.* Protein Eng, 1990. **4**(1): p. 49-56.
16. Glusker, J.P., M. Lewis, and M. Rossi, *Crystal structure analysis for chemists and biologists*. 1994, New York: VCH. xvii, 854 p.
17. Harding, M.M., *Geometry of metal-ligand interactions in proteins.* Acta Crystallogr D Biol Crystallogr, 2001. **57**(Pt 3): p. 401-11.
18. Harding, M.M., *The geometry of metal-ligand interactions relevant to proteins.* Acta Crystallogr D Biol Crystallogr, 1999. **55**(Pt 8): p. 1432-43.
19. Harding, M.M., *The geometry of metal-ligand interactions relevant to proteins. II. Angles at the metal atom, additional weak metal-donor interactions.* Acta Crystallogr D Biol Crystallogr, 2000. **56**(Pt 7): p. 857-67.
20. Busenlehner, L.S. and D.P. Giedroc, *Kinetics of metal binding by the toxic metal-sensing transcriptional repressor Staphylococcus aureus pI258 CadC.* J Inorg Biochem, 2006. **100**(5-6): p. 1024-34.
21. Fahmy, K., et al., *Secondary structure and Pd(II) coordination in S-layer proteins from Bacillus sphaericus studied by infrared and X-ray absorption spectroscopy.* Biophys J, 2006. **91**(3): p. 996-1007.
22. Ye, J., et al., *Crystal structure of the Staphylococcus aureus pI258 CadC Cd(II)/Pb(II)/Zn(II)-responsive repressor.* J Bacteriol, 2005. **187**(12): p. 4214-21.
23. Borremans, B., et al., *Cloning and functional analysis of the pbr lead resistance determinant of Ralstonia metallidurans CH34.* J Bacteriol, 2001. **183**(19): p. 5651-8.

24. CDC. *Children's Blood Lead Levels in the United States*. 2009 05/05/2010 [cited 2010 June 10]; Available from: http://www.cdc.gov/nceh/lead/data/national.htm.
25. Wang, S. and J. Zhang, *Blood lead levels in children, China.* Environmental Research, 2006. **101**(3): p. 412-418.
26. George, A. *Project lead-free: A study of lead poisoning in major Indian cities.* in *International Conference on Lead Poisoning Prevention and Treatment*. 1999. Bangalore, India.
27. Mathee, A., et al., *A survey of blood lead levels among young Johannesburg school children.* Environmental Research, 2002. **90**(3): p. 181-184.
28. Despres, C., et al., *Neuromotor functions in Inuit preschool children exposed to Pb, PCBs, and Hg.* Neurotoxicol Teratol, 2005. **27**(2): p. 245-57.
29. Bressler, J., et al., *Molecular Mechanisms of Lead Neurotoxicity.* Neurochemical Research, 1999. **24**(4): p. 595-600.
30. Bouton, C.M., et al., *Synaptotagmin I is a molecular target for lead.* J Neurochem, 2001. **76**(6): p. 1724-35.
31. Chetty, C.S., et al., *Perinatal lead exposure alters the expression of neuronal nitric oxide synthase in rat brain.* Int J Toxicol, 2001. **20**(3): p. 113-20.
32. Reddy, G.R. and N.H. Zawia, *Lead exposure alters Egr-1 DNA-binding in the neonatal rat brain.* Int J Dev Neurosci, 2000. **18**(8): p. 791-5.
33. Moore, M.R., A. Goldberg, and A.A. Yeung-Laiwah, *Lead effects on the heme biosynthetic pathway. Relationship to toxicity.* Ann N Y Acad Sci, 1987. **514**: p. 191-203.
34. Aub, J.C. and P. Reznikoff, *Lead Studies : Iii. The Effects of Lead on Red Blood Cells. Part 3. A Chemical Explanation of the Reaction of Lead with Red Blood Cells.* J Exp Med, 1924. **40**(2): p. 189-208.
35. Nolan, C.V. and Z.A. Shaikh, *Lead nephrotoxicity and associated disorders: biochemical mechanisms.* Toxicology, 1992. **73**(2): p. 127-46.
36. Khalil-Manesh, F., et al., *Lead-induced hypertension: possible role of endothelial factors.* Am J Hypertens, 1993. **6**(9): p. 723-9.
37. Apostoli, P., et al., *The effect of lead on male fertility: a time to pregnancy (TTP) study.* Am J Ind Med, 2000. **38**(3): p. 310-5.
38. Hernandez-Ochoa, I., et al., *Low lead environmental exposure alters semen quality and sperm chromatin condensation in northern Mexico.* Reprod Toxicol, 2005. **20**(2): p. 221-8.
39. Ronis, M.J., et al., *Endocrine mechanisms underlying the growth effects of developmental lead exposure in the rat.* J Toxicol Environ Health A, 1998. **54**(2): p. 101-20.
40. Johnson, F.M., *The genetic effects of environmental lead.* Mutat Res, 1998. **410**(2): p. 123-40.
41. Sanders, T., et al., *Neurotoxic effects and biomarkers of lead exposure: a review.* Rev Environ Health, 2009. **24**(1): p. 15-45.
42. Lanphear, B.P., et al., *Cognitive deficits associated with blood lead concentrations <10 microg/dL in US children and adolescents.* Public Health Rep, 2000. **115**(6): p. 521-9.
43. Bridges, C.C. and R.K. Zalups, *Molecular and ionic mimicry and the transport of toxic metals.* Toxicol Appl Pharmacol, 2005. **204**(3): p. 274-308.
44. Flora, S.J., M. Mittal, and A. Mehta, *Heavy metal induced oxidative stress & its possible reversal by chelation therapy.* Indian J Med Res, 2008. **128**(4): p. 501-23.
45. Bitto, E., et al., *Structure of pyrimidine 5'-nucleotidase type 1. Insight into mechanism of action and inhibition during lead poisoning.* J Biol Chem, 2006. **281**(29): p. 20521-9.
46. Kim, Y., et al., *Evaluation of activity of erythrocyte pyrimidine 5'-nucleotidase (P5N) in lead exposed workers: with focus on the effect on hemoglobin.* Ind Health, 2002. **40**(1): p. 23-7.
47. Chauhan, S., D.E. Titus, and M.R. O'Brian, *Metals control activity and expression of the heme biosynthesis enzyme delta-aminolevulinic acid dehydratase in Bradyrhizobium japonicum.* J Bacteriol, 1997. **179**(17): p. 5516-20.
48. Ballatori, N., *Transport of toxic metals by molecular mimicry.* Environ Health Perspect, 2002. **110 Suppl 5**: p. 689-94.
49. Andersen, R.J., et al., *Characterization of the first N2S(alkylthiolate)lead compound: a model for three-coordinate lead in biological systems.* Inorg Chem, 2006. **45**(17): p. 6574-6.
50. Battistuzzi, G., et al., *Amide Group Coordination to the Pb(2+) Ion.* Inorg Chem, 1996. **35**(14): p. 4239-4247.

51. Godwin, H.A., *The biological chemistry of lead.* Current Opinion in Chemical Biology, 2001. **5**: p. 223-227.
52. Goering, P.L., *Lead-protein interactions as a basis for lead toxicity.* Neurotoxicology, 1993. **14**(2-3): p. 45-60.
53. Goering, P.L., P. Mistry, and B.A. Fowler, *A low molecular weight lead-binding protein in brain attenuates lead inhibition of delta-aminolevulinic acid dehydratase: comparison with a renal lead-binding protein.* J Pharmacol Exp Ther, 1986. **237**(1): p. 220-5.
54. Goyer, R.A., *Toxic and essential metal interactions.* Annu Rev Nutr, 1997. **17**: p. 37-50.
55. Dowd, T.L., et al., *The displacement of calcium from osteocalcin at submicromolar concentrations of free lead.* Biochim Biophys Acta, 1994. **1226**(2): p. 131-7.
56. Fowler, B.A., *Roles of lead-binding proteins in mediating lead bioavailability.* Environ Health Perspect, 1998. **106 Suppl 6**: p. 1585-7.
57. Fullmer, C.S., S. Edelstein, and R.H. Wasserman, *Lead-binding properties of intestinal calcium-binding proteins.* J Biol Chem, 1985. **260**(11): p. 6816-9.
58. Forsen, S., E. Thulin, and H. Lilja, *113Cd NMR in the study of calcium binding proteins: troponin C.* FEBS Lett, 1979. **104**(1): p. 123-6.
59. Mills JS, J.J., *Metal ions as allosteric regulators of calmodulin.* J Biol Chem, 1985. **260**(28): p. 15100-15105.
60. Wang, C.L., P.C. Leavis, and J. Gergely, *Kinetic studies show that Ca2+ and Tb3+ have different binding preferences toward the four Ca2+-binding sites of calmodulin.* Biochemistry, 1984. **23**(26): p. 6410-5.
61. Pidcock E, M.G., *Structural characteristics of protein binding sites for calcium and lanthanide ions.* J Biol Inorg Chem, 2001. **6**: p. 479-489.
62. Yang, W., et al., *Design of a calcium-binding protein with desired structure in a cell adhesion molecule.* J Am Chem Soc, 2005. **127**(7): p. 2085-93.
63. Simons, T.J. and G. Pocock, *Lead enters bovine adrenal medullary cells through calcium channels.* J Neurochem, 1987. **48**(2): p. 383-9.
64. Tomsig, J.L. and J.B. Suszkiw, *Permeation of Pb2+ through calcium channels: fura-2 measurements of voltage- and dihydropyridine-sensitive Pb2+ entry in isolated bovine chromaffin cells.* Biochim Biophys Acta, 1991. **1069**(2): p. 197-200.
65. Atchison, W.D., *Effects of toxic environmental contaminants on voltage-gated calcium channel function: from past to present.* J Bioenerg Biomembr, 2003. **35**(6): p. 507-32.
66. Chao, S.H., C.H. Bu, and W.Y. Cheung, *Activation of troponin C by Cd2+ and Pb2+.* Arch Toxicol, 1990. **64**(6): p. 490-6.
67. Vig, P.J., R. Nath, and D. Desaiah, *Metal inhibition of calmodulin activity in monkey brain.* J Appl Toxicol, 1989. **9**(5): p. 313-6.
68. Long, G.J., J.F. Rosen, and F.A. Schanne, *Lead activation of protein kinase C from rat brain. Determination of free calcium, lead, and zinc by 19F NMR.* J Biol Chem, 1994. **269**(2): p. 834-7.
69. Markovac, J. and G.W. Goldstein, *Picomolar concentrations of lead stimulate brain protein kinase C.* Nature, 1988. **334**(6177): p. 71-3.
70. Cox, J.L. and S.D. Harrison, Jr., *Correlation of metal toxicity with in vitro calmodulin inhibition.* Biochem Biophys Res Commun, 1983. **115**(1): p. 106-11.
71. Chattopadhyaya, R., et al., *Calmodulin structure refined at 1.7 A resolution.* J Mol Biol, 1992. **228**(4): p. 1177-92.
72. Wilson, M.A. and A.T. Brunger, *The 1.0 A crystal structure of Ca(2+)-bound calmodulin: an analysis of disorder and implications for functionally relevant plasticity.* J Mol Biol, 2000. **301**(5): p. 1237-56.
73. Jaren, O.R., et al., *Calcium-induced conformational switching of Paramecium calmodulin provides evidence for domain coupling.* Biochemistry, 2002. **41**(48): p. 14158-66.
74. Vogel, H.J., *The Merck Frosst Award Lecture 1994. Calmodulin: a versatile calcium mediator protein.* Biochem Cell Biol, 1994. **72**(9-10): p. 357-76.
75. Heidorn, D.B. and J. Trewhella, *Comparison of the crystal and solution structures of calmodulin and troponin C.* Biochemistry, 1988. **27**(3): p. 909-15.
76. Forsen, S., et al., *Ca2+ binding in proteins of the calmodulin superfamily: cooperativity, electrostatic contributions and molecular mechanisms.* Ciba Found Symp, 1991. **161**: p. 222-36.

77. Hiraoki, T. and H.J. Vogel, *Structure and function of calcium-binding proteins.* J Cardiovasc Pharmacol, 1987. **10 Suppl 1**: p. S14-31.
78. Shea, M.A., A.S. Verhoeven, and S. Pedigo, *Calcium-induced interactions of calmodulin domains revealed by quantitative thrombin footprinting of Arg37 and Arg106.* Biochemistry, 1996. **35**(9): p. 2943-57.
79. Fefeu, S., et al., *Calcium-induced refolding of the calmodulin V136G mutant studied by NMR spectroscopy: evidence for interaction between the two globular domains.* Biochemistry, 2000. **39**(51): p. 15920-31.
80. Ikura, M., et al., *113Cd-NMR evidence for cooperative interaction between amino- and carboxyl-terminal domains of calmodulin.* Biochem Biophys Res Commun, 1989. **161**(3): p. 1233-8.
81. Wu, X. and R.E. Reid, *Structure/calcium affinity relationships of site III of calmodulin: testing the acid pair hypothesis using calmodulin mutants.* Biochemistry, 1997. **36**(28): p. 8649-56.
82. Yazawa, M., et al., *Communication between two globular domains of calmodulin in the presence of mastoparan or caldesmon fragment. Ca2+ binding and 1H NMR.* J Biol Chem, 1987. **262**(23): p. 10951-4.
83. Kern, M., et al., *Inorganic lead and calcium interact positively in activation of calmodulin.* Neurotoxicology, 2000. **21**(3): p. 353-63.
84. Shirran, S.L. and P.E. Barran, *The use of ESI-MS to probe the binding of divalent cations to calmodulin.* J Am Soc Mass Spectrom, 2009. **20**(6): p. 1159-71.
85. Chao, S.H., et al., *Activation of calmodulin by various metal cations as a function of ionic radius.* Mol Pharmacol, 1984. **26**(1): p. 75-82.
86. Chao, S.H., C.H. Bu, and W.Y. Cheung, *Stimulation of myosin light-chain kinase by Cd2+ and Pb2+*. Arch Toxicol, 1995. **69**(3): p. 197-203.
87. Goldstein, G.W. and D. Ar, *Lead activates calmodulin sensitive processes.* Life Sci, 1983. **33**(10): p. 1001-6.
88. Habermann, E., K. Crowell, and P. Janicki, *Lead and other metals can substitute for Ca2+ in calmodulin.* Arch Toxicol, 1983. **54**(1): p. 61-70.
89. Milos, M., et al., *Calcium-proton and calcium-magnesium antagonisms in calmodulin: microcalorimetric and potentiometric analyses.* Biochemistry, 1986. **25**(20): p. 6279-87.
90. Bertini, I., et al., *Tuning the affinity for lanthanides of calcium binding proteins.* Biochemistry, 2003. **42**(26): p. 8011-21.
91. Wu, H.Y., K. Tomizawa, and H. Matsui, *Calpain-calcineurin signaling in the pathogenesis of calcium-dependent disorder.* Acta Med Okayama, 2007. **61**(3): p. 123-37.
92. Mattiazzi, A., L. Vittone, and C. Mundina-Weilenmann, *Ca2+/calmodulin-dependent protein kinase: a key component in the contractile recovery from acidosis.* Cardiovasc Res, 2007. **73**(4): p. 648-56.
93. DeLano, W.L., *The PyMOL Molecular Graphics System*. 2002.
94. Maximciuc, A.A., et al., *Complex of calmodulin with a ryanodine receptor target reveals a novel, flexible binding mode.* Structure, 2006. **14**(10): p. 1547-56.
95. Yamaguchi, N., et al., *Early cardiac hypertrophy in mice with impaired calmodulin regulation of cardiac muscle Ca release channel.* J Clin Invest, 2007. **117**(5): p. 1344-53.
96. Fruen, B.R., et al., *Direct detection of calmodulin tuning by ryanodine receptor channel targets using a Ca2+-sensitive acrylodan-labeled calmodulin.* Biochemistry, 2005. **44**(1): p. 278-84.
97. Fruen, B.R., et al., *Differential Ca(2+) sensitivity of skeletal and cardiac muscle ryanodine receptors in the presence of calmodulin.* Am J Physiol Cell Physiol, 2000. **279**(3): p. C724-33.
98. Fruen, B.R., et al., *Regulation of the RYR1 and RYR2 Ca2+ release channel isoforms by Ca2+-insensitive mutants of calmodulin.* Biochemistry, 2003. **42**(9): p. 2740-7.
99. Thandroyen, F.T., et al., *Intracellular calcium transients and arrhythmia in isolated heart cells.* Circ Res, 1991. **69**(3): p. 810-9.
100. Dekker, L.R., et al., *Intracellular Ca2+, intercellular electrical coupling, and mechanical activity in ischemic rabbit papillary muscle. Effects of preconditioning and metabolic blockade.* Circ Res, 1996. **79**(2): p. 237-46.
101. Saez, J.C., et al., *Plasma membrane channels formed by connexins: their regulation and functions.* Physiol Rev, 2003. **83**(4): p. 1359-400.
102. Severs, N.J., *The cardiac muscle cell.* Bioessays, 2000. **22**(2): p. 188-99.

103. van Veen, A.A., H.V. van Rijen, and T. Opthof, *Cardiac gap junction channels: modulation of expression and channel properties.* Cardiovasc Res, 2001. **51**(2): p. 217-29.
104. Oosthoek, P.W., et al., *Immunohistochemical delineation of the conduction system. II: The atrioventricular node and Purkinje fibers.* Circ Res, 1993. **73**(3): p. 482-91.
105. Oosthoek, P.W., et al., *Immunohistochemical delineation of the conduction system. I: The sinoatrial node.* Circ Res, 1993. **73**(3): p. 473-81.
106. Kirchhoff, S., et al., *Abnormal cardiac conduction and morphogenesis in connexin40 and connexin43 double-deficient mice.* Circ Res, 2000. **87**(5): p. 399-405.
107. Kumai, M., et al., *Loss of connexin45 causes a cushion defect in early cardiogenesis.* Development, 2000. **127**(16): p. 3501-12.
108. Vaidya, D., et al., *Null mutation of connexin43 causes slow propagation of ventricular activation in the late stages of mouse embryonic development.* Circ Res, 2001. **88**(11): p. 1196-202.
109. Balshaw, D.M., N. Yamaguchi, and G. Meissner, *Modulation of intracellular calcium-release channels by calmodulin.* J Membr Biol, 2002. **185**(1): p. 1-8.
110. Fill, M. and J.A. Copello, *Ryanodine receptor calcium release channels.* Physiol Rev, 2002. **82**(4): p. 893-922.
111. Franzini-Armstrong, C. and F. Protasi, *Ryanodine receptors of striated muscles: a complex channel capable of multiple interactions.* Physiol Rev, 1997. **77**(3): p. 699-729.
112. Meissner, G., *Regulation of mammalian ryanodine receptors.* Front Biosci, 2002. **7**: p. d2072-80.
113. Jongsma, H.J. and R. Wilders, *Gap junctions in cardiovascular disease.* Circ Res, 2000. **86**(12): p. 1193-7.
114. Zhou, Y., et al., *Identification of the calmodulin binding domain of connexin 43.* J Biol Chem, 2007. **282**(48): p. 35005-17.
115. Wallace, R.W., et al., *Calcium binding domains of calmodulin. Sequence of fill as determined with terbium luminescence.* J Biol Chem, 1982. **257**(4): p. 1845-54.
116. Andersson, A., et al., *A 113Cd and 1H NMR study of the interaction of calmodulin with D600, trifluoperazine and some other hydrophobic drugs.* Eur J Biochem, 1983. **134**(3): p. 459-65.
117. Baudier, J., et al., *Zinc ion binding to human brain calcium binding proteins, calmodulin and S100b protein.* Biochem Biophys Res Commun, 1983. **114**(3): p. 1138-46.
118. Wilkins, A.L., et al., *Metal-binding studies for a de novo designed calcium-binding protein.* Protein Eng, 2002. **15**(7): p. 571-4.
119. Fillion, M., et al., *A preliminary study of mercury exposure and blood pressure in the Brazilian Amazon.* Environ Health, 2006. **5**: p. 29.
120. Passos, C.J., et al., *Epidemiologic confirmation that fruit consumption influences mercury exposure in riparian communities in the Brazilian Amazon.* Environ Res, 2007. **105**(2): p. 183-93.
121. Passos, C.J., et al., *Fish consumption and bioindicators of inorganic mercury exposure.* Sci Total Environ, 2007. **373**(1): p. 68-76.
122. Houston, M.C., *The role of mercury and cadmium heavy metals in vascular disease, hypertension, coronary heart disease, and myocardial infarction.* Altern Ther Health Med, 2007. **13**(2): p. S128-33.
123. Tomera, J.F. and C. Harakal, *Multiple linear regression analysis of blood pressure, hypertrophy, calcium and cadmium in hypertensive and non-hypertensive states.* Food Chem Toxicol, 1997. **35**(7): p. 713-8.
124. Tomera, J.F., K. Lilford, and C. Harakal, *Multiple linear regression analysis of hypertrophy, calcium and cadmium in hypertensive and non-hypertensive states.* Food Chem Toxicol, 1995. **33**(6): p. 529-35.
125. Lustberg, M. and E. Silbergeld, *Blood lead levels and mortality.* Arch Intern Med, 2002. **162**(21): p. 2443-9.
126. Menke, A., et al., *Blood lead below 0.48 micromol/L (10 microg/dL) and mortality among US adults.* Circulation, 2006. **114**(13): p. 1388-94.
127. Navas-Acien, A., et al., *Lead, cadmium, smoking, and increased risk of peripheral arterial disease.* Circulation, 2004. **109**(25): p. 3196-201.
128. Schober, S.E., et al., *Blood lead levels and death from all causes, cardiovascular disease, and cancer: results from the NHANES III mortality study.* Environ Health Perspect, 2006. **114**(10): p. 1538-41.

129. Yang W, J.L., Isley L, Ye Y, Lee HW, Wilkins AL, Liu Z, Hellinga HW, Malchow R, Ghazi M, Yang JJ, *Rational Design of a Calcium-Binding Protein.* Journal of the American Chemical Society, 2003. **125**: p. 6165-6171.
130. Nelson, M.R., et al., *The EF-hand domain: a globally cooperative structural unit.* Protein Sci, 2002. **11**(2): p. 198-205.
131. Strynadka, N.C. and M.N. James, *Crystal structures of the helix-loop-helix calcium-binding proteins.* Annu Rev Biochem, 1989. **58**: p. 951-98.
132. Yap, K.L., et al., *Calmodulin target database.* J Struct Funct Genomics, 2000. **1**(1): p. 8-14.
133. Ouyang, H. and H.J. Vogel, *Metal ion binding to calmodulin: NMR and fluorescence studies.* Biometals, 1998. **11**(3): p. 213-22.
134. Wilson, M.A. and A.T. Brunger, *Domain flexibility in the 1.75 A resolution structure of Pb2+-calmodulin.* Acta Crystallogr D Biol Crystallogr, 2003. **59**(Pt 10): p. 1782-92.
135. Aramini, J.M., et al., *Lead-207 NMR: a novel probe for the study of calcium-binding proteins.* Journal of Biological Inorganic Chemistry, 1996. **1**(1): p. 39-48.
136. Kirberger, M. and J.J. Yang, *Structural differences between Pb(2+)- and Ca(2+)-binding sites in proteins: Implications with respect to toxicity.* J Inorg Biochem, 2008.
137. Ferguson, C., M. Kern, and G. Audesirk, *Nanomolar concentrations of inorganic lead increase Ca2+ efflux and decrease intracellular free Ca2+ ion concentrations in cultured rat hippocampal neurons by a calmodulin-dependent mechanism.* Neurotoxicology, 2000. **21**(3): p. 365-78.
138. Suzuki, Y., et al., *Stimulation of calmodulin by cadmium ion.* Arch Toxicol, 1985. **57**(3): p. 205-11.
139. Linse, S., A. Helmersson, and S. Forsen, *Calcium binding to calmodulin and its globular domains.* J Biol Chem, 1991. **266**(13): p. 8050-4.
140. Ikura, M., et al., *Nuclear magnetic resonance studies on calmodulin: calcium-induced conformational change.* Biochemistry, 1983. **22**(10): p. 2573-9.
141. Andersson, A., et al., *Cadmium-113 nuclear magnetic resonance studies of proteolytic fragments of calmodulin: assignment of strong and weak cation binding sites.* Biochemistry, 1983. **22**(10): p. 2309-13.
142. Palmer, A.G., M. Rance, and P.E. Wright, *Intramolecular motions of a zinc finger DNA-binding domain from Xfin characterized by proton-detected natural abundance carbon-13 heteronuclear NMR spectroscopy.* Journal of the American Chemical Society, 1991. **113**(12): p. 4371-4380.
143. Mandel, A.M., M. Akke, and A.G. Palmer, 3rd, *Backbone dynamics of Escherichia coli ribonuclease HI: correlations with structure and function in an active enzyme.* J Mol Biol, 1995. **246**(1): p. 144-63.
144. Kohler, G. and C. Milstein, *Continuous cultures of fused cells secreting antibody of predefined specificity.* Nature, 1975. **256**(5517): p. 495-7.
145. Milenic, D.E., E.D. Brady, and M.W. Brechbiel, *Antibody-targeted radiation cancer therapy.* Nat Rev Drug Discov, 2004. **3**(6): p. 488-99.
146. Milenic, D.E., *Monoclonal antibody-based therapy strategies: providing options for the cancer patient.* Curr Pharm Des, 2002. **8**(19): p. 1749-64.
147. Schroff, R.W., et al., *Human anti-murine immunoglobulin responses in patients receiving monoclonal antibody therapy.* Cancer Res, 1985. **45**(2): p. 879-85.
148. Hortobagyi, G.N. and E.A. Perez, *Integration of trastuzumab into adjuvant systemic therapy of breast cancer: ongoing and planned clinical trials.* Semin Oncol, 2001. **28**(5 Suppl 16): p. 41-6.
149. Pagel, J.M., et al., *The use of radioimmunoconjugates in stem cell transplantation.* Bone Marrow Transplant, 2002. **29**(10): p. 807-16.
150. Gopal, A.K., et al., *High-dose radioimmunotherapy versus conventional high-dose therapy and autologous hematopoietic stem cell transplantation for relapsed follicular non-Hodgkin lymphoma: a multivariable cohort analysis.* Blood, 2003. **102**(7): p. 2351-7.
151. Ruegg, C.L., et al., *Improved in vivo stability and tumor targeting of bismuth-labeled antibody.* Cancer Res, 1990. **50**(14): p. 4221-6.
152. Milenic, D.E., et al., *In vivo evaluation of bismuth-labeled monoclonal antibody comparing DTPA-derived bifunctional chelates.* Cancer Biother Radiopharm, 2001. **16**(2): p. 133-46.
153. Jurcic, J.G., et al., *Targeted alpha particle immunotherapy for myeloid leukemia.* Blood, 2002. **100**(4): p. 1233-9.

154. Alvarez, R.D., et al., *Intraperitoneal radioimmunotherapy of ovarian cancer with 177Lu-CC49: a phase I/II study.* Gynecol Oncol, 1997. **65**(1): p. 94-101.
155. Milenic, D.E., et al., *In vivo comparison of macrocyclic and acyclic ligands for radiolabeling of monoclonal antibodies with 177Lu for radioimmunotherapeutic applications.* Nucl Med Biol, 2002. **29**(4): p. 431-42.
156. Roselli, M., et al., *In vivo comparison of CHX-DTPA ligand isomers in athymic mice bearing carcinoma xenografts.* Cancer Biother Radiopharm, 1999. **14**(3): p. 209-20.
157. Barbalace, K.L. *EnvironmentalChemistry.com*. 2009; Available from: http://environmentalchemistry.com/yogi/periodic/.
158. Mulligan, T., et al., *Phase I study of intravenous Lu-labeled CC49 murine monoclonal antibody in patients with advanced adenocarcinoma.* Clin Cancer Res, 1995. **1**(12): p. 1447-54.
159. O'Donnell, R.T., et al., *A clinical trial of radioimmunotherapy with 67Cu-2IT-BAT-Lym-1 for non-Hodgkin's lymphoma.* J Nucl Med, 1999. **40**(12): p. 2014-20.
160. Humm, J.L., *Dosimetric aspects of radiolabeled antibodies for tumor therapy.* J Nucl Med, 1986. **27**(9): p. 1490-7.
161. Bass, L.A., et al., *In vivo transchelation of copper-64 from TETA-octreotide to superoxide dismutase in rat liver.* Bioconjug Chem, 2000. **11**(4): p. 527-32.
162. Rogers, B.E., et al., *Comparison of four bifunctional chelates for radiolabeling monoclonal antibodies with copper radioisotopes: biodistribution and metabolism.* Bioconjug Chem, 1996. **7**(4): p. 511-22.
163. Kurtzman, S.H., et al., *212Bismuth linked to an antipancreatic carcinoma antibody: model for alpha-particle-emitter radioimmunotherapy.* J Natl Cancer Inst, 1988. **80**(6): p. 449-52.
164. McDevitt, M.R., et al., *Radioimmunotherapy with alpha-emitting nuclides.* Eur J Nucl Med, 1998. **25**(9): p. 1341-51.
165. Hassfjell, S. and M.W. Brechbiel, *The development of the alpha-particle emitting radionuclides 212Bi and 213Bi, and their decay chain related radionuclides, for therapeutic applications.* Chem Rev, 2001. **101**(7): p. 2019-36.
166. Geerlings, M.W., *Radionuclides for radioimmunotherapy: criteria for selection.* Int J Biol Markers, 1993. **8**(3): p. 180-6.
167. McDevitt, M.R., et al., *Tumor therapy with targeted atomic nanogenerators.* Science, 2001. **294**(5546): p. 1537-40.
168. Jones, L.M., et al., *Rational design of a novel calcium-binding site adjacent to the ligand-binding site on CD2 increases its CD48 affinity.* Protein Sci, 2008. **17**(3): p. 439-49.
169. Li, S., et al., *Rational design of a conformation-switchable Ca2+- and Tb3+-binding protein without the use of multiple coupled metal-binding sites.* Febs J, 2008. **275**(20): p. 5048-61.
170. Yang, J.J., A. Gawthrop, and Y. Ye, *Obtaining site-specific calcium-binding affinities of calmodulin.* Protein Pept Lett, 2003. **10**(4): p. 331-45.
171. Yang, W., et al., *Structural analysis, identification and design of calcium-binding sites in proteins.* Proteins, 2002. **47**: p. 344-356.
172. Yang, W., et al., *The effects of Ca2+ binding on the dynamic properties of a designed Ca2+-binding protein.* Biochemistry, 2005. **44**(23): p. 8267-73.
173. Ye, Y., et al., *Probing site-specific calmodulin calcium and lanthanide affinity by grafting.* J Am Chem Soc, 2005. **127**(11): p. 3743-50.
174. Ye, Y., et al., *Metal binding affinity and structural properties of an isolated EF-loop in a scaffold protein.* Protein Eng, 2001. **14**(12): p. 1001-13.
175. Ye, Y., et al., *Calcium and lanthanide affinity of the EF-loops from the C-terminal domain of calmodulin.* J Inorg Biochem, 2005. **99**(6): p. 1376-83.
176. Yang, W., et al., *Rational design of a calcium-binding protein.* J Am Chem Soc, 2003. **125**(20): p. 6165-71.
177. Maniccia, A.W., et al., *Using protein design to dissect the effect of charged residues on metal binding and protein stability.* Biochemistry, 2006. **45**(18): p. 5848-56.
178. Zhou, Y., et al., *Prediction of EF-hand calcium-binding proteins and analysis of bacterial EF-hand proteins.* Proteins, 2006. **65**(3): p. 643-55.
179. Harding, M.M., *The architecture of metal coordination groups in proteins.* Acta Crystallogr D Biol Crystallogr, 2004. **60**(Pt 5): p. 849-59.

180. Harding, M.M., *Metal-ligand geometry relevant to proteins and in proteins: sodium and potassium.* Acta Crystallogr D Biol Crystallogr, 2002. **58**(Pt 5): p. 872-4.
181. Dudev, T., et al., *First-second shell interactions in metal binding sites in proteins: a PDB survey and DFT/CDM calculations.* J Am Chem Soc, 2003. **125**(10): p. 3168-80.
182. Nayal, M. and E. Di Cera, *Predicting Ca(2+)-binding sites in proteins.* Proc Natl Acad Sci U S A, 1994. **91**(2): p. 817-21.
183. Deng, H., et al., *Predicting calcium-binding sites in proteins - a graph theory and geometry approach.* Proteins, 2006. **64**(1): p. 34-42.
184. Thompson, J.D., D.G. Higgins, and T.J. Gibson, *CLUSTAL W: improving the sensitivity of progressive multiple sequence alignment through sequence weighting, position-specific gap penalties and weight matrix choice.* Nucleic Acids Res, 1994. **22**(22): p. 4673-80.
185. Page, R.D., *TreeView: an application to display phylogenetic trees on personal computers.* Comput Appl Biosci, 1996. **12**(4): p. 357-8.
186. Murzin, A.G., et al., *SCOP: a structural classification of proteins database for the investigation of sequences and structures.* J Mol Biol, 1995. **247**(4): p. 536-40.
187. Sarret G, M.A., Spadini L, Roux JC, Hazemann JL, Soldo Y, Eybert-Berard L, Menthonnex JJ, *Structural Determination of Zn and Pb Binding Sites in Penicillium chrysogenum Cell Walls by EXAFS Spectroscopy.* Environ Sci Technol, 1998. **32**: p. 1648-1655.
188. Swain, A.L., R.H. Kretsinger, and E.L. Amma, *Restrained least squares refinement of native (calcium) and cadmium-substituted carp parvalbumin using X-ray crystallographic data at 1.6-A resolution.* J Biol Chem, 1989. **264**(28): p. 16620-8.
189. Cruickshank, D.W., *Remarks about protein structure precision.* Acta Crystallogr D Biol Crystallogr, 1999. **55**(Pt 3): p. 583-601.
190. Sorensen, B.R. and M.A. Shea, *Interactions between domains of apo calmodulin alter calcium binding and stability.* Biochemistry, 1998. **37**(12): p. 4244-53.
191. VanScyoc, W.S., et al., *Calcium binding to calmodulin mutants monitored by domain-specific intrinsic phenylalanine and tyrosine fluorescence.* Biophys J, 2002. **83**(5): p. 2767-80.
192. Yang, J.J., et al., *Rational design of protein-based MRI contrast agents.* J Am Chem Soc, 2008. **130**(29): p. 9260-7.
193. Horniak, J. *The Basics of NMR*. 2011 [cited 2011; Available from: http://www.cis.rit.edu/htbooks/nmr/.
194. Delaglio, F., *NMRPipe*. 2009.
195. Goddard, T. and D. Kneller, *Sparky 3*: San Francisco. p. NMR Data Processing.
196. Farrow, N.A., et al., *Backbone dynamics of a free and phosphopeptide-complexed Src homology 2 domain studied by 15N NMR relaxation.* Biochemistry, 1994. **33**(19): p. 5984-6003.
197. Kay, L.E., *Pulsed field gradient multi-dimensional NMR methods for the study of protein structure and dynamics in solution.* Prog Biophys Mol Biol, 1995. **63**(3): p. 277-99.
198. Lee, H.W., et al., *Isolated EF-loop III of calmodulin in a scaffold protein remains unpaired in solution using pulsed-field-gradient NMR spectroscopy.* Biochim Biophys Acta, 2002. **1598**(1-2): p. 80-7.
199. Seifert, M.H., et al., *Backbone dynamics of green fluorescent protein and the effect of histidine 148 substitution.* Biochemistry, 2003. **42**(9): p. 2500-12.
200. Lipari, G. and A. Szabo, *Effect of librational motion on fluorescence depolarization and nuclear magnetic resonance relaxation in macromolecules and membranes.* Biophys J, 1980. **30**(3): p. 489-506.
201. Bruschweiler, R. and P.E. Wright, *NMR Order Parameters of Biomolecules: A New Analytical Representation and Application to the Gaussian Axial Fluctuation Model.* J Am Chem Soc, 1994. **116**(18): p. 8426-8427.
202. Palmer, A.G., 3rd, *Nmr probes of molecular dynamics: overview and comparison with other techniques.* Annu Rev Biophys Biomol Struct, 2001. **30**: p. 129-55.
203. Mann, K.G., et al., *Surface-dependent reactions of the vitamin K-dependent enzyme complexes.* Blood, 1990. **76**(1): p. 1-16.
204. Herzberg, O., J. Moult, and M.N. James, *A model for the Ca2+-induced conformational transition of troponin C. A trigger for muscle contraction.* J Biol Chem, 1986. **261**(6): p. 2638-44.
205. Holmes, K.C., et al., *Atomic model of the actin filament.* Nature, 1990. **347**(6288): p. 44-9.

206. Carafoli, E., *The signaling function of calcium and its regulation.* J Hypertens Suppl, 1994. **12**(10): p. S47-56.
207. Santella, L. and E. Carafoli, *Calcium signaling in the cell nucleus.* Faseb J, 1997. **11**(13): p. 1091-109.
208. Martin, R., *Bioinorganic Chemistry of Calcium.* . Metal Ions in Biological Systems, ed. H. Sigel. Vol. 17. 1984, New York: Marcel Dekker. 1-49.
209. Nelson, M.R. and W.J. Chazin, *An interaction-based analysis of calcium-induced conformational changes in Ca2+ sensor proteins.* Protein Sci, 1998. **7**(2): p. 270-82.
210. Jiang, Y., et al., *Elucidation of a novel extracellular calcium-binding site on metabotropic glutamate receptor 1{alpha} (mGluR1{alpha}) that controls receptor activation.* J Biol Chem, 2010. **285**(43): p. 33463-74.
211. Huang, Y., et al., *Calmodulin regulates Ca2+-sensing receptor-mediated Ca2+ signaling and its cell surface expression.* J Biol Chem, 2010. **285**(46): p. 35919-31.
212. Huang, Y., et al., *A single EF-hand isolated from STIM1 forms dimer in the absence and presence of Ca2+*. Febs J, 2009. **276**(19): p. 5589-97.
213. Zhou, Y., T.K. Frey, and J.J. Yang, *Viral calciomics: interplays between Ca2+ and virus.* Cell Calcium, 2009. **46**(1): p. 1-17.
214. Perm*i*akov, E.A. and R.H. Kretsinger, *Calcium binding proteins*. Wiley series in protein and peptide science. 2010, Hoboken, N.J.: Wiley.
215. Hill, E., et al., *Cadherin superfamily proteins in Caenorhabditis elegans and Drosophila melanogaster.* J Mol Biol, 2001. **305**(5): p. 1011-24.
216. Truong, K. and M. Ikura, *The cadherin superfamily database.* J Struct Funct Genomics, 2002. **2**(3): p. 135-43.
217. Yang, J.J. and W. Yang, *Encyclopedia of inorganic chemistry*. 2nd ed, ed. R.B. King. 2005, New York: Wiley.
218. Marsden, B.J., G.S. Shaw, and B.D. Sykes, *Calcium binding proteins. Elucidating the contributions to calcium affinity from an analysis of species variants and peptide fragments.* Biochem Cell Biol, 1990. **68**(3): p. 587-601.
219. McPhalen, C.A., N.C. Strynadka, and M.N. James, *Calcium-binding sites in proteins: a structural perspective.* Adv Protein Chem, 1991. **42**: p. 77-144.
220. Einspahr, H., W.J. Cook, and C.E. Bugg, *Conformational flexibility in single-stranded oligonucleotides: crystal structure of a hydrated calcium salt of adenylyl-(3'--5')-adenosine.* Biochemistry, 1981. **20**(20): p. 5788-94.
221. Shimoni-Livny, L., J.P. Glusker, and C.W. Bock, *Lone pair functionality in divalent lead compounds.* Inorganic Chemistry, 1998. **37**(8): p. 1853-1867.
222. Wang, X., et al., *Towards predicting Ca(2+)-binding sites with different coordination numbers in proteins with atomic resolution.* Proteins, 2008. **75**(4): p. 787-798.
223. Nelson, M.R. and W.J. Chazin, *The EF-Hand Calcium-Binding Proteins Data Library*. 1997.
224. Kawasaki, H., S. Nakayama, and R.H. Kretsinger, *Classification and evolution of EF-hand proteins.* Biometals, 1998. **11**(4): p. 277-95.
225. Kretsinger, R.H. and C.E. Nockolds, *Carp muscle calcium-binding protein. II. Structure determination and general description.* J Biol Chem, 1973. **248**(9): p. 3313-26.
226. Harding, M.M., *Small revisions to predicted distances around metal sites in proteins.* Acta Crystallogr D Biol Crystallogr, 2006. **62**(Pt 6): p. 678-82.
227. Einspahr H and C.E. Bugg, *Crystal Structure Studies of Calcium Complexes and Implications for Biological Systems*, in *Calcium and its role in biology*, H. Sigel, Editor. 1984, M. Dekker: New York. p. 52-97.
228. Vyas, M.N., B.L. Jacobson, and F.A. Quiocho, *The calcium-binding site in the galactose chemoreceptor protein. Crystallographic and metal-binding studies.* J Biol Chem, 1989. **264**(34): p. 20817-21.
229. Kirberger, M., et al., *Statistical analysis of structural characteristics of protein Ca(2+)-binding sites.* J Biol Inorg Chem, 2008.
230. Biekofsky, R.R., et al., *Ab initio study of NMR 15N chemical shift differences induced by Ca2+ binding to EF-hand proteins.* Biochemistry, 2004. **43**(21): p. 6554-64.

231. Ishida, H., et al., *Solution structures of the N-terminal domain of yeast calmodulin: Ca2+-dependent conformational change and its functional implication.* Biochemistry, 2000. **39**(45): p. 13660-8.
232. Grabarek, Z., *Structural basis for diversity of the EF-hand calcium-binding proteins.* J Mol Biol, 2006. **359**(3): p. 509-25.
233. Gifford, J.L., M.P. Walsh, and H.J. Vogel, *Structures and metal-ion-binding properties of the Ca2+-binding helix-loop-helix EF-hand motifs.* Biochem J, 2007. **405**(2): p. 199-221.
234. Stathopulos, P.B., et al., *Structural and mechanistic insights into STIM1-mediated initiation of store-operated calcium entry.* Cell, 2008. **135**(1): p. 110-22.
235. Donato, R., *S100: a multigenic family of calcium-modulated proteins of the EF-hand type with intracellular and extracellular functional roles.* Int J Biochem Cell Biol, 2001. **33**(7): p. 637-68.
236. Rigden, D.J. and M.Y. Galperin, *The DxDxDG motif for calcium binding: multiple structural contexts and implications for evolution.* J Mol Biol, 2004. **343**(4): p. 971-84.
237. Korndorfer, I.P., F. Brueckner, and A. Skerra, *The crystal structure of the human (S100A8/S100A9)2 heterotetramer, calprotectin, illustrates how conformational changes of interacting alpha-helices can determine specific association of two EF-hand proteins.* J Mol Biol, 2007. **370**(5): p. 887-98.
238. Nalefski, E.A. and J.J. Falke, *Cation charge and size selectivity of the C2 domain of cytosolic phospholipase A(2).* Biochemistry, 2002. **41**(4): p. 1109-22.
239. Mellanby, J. and V.J. Woolley, *The ferments of the pancreas: Part II. The action of calcium salts in the generation of trypsin from trypsinogen.* J Physiol, 1913. **46**(2): p. 159-72.
240. Tajima, M., et al., *Role of calcium ions in the thermostability of thermolysin and Bacillus subtilis var. amylosaccharitícus neutral protease.* Eur J Biochem, 1976. **64**(1): p. 243-7.
241. Betzel, C., G.P. Pal, and W. Saenger, *Three-dimensional structure of proteinase K at 0.15-nm resolution.* Eur J Biochem, 1988. **178**(1): p. 155-71.
242. Shin, S., et al., *The Tightly Bound Calcium of MauG Is Required for Tryptophan Tryptophylquinone Cofactor Biosynthesis.* Biochemistry, 2010.
243. Schreiber, M. and L. Salkoff, *A novel calcium-sensing domain in the BK channel.* Biophys J, 1997. **73**(3): p. 1355-63.
244. Falke, J.J., et al., *Molecular tuning of ion binding to calcium signaling proteins.* Q Rev Biophys, 1994. **27**(3): p. 219-90.
245. Yang, W., et al., *Structural analysis, identification, and design of calcium-binding sites in proteins.* Proteins, 2002. **47**(3): p. 344-56.
246. Cheng, Y., et al., *Crystallographic identification of Ca2+ and Sr2+ coordination sites in synaptotagmin I C2B domain.* Protein Sci, 2004. **13**(10): p. 2665-72.
247. Tanaka, Y., et al., *Structural and mutational analyses of Drp35 from Staphylococcus aureus: a possible mechanism for its lactonase activity.* J Biol Chem, 2007. **282**(8): p. 5770-80.
248. Brux, C., et al., *The structure of an inverting GH43 beta-xylosidase from Geobacillus stearothermophilus with its substrate reveals the role of the three catalytic residues.* J Mol Biol, 2006. **359**(1): p. 97-109.
249. Vallee, F., et al., *Barley alpha-amylase bound to its endogenous protein inhibitor BASI: crystal structure of the complex at 1.9 A resolution.* Structure, 1998. **6**(5): p. 649-59.
250. Honig, B. and A. Nicholls, *Classical electrostatics in biology and chemistry.* Science, 1995. **268**(5214): p. 1144-9.
251. Rocchia, W., E. Alexov, and B. Honig, *Extending the applicability of the nonlinear Poisson-Boltzmann equation: Multiple dielectric constants and multivalent ions.* Journal of Physical Chemistry B, 2001. **105**(28): p. 6507-6514.
252. Yang, A.S., et al., *On the Calculation of Pk(a)S in Proteins.* Proteins-Structure Function and Genetics, 1993. **15**(3): p. 252-265.
253. Gilson, M.K. and B. Honig, *Calculation of the total electrostatic energy of a macromolecular system: solvation energies, binding energies, and conformational analysis.* Proteins, 1988. **4**(1): p. 7-18.
254. Nicholls, A. and B. Honig, *A rapid finite difference algorithm, utilizing successive over-relaxation to solve the Poisson-Boltzmann equation.* J Comp Chem, 1991. **12**: p. 435-445.
255. Wenk, M., et al., *The domains of protein S from Myxococcus xanthus: structure, stability and interactions.* J Mol Biol, 1999. **286**(5): p. 1533-45.

256. Linse, S., et al., *The role of protein surface charges in ion binding.* Nature, 1988. **335**(6191): p. 651-2.
257. Linse, S. and S. Forsen, *Determinants that govern high-affinity calcium binding.* Adv Second Messenger Phosphoprotein Res, 1995. **30**: p. 89-151.
258. Vogt, G., S. Woell, and P. Argos, *Protein thermal stability, hydrogen bonds, and ion pairs.* J Mol Biol, 1997. **269**(4): p. 631-43.
259. Magyar, J.S., et al., *Reexamination of lead(II) coordination preferences in sulfur-rich sites: implications for a critical mechanism of lead poisoning.* J Am Chem Soc, 2005. **127**(26): p. 9495-505.
260. Willard, L., et al., *VADAR: a web server for quantitative evaluation of protein structure quality.* Nucleic Acids Res, 2003. **31**(13): p. 3316-9.
261. Bergdahl, I.A., et al., *Lead binding to delta-aminolevulinic acid dehydratase (ALAD) in human erythrocytes.* Pharmacol Toxicol, 1997. **81**(4): p. 153-8.
262. Kelada, S.N., et al., *Delta-aminolevulinic acid dehydratase genotype and lead toxicity: a HuGE review.* Am J Epidemiol, 2001. **154**(1): p. 1-13.
263. Erskine, P.T., et al., *MAD analyses of yeast 5-aminolaevulinate dehydratase: their use in structure determination and in defining the metal-binding sites.* Acta Crystallogr D Biol Crystallogr, 2000. **56**(Pt 4): p. 421-30.
264. Wang, Y., L. Hemmingsen, and D.P. Giedroc, *Structural and functional characterization of Mycobacterium tuberculosis CmtR, a PbII/CdII-sensing SmtB/ArsR metalloregulatory repressor.* Biochemistry, 2005. **44**(25): p. 8976-88.
265. Kirberger, M.P., *Analyses and applications of metalloprotein complexes*. 2007.
266. Ye, Y., et al., *A grafting approach to obtain site-specific metal-binding properties of EF-hand proteins.* Protein Eng, 2003. **16**(6): p. 429-34.
267. Jiang, J., et al., *Site-specific modification of calmodulin Ca(2)(+) affinity tunes the skeletal muscle ryanodine receptor activation profile.* Biochem J, 2010. **432**(1): p. 89-99.
268. Kuboniwa, H., et al., *Solution structure of calcium-free calmodulin.* Nat Struct Biol, 1995. **2**(9): p. 768-76.
269. Torizawa, T., et al., *Efficient production of isotopically labeled proteins by cell-free synthesis: a practical protocol.* J Biomol NMR, 2004. **30**(3): p. 311-25.
270. Biekofsky, R.R., et al., *Ca2+ coordination to backbone carbonyl oxygen atoms in calmodulin and other EF-hand proteins: 15N chemical shifts as probes for monitoring individual-site Ca2+ coordination.* Biochemistry, 1998. **37**(20): p. 7617-29.
271. Barbato, G., et al., *Backbone dynamics of calmodulin studied by 15N relaxation using inverse detected two-dimensional NMR spectroscopy: the central helix is flexible.* Biochemistry, 1992. **31**(23): p. 5269-78.
272. Kursula, P. and V. Majava, *A structural insight into lead neurotoxicity and calmodulin activation by heavy metals.* Acta Crystallogr Sect F Struct Biol Cryst Commun, 2007. **63**(Pt 8): p. 653-6.
273. Wang, X., et al., *Analysis and prediction of calcium-binding pockets from apo protein structures exhibiting calcium-induced localized conformational changes.* Protein Sci, 2010.
274. Raos, N. and K.S. Kasprzak, *Allosteric binding of nickel(II) to calmodulin.* Fundam Appl Toxicol, 1989. **13**(4): p. 816-22.
275. Dowd, T.L., L. Li, and C.M. Gundberg, *The (1)H NMR structure of bovine Pb(2+)-osteocalcin and implications for lead toxicity.* Biochim Biophys Acta, 2008. **1784**(11): p. 1534-45.
276. Fallon, J.L. and F.A. Quiocho, *A closed compact structure of native Ca(2+)-calmodulin.* Structure, 2003. **11**(10): p. 1303-7.
277. McCall, K.A. and C.A. Fierke, *Colorimetric and fluorimetric assays to quantitate micromolar concentrations of transition metals.* Anal Biochem, 2000. **284**(2): p. 307-15.
278. Hunt, J.B., S.H. Neece, and A. Ginsburg, *The use of 4-(2-pyridylazo)resorcinol in studies of zinc release from Escherichia coli aspartate transcarbamoylase.* Anal Biochem, 1985. **146**(1): p. 150-7.
279. Invitrogen. Available from: http://www.invitrogen.com/site/us/en/home/Products-and-Services/Applications/Drug-Discovery/Target-and-Lead-Identification-and-Validation/g-protein_coupled_html/cell-based-second-messenger-assays/Fura-2-calcium-indicator.html.

9 Appendix

9.1 Derivation of quadratic equation for data curve-fitting

$$MP \overset{K_d}{\Leftrightarrow} M + P \quad \text{(Eq. A1)}$$

$$K_d = ([M]_{free}[P]_{free}) / [MP] \quad \text{(Eq. A2)}$$

$$K_d = k_{off} / k_{on} \quad \text{(Eq. A3)}$$

$$F = \frac{[MP]}{[P]_T} = \frac{[MP]}{[M]_{free} + [MP]} \quad \text{(Eq. A4)}$$

$$F[P]_T = [MP] \quad \text{(Eq. A5)}$$

$$[P]_{free} = [P]_T - [MP] \quad \text{(Eq. A6)}$$

$$[P]_{free} = [P]_T - F[P]_T \quad \text{(Eq. A7)}$$

$$[P]_{free} = [P]_T (1 - F) \quad \text{(Eq. A8)}$$

$$[M]_T = [M]_{free} + [MP] \quad \text{(Eq. A9)}$$

$$[M]_{free} = [M]_T - [MP] \quad \text{(Eq. A10)}$$

$$[M]_{free} = [M]_T - F[P]_T \quad \text{(Eq. A11)}$$

$$K_d = ([M]_T - F[P]_T)([P]_T (1 - F)) / F[P]_T \quad \text{(Eq. A12)}$$

$$F = \frac{([P]_T + [M]_T + K_d) - (([P]_T + [M]_T + K_d)^2 - 4[P]_T[M]_T)^{1/2}}{2[P]_T} \quad \text{(Eq. A13)}$$

9.2 Explanation for Eq. 3

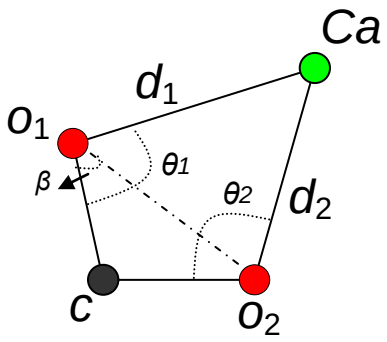

In the observed figure, we make the following two assumptions:

(1) The carbon atom *c*, its associated two oxygen atoms o_1, o_2, and the calcium ion *Ca* are lying on the same plane.
(2) The length between *c* and o_1 is equivalent to that between *c* and o_2.

In triangle $o_1o_2c_a$, according to the law of sines, we have:

$$\frac{d_1}{\sin\angle c_a o_2 o_1} = \frac{d_2}{\sin\angle c_a o_1 o_2} \Leftrightarrow \frac{d_1}{\sin(\theta_2-\beta)} = \frac{d_2}{\sin(\theta_1-\beta)} \Leftrightarrow \frac{d_1}{d_2} = \frac{\sin(\theta_2-\beta)}{\sin(\theta_1-\beta)}$$

According to our statistical analysis results, the dihedral angle measured between the plane formed by *c*, o_1 and o_2, and the plane formed by o_1, o_2, and c_a had a mean value of 170.6 ± 7.1 (°), which is the basis for assumption (1). Furthermore, the length between *c* and o_1 (d_1) is very close to that between c and o_2 (d_2) which is the basis for assumption (2).

9.3 Supplementary figures and tables

Table A.1 PDB data by Pb^{2+} -binding site

PDB_ID	SN	PL	PLW	FC	Binding	PDB_ID	SN	PL	PLW	FC	Binding
1afv	9029	2	2	-1	O	*1n0y	1322	7	8	-4	D (Ca)
1e9n	4341	3	4	-1	D (Mg)	*1n0y	1323	2	3	-1	O
1e9n	4342	1	2	-1	D (Mg)	*1n0y	1324	6	7	-3	D (Ca)
1fjr	3168	2	5	-1	O	*1na0	1973	1	1	-1	O
1fjr	3169	2	2	-1	O	*1na0	1975	2	2	-1	O
1hd7	2072	3	7	-2	D (Mg)	*1na0	1976	2	2	-2	O
*1hqj	1645	1	3	-1	O	1qnv	2548	4	4	-3	D (Zn)
*1hqj	1646	1	2	-1	O	1qnv	2549	2	2	-1	O
*1hqj	1647	1	2	0	O	1qr7	10296	5	5	-3	D (Mn)
*1hqj	1648	1	3	-1	O	1sn8	1330	1	1	0	O
*1hqj	1649	3	4	-2	O	1sn8	1331	2	3	-1	O
*1hqj	1650	2	2	-1	O	*1syy	2617	2	2	-1	D (Fe)
*1hqj	1651	2	2	-2	O	1v0d	1940	1	1	-1	U
1iw7	53577	4	4	-3	D (Zn)	1xxa	3715	2	4	0	O
1iw7	53578	4	4	-4	D (Zn)	1xxa	3716	1	3	0	O
1ka4	4165	3	4	-1	O	*1zhw	3516	2	2	-1	O
*1n0y	1314	4	4	-3	O	*1zhy	3516	3	3	-1	O
*1n0y	1315	8	9	-4	D (Ca)	*1zhy	3517	2	2	-1	O
*1n0y	1316	2	2	-1	O	2ani	2618	2	3	-1	O
*1n0y	1317	7	8	-3	D (Ca)	2ch7	4633	4	4	-2	D (Zn)
*1n0y	1318	4	4	-2	O	2ch7	4634	3	4	-2	D (Zn)
*1n0y	1319	5	6	-3	O	*2fp1	2705	5	7	-2	O
*1n0y	1320	3	3	-2	O	*2fp1	2706	4	4	-2	O
*1n0y	1321	4	5	-3	O	2g0a	4655	4	7	-2	D (Mg)

PDB_ID indicates PDB Identification. PDB_ID values preceded by ***** indicate structural resolution of 1.75 Å or better. **SN** is the PDB serial number for ion. **PL** is the number of protein ligands. **PLW** is the number of ligands from the protein and water. **FC** is the formal charge within the binding site. **Binding** indicates either opportunistic (O) where no apparent binding site is present, displacement (D) indicating other ions (listed to the right of D) previously identified with binding that may be displaced by Pb^{2+}, or unknown (U).

Table A.2 Summary of selected Ca^{2+}-binding sites

PDB ID	Ca Seq ID	PDB ID	Ca Seq ID	PDB ID	Ca Seq ID	PDB ID	Ca Seq ID	PDB ID	Ca Seq ID
1A0J	247	1JAE	500	1SVY	1	1YLI	4	2I1Q	504
1A75	109	1JE5	502	1SXN	154	1YN8	1001	2I4B	454
1A75	110	1JI1	2001	1SXN	154	1YN8	1002	2I6H	501
1A75	109	1JI1	2002	1SZO	2001	1YN8	1003	2I6H	502
1A75	110	1JI1	2003	1SZO	2002	1YN8	1004	2I6H	503
1AG9	200	1JI1	2004	1SZO	2003	1YN8	1005	2I6O	1308
1AG9	1000	1JI1	2005	1SZO	2004	1YN8	1006	2I7A	2
1AG9	300	1JI1	2006	1T0I	201	1YN8	1007	2I8T	400
1AG9	350	1JIX	600	1T0I	202	1YN8	1008	2I8T	402
1AJK	1	1JTG	645	1T1G	358	1YN8	1009	2ID3	601
1AJK	2	1JTG	702	1T61	813	1YN8	1010	2ID3	602
1ATL	403	1JUG	126	1T61	814	1YOE	1001	2ID3	603
1ATL	404	1JX6	401	1T64	389	1YRO	124	2ID3	604
1AVA	500	1K12	160	1T64	390	1YRO	124	2ID3	605
1AVA	501	1K3I	701	1T64	1390	1YS1	400	2ID3	606
1AVA	502	1K3I	702	1T6C	502	1YS6	1001	2ID3	607
1AVA	503	1K7I	480	1T9H	412	1YS6	1002	2ID4	901
1AVA	500	1K7I	481	1T9H	413	1YU0	501	2ID4	902
1AVA	501	1K7I	482	1T9H	414	1YU0	502	2ID4	903
1AVA	502	1K7I	483	1T9H	415	1YXH	1001	2ID4	904
1AVA	503	1K7I	484	1TAD	352	1YYD	371	2IE7	401
1AXN	351	1K7I	485	1TAD	352	1YYD	372	2IE7	402
1AXN	352	1K7I	487	1TAD	352	1Z0W	901	2IE7	403
1AXN	353	1K94	997	1TE2	701	1Z0W	902	2IE7	404
1AXN	354	1K94	998	1TE2	702	1Z32	497	2IE7	405
1AXN	355	1K94	999	1TE2	703	1Z6O	5302	2IE7	407
1AYO	1	1K96	91	1TE2	704	1Z6O	5303	2IE7	408
1B1C	200	1K96	92	1TF4	3001	1Z6O	6302	2IEW	501
1B2L	301	1K9U	1001	1TF4	3002	1Z6O	6303	2IG9	601
1B2V	199	1K9U	1002	1TF4	3003	1Z6O	7302	2II1	400
1B9O	124	1K9U	1003	1TF4	3004	1Z6O	7303	2II1	401
1BF2	751	1K9U	1004	1THM	301	1Z6O	8302	2II1	400
1BG7	174	1KA1	401	1THM	302	1Z6O	8303	2II1	401
1BGP	501	1KAP	614	1TKJ	905	1Z70	3001	2II1	400
1BH6	501	1KAP	615	1TN3	182	1Z70	3002	2II1	401
1BK9	200	1KAP	616	1TN3	183	1ZCH	303	2II1	400
1BLX	0	1KAP	617	1TO2	450	1ZCM	1001	2II1	401
1BN8	400	1KAP	618	1TRK	681	1ZCM	1002	2II1	1
1BQB	351	1KAP	619	1TRK	681	1ZDE	291	2II1	2
1BQB	352	1KAP	620	1TVG	221	1ZDE	292	2II1	3
1BQB	353	1KAP	621	1TZW	900	1ZED	906	2II1	4
1BU3	109	1KB0	801	1U4G	401	1ZH2	201	2II1	5
1BU3	110	1KIC	328	1U94	701	1ZH2	202	2II1	6
1BUD	900	1KIC	328	1U94	702	1ZJA	7000	2II1	7
1BYF	201	1KP4	200	1U94	703	1ZJA	7001	2IIM	600
1BYF	201	1KSC	500	1UCN	1162	1ZL7	1001	2IPX	301
1BYF	202	1KV9	802	1UCN	2162	1ZUD	601	2IPX	302

1BYF	202	1L6R	901	1UCN	3162	1ZUD	602	2IQY	501
1C1Y	173	1L6R	902	1UCN	1001	1ZW6	201	2IUF	1696
1C7I	746	1L6R	903	1UCN	1002	1ZW6	202	2IUF	1697
1C7K	134	1L6R	904	1UET	501	2A2R	1	2IUF	1697
1CB8	3000	1L6R	905	1UET	503	2A8K	401	2IUF	1698
1CEL	440	1L7L	201	1UET	504	2A8K	402	2IUF	1710
1CGT	685	1L8S	313	1UHA	100	2A8K	403	2IUF	1711
1CGT	686	1L8S	314	1UIS	1003	2A8K	404	2IVZ	1432
1CLC	591	1LE6	461	1UIS	1004	2AAO	293	2IVZ	1433
1CLC	592	1LE6	462	1UJC	157	2AAO	294	2IVZ	1432
1CLC	593	1LE6	463	1UKG	1262	2AAO	295	2IVZ	1432
1CPN	209	1LED	251	1UKG	2262	2AAO	296	2IVZ	1433
1CRU	901	1LLP	351	1UL3	601	2AAO	297	2IVZ	1432
1CRU	902	1LLP	352	1UL3	602	2AAO	298	2IVZ	1433
1CRU	903	1LOM	103	1UOW	1419	2AAO	299	2IWA	501
1CRU	904	1LOM	104	1UOW	1420	2AAO	300	2IWK	1606
1CRU	908	1LQV	34	1UPS	501	2AAO	301	2IWK	1607
1CRU	909	1LQV	35	1UPS	501	2AD6	702	2IWK	1608
1CVL	320	1LQV	36	1USR	1574	2AD6	704	2IWK	1609
1CVR	648	1LQV	37	1USR	1573	2AEF	601	2IWK	1610
1CVR	501	1LQV	38	1UV4	502	2AEF	602	2IWK	1611
1CVR	477	1LQV	39	1UV4	1294	2APR	1	2IWK	1612
1CVR	686	1LQV	40	1UWW	1192	2AYH	417	2IWK	1613
1CVR	678	1LQV	41	1UWW	1193	2B50	1303	2IWK	1614
1CVR	723	1LQV	42	1UWW	1194	2B50	2303	2IWK	1615
1CXL	688	1LQV	43	1UWW	1195	2B6N	300	2IWK	1616
1CXL	689	1LQV	44	1UWW	1191	2B9L	308	2IWK	1617
1D0B	201	1LQV	45	1UWW	1192	2BF6	1693	2IWK	1618
1D0B	202	1LQV	46	1UX6	2001	2BF6	1694	2IWK	1619
1D0L	400	1LQV	47	1UX6	2002	2BIB	1551	2IWK	1620
1D2S	401	1M1N	6492	1UX6	2003	2BIB	1552	2IWK	1621
1D2S	501	1M1N	7492	1UX6	2004	2BKO	1199	2IWK	1639
1DAF	227	1M1N	8492	1UX6	2005	2BKO	1200	2IWK	1606
1DBI	701	1M1N	9492	1UX6	2006	2BKO	1201	2IWK	1607
1DBI	703	1M6S	1300	1UX6	2007	2BKO	1202	2IWK	1608
1DBI	704	1M6S	1301	1UX6	2008	2BKO	1203	2IWK	1609
1DFX	150	1M6S	1302	1UX6	2009	2BL0	1146	2IWK	1610
1DL2	901	1M6S	1303	1UX6	2010	2BL0	1155	2IWK	1611
1DM5	1121	1M6S	1304	1UX6	2011	2BOQ	1351	2IWK	1612
1DM5	1122	1M6S	1305	1UX6	2012	2BOQ	1352	2IWK	1613
1DM5	1123	1MDW	1	1UX6	2013	2BOU	157	2IWK	1614
1DM5	1124	1MDW	2	1UX6	2014	2BOU	158	2IWK	1615
1DM5	1125	1MDW	3	1UX6	2015	2BQ4	1119	2IXT	1310
1DM5	1126	1MDW	4	1UX6	2016	2BQ4	1120	2IXT	1311
1DM5	1131	1MMQ	3	1UXX	1130	2BU3	1242	2IXT	1312
1DM5	1132	1MMQ	4	1UY4	1147	2BU3	1242	2IXT	1313
1DM5	1133	1MNZ	390	1UYY	1132	2BV2	1084	2IXT	1314
1DM5	1134	1MPX	638	1UYY	1133	2BV2	1085	2IXT	1311
1DM5	1135	1MPX	638	1UYY	1132	2BV2	1084	2IXT	1312
1DNU	1	1MPX	638	1UYY	1133	2BV2	1085	2IXT	1313

1DNU	2	1MPX	638	1UZK	2512	2BV4	200	2IXT	1314
1DPO	246	1MU5	1	1UZV	997	2BV4	300	2IXT	1315
1DYK	4001	1MU5	2	1UZV	998	2BV4	200	2J12	1139
1DYK	4002	1MVE	400	1UZV	997	2BV4	300	2J1A	1769
1E29	225	1MVQ	237	1UZV	998	2BWR	500	2J1G	1290
1E29	226	1MXG	438	1UZV	997	2BWR	501	2J1G	1291
1E29	227	1N28	125	1UZV	998	2BWR	500	2J1G	1289
1E43	501	1N28	126	1UZV	997	2BWR	501	2J1G	1290
1E43	502	1N28	127	1UZV	998	2BZ6	1260	2J1G	1291
1E43	503	1N28	128	1V0A	1176	2C1V	403	2J1V	1152
1E43	504	1N7S	501	1V0A	1177	2C1V	403	2J1V	1152
1E8A	89	1N7S	502	1V0Z	1477	2C2H	1183	2J1Y	1291
1E8A	90	1N7S	503	1V0Z	1477	2C2H	1184	2J1Y	1291
1E8A	89	1NBC	1	1V0Z	1477	2C2H	1185	2J1Y	1291
1E8A	90	1NBC	1	1V0Z	1477	2C2H	1186	2J1Y	1291
1ECS	390	1NKG	800	1V3E	4001	2C2H	1187	2J22	1150
1EDM	3	1NL1	201	1V3E	2001	2C2H	1193	2J45	1401
1EDM	1	1NL1	202	1V3W	3002	2C2H	1182	2J45	1401
1EDM	2	1NL1	203	1V3W	3003	2C2H	1183	2J5Z	1277
1EJ8	218	1NL1	204	1V3W	3004	2C2H	1184	2J5Z	1277
1EK3	498	1NL1	205	1V3W	3005	2C2H	1185	2J5Z	1277
1EK3	499	1NL1	206	1V73	2001	2C2H	1186	2J78	1447
1EL1	130	1NL1	207	1V73	2002	2C2H	1191	2J78	1448
1EL1	130	1NLS	240	1V7W	1001	2C42	2239	2J78	1445
1ELT	300	1NNL	2001	1V7W	1002	2C42	2239	2J7T	332
1EPF	5001	1NNL	2002	1V7W	1003	2C4X	1252	2J7T	333
1EX0	1320	1NNL	2003	1V97	3008	2C4X	1253	2J7T	1318
1EX0	1321	1NPC	319	1V97	4008	2C60	1123	2J7T	1319
1EXR	1000	1NPC	320	1VBL	417	2C8S	1174	2J7T	1320
1EXR	1001	1NPC	321	1VCH	1006	2CCM	1192	2J7T	1321
1EXR	1002	1NPC	322	1VCL	1001	2CCM	1193	2J7T	1322
1EXR	1003	1NPS	90	1VCL	1002	2CCM	1194	2JAM	1306
1EXR	1004	1NPS	145	1VCL	1003	2CCM	1192	2JBH	1228
1F4N	101	1NQD	1009	1VCL	1004	2CCM	1193	2JBH	1229
1F4N	102	1NQD	1010	1VCL	1005	2CCM	1194	2JBH	1228
1F4N	103	1NQD	1009	1VCL	1001	2CDO	1139	2JBH	1229
1F4N	104	1NQD	1010	1VCL	1002	2CDO	1140	2JDA	1146
1F7L	130	1NRW	903	1VCL	1003	2CDO	1139	2JDA	1146
1F7L	132	1NSC	468	1VCL	1004	2CDO	1140	2JEP	1398
1F8E	999	1NSC	469	1VCL	1005	2CDO	1139	2JEP	1397
1F8E	998	1NSC	470	1VEM	930	2CDO	1140	2JFP	1271
1FKQ	124	1NXC	1	1VJJ	911	2CDO	1139	2JFP	1271
1FMJ	402	1NZI	1001	1VJJ	912	2CDO	1140	2MCM	163
1FMJ	502	1NZI	1002	1VJJ	913	2CF7	2173	2MSB	1
1FNY	500	1O4Y	700	1VJJ	941	2CF7	2174	2MSB	2
1FOB	400	1O5K	601	1VJJ	942	2CF7	2175	2MSB	3
1FS7	651	1O6V	1497	1VJJ	943	2CFT	1297	2MSB	1
1G1T	160	1O6V	1497	1VLF	900	2CFT	1298	2MSB	2
1G4I	124	1O9I	269	1VLF	901	2CHH	1114	2MSB	3
1G87	18	1O9I	269	1VLF	900	2CHH	1115	2NQ6	404

1G87	19	1O9I	269	1VLF	901	2CHI	210	2NVO	1
1G87	20	1O9I	269	1VLF	900	2CHI	211	2NWH	401
1G87	21	1O9I	269	1VLF	901	2CHI	218	2NWH	402
1G8F	517	1O9I	269	1VLF	900	2CHO	1717	2O1K	501
1G8F	519	1OAC	802	1VLF	901	2CHO	1716	2O4V	701
1G8F	520	1OAC	803	1VLF	900	2CKI	997	2O4V	702
1G8I	1597	1OAC	802	1VLF	901	2CKI	998	2O4V	703
1G8I	1598	1OAC	803	1VLF	900	2CKI	1403	2OAI	101
1G8I	1599	1OCN	456	1VLF	901	2CKI	997	2OAI	102
1G8I	1600	1OCN	457	1VLY	505	2CKI	998	2OBL	1001
1G8I	1601	1OD3	1153	1VZI	1126	2CM5	1678	2OEE	1
1G8I	1602	1OFL	528	1VZI	1127	2CM5	1679	2OEE	2
1G8K	5007	1OH4	1186	1W07	1661	2CN3	1778	2OG9	401
1G8K	5008	1OMR	501	1W0N	1132	2CN3	1777	2OG9	402
1G8K	5107	1OS1	999	1W0P	1779	2CNH	1299	2OLG	2001
1G8K	5108	1OS8	249	1W0P	1780	2CY5	1500	2OPO	301
1G8K	5207	1OU9	1	1W0P	1781	2CYY	2001	2OPO	302
1G8K	5208	1OU9	2	1W0P	1782	2CYY	2002	2OPO	303
1G8K	5307	1OVA	500	1W15	1001	2CYY	2003	2OPO	304
1G8K	5308	1OYG	500	1W15	1002	2CYY	2004	2OPO	305
1G94	800	1P6O	402	1W15	1003	2D39	1401	2OPO	306
1G9G	398	1P6O	403	1W32	1347	2D39	2401	2OPO	307
1G9K	700	1PA2	307	1W32	1347	2D3D	101	2OPO	308
1G9K	701	1PA2	308	1W3M	2013	2D3N	501	2OR4	1753
1G9K	702	1PAM	1	1W3M	2015	2D3N	502	2OTM	1
1G9K	703	1PAM	2	1W3M	2016	2D3N	503	2OVX	405
1G9K	704	1PAM	1	1W3M	2017	2D73	801	2OVX	406
1G9K	705	1PAM	2	1W3M	2014	2D73	802	2OVX	407
1G9K	706	1PG6	201	1W3M	2015	2DDF	400	2OVX	408
1GA6	374	1PG6	202	1W3M	2016	2DDR	1324	2OVX	409
1GBG	373	1PJX	491	1W3M	2013	2DDR	1325	2OVX	410
1GCI	277	1PJX	492	1W3M	2014	2DDR	1326	2OVX	411
1GCI	278	1PK6	1	1W3M	2013	2DDR	1327	2OVX	412
1GCY	451	1PMH	300	1W3M	2014	2DDR	1328	2OVX	413
1GCY	452	1POA	201	1W3M	2013	2DDR	1329	2OVX	414
1GGZ	148	1POA	401	1W3M	2014	2DDR	1330	2OX9	801
1GGZ	149	1POC	501	1W3M	2015	2DDR	1331	2OX9	802
1GGZ	150	1PVA	110	1W3M	2016	2DG1	3001	2OX9	803
1GGZ	151	1PVA	111	1W3M	2017	2DG1	3002	2OX9	804
1GK9	1579	1PVA	110	1W3M	2016	2DG1	3003	2OX9	801
1GR3	901	1PVA	111	1W3M	2017	2DG1	3004	2OX9	802
1GR3	903	1PWB	401	1W3M	2013	2DG1	3005	2OX9	803
1GTT	1430	1PWB	402	1W3M	2014	2DG1	3006	2OX9	804
1GTT	1430	1PWB	403	1W3M	2014	2DG1	3007	2OX9	801
1GTT	1430	1PWB	401	1W3M	2015	2DG1	3008	2OX9	802
1GTT	1430	1PWB	402	1W3M	2015	2DG1	3009	2OX9	803
1GUI	200	1PWB	403	1W3M	2016	2DG1	3010	2OX9	804
1GUN	1071	1PWB	401	1W3M	2013	2DG1	3011	2OX9	801
1GUN	1071	1PWB	402	1W3W	1328	2DG1	3012	2OX9	802
1GVK	1246	1PWB	403	1W6S	1599	2DOB	601	2OX9	803

1GWU	1307	1PZ7	701	1W6S	3599	2DPQ	101	2OX9	804
1GWU	1308	1PZ7	702	1W7C	802	2DPQ	102	2OZI	503
1GXR	1003	1Q6Z	532	1W7C	803	2DPQ	103	2P3U	501
1GZC	290	1Q6Z	533	1WAD	116	2DPR	101	2P3U	502
1H0H	1100	1Q6Z	534	1WDC	501	2DPR	102	2P5V	1001
1H0H	1100	1Q8F	2001	1WKY	503	2DPR	103	2P5V	1002
1H1A	1195	1Q8F	2002	1WL7	314	2DPR	104	2P5V	1003
1H4W	260	1Q8F	2003	1WMD	1001	2DS5	299	2P5V	1004
1H5V	305	1Q8F	2004	1WMD	1002	2DSN	2011	2P5V	1005
1H5V	306	1Q8H	71	1WMD	1003	2DSN	2012	2P5V	1006
1H5V	307	1Q8H	72	1WMZ	201	2DUR	1	2P5V	1007
1H5V	308	1Q8H	73	1WMZ	202	2DUR	2	2P5V	1008
1H5V	309	1QDB	520	1WMZ	203	2E26	601	2PAG	201
1H5V	310	1QDB	520	1WMZ	201	2E26	602	2PAG	202
1H5V	311	1QDB	520	1WMZ	202	2E26	604	2PKT	201
1H5V	312	1QGD	675	1WMZ	203	2E26	605	2PKT	202
1H5V	313	1QGD	675	1WMZ	201	2E3B	501	2PLT	101
1H5V	314	1QGJ	2001	1WMZ	202	2E3B	502	2PNY	1
1H6L	401	1QGJ	2002	1WMZ	203	2E4T	701	2POR	302
1H6L	402	1QGJ	2001	1WMZ	201	2E6U	201	2POR	303
1H6L	403	1QGJ	2002	1WMZ	202	2EAB	1	2POR	304
1H6L	404	1QH4	382	1WMZ	203	2EAB	2	2PQX	500
1H6L	405	1QHD	503	1WWS	1	2EJN	1001	2PR7	1
1H6L	406	1QHD	508	1WWS	2	2EJN	1002	2PR7	2
1H6L	407	1QHD	601	1WWS	4	2EJN	1003	2PVB	110
1H80	1492	1QHD	602	1WWS	5	2EJN	1004	2PVB	111
1H80	1493	1QHD	603	1WWS	6	2ERV	195	2PVZ	1001
1H80	1494	1QHO	696	1WWS	7	2ESL	1	2PVZ	1002
1H80	1492	1QHO	697	1WZA	601	2ESL	2	2PVZ	1003
1H80	1493	1QHO	698	1WZA	602	2ESL	3	2PVZ	1004
1H80	1494	1QMP	301	1WZL	1601	2ESS	1	2PWA	1280
1H9W	239	1QMP	301	1WZL	2601	2EU8	1	2PY2	901
1H9W	239	1QMP	301	1X1N	2001	2EXH	2001	2PY2	902
1H9W	243	1QMP	301	1X7I	1251	2EXH	2002	2PY2	903
1HDH	1528	1QPA	351	1X9D	1001	2EXH	2003	2PY2	904
1HDH	1528	1QPA	352	1XF1	1109	2EXH	2004	2PY2	905
1HFC	277	1QPA	351	1XF1	1110	2F1W	301	2PY2	906
1HFX	124	1QPA	352	1XK4	1501	2F1W	302	2QLT	278
1HJ8	1001	1QV1	403	1XK4	1502	2FCW	3001	2QNG	201
1HJ9	1001	1QX2	1001	1XK4	2501	2FCW	3002	2QNG	202
1HL5	156	1QX2	1002	1XK4	2502	2FGQ	502	2QP2	512
1HL5	156	1QX2	1005	1XK4	3501	2FGQ	503	2QU1	239
1HL5	156	1QX2	1006	1XK4	3502	2FGQ	501	2QUB	614
1HLE	647	1R0R	301	1XK4	4501	2FH1	2001	2QUB	615
1HM9	1901	1R0R	302	1XK4	4502	2FH1	2002	2QUB	616
1HM9	1902	1R0R	303	1XK4	1511	2FH1	2003	2QUB	617
1HM9	1903	1R0R	305	1XK4	1512	2FH1	3001	2QUB	618
1HM9	1904	1R17	501	1XK4	2511	2FH1	3002	2QUB	619
1HM9	2901	1R17	502	1XK4	2512	2FH1	3003	2QUB	620
1HM9	2902	1R55	402	1XK4	3511	2FH1	4001	2QUB	621

1HM9	2903	1R6V	1	1XK4	3512	2FH1	4002	2QUB	614
1HM9	2904	1RDO	1	1XK4	4511	2FH1	4003	2QUB	615
1HT6	500	1RDO	2	1XK4	4512	2FHF	2401	2QUB	616
1HT6	501	1RDO	1	1XK4	1521	2FHF	2402	2QUB	617
1HT6	502	1RDO	2	1XK4	1522	2FHF	2403	2QUB	618
1HVX	501	1RK8	9001	1XK4	2521	2FHF	2404	2QUB	619
1HVX	502	1RK8	9002	1XK4	2522	2FHF	2405	2QUB	620
1HVX	503	1RK8	9003	1XK4	3521	2FI1	1	2QUB	621
1HX0	500	1RM8	502	1XK4	3522	2FMD	301	2QUB	614
1HY7	303	1RM8	504	1XK4	4521	2FPW	503	2QUB	615
1HY7	304	1RRO	109	1XK4	4522	2FPW	504	2QUB	616
1HY7	305	1RRO	110	1XO5	1	2FPW	505	2QUB	617
1HY7	803	1RRO	124	1XO5	2	2FVY	308	2QUB	618
1HY7	804	1RRO	135	1XO5	3	2FXF	301	2QUB	619
1HY7	805	1RU4	1	1XO5	4	2FXF	302	2QUB	620
1HYO	1006	1RU4	2	1XO5	5	2FXF	304	2QUB	621
1HYO	1007	1RWY	421	1XO5	6	2FXF	305	2QUB	614
1I0V	105	1RWY	422	1XO5	7	2FXU	100	2QUB	615
1I40	302	1RWY	423	1XO5	8	2FXU	200	2QUB	616
1I40	303	1RWY	424	1XPH	402	2FXU	300	2QUB	617
1I40	304	1RWY	425	1XVB	1174	2FXU	400	2QUB	618
1I40	305	1RWY	426	1XYN	601	2G0I	1001	2QUB	619
1I40	306	1RZ3	555	1XZO	1005	2G0I	1002	2QUB	620
1I4A	401	1S0E	1292	1XZO	1006	2G8J	301	2QUB	621
1I4A	410	1S0E	1293	1XZO	1007	2G8J	302	2QUB	614
1I52	2001	1S1D	1001	1XZO	1008	2G8S	2001	2QUB	615
1I76	996	1S1D	1002	1XZO	1009	2G8S	2002	2QUB	616
1I76	997	1S3X	385	1XZO	1010	2GEB	201	2QUB	617
1I8A	190	1S3X	386	1XZO	1011	2GEB	202	2QUB	618
1I8A	191	1S6C	201	1XZO	1012	2GF6	1	2QUB	619
1I8A	192	1S6C	202	1XZO	1013	2GJP	1486	2QUB	620
1I9Z	301	1S99	801	1XZO	1014	2GJP	1487	2QUB	621
1IA6	1263	1SAC	1	1XZO	1015	2GJP	1488	2QUB	614
1IAG	250	1SAC	2	1XZO	1016	2GKO	610	2QUB	615
1IQC	410	1SAC	1	1XZO	1017	2GKO	611	2QUB	616
1IQC	1411	1SAC	2	1XZO	1018	2GKO	612	2QUB	617
1IQC	410	1SAC	1	1Y1X	201	2GKO	613	2QUB	618
1IQC	410	1SAC	2	1Y1X	202	2GQT	501	2QUB	619
1IQC	410	1SAC	1	1Y1X	211	2GSM	3007	2QUB	620
1IVG	470	1SAC	2	1Y1X	212	2GSM	4007	2QUB	621
1IVG	470	1SAC	1	1Y3N	493	2GUY	601	2R01	210
1IYI	1900	1SAC	2	1Y4J	1001	2GXS	601	2SCP	190
1IYI	1901	1SAT	473	1Y4J	1002	2GXS	602	2SCP	191
1IZ7	2002	1SAT	474	1Y4J	1003	2GXS	603	2SCP	192
1IZ7	2003	1SAT	475	1Y4J	1004	2GXS	604	2SCP	193
1IZ7	2004	1SAT	476	1Y5Y	201	2GXS	605	2SCP	194
1J0H	601	1SAT	477	1Y7B	3001	2H2K	301	2SCP	195
1J0H	602	1SAT	478	1Y7B	3002	2H2K	302	2UZP	1296
1J1N	493	1SAT	479	1Y7B	3003	2H2K	303	2UZP	1297
1J1N	493	1SEO	806	1Y7B	3004	2H2K	304	2UZP	1298

1J1T	301	1SH7	1290	1Y93	266	2H2T	160	2UZP	1296
1J24	1001	1SH7	1291	1Y93	267	2H9D	301	2UZP	1297
1J34	502	1SH7	1292	1Y93	268	2HD9	2001	2UZP	1298
1J34	503	1SH7	2290	1Y9I	501	2HES	400	2UZP	1296
1J34	504	1SH7	2291	1Y9I	502	2HNF	301	2UZP	1297
1J34	505	1SH7	2292	1Y9I	503	2HNF	302	2UZP	1298
1J34	506	1SL4	401	1Y9I	504	2HNF	303	3CSU	53
1J34	511	1SL4	402	1Y9Z	603	2HNF	304	3CSU	114
1J34	512	1SL4	403	1Y9Z	604	2HQ8	201	3LHM	131
1J3B	1001	1SL8	669	1Y9Z	605	2HQ8	202	3STD	501
1J3B	1002	1SL8	670	1Y9Z	606	2HQ8	203	3STD	502
1J4G	1201	1SL8	671	1YDY	903	2HQ8	301	4DFR	3
1J4G	1202	1SNC	142	1YDY	904	2HQ8	302	4ICB	76
1J4G	1203	1SNN	403	1YFQ	800	2HQ8	303	4ICB	77
1J4G	1204	1SNN	503	1YFQ	801	2HRG	1001	5CHY	401
1J55	101	1SNN	601	1YFQ	802	2HRG	1002	5PAL	110
1J55	102	1SNN	602	1YFQ	803	2HRG	1003	5PAL	111
1J5U	301	1SPJ	300	1YII	401	2HYV	601	830C	264
1J83	4000	1SPJ	301	1YII	402	2HYV	602	830C	263
1J83	4001	1SRA	301	1YII	403	2HYV	605	8DFR	200
1J8E	201	1SRA	302	1YLE	701	2HYV	607	8TLN	317
1J9L	1301	1SRA	303	1YLI	1	2HYV	608	8TLN	318
1J9L	1302	1SRR	531	1YLI	2	2I1Q	502	8TLN	319
1J9L	1303	1SRR	532	1YLI	3	2I1Q	503	8TLN	320

Summary list of all Ca^{2+}-binding sites evaluated in statistical analysis. **PDB ID:** Protein Data Bank structural data file identifier. **Ca Seq ID:** PDB identifier for sequence number of Ca^{2+} ion.

Table A.3 Summary data for examples of zero charge Non-EF-Hand binding sites

PDB ID	Ca^{2+} Site	Res	Atom ID	Res Seq #	Chain	D_{ligand} (Å)	CLI Angle (°)	Ligand Type	2° Structure
1AVA	503	HOH	O	113	---	2.9	---	HOH	---
1AVA	503	HOH	O	702	---	2.7	---	HOH	---
1AVA	503	HOH	O	562	---	2.4	---	HOH	---
1AVA	503	HOH	O	97	---	2.4	---	HOH	---
1AVA	503	HOH	O	114	---	2.3	---	HOH	---
1AVA	503	HOH	O	152	---	2.2	---	HOH	---
1AVA	503	HOH	O	98	---	2.1	---	HOH	---
1AVA	503	GLU	OE2	168	D	4.5	---	O	Loop
1AVA	503	TYR	OH	170	D	4.7	---	O	Loop
1AVA	503	ASP	OD1	179	B	4.3	---	O	Loop
1AVA	503	ASP	OD2	179	B	4.9	---	O	Loop
1AVA	503	GLU	OE2	204	B	4.9	---	O	Loop
1AVA	503	GLU	OE1	204	B	5.0	---	O	Loop
1AVA	503	ASP	OD2	289	B	4.4	---	O	Loop
1AVA	503	ASP	OD1	289	B	4.7	---	O	Loop
2DG1	3012	TYR	O	135	F	2.6	135.88	MC O	Loop
2DG1	3012	TYR	N	135	F	3.4	97.43	MC N	Loop
2DG1	3012	THR	O	133	F	2.6	109.64	MC O	Loop
2DG1	3012	THR	OG1	133	F	2.5	135.96	SC O	Loop
2DG1	3012	ASP	O	130	F	2.5	133.96	MC O	Loop
2DG1	3012	GLY	O	112	F	2.5	138.63	MC O	Loop
2DG1	3012	GLY	N	112	F	3.4	107.09	MC N	Loop
2DG1	3012	SER	O	110	F	2.3	149.99	MC O	Loop
2EXH	2003	ASP	O	333	C	2.4	132.19	MC O	Loop
2EXH	2003	GLY	O	362	C	2.7	109.84	MC O	Loop
2EXH	2003	ASP	O	528	C	2.3	138.9	MC O	Beta
2EXH	2003	HOH	O	709	C	2.6	---	HOH	---
2EXH	2003	HOH	O	779	C	2.4	---	HOH	---
2EXH	2003	HOH	O	904	C	3.1	---	HOH	---

PDB ID indicates the code associated with structural data deposited in Protein Data Bank; **Ca^{2+} Site** is the PDB sequence number associated with the calcium ion; **Res** is the amino acid providing the ligand atom; **Atom ID** indicates the atom type; **Res Seq #** is the primary sequence number of the residue; **Chain** is the PDB chain identifier; **D_{ligand}** is the distance between the ion and the ligand atom; **CLI Angle** is the angle between the calcium ion, the binding ligand atom and its associated carbon; **Ligand Type** indicates whether the ligand atom (N or O) is from the mainchain, sidechain, or water; and **2° Structure** indicates secondary structure origin of ligand.

Table A.4 Charge-charge interactions beyond primary Ca^{2+}-binding coordination

		Primary Ligand			*Charge-Charge Network*			
PDB ID	**Ca^{2+} Site**	**Residue**	**Res Seq #**	**Atom ID**	**Residue**	**Res Seq #**	**Atom ID**	**$D_{chg-chg}$ (Å)**
2DG1	3012	SER	110	N	ASP	107	OD2	2.9
2DG1	3012	ASP	130	OD2	LYS	86	NZ	3.0
2EXH	2003	ASP	528	OD2	LYS	395	NZ	3.0
2EXH	2003	ASP	528	OD1	HIS	363	NE2	2.8
2EXH	2003	ASP	333	N	LYS	331	O	3.1
2EXH	2003	ASP	333	OD2	LYS	331	NZ	4.1

PDB ID indicates the code associated with structural data deposited in Protein Data Bank; **Ca^{2+} Site** is the PDB sequence number associated with the calcium ion; **Res** is the amino acid providing the ligand atom; **Res Seq #** is the primary sequence number of the residue; **Atom ID** indicates the atom type; **$D_{chg-chg}$** is the distance between the primary ligand and charged atoms beyond the second shell.

Table A.5 Peak differentiation for EF-Hand sidechain and mainchain Ca-O-C angles in bimodal distribution

PDB ID	[a]SC R1	[b]SC R2	[c]MC R1	[d]MC R2	Description	[e]Family
1QX2	3	3	7	3	calbindomodulin	Calbindin D9K
4ICB	1	2	3	2	calbindin D9K	Calbindin D9K
1EXR	7	5	4	0	Calmodulin	Calmodulin-like
1G8I	6	11	1	5	neuronal Ca sensor	Calmodulin-like
1GGZ	8	4	1	3	calmodulin-like protein	Calmodulin-like
1OMR	2	1	0	1	bovine recoverin	Calmodulin-like
1QV1	1	2	0	1	Obelin	Calmodulin-like
1S6C	1	5	1	1	KChIP1/Kv4.2 N1-30	Calmodulin-like
1SL8	3	6	1	2	apo-aequorin	Calmodulin-like
1WDC	2	1	3	0	scallop myosin	Calmodulin-like
1XO5	6	8	4	1	CIB1	Calmodulin-like
2BL0	0	3	1	0	polycelphalin myosin II	Calmodulin-like
2SCP	7	9	1	5	sarcoplasmic CaBP	Calmodulin-like
1SRA	3	2	2	1	osteonectin	Osteonectin
1A75	10	3	2	2	parvalbumin	Parvalbumin
1BU3	5	2	1	1	parvalbumin	Parvalbumin
1PVA	8	6	1	3	parvalbumin	Parvalbumin
1RRO	4	2	0	2	rat oncomodulin	Parvalbumin
1RWY	13	8	3	3	alpha-parvalbumin	Parvalbumin
2PVB	5	2	1	1	parvalbumin	Parvalbumin
5PAL	5	2	0	2	alpha-parvalbumin	Parvalbumin
1K94	5	4	3	1	grancalcin	Penta-EF-Hand
1Y1X	7	5	0	4	cell death 6 protein	Penta-EF-Hand
1K9U	3	7	2	2	polcalcin	Polcalcin
1E8A	2	3	6	4	human S100A12	S100 Proteins
1J55	1	2	4	1	human S100P	S100 Proteins
1K96	2	1	3	2	human S100A6	S100 Proteins
1XK4	15	24	46	14	human calprotectin	S100 Proteins
2H2K	3	3	5	5	human S100A13	S100 Proteins
2AAO	13	8	2	5	protein kinase	**SCU
2CCM	8	10	0	6	calexcitin	**SCU
2HQ8	10	8	4	2	coelenterazine-binding	**SCU
2OPO	15	9	2	6	polcalcin che a 3	**SCU

[a]Sidechain Region 1 (116.00°-138.49°); [b]Sidechain Region 2 (138.50° - 170.00°);
[c]Mainchain Region 1 (116.00°-163.49°); [d]Mainchain Region 2 (163.50° - 180.00°);
[e]SCOP Classifications; *Contains both EF-Hand/S100 Sites;
**SCOP Classification Unavailable

Table A.6 Crystallized PDB proteins found to bind Pb^{2+} ions

[a]PDB ID	Description	[b]Res (Å)	Total Pb^{2+} Sites	Retained Pb^{2+} Sites
1AFV	Hiv-1 Capsid Protein (P24) Complex	3.7	2	1
1E9N	Human apurinic/apyrimidin endonuclease	2.2	4	2
1FJR	Crystal Ectodomain Of Methuselah	2.3	4	2
1HD7	apurinic/apyrimidin endonuclease	1.95	1	1
1HQJ	De Novo Designed coiled-coil peptide	1.2	9	7
1IW7	Bacterial Rna Polymerase...	2.6	4	2
1KA4	Pyrococcus Furiosus Carboxypeptidase	3	1	1
1N0Y	Crystal Pb-Bound Calmodulin	1.75	14	11
1NA0	Tetratricopeptide repeat	1.6	5	3
1QNV	Yeast 5-Aminolaevulinic Acid...	2.5	2	2
1QR7	3-deoxy-D-arabino-heptulosonate-7-phosphate synthase	2.6	4	1
1SN8	S1 Domain Of Rnase E	2	2	2
1SYY	Ribonucleotide Reductase	1.7	1	1
1V0D	Caspase-Activated DNAse (Cad)	2.6	1	1
1XXA	E.Coli ARG Repressor	2.2	4	2
1ZHW	Yeast Oxysterol Binding Protein Osh4	1.7	1	1
1ZHY	Yeast Oxysterol Binding Protein Osh4	1.6	2	2
2ANI	F127y Mutant Ribonucleotide Reductase	2	1	1
2CH7	Cytoplasmic Domain, Bacterial Chemoreceptor	2.5	2	2
2FP1	Chorismate Mutase	1.55	2	2
2G0A	Mouse Pyrimidine 5'-Nucleotidase	2.35	2	1
		Total	68	48

[a]Protein DataBank Identification
[b]Resolution

Table A.7 Selected metal properties

Z	Ion	[a]Ionic Radius (Å)	[a]Pauling EN	[a]Electron Configuration	[b]Acid Type	[b]Ligand Preference
20	Ca^{2+}	0.99	1	$[Ar]4s^0$	Hard	Oxygen
30	Zn^{2+}	0.74	1.65	$[Ar]3d^{10}\ 4s^0$	Borderline	Nitrogen
82	Pb^{2+}	1.19	2.33	$[Xe]4f^{14}5d^{10}6s^26p^0$	Borderline	Nitrogen

[a]http://environmentalchemistry.com/yogi/periodic/
[b]Glusker et al. [5]

Table A.8 Binding site data for Ca^{2+} (1exr, *R*=1.00 Å) and Pb^{2+} (1n0y, *R*=1.75 Å) in CaM EF loops I-IV

Res Seq Nbr	Ca^{2+} Lig Res	Ca^{2+} Lig Atom	Ca^{2+} Bind Dist (Å)	Ca^{2+} CLI Angle (°)	Pb^{2+} Lig Res	Pb^{2+} Lig Atom	Pb^{2+} Bind Dist (Å)	Pb^{2+} CLI Angle (°)	Bind Δ_{Dist}	CLI Δ_{Angle}
		1exr				1n0y				
20	ASP	OD1	2.31	144.80	ASP	OD1	2.30	146.18	-0.01	1.38
22	ASP	OD1	2.44	143.85	ASP	OD1	2.51	129.63	0.07	-14.22
24	ASP	OD1	2.35	133.89	ASP	OD1	2.62	117.80	0.27	-16.09
26	THR	O	2.35	155.06	THR	O	2.67	134.14	0.32	-20.92
26	THR	*OG1	--	--	THR	‡OG1	3.49	130.31	--	--
31	GLU	OE1	2.47	92.41	GLU	OE1	2.58	90.19	0.11	-2.22
31	GLU	OE2	2.48	92.02	GLU	OE2	2.54	92.06	0.06	0.04
EFI								**Mean**	0.14	-8.67
56	ASP	OD1	2.34	133.03	ASP	OD1	2.25	154.66	-0.09	21.63
58	ASP	OD1	2.43	146.8	ASP	OD1	2.45	109.63	0.02	-37.17
58	ASP	*OD2	--	--	ASP	‡OD2	3.13	77.27	--	--
60	ASN	OD1	2.40	127.89	ASN	OD1	2.35	118.54	-0.05	-9.35
62	THR	O	2.41	159.42	THR	O	2.52	153.61	0.11	-5.81
64	ASP	*OD2	--	--	ASP	‡OD2	3.34	112.38		
67	GLU	OE1	2.47	96.4	GLU	OE1	2.75	93.73	0.28	-2.67
67	GLU	OE2	2.60	89.39	GLU	OE2	2.82	90.49	0.22	1.10
EFII								**Mean**	0.08	-5.38
93	ASP	OD1	2.30	161.87	ASP	OD1	2.36	166.97	0.06	5.10
95	ASP	OD1	2.33	130.85	ASP	OD1	2.35	122.79	0.02	-8.06
97	ASN	OD1	2.42	132.81	ASN	OD1	2.36	136.53	-0.06	3.72
99	LEU	O	2.28	162.46	LEU	O	2.28	157.24	0.00	-5.22
104	GLU	OE1	2.46	94.51	GLU	OE1	2.49	91.74	0.03	-2.77
104	GLU	OE2	2.54	89.99	GLU	OE2	2.54	89.17	0.00	-0.82
EFIII								**Mean**	0.01	-1.34
129	ASP	OD1	2.30	150.12	ASP	OD1	2.37	145.6	0.07	-4.52
131	ASP	OD1	2.34	123.46	ASP	OD1	2.47	110.61	0.13	-12.85
131	ASP	*OD2	--	--	ASP	‡OD2	3.19	75.87	--	--
133	ASP	OD1	2.38	127.08	ASP	OD1	2.25	134.04	-0.13	6.96
135	HIS	O	2.35	149.88	HIS	O	2.52	133.14	0.17	-16.74
140	GLU	OE1	2.44	96.06	GLU	OE1	2.47	100.58	0.03	4.52
140	GLU	OE2	2.55	91.05	GLU	OE2	2.78	86.05	0.23	-5.00
EFIV								**Mean**	0.08	-4.61

ResSeqNbr: residue sequence number. **Ca^{2+} LigRes**: ligand residue for calcium-binding. **Ca^{2+} LigAtom**: ligand atom. **Ca^{2+} BindDist**: distance between the Ca^{2+} ion and the ligand atom. **Ca^{2+} CLI Angle**: carbon-ligand-ion angle for the Ca^{2+} ion. Columns are repeated for Pb^{2+}. **Bind Δ_{Dist}**: difference in binding distance between Ca^{2+} and Pb^{2+} for identical ligands. **CLI Δ_{Angle}**: difference in carbon-ligand-ion angles. Ligand atoms labeled with * indicate non-binding. Ligand atoms labeled with ‡ indicate possible binding.

Table A.9 Binding site data for Zn^{2+} (1eb3, *R*=1.75 Å) and Pb^{2+} (1qnv, *R*=2.50 Å) in ALAD

	1eb3				1qnv					
Res Seq Nbr	**Zn^{2+} Lig Res**	**Zn^{2+} Lig Atom**	**Zn^{2+} Bind Dist (Å)**	**Zn^{2+} CLI Angle (°)**	**Pb^{2+} Lig Res**	**Pb^{2+} Lig Atom**	**Pb^{2+} Bind Dist (Å)**	**Pb^{2+} CLI Angle (°)**	**Bind Δ_{Dist}**	**CLI Δ_{Angle}**
133	CYS	SG	2.26	107.96	CYS	SG	2.74	97.53	0.48	-10.43
135	CYS	SG	2.26	105.77	CYS	SG	2.82	81.99	0.56	-23.78
143	CYS	SG	2.27	105.71	CYS	SG	2.84	106.05	0.57	0.34
179	SER	*OG	4.19	128.94	SER	*OG	3.99	128.22	--	--
179	SER	*O	4.28	106.69	SER	O	3.38	164.63	--	--
								Mean	0.54	-11.29

ResSeqNbr: residue sequence number. **Zn^{2+} LigRes**: ligand residue for zinc-binding. **Zn^{2+} LigAtom**: ligand atom. **Zn^{2+} BindDist**: distance between the Zn^{2+} ion and the ligand atom. **Zn^{2+} CLI Angle**: carbon-ligand-ion angle for the Zn^{2+} ion. Columns are repeated for Pb^{2+}. **Bind Δ_{Dist}**: difference in binding distance between Zn^{2+} and Pb^{2+} for identical ligands. **CLI Δ_{Angle}**: difference in carbon-ligand-ion angles. Ligand atoms labeled with * indicate non-binding.

Table A.10 Ca/CaM chemical exchange

Slow	Intermediate	Fast
K77	D20	I9
E83	K21	A10
E84	D22	E11
I85	G23	F12
D93	D24	K13
D95	G25	E14
G96	T26	A15
A103	I27	F16
V108	T28	S17
T110	T29	L18
N111	K30	F19
L112	E31	L32
G113	D56	G33
K115	A57	T34
D118	G61	V35
E119	T62	R37
V121	I63	S38
I125	D64	L39
R126	F65	G40
E127	E67	A46
D129	T79	E47
G132	S81	L48
Q135	E82	Q49
E140	E87	D50
F141	K94	M51
V142	N97	I52
T146	G98	N53
A147	Y99	E54
	I100	V55
	S101	D58
	A102	G59
	R106	F68
	E114	L69
	L116	T70
	A128	M72
	I130	A73
	D131	K75
	D133	M76
	G134	
	V136	
	N137	
	Y138	
	E139	
	Q143	
	M144	
	M145	

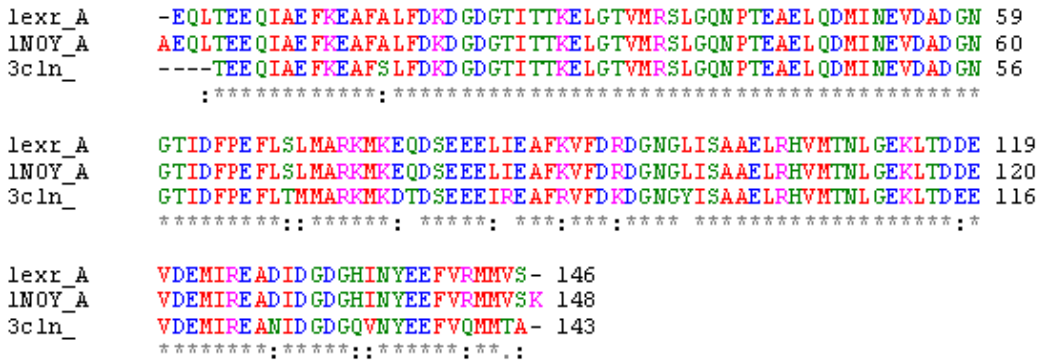

Figure A.1 ClustalW (1.83) MSA (Multiple Sequence Alignment) for three calmodulin sequences from different PDB files

9.4 HNCA/HSQC assignment: apo-CaM

1 mM apo-CaM, 37 °C, pH 6.5, 0.1 mM NaN_3, 100 mM KCl, 10 mM EGTA

Assignment	w1	w2	w3
Q3H-C-N	8.227	55.680	118.259
L4H-C-N	8.248	54.518	121.498
T5H-C-N	8.716	60.532	112.570
E6H-C-N	9.025	60.182	120.139
E7H-C-N	8.741	60.167	118.976
Q8H-C-N	7.731	58.748	120.089
I9H-C-N	8.265	66.408	118.321
A10H-C-N	7.978	55.528	120.400
E11H-C-N	7.808	59.571	119.716
F12H-C-N	8.778	58.611	119.839
K13H-C-N	9.239	59.874	121.104
E14H-C-N	8.130	59.647	120.253
A15H-C-N	7.721	55.231	120.636
F16H-C-N	8.545	61.941	117.473
S17H-C-N	8.436	61.775	110.788
L18H-C-N	7.429	57.201	120.965
F19H-C-N	7.413	58.477	114.440
D20H-C-N	7.380	52.937	122.108
K21H-C-N	8.113	58.483	123.421
D22H-C-N	8.680	54.709	116.867
G23H-C-N	8.080	47.276	110.026
D24H-C-N	8.790	54.071	120.641
G25H-C-N	10.213	46.502	111.825
T26H-C-N	7.678	60.124	109.975
I27H-C-N	8.337	59.454	110.845
T28H-C-N	8.344	60.733	110.700
T29H-C-N	8.353	65.077	112.491
K30H-C-N	7.696	58.482	118.781

E31H-C-N	7.570	56.365	117.240
L32H-C-N	7.448	58.738	120.647
G33H-C-N	8.811	48.459	105.118
T34H-C-N	7.541	65.936	118.122
V35H-C-N	7.997	66.241	122.653
M36H-C-N	8.446	60.193	118.068
R37H-C-N	8.496	59.386	119.305
S38H-C-N	8.184	61.859	118.796
L39H-C-N	7.419	54.720	120.734
G40H-C-N	7.976	46.289	106.923
Q41H-C-N	7.842	54.262	117.627
T44H-C-N	8.744	60.817	112.777
E45H-C-N	8.871	60.129	120.431
A46H-C-N	8.309	55.194	120.628
E47H-C-N	7.754	59.014	118.807
L48H-C-N	8.359	58.141	119.874
Q49H-C-N	8.121	58.854	117.368
D50H-C-N	7.868	57.579	118.818
M51H-C-N	8.009	59.792	118.799
I52H-C-N	8.363	65.202	118.757
N53H-C-N	8.261	55.541	117.241
E54H-C-N	7.656	58.497	117.301
V55H-C-N	7.691	62.432	113.037
D56H-C-N	8.487	53.782	121.840
A57H-C-N	8.141	54.771	124.631
D58H-C-N	8.432	54.713	114.818
G59H-C-N	7.971	47.265	108.722
N60H-C-N	9.252	54.438	119.536
G61H-C-N	9.946	46.392	109.863
T62H-C-N	7.627	59.928	110.766
I63H-C-N	8.922	60.055	118.813
D64H-C-N	8.616	52.361	124.422
F65H-C-N	8.679	62.977	118.857
E67H-C-N	8.047	59.393	117.600
F68H-C-N	8.473	61.485	122.168
L69H-C-N	8.486	57.965	118.494
T70H-C-N	7.765	66.378	115.014
M71H-C-N	7.785	59.127	121.154
M72H-C-N	8.043	56.125	117.201
A73H-C-N	8.353	55.049	120.987
R74H-C-N	7.543	58.724	116.370
K75H-C-N	7.752	56.832	117.972
M76H-C-N	7.952	56.639	117.529
K77H-C-N	7.754	56.981	120.244
D78H-C-N	8.325	54.911	121.687
T79H-C-N	8.137	62.438	114.288
D80H-C-N	8.458	54.979	122.946
S81H-C-N	8.443	59.923	116.716
E82H-C-N	8.487	59.277	121.897
E83H-C-N	8.233	58.979	118.683
E84H-C-N	8.072	59.164	119.099
I85H-C-N	8.202	66.522	120.425

E87H-C-N	8.386	58.850	117.162
A88H-C-N	7.600	54.730	121.159
F89H-C-N	7.555	60.125	114.091
R90H-C-N	8.222	58.971	117.994
V91H-C-N	7.262	64.923	116.807
D93H-C-N	7.914	52.849	121.140
K94H-C-N	8.388	58.723	123.729
D95H-C-N	8.596	54.694	116.293
G96H-C-N	8.086	47.289	109.922
N97H-C-N	9.009	53.519	118.629
S101H-C-N	8.897	58.187	117.284
A102H-C-N	8.811	55.524	124.702
A103H-C-N	8.266	55.028	118.873
R106H-C-N	8.063	59.881	117.154
H107H-C-N	7.753	59.364	118.939
V108H-C-N	8.131	66.149	119.322
M109H-C-N	8.227	58.109	115.525
T110H-C-N	7.985	64.527	111.023
N111H-C-N	7.740	54.818	119.560
L112H-C-N	7.807	55.568	119.729
G113H-C-N	8.168	46.693	107.635
E114H-C-N	8.178	56.778	120.127
K115H-C-N	8.261	57.060	119.831
L116H-C-N	7.831	54.334	121.093
T117H-C-N	8.876	60.923	113.120
D118H-C-N	8.764	57.758	120.837
E119H-C-N	8.603	59.780	118.004
V121H-C-N	7.966	64.258	119.996
E123H-C-N	7.915	57.752	118.913
M124H-C-N	7.967	59.178	118.538
I125H-C-N	8.318	64.859	118.241
R126H-C-N	7.998	59.184	119.783
E127H-C-N	7.921	57.383	117.176
A128H-C-N	7.687	52.741	121.447
D129H-C-N	8.347	54.296	119.406
I130H-C-N	7.851	61.076	120.613
D131H-C-N	8.593	54.050	123.904
G132H-C-N	8.358	46.990	107.799
D133H-C-N	8.343	54.290	119.536
G134H-C-N	8.572	46.337	109.145
Q135H-C-N	8.321	55.261	119.218
N137H-C-N	8.801	52.513	124.755
Y138H-C-N	7.682	59.253	122.393
E139H-C-N	8.160	59.527	125.044
E140H-C-N	7.850	58.936	117.333
F141H-C-N	7.646	61.284	118.917
V142H-C-N	8.182	66.435	119.563
M144H-C-N	7.823	58.482	117.932
M145H-C-N	8.011	57.341	116.213
T146H-C-N	7.766	62.596	110.194
A147H-C-N	7.686	52.936	125.278
K148H-C-N	7.688	57.781	125.246

9.5 HSQC assignment: apo-CaM

500 µM apo-CaM, 37 °C, pH 7.4, 100 mM TRIS, 100 mM KCl, 10 mM EGTA

Assignment	w1	w2
Q3NH-N	8.229	118.278
L4NH-N	8.251	121.560
T5NH-N	8.730	112.664
E6NH-N	9.025	120.139
E7NH-N	8.755	119.038
Q8NH-N	7.729	120.182
Q8E2NH-N	6.740	110.748
Q8E2NH-N	7.574	110.752
I9NH-N	8.261	118.315
A10NH-N	7.973	120.295
F12NH-N	8.788	119.920
K13NH-N	9.235	121.138
E14NH-N	8.119	120.337
A15NH-N	7.706	120.700
F16NH-N	8.547	117.499
S17NH-N	8.445	110.852
L18NH-N	7.422	120.871
F19NH-N	7.421	114.498
D20NH-N	7.364	122.231
K21NH-N	8.085	123.439
D22NH-N	8.683	116.838
G23NH-N	8.068	110.111
D24NH-N	8.780	120.693
G25NH-N	10.224	111.870
T26NH-N	7.704	110.088
I27NH-N	8.327	110.770
T28NH-N	8.327	110.770
T29NH-N	8.357	112.623
K30NH-N	7.695	118.797
E31NH-N	7.568	117.212
L32NH-N	7.422	120.871
G33NH-N	8.827	105.178
T34NH-N	7.539	118.120
V35NH-N	7.994	122.643
M36NH-N	8.450	118.160
R37NH-N	8.500	119.278
S38NH-N	8.172	118.803
L39NH-N	7.422	120.871
G40NH-N	7.963	106.967
Q41NH-N	7.837	117.722
Q41E2NH-N	6.694	110.943
Q41E2NH-N	7.497	110.948

N42D2NH-N	6.753	111.841
T44NH-N	8.769	112.904
E45NH-N	8.866	120.394
A46NH-N	8.307	120.781
E47NH-N	7.757	118.721
L48NH-N	8.358	119.899
Q49NH-N	8.109	117.428
Q49E2NH-N	7.495	112.631
Q49E2NH-N	6.623	112.800
D50NH-N	7.864	118.831
M51NH-N	7.998	118.877
I52NH-N	8.362	118.822
N53NH-N	8.266	117.311
N53D2NH-N	6.909	111.445
N53D2NH-N	7.783	111.443
E54NH-N	7.648	117.318
V55NH-N	7.694	113.136
D56NH-N	8.486	121.874
A57NH-N	8.152	124.737
D58NH-N	8.433	114.757
G59NH-N	7.962	108.795
N60NH-N	9.268	119.672
N60D2NH-N	7.780	113.853
G61NH-N	9.993	110.019
T62NH-N	7.619	110.773
I63NH-N	8.918	118.748
D64NH-N	8.653	124.545
F65NH-N	8.661	118.815
E67NH-N	8.063	117.692
F68NH-N	8.473	122.162
L69NH-N	8.481	118.571
T70NH-N	7.761	115.063
M71NH-N	7.774	121.192
M72NH-N	8.035	117.247
A73NH-N	8.331	120.985
R74NH-N	7.535	116.438
K75NH-N	7.748	117.979
M76NH-N	7.941	117.700
K77NH-N	7.760	120.427
D78NH-N	8.339	121.855
T79NH-N	8.147	114.393
D80NH-N	8.463	123.038
S81NH-N	8.443	116.842
E82NH-N	8.486	121.874
E83NH-N	8.223	118.806
E84NH-N	8.080	119.231
I85NH-N	8.205	120.465
E87NH-N	8.394	117.304
R90NH-N	8.229	118.278
D93NH-N	7.920	121.311
K94NH-N	8.369	123.763
D95NH-N	8.606	116.346

G96NH-N	8.064	109.966
A102NH-N	8.795	124.666
A103NH-N	8.264	119.055
R106NH-N	8.058	117.268
H107NH-H	7.767	119.157
V108NH-N	8.116	119.331
M109NH-N	8.241	115.685
T110NH-N	7.986	110.938
N111NH-N	7.760	119.829
N111D2NH-N	7.436	110.571
N111D2NH-N	6.646	110.569
L112NH-N	7.804	119.817
G113NH-N	8.175	107.766
K115NH-N	8.250	119.889
L116NH-N	7.859	121.164
D118NH-N	8.756	120.869
E119NH-N	8.605	117.968
V121NH-N	7.973	120.295
E123NH-N	7.924	119.054
M124NH-N	7.972	118.598
I125NH-N	8.311	118.340
R126NH-N	8.003	120.030
A128NH-N	7.700	121.478
I130NH-N	7.851	120.699
D131NH-N	8.588	123.846
G132NH-N	8.351	107.967
D133NH-N	8.349	119.430
G134NH-N	8.582	109.259
Q135NH-N	8.324	119.257
N137NH-N	8.795	124.666
E139NH-N	8.163	125.026
E140NH-N	7.856	117.503
F141NH-N	7.649	118.955
V142NH-N	8.167	119.741
M144NH-N	7.847	118.170
M145NH-N	8.021	116.338
T146NH-N	7.773	110.411
A147NH-N	7.697	125.339
K148NH-N	7.697	125.339